Three Dimensional Population Gradients in NGC 891: Constraining the Phase-Space Evolution of Stellar Populations Using the World's First Variable Pitch Integral Field Spectrograph

by

Arthur Eigenbrot

A dissertation submitted in partial fulfillment of

the requirements for the degree of

Doctor of Philosophy

(Astronomy)

at the

University of Wisconsin–Madison

2016

Date of final oral examination: 30 August 2016

The dissertation is approved by the following members of the Final Oral Committee:

Dr. Matthew Bershady, Professor, Astronomy
Dr. Christy Tremonti, Assistant Professor, Astronomy
Dr. Marsha Wolf, Senior Scientist, Astronomy
Dr. Eric Wilcots, Professor, Astronomy
Dr. Dan McCammon, Professor, Physics

Abstract

Studies of the Milky Way show that the vertical velocity dispersion of stars in the disk tends to increase with age. However it is not clear how this "heating" ties into the formation of the observed Milky Way disk structure, or disk galaxies in general. In this thesis I present a study of stellar populations in NGC 891 that adds information to our information on the structure of galaxies outside the Milky Way.

This study was enabled by the construction of HexPak/∇Pak, two fiber integral field units that together form the worlds first dual-head, multi-pitch fiber instrument. The unique design of ∇Pak allowed for the rapid collection of high quality data over a large range in surface brightness and at a high filling factor.

Using ∇Pak I measure trends in stellar population as revealed by both spectral indices and full-spectrum fitting. I find that the overall picture of disk heating in NGC 891 is remarkably similar to trends measured in the Milky Way; the presence of young populations is abruptly cut off at $\sim$1 scale height. Furthermore I find that populations generally get younger farther from the center of NGC 891, perhaps the signature of an inside-out formation scenario. It also appears that each generation of stars forms a flared disk, with later generations forming flares at larger radii.

Finally, I identify two distinct epochs in the enrichment history of NGC 891: (i) a period of self-enrichment lasting from galaxy formation until $\sim$6 Gyr ago, and (ii) a period of decreasing metallicity caused by the infall of pristine gas from outside the galaxy that began 6 Gyr ago and continues today.

Acknowledgments

Humans cannot live on work alone, and without a good outlet for frustration and pent up energy I would probably be on a lot more governmental watchlists. Credit must first be given to Matt Bershady; without your expert guidance and truly shocking (dangerous?) willingness to listen to what I had to say none of this would have been possible. You always pushed me just past my comfort zone and told me *what* to do, not *how* to do it (until I did it wrong a few times). The past six years rank extremely high in the epochs of my development as a legit scientist, and I expect them to remain there for a long time.

Beneath the Ivory Tower, in the beautiful slums of grad school, the passage of time has been eased immeasurably by many of my fellow travelers. To Andrew and Corey, thanks for being great research partners. To Danielle and Britt, your feline obsession did little to temper the pleasure of spending my first 2 years in your company. To the Atom: Anna, Chris, Jenna, and John; thanks for giving me a couch that I could use to get away from the cat talk. That and a lot of snacks and scientific insight. Special mention is gladly given to Jenna, who unwittingly accompanied me through the last 10 years. From throwing lemons at East to biking to Michael's; it's been real. To Diego, DK, Julie, and Max, the Young Blood that keeps me energized, thanks for reducing the thickness of my jade layer with your youthful enthusiasm and adorable 1st year problems. Me gùsta. To Claire and Elijah; sometimes a trip down the hall was all I needed and you tolerated my interruptions with grace and good humor.

It would be impossible understate the importance of my family to my apparent success. Unwavering support, unconditional love, and copious amounts of Night Train are all crucial ingredients in the foundation of this work.

To Mary, you have been with me through the thickest and the thinnest and for that I will be forever grateful. You drive me to be the person you think I am and are always willing to forgive my failings.

To Anna, the best student I ever had, your steadfast determination to move forward despite fear and uncertainty is a continuing inspiration.

Thank you so much to The Begowatts, members past and present; you gave me an outlet for the squishier parts of my brain and something to do when I just wanted to hit something.

A very special thanks to the City Bar for being a refuge from the storm. Kevin and MJ, you are the best bartenders I've ever had the privilege to buy beer from; thanks for providing a welcoming environment and slinging some wicked suds.

And finally, without music to dull the baser parts of my psyche none of this would have happened. In the end recognition must be given to The Boss for reminding me that being earnest can be cool, The Band for so much joy (and especially "Ophelia"), NRW[1] for a great background, and BÖC for being with me from the beginning.

[1] https://www.youtube.com/channel/UCAZ77vdqYbuGbCAWB62WbqQ

Contents

List of Figures

List of Tables

Chapter 1

Introduction

I have come here to chew bubblegum and kick ass, and I'm all out of bubblegum

---

Nada

It has long been known that stars in the solar neighborhood have vertical scale-heights and velocity dispersions that increase with age (e.g., Wielen 1974). This phenomenon is referred to as "disk heating", and the origin of this heating process has never been settled. Unfortunately, our empirical constraints on disk heating come only from the solar cylinder in the Milky Way and a few crude measurements of low-mass edge-on spirals close enough for HST star-counts (Seth et al. 2005). This scant data is insufficient to resolve several outstanding questions: How does the heating rate evolve with time and radius? Why does disk heating in the Milky Way appear to saturate after about 5 Gyr? What, then, gives rise to the thick disk? And is heating in the Milky Way representative of disk galaxies in general? Answers to these questions have critical implications for our picture of disk evolution, all the more poignant given recent observational claims that high-redshift ionized gas disks are dynamically hot, clumpy, and thick (Förster Schreiber et al. 2009) and models (Bird et al. 2013) that predict the formation of observed current disk structure from these high-redshift disks.

Clearly more data is needed, and the rise of resolved spectroscopic surveys of external galaxies (e.g., MaNGA, SAMI, CALIFA) will offer a new window into the distribution of stellar populations outside the Milky Way. However, these surveys lack the spatial resolution necessary to make detailed comparisons to the substructures seen in the Milky Way and it is crucial to complement their broad scope with focused measurements of nearby galaxies. NGC 891 offers an attractive target for such a study; it is nearby, almost perfectly edge-on, and is thought to be a good Milky Way analog. In this thesis I present a study of stellar populations in NGC 891, specifically where these populations fall in a six dimensional space containing three position dimensions along with age, metallicity, and extinction.

The rest of this chapter is organized as follows: in §1.1 I review the picture of disk

formation as revealed locally in the Milky Way; in §1.2 I discuss the details of the methods (namely full-spectral fitting) that will be used to measure populations in NGC 891; and in §1.3 I give a brief overview of fiber integral field units (IFU) and lay the groundwork for the introduction of HexPak/∇Pak; the world's first dual-head, variable-pitch IFU.

1.1 Stellar Populations in the Milky Way

By the middle of the last century it was well established that the scale-heights and velocity dispersions of stars in the solar neighborhood increase with age (see Blaauw & Schmidt 1965, for a summary of this early work, particularly the chapters contributed by Elvius and Delhaye). The seminal work by Roman (1950) demonstrated that the disk kinematics also depended on metallicity. Today these patterns are known in the literature on Galactic archaeology as age-velocity-metallicity (abundance) relations (AVMα-R; e.g., Aumer & Binney 2009; Minchev et al. 2014). Observational advances continued for the solar neighborhood (e.g., Edvardsson et al. 1993; Dehnen & Binney 1998; Nordström et al. 2004), and by the beginning of this century the complexity of these relations had been

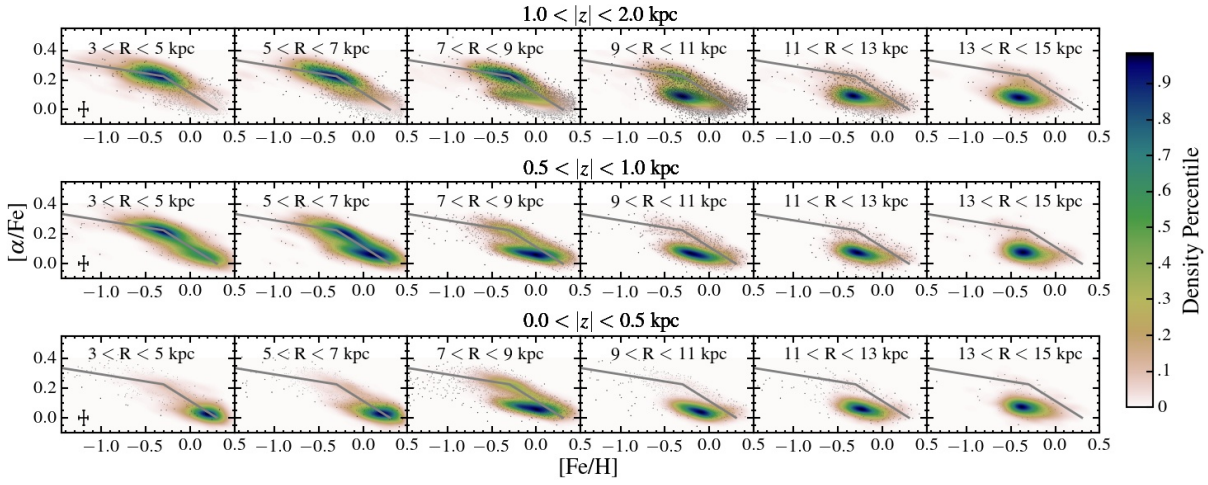

Figure 1.1 The distribution of stars near the Sun in the [α/Fe] vs. [Fe/H] plane, presented in a grid of radius and height. From Hayden et al. (2015).

mapped throughout much of Milky Way (MW) by wide-field spectroscopic surveys (e.g., RAVE, Steinmetz et al. 2006; BRAVA, Howard et al. 2008, SEGUE, Yanny et al. 2009, LAMOST, Zhao et al. 2012 GALAH, De Silva et al. 2015, Gaia-ESO,Gilmore et al. 2012; and APOGEE-1 and -2, Majewski et al. 2015). The radial gradients in these relations are beautifully shown in Figure 1.1 (from Hayden et al. (2015)), illustrating the usefulness of both metallicity and abundance as well-known, complementary chemical-evolutionary tracers. Despite a century of remarkable progress, two broad but intertwined questions remain: (i) What are the astrophysical processes (i.e., the chemo-dynamical explanation) leading to the observed relations?; and (ii) are these patterns generic for spiral disks or specific to the Milky Way?

Setting aside chemical evolution for simplicity, there has been a long-standing debate about the origin of the vertical stratification of disk stars in phase-space as a function of age. This stratification is known as the the age-velocity relation, or AV-R. Historically

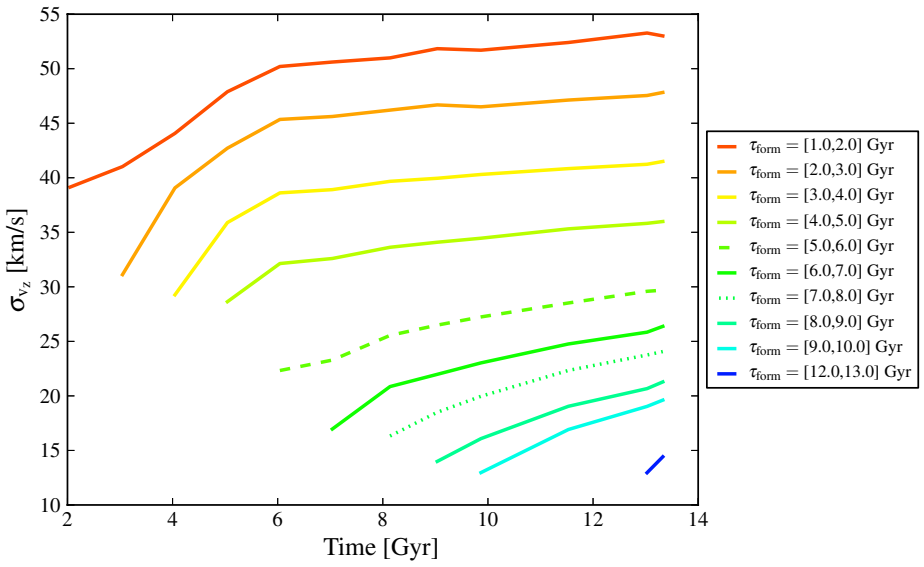

Figure 1.2 Vertical velocity dispersion of stellar populations with different formation ages as a function of time. These models are based on hydrodynamical simulations of a Milky-Way-like disk galaxy. From Bird et al. (2013)

the argument has been in the context of dynamical heating from two-body scattering (Spitzer & Schwarzschild 1951), but the source of this scattering has been debated (e.g., giant molecular clouds, transient spiral structure, or dwarf satellite galaxies Spitzer & Schwarzschild 1951, 1953; Wielen 1977; Quinn et al. 1993; Binney et al. 2000), and none have proven satisfactory to explain the MW's thick disk. This framework has been salvaged but also up-ended by relatively recent evidence for the increasing turbulence (and presumably thickness) of ionized gas in disks at higher redshifts (Weiner et al. 2006; Förster Schreiber et al. 2009; Wisnioski et al. 2015). It seems plausible that early phases of disk formation involved gas cooling, leaving behind an old, thick-disk stellar component (Brook et al. 2004; Bournaud et al. 2009). However, thinner relic layers would also emerge as time progressed (Bird et al. 2013), depending critically on the cooling time-scale for the gas in the presence of star-formation, AGN feedback, and accretion. Figure 1.2 shows an example of this theory; vertical velocity dispersion does slightly increase as stars age (i.e. "heating"), but the dominant trend is that more recently formed populations are dynamically cooler. Ironically, this "settling" of the stellar disk is not unlike the predictions of monolithic collapse from Eggen et al. (1962), albeit now consistent in the context of bottom-up, or hierarchical structure formation as seen in recent simulations (e.g., Bird et al. 2013; Martig et al. 2014). It is no longer clear if, loosely speaking, disks "heat" or "cool" to form the the vertical stratification of disk stars in phase-space, and likely both modes play a role at late and early times, respectively. For this reason we refer instead to "dynamical stratification" as a phenomenon that captures both general physical processes.

The recent simulations noted above show there is a rich history of radial and vertical build up of stellar populations that involves an interplay between the cooling of the gas, the impact of mergers and accretion, and, at late times, the classical heating processes noted above. This richness suggests the possibility for a diversity of astrophysical paths in

disk formation that could lead to significantly different structure in galaxies, exhibited in their AVMα-Rs. Hence, the broader question of whether the MW is representative of the external disk galaxy population becomes salient.

Little is known about the dynamical stratification rates for stars in spiral galaxies outside the Milky Way, but recent studies of stellar populations and dynamical stratification in low-mass spiral galaxies (Seth et al. 2005; Bernard et al. 2015) have shown dramatic differences in the age-metallicty and age-velocity dispersion relations when compared to the Milky Way. Recent measurements of the stellar velocity dispersions in M31 (Dorman et al. 2015) show that there are gradients in dispersion with age and metallicity, but with amplitudes and time-scales that are larger than in the MW. Differences in velocity dispersion amplitudes may reflect a more massive or thinner M31 disk, but possibly also a different dynamical history – for gas settling or stellar dynamical heating. Clearly more data on the stellar properties of external galaxies is needed. The above studies serve as a gold standard since they are based on studies of resolved stellar populations. Because there are no massive spiral galaxies outside of the Local Group for which we can resolve stellar populations at surface-densities high enough to probe most of the disk, it is imperative to undertake studies based on integrated starlight.

1.2 Deriving Population Properties with Full Spectrum Fitting

In this work we employ full-spectral fitting to measure age, metallicity, and extinction as a function of radius and height in NGC 891. The idea of modeling integrated starlight (i.e., a spectrum) to measure galaxies properties has a long history since the pioneering work of Tinsley (1968) and Spinrad & Taylor (1971), and modern techniques employ a variety of sophisticated methods to extract the maximum amount of data from each wavelength. Regardless of the specific method, all attempts at full-spectrum fitting require

the same basic ingredients: (i) a library of stellar spectra, whether empirical or synthetic, (ii) a set of isochrones that encapsulate how stars evolve with time, and (iii) an initial mass function (IMF). With these three components Astronomers can construct simple stellar populations (SSPs); a set of stars of the same age and same metallicity/abundance

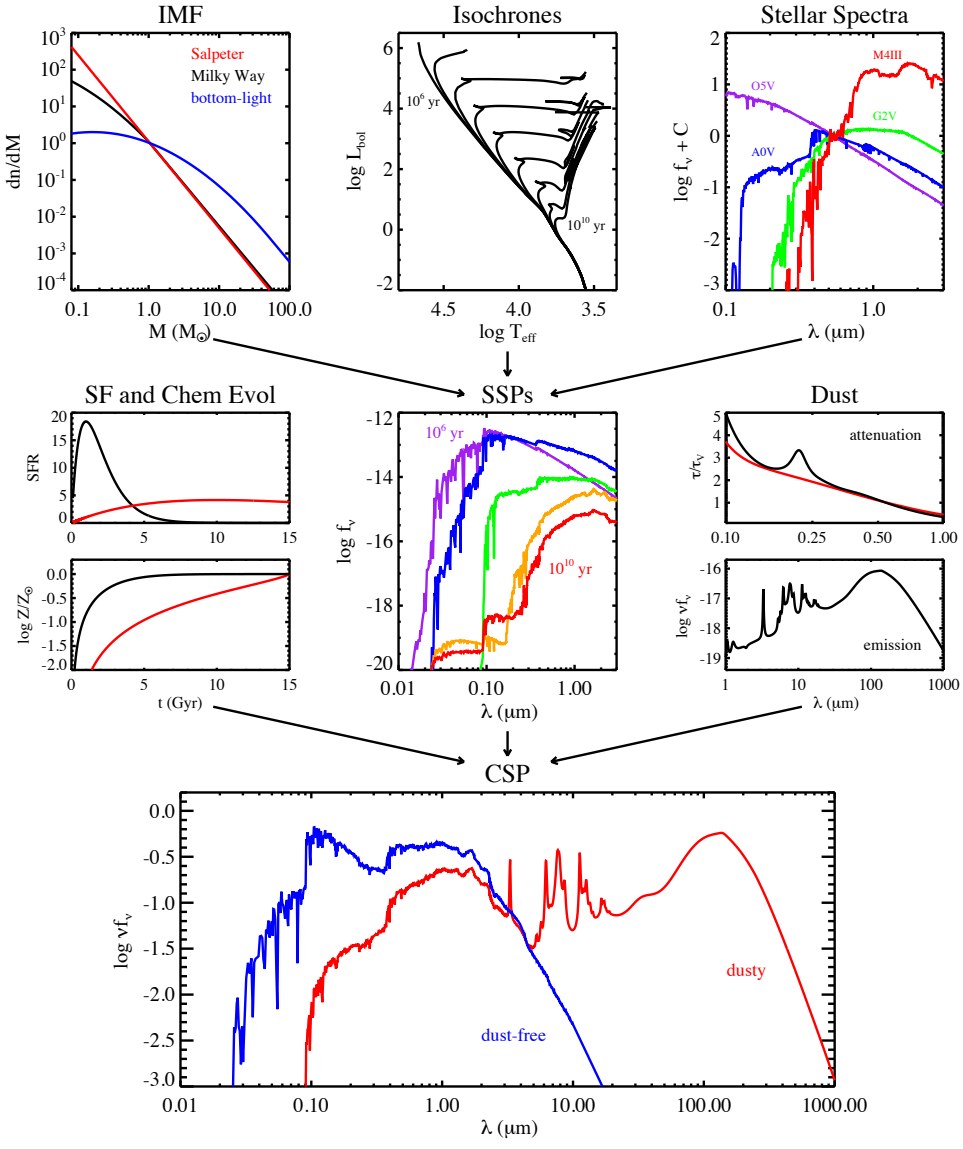

Figure 1.3 The important components of full spectrum fitting. An initial mass function (IMF), isochrones, and spectra are combined to construct individual SSPs. Multiple SSPs are then combined, with an assumed star formation history and dust properties, to form a model galaxy. From Conroy (2013).

with a mass distribution determined by the IMF. To simulate an entire galaxy multiple SSPs of different ages and metallicities are combine together to produce a complex stellar population (CSP), which requires assuming both a star formation history (SFH) and the distribution/properties of dust in the galaxy. An excellent discussion of this process can be found in Conroy (2013, and his diagram shown in Figure 1.3).

Within the general picture painted above there exists a wide range of options and data. It is common for SSP libraries to be constructed with the Padova isochrones (Bertelli et al. 1994; Girardi et al. 2000; Marigo et al. 2008) because these models cover the widest range of stellar age and chemical compositions, but other models are often used for their focus on specific epochs of stellar evolution. For example high-mass stars (Geneva (Schaller et al. 1992; Meynet & Maeder 2000)), low-mass stars (Y^2 (Yi et al. 2001, 2003), or Dartmouth (Dotter et al. 2008)), and even very low-mass stars (Lyon (Chabrier & Baraffe 1997; Baraffe et al. 1998)). In this work we use exclusively the Padova isochrones because our observations, by their very nature, are light-weighted and therefore the specific details of low mass stars are relatively unimportant.

The choice of IMF can also affect the final modeled galaxy spectrum. The canonical IMF of Salpeter (1955) was based on observations of the Solar Cylinder in the Milky Way, and there is so far little evidence that the IMF is appreciably different elsewhere in the Universe (Bastian et al. 2010). More recent observations have refined the specific form of the IMF (Kroupa 2001; Chabrier 2003), but the general picture remains the same. We use the IMF of Chabrier (2003) because it is physically motivated and provides a good fit to low-mass and brown dwarf star counts in the Milky Way (Bruzual & Charlot 2003; Chabrier 2001, 2003).

Finally, the construction of SSPs depends on the stellar library used. In this work we consider only empirical stellar libraries, and more specifically the STELIB (Le Borgne et al.

2003) and MILES (Sánchez-Blázquez et al. 2006) libraries. The main strength of empirical libraries is that they get the chemistry right by default, as indeed they must. The cost of this accuracy, however, is a very limited sampling of the entire parameter space of stellar evolution. For example, as is discussed in §5.5.3, the MILES library very coarsely samples the metallicty/age plane and doesn't have any spectra for ages below 6.5 Myr. As discussed in §5.5 we ultimately use the SSPs of Bruzual & Charlot (2003), which are constructed with the Padova isochrones, Chabrier IMF, and STELIB library. We note, however, that over the wavelength range we consider (3800 Å $\leq \lambda \leq$ 6800 Å) the differences in spectral shape caused by different assumptions/models are minimal.

More directly relevant to our work is the assumption about the SFH that is used to construct galaxies (CSPs) from SSPs. A common choice for SFH is the so called τ-model where the star formation rate (SFR) follows an exponential function with a single scale parameter, $\tau_{\rm SF}$. This analytic form is based on closed-box models where the SFR depends linearly on gas density (Schmidt 1959) and offers an attractive, one parameter, parameterization of the SFH. In this work we chose to use a non-parametric SFH (as discussed in §5.3.1) which allows us to reduce the systematics in our results that arise from forcing an analytic form of the SFR (systematics are not completely eliminated, however, as discussed in §5.7.2). Using this method results in a much larger set of free parameters and puts more strain on the fitting code, but our data have high enough signal to noise ($\sim$30 px^{-1}) to make it a viable option.

Once model galaxies are constructed there are a multitude of methods available to fit them to our data, for example those of (Cappellari & Emsellem 2004; Tojeiro et al. 2007; Chen et al. 2012; Cid Fernandes et al. 2005; Ocvirk et al. 2006; Wilkinson et al. 2015; Sánchez et al. 2016). Regardless of the method used these fits face the same common issues; namely how to deal with known degeneracies between age, metallicity,

and extinction (O'Connell 1976; Aaronson et al. 1978; Worthey et al. 1994; Gil de Paz & Madore 2002). In some methods the extinction degeneracy can be mitigated by removing the overall continuum from both the data and models before fitting (e.g., Ocvirk et al. 2006; Wilkinson et al. 2015) and then recovering an extinction estimate either by measurements of gas emission (i.e., the Balmer decrement) or separate analysis of the "best fit" galaxy spectrum. Metallicity and age are more closely entwined and the degeneracy between them more difficult to break. In this work we attempt to quantify the uncertainties that arise from similarities between SSPs that are degenerate with age and metallicity (see §5.7.1), but note that we have not addressed systematic uncertainties that may arise from our choice of model SSPs.

1.3 A Fiber Optic Primer

The use of fused silica optical fibers for astronomical observations was first suggested by Angel et al. (1977), and in the intervening decades their importance and usefulness to Astronomy has only increased. The astronomical benefits of fiber optics are essentially two fold: Firstly, they allow instruments to be decoupled from the telescope focal plane, which enables the construction of very large and sensitive spectrographs that are free from the unstable environmental conditions often found on the observing floor. Secondly, they can be easily placed at an arbitrary position on the sky while maintaining a consistent spectrograph input.

A class of fiber optic instruments called integral field units (IFUs) make great use of this second point. IFUs are a collection of fibers that are placed in some two-dimensional configuration on the sky and therefore produce data that exist in three dimensions (two spatial and one spectral). Some IFUs are designed to efficiently measure the spectra of a large field of stars, for example HYDRA (Barden et al. 1993), and can have the location

of their fibers changed from program to program. Others have a fiber layout that is fixed and usually intended for observations of extended objects. SparsePak (Bershady et al. 2004, 2005) is an excellent example of and IFU of this type. The trade off for the lack of reconfigurability in fixed IFUs is a generally tighter fiber packing and therefore improved spatial coverage.

In the past, difficulties in construction resulted in a cottage industry of IFU builders, but more recently there has been an explosion of mass-produced IFUs that have allowed large, resolved spectrographic surveys like MaNGA (Bundy et al. 2015), SAMI (Croom et al. 2012), and CALIFA (Sánchez et al. 2012) to rapidly expand our view of the Universe. In this thesis I present ∇Pak and HexPak, a set of IFUs that are the first in the world to contain fibers of different sizes, each configured to serve a specific scientific purpose.

With great power comes great responsibility, however, and fiber optics affect the

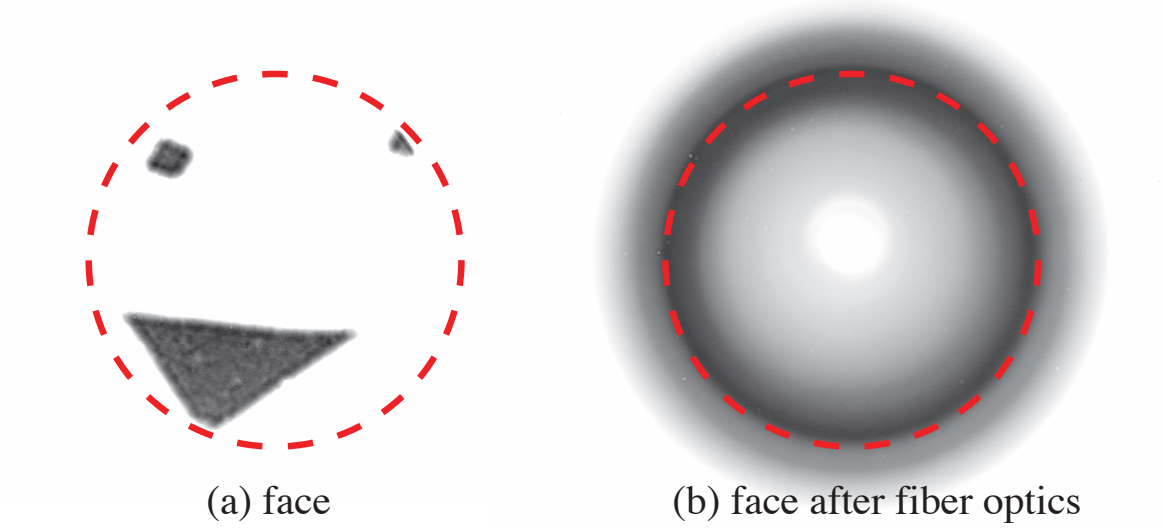

Figure 1.4 The effects of fiber optics on an input signal. Both images are of a far-field (i.e., collimated) beam profile. The face in (a) is smeared both azimuthally and radially during its journey through an optical fiber. The radial smearing is reffered to as FRD. The red circle corresponds to the same angle at the input/output of the fiber.

light passing through them in ways that have profound implications for data quality and instrument design. In particular, fiber optics not only attenuate precious astronomical light, but also increase the entropy in the beam. The latter effect is referred to as focal ratio degradation (FRD, see, e.g., Ramsey 1988), whereby light injected into a fiber at a particular angle emerges from the fiber at a larger angle. An example of this is seen in Figure 1.4; the light coming out of the fiber (b) has been smeared to angles outside of the maximum input angle (red circle). This increase in entropy creates a need for larger (and more expensive) spectrograph optics and can decrease the total system throughput if not properly accounted for. An understanding of the causes of FRD can help mitigate its effects and the first theories placed the blame on microbends along the length of the fiber (Gloge 1972; Carrasco & Parry 1994). Recent studies have suggested however, that most FRD is caused by scattering at the surface of the fiber (Avila 1998; Haynes et al. 2011; Eigenbrot et al. 2012). In the latter scenario it is likely that surface treatments (i.e., anti-reflective coatings) can mitigate the effects of FRD.

References

Aaronson, M., Cohen, J. G., Mould, J., & Malkan, M. 1978, ApJ, 223, 824

Angel, J. R. P., Adams, M. T., Boroson, T. A., & Moore, R. L. 1977, ApJ, 218, 776

Aumer, M., & Binney, J. J. 2009, MNRAS, 397, 1286

Avila, G. 1998, in Astronomical Society of the Pacific Conference Series, Vol. 152, Fiber Optics in Astronomy III, ed. S. Arribas, E. Mediavilla, & F. Watson, 44

Baraffe, I., Chabrier, G., Allard, F., & Hauschildt, P. H. 1998, A&A, 337, 403

Barden, S. C., Armandroff, T., Massey, P., et al. 1993, in Astronomical Society of the Pacific Conference Series, Vol. 37, Fiber Optics in Astronomy II, ed. P. M. Gray, 185

Bastian, N., Covey, K. R., & Meyer, M. R. 2010, ARA&A, 48, 339

Bernard, E. J., Ferguson, A. M. N., Chapman, S. C., et al. 2015, MNRAS, 453, L113

Bershady, M. A., Andersen, D. R., Harker, J., Ramsey, L. W., & Verheijen, M. A. W. 2004, PASP, 116, 565

Bershady, M. A., Andersen, D. R., Verheijen, M. A. W., et al. 2005, ApJS, 156, 311

Bertelli, G., Bressan, A., Chiosi, C., Fagotto, F., & Nasi, E. 1994, A&AS, 106

Binney, J., Dehnen, W., & Bertelli, G. 2000, MNRAS, 318, 658

Bird, J. C., Kazantzidis, S., Weinberg, D. H., et al. 2013, ApJ, 773, 43

Blaauw, A., & Schmidt, M., eds. 1965, Galactic structure

Bournaud, F., Elmegreen, B. G., & Martig, M. 2009, ApJ, 707, L1

Brook, C. B., Kawata, D., Gibson, B. K., & Freeman, K. C. 2004, ApJ, 612, 894

Bruzual, G., & Charlot, S. 2003, MNRAS, 344, 1000

Bundy, K., Bershady, M. A., Law, D. R., et al. 2015, ApJ, 798, 7

Cappellari, M., & Emsellem, E. 2004, PASP, 116, 138

Carrasco, E., & Parry, I. R. 1994, MNRAS, 271, 1

Chabrier, G. 2001, ApJ, 554, 1274

—. 2003, PASP, 115, 763

Chabrier, G., & Baraffe, I. 1997, A&A, 327, 1039

Chen, Y.-M., Kauffmann, G., Tremonti, C. A., et al. 2012, MNRAS, 421, 314

Cid Fernandes, R., Mateus, A., Sodré, L., Stasińska, G., & Gomes, J. M. 2005, MNRAS, 358, 363

Conroy, C. 2013, ARA&A, 51, 393

Croom, S. M., Lawrence, J. S., Bland-Hawthorn, J., et al. 2012, MNRAS, 421, 872

De Silva, G. M., Freeman, K. C., Bland-Hawthorn, J., et al. 2015, MNRAS, 449, 2604

Dehnen, W., & Binney, J. J. 1998, MNRAS, 298, 387

Dorman, C. E., Guhathakurta, P., Seth, A. C., et al. 2015, ApJ, 803, 24

Dotter, A., Chaboyer, B., Jevremović, D., et al. 2008, ApJS, 178, 89

Edvardsson, B., Andersen, J., Gustafsson, B., et al. 1993, A&A, 275, 101

Eggen, O. J., Lynden-Bell, D., & Sandage, A. R. 1962, ApJ, 136, 748

Eigenbrot, A. D., Bershady, M. A., & Wood, C. M. 2012, in Proc. SPIE, Vol. 8446, Ground-based and Airborne Instrumentation for Astronomy IV, 84465W

Förster Schreiber, N. M., Genzel, R., Bouché, N., et al. 2009, ApJ, 706, 1364

Gil de Paz, A., & Madore, B. F. 2002, AJ, 123, 1864

Gilmore, G., Randich, S., Asplund, M., et al. 2012, The Messenger, 147, 25

Girardi, L., Bressan, A., Bertelli, G., & Chiosi, C. 2000, A&AS, 141, 371

Gloge, D. 1972, Appl. Opt., 11, 2506

Hayden, M. R., Bovy, J., Holtzman, J. A., et al. 2015, ApJ, 808, 132

Haynes, D. M., Withford, M. J., Dawes, J. M., Lawrence, J. S., & Haynes, R. 2011, MNRAS, 414, 253

Howard, C. D., Rich, R. M., Reitzel, D. B., et al. 2008, ApJ, 688, 1060

Kroupa, P. 2001, MNRAS, 322, 231

Le Borgne, J.-F., Bruzual, G., Pelló, R., et al. 2003, A&A, 402, 433

Majewski, S. R., Schiavon, R. P., Frinchaboy, P. M., et al. 2015, ArXiv e-prints, arXiv:1509.05420

Marigo, P., Girardi, L., Bressan, A., et al. 2008, A&A, 482, 883

Martig, M., Minchev, I., & Flynn, C. 2014, MNRAS, 442, 2474

Meynet, G., & Maeder, A. 2000, A&A, 361, 101

Minchev, I., Chiappini, C., & Martig, M. 2014, A&A, 572, A92

Nordström, B., Mayor, M., Andersen, J., et al. 2004, A&A, 418, 989

O'Connell, R. W. 1976, ApJ, 206, 370

Ocvirk, P., Pichon, C., Lançon, A., & Thiébaut, E. 2006, MNRAS, 365, 74

Quinn, P. J., Hernquist, L., & Fullagar, D. P. 1993, ApJ, 403, 74

Ramsey, L. W. 1988, in Astronomical Society of the Pacific Conference Series, Vol. 3, Fiber Optics in Astronomy, ed. S. C. Barden, 26–39

Roman, N. G. 1950, ApJ, 112, 554

Salpeter, E. E. 1955, ApJ, 121, 161

Sánchez, S. F., Kennicutt, R. C., Gil de Paz, A., et al. 2012, A&A, 538, A8

Sánchez, S. F., Pérez, E., Sánchez-Blázquez, P., et al. 2016, Rev. Mexicana Astron. Astrofis., 52, 21

Sánchez-Blázquez, P., Peletier, R. F., Jiménez-Vicente, J., et al. 2006, MNRAS, 371, 703

Schaller, G., Schaerer, D., Meynet, G., & Maeder, A. 1992, A&AS, 96, 269

Schmidt, M. 1959, ApJ, 129, 243

Seth, A. C., Dalcanton, J. J., & de Jong, R. S. 2005, AJ, 130, 1574

Spinrad, H., & Taylor, B. J. 1971, ApJS, 22, 445

Spitzer, Jr., L., & Schwarzschild, M. 1951, ApJ, 114, 385

—. 1953, ApJ, 118, 106

Steinmetz, M., Zwitter, T., Siebert, A., et al. 2006, The Astronomical Journal, 132, 1645

Tinsley, B. M. 1968, ApJ, 151, 547

Tojeiro, R., Heavens, A. F., Jimenez, R., & Panter, B. 2007, MNRAS, 381, 1252

Weiner, B. J., Willmer, C. N. A., Faber, S. M., et al. 2006, ApJ, 653, 1027

Wielen, R. 1974, Highlights of Astronomy, 3, 395

Wielen, R. 1977, A&A, 60, 263

Wilkinson, D. M., Maraston, C., Thomas, D., et al. 2015, MNRAS, 449, 328

Wisnioski, E., Förster Schreiber, N. M., Wuyts, S., et al. 2015, ApJ, 799, 209

Worthey, G., Faber, S. M., Gonzalez, J. J., & Burstein, D. 1994, ApJS, 94, 687

Yanny, B., Rockosi, C., Newberg, H. J., et al. 2009, AJ, 137, 4377

Yi, S., Demarque, P., Kim, Y.-C., et al. 2001, ApJS, 136, 417

Yi, S. K., Kim, Y.-C., & Demarque, P. 2003, ApJS, 144, 259

Zhao, G., Zhao, Y.-H., Chu, Y.-Q., Jing, Y.-P., & Deng, L.-C. 2012, Research in Astronomy and Astrophysics, 12, 723

Chapter 2

The Angular and Wavelength Dependence of Fiber Focal Ratio Degradation

Every hidden cell is throbbing with music and life, every fiber thrilling like harp strings.

John Muir

A version of this chapter has previously appeared in
Ground-based and Airborne Instrumentation for Astronomy IV. Proceedings of the SPIE
Eigenbrot, Bershady, and Wood 2012. Volume 8446 article 84465W

Abstract

We present measurements of how multimode fiber focal-ratio degradation (FRD) and throughput vary with levels of fiber surface polish from 60 to 0.5 micron grit. Measurements used full-beam and laser injection methods at wavelengths between 0.4 and 0.8 microns on 17 meter lengths of Polymicro FBP 300 and 400 μm core fiber. Full-beam injection probed input focal-ratios between $f/3$ and $f/13.5$, while laser injection allowed us to isolate FRD at discrete injection angles up to 17 degrees ($f/1.6$ marginal ray). We find (1) FRD effects decrease as grit size decreases, with the largest gains in beam quality occurring at grit sizes above 5 μm; (2) total throughput increases as grit size decreases, reaching 90% at 790 nm with the finest polishing levels; (3) total throughput is higher at redder wavelengths for coarser polishing grit, indicating surface-scattering as the primary source of loss. We also quantify the angular dependence of FRD as a function of polishing level. Our results indicate that a commonly adopted micro-bending model for FRD is a poor descriptor of the observed phenomenon.

2.1 Introduction

Multimode optical fibers provide the most cost-effective coupling between telescopes and spectrographs that allow spectrographs to be placed in stable environments. However, these fiber optics contribute to light loss from attenuation within the fiber material and surface-scattering of their ends, and increase entropy in the optical beam. The latter effect is referred to as focal ratio degradation (FRD), whereby light injected into a fiber at a particular f-ratio emerges at a faster (smaller) f-ratio. Ever since the first efforts to characterize FRD in astronomical applications (Angel et al. 1977) astronomers have attempted to understand its cause(s) in the hope to lessen its effects (Carrasco & Parry 1994; de Oliveira et al. 2011). Microbends have historically been a favored culprit (Carrasco & Parry 1994; Gloge 1972), but recently it has been suggested (Haynes et al. 2011; Avila 1998) that scattering caused by surface-roughness on the fiber face contributes significantly to FRD.

We discuss the results of two experiments designed to measure how the amount of FRD depends on surface roughness, wavelength, and input angle. The experiments described here use both full-beam and laser injection methods (Carrasco & Parry 1994) standard for FRD tests in astronomical applications. The full-beam method is useful for characterizing how a fiber would perform when fed by a telescope, and provides a straightforward way to compute practical metrics useful for designing spectroscopic instruments. The laser injection method allows light to be injected into the fiber at discrete input angles (compared to a filled ray-bundle cone). This angular dependence of scattering is a particularly sensitive diagnostic of the physical mechanisms responsible for FRD.

The method and results of our experiment of FRD dependence on surface roughness

are presented in §2.2. Results for the wavelength dependence of FRD are reported in §2.2.4.2. The dependence of scattering on input angle is reported in §2.3, and the implications of our work are discussed in §2.4.

2.2 Grit Size and Wavelength Dependence

2.2.1 Polishing Method

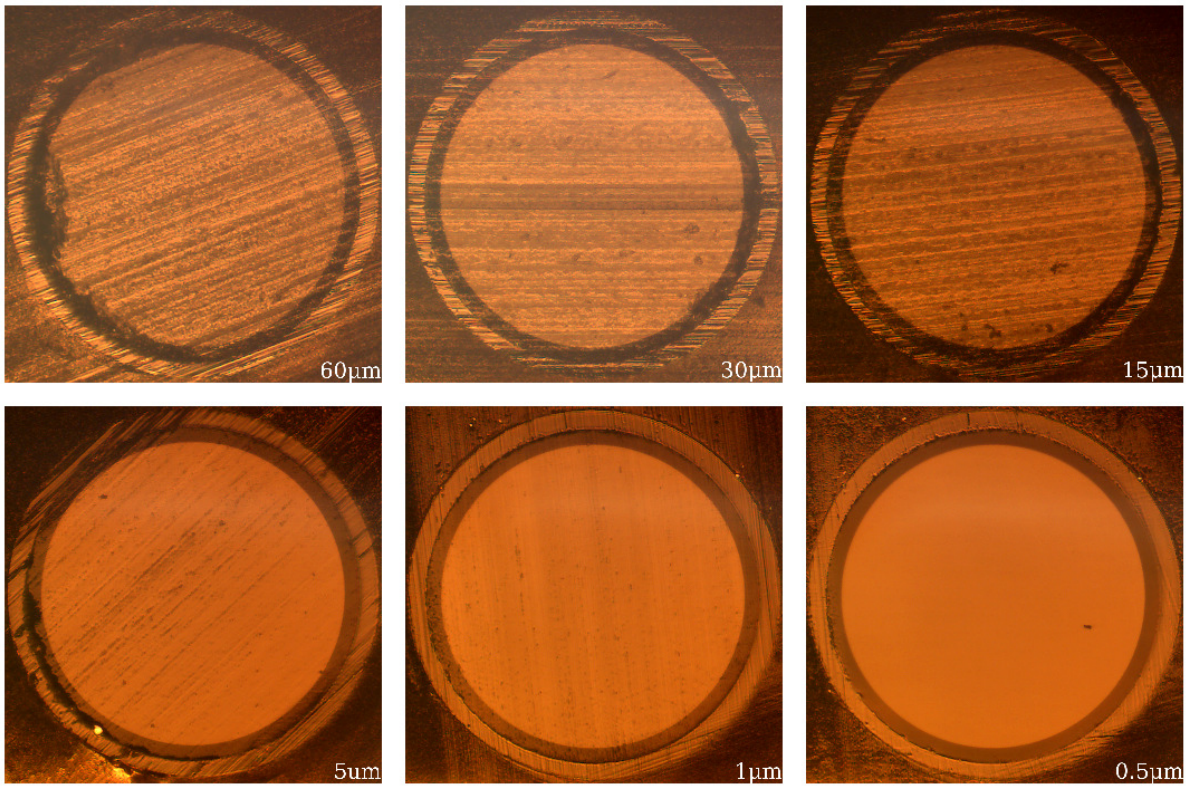

Figure 2.1 Images of the "test" surface of the fiber cable showing the appearance of the fiber face at each of the six stages of polishing. The number in the bottom right corner of each panel denotes the size of grit used. The fiber core diameter is 300μm.

Our tests used Polymicro Technologies stepped-index broadband optical fibers, cut to ∼17 meters in length. FBP300330370 has core:clad:buffer diameters of 300:330:370 μm, respectively; a second length of FBP400440480 has 400:440:480 μm diameters. We mounted

each fiber end into 0.25 inch cylindrical brass ferrules using Norland Optical Adhesive 61 ultraviolet-curing epoxy.

The experiment was designed to maintain one end of each fiber cable as a "control" surface, well-polished (0.5 μm) at the beginning of testing, and to use the other end of the fiber cable as the "test" surface, initially polished using a coarse grit and then re-polished with successively finer grit sizes after each measurement. For creating the progression of decreasing surface roughness we performed consecutive polishing steps on the test surface using silicon carbide lapping disks of 60, 30, 15, 5, and 1 μm grit as well as 0.5 μm grit aluminum oxide disks.

The fiber cable was polished using an Ultra Tec Manufacturing, Inc., ULTRAPOL 1200-series lapping machine. We considered a fiber surface to be adequately polished when, under visual inspection, surface grooves appeared to be relatively even across the face with very few surface features larger than the grit size used to polish the surface. We imaged each end of the fiber using a Newport Corporation F-ML1 fiber inspection microscope for magnification and a Motic Corporation Moticam 2300 CMOS detector. We took images after each polishing step in order to confirm that the test surface was adequately polished and that the control surface remained undamaged. We also captured images after each FRD measurement step in order to determine if the fiber faces had been damaged during handling, as any potential damage could affect the test results. A mosaic of images of the test surface, as seen after the FRD measurement at each grit size, is seen in Figure 2.1.

2.2.2 Data Collection

The experimental apparatus is a modified version of the far-field differential beam comparator using a double re-imaging system described in Crause et al. (2008), which is based of the FRD test apparatus used to characterize the fibers of SPARSPAK (Bershady

et al. 2004). The final collimating lens (L3 in Crause et al. (2008)) was replaced with a Canon $f/1.2$ camera lens to eliminate ghost images caused by very fast output beams. Stray light was further reduced by covering everything downstream of the focus plane with a black photographer's cloth. The fiber input stage was replaced with a highly stable, purpose-built three-axis translation stage that ensures the fiber face is telecentric to within 0.01°. Finally, a filter magazine was added to the pinhole assembly to facilitate the rapid changing of filters.

Basic operation involves recording data from two imaging modes; the far-field fiber output, and the far-field image of the direct beam. The level of FRD is then computed by comparing the two modes. Examples of these images are shown in Figure 2.2, illustrating the increasing impact of FRD at slower beam-speeds. Data were taken in three filters: Johnson I and B and Stromgren y, with central wavelengths of 790 nm, 440 nm, 551 nm, and widths of $\Delta\lambda/\lambda = 0.22$, 0.19, 0.045, respectively; four f-ratios ($f/3$, $f/4.2$, $f/6.3$, and $f/13.5$); and five polish levels (60, 30, 15, 5, and 1 μm). The range in f-ratios was chosen so that results are applicable to a wide range of telescope designs. The Wisconsin Indiana Yale NOAO (WIYN) 3.5m telescope has a $f/6.3$ Nasmyth port; the Sloan Digital Sky Survey Telescope fibers are fed at $f/5$; and the South African Large Telescope (SALT) feeds its prime focus instrument package at $f/4.2$ (similar to the Hobby Eberly Telescope).

Throughput measurements require very precise knowledge of the intrinsic lamp output (the light input to the system). Experiments in lab showed that, while the stochastic variations of the lamp are negligible, there is a secular drift towards lower lamp output. Subsequent to the experiment reported here a photo-diode monitoring system has been implemented to correct for this trend. The data presented here accounted for this trend by: 1) taking a set of images for one filter with the fiber in place, 2) taking a set of direct beam images in the same filter, 3) repeating this alternating scheme until three groups of

fiber images, separated by two groups of direct beam images were taken. This alternating fiber-direct-fiber scheme is used to remove stochastic lamp variability.

Images were cleaned of detector artifacts and combined to produce five images for each filter at each polish level: three fiber images and two direct beam images. Lamp variations were removed by using the three fiber images as data points to determine a lamp normalization (relative to the first fiber image) as a function of time. This function was then used to find normalizations for the direct beam images. The lamp was found to have no significant variation (10% of the shot noise) within the time required to take one set of data in a particular filter.

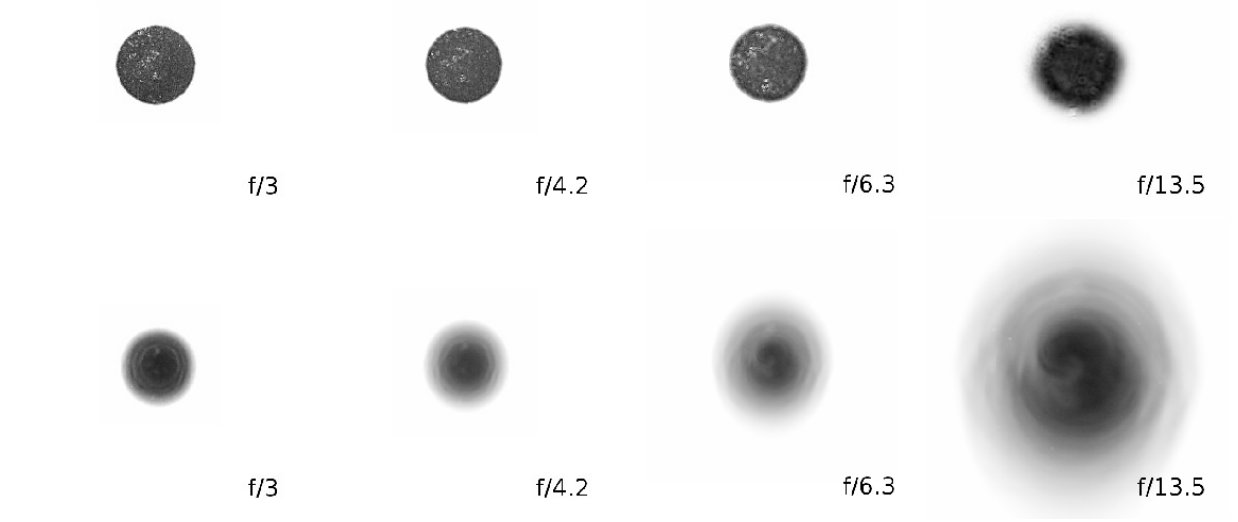

Figure 2.2 Far-field images of the direct-beam (top) and fiber-beam (bottom) outputs for all f-ratios tested. Data shown is at 551 nm for the FBP300330370 fiber, 17m in length. Direct and fiber beam images for a given f-ratio have identical spatial scales, and are adjusted such that the direct beam images are the same apparent size for all f-ratios.

2.2.3 Analysis

A custom data reduction pipeline was created to consistently and efficiently analyze the large volume of data associated with the multiple filters and polish levels. Analysis

consisted of measuring the total light contained within annuli of constant width and increasing radius centered on the center of the beam. This information was then used to construct a curve of growth that shows the fractional encircled energy (EE) as a function of radius.

In addition to FRD, there are aberrations inherent in our test apparatus that will affect both the direct beam and fiber beam in the same way. To remove the effects of these aberrations the difference between the direct beam and a theoretical ideal beam (no aberrations) is computed and applied to both the fiber and direct beams; Crause et al. (2008) provide a complete description of the method used. Once the corrections have been applied the only differences between the fiber and direct beams are caused by FRD.

2.2.4 Results

Figure 2.3 shows a characteristic set of FRD analysis plots at a 30 μm end-polish at $f/4.2$ and $f/6.3$. (See Figure 2.4 for more grit-sizes and §2.2.4.1 for discussion). The left panels, which consist of normalized curves of growth (COG) for both the direct and fiber beams, show how FRD scatters light out to larger radii. The dashed and solid lines are the data before and after the correction described above (Crause et al. 2008).

The right panels plot the effective f-ratio as a function of EE. These plots only show information about relative light (re)distribution; they do not contain any information about total throughput. Where the fiber curve intersects the ideal beam tells us what percentage of the original beam's information is being captured by a spectrograph with an f-ratio equal to that of the optics feeding the fibers. This plot can also be used to estimate how much faster a spectrograph would have to be to capture more of the input beam. For example, from figure 2.3 and for fibers polished to 30 μm, an $f/4.2$ spectrograph only captures about 53% of the light fed into the fibers at $f/4.2$. If we wanted to capture 90% of the input light

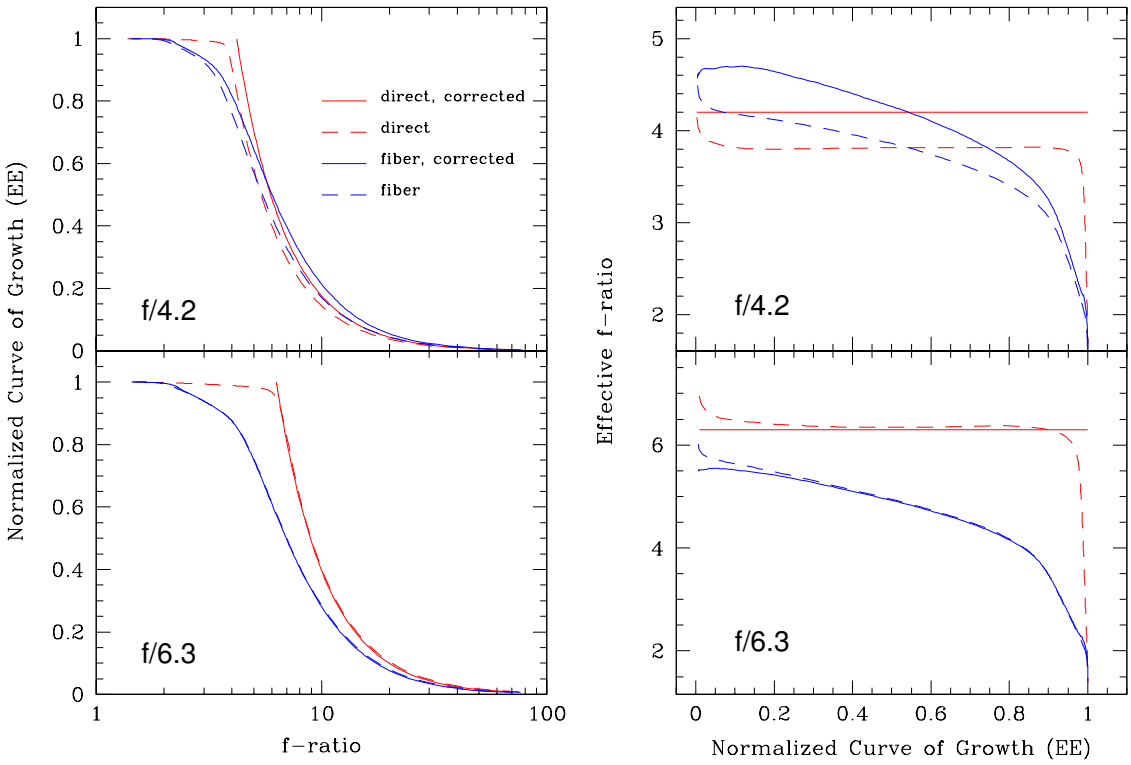

Figure 2.3 FRD effects at 551 nm, $f/4.2$ and $f/6.3$, and with the output face polished to 30 μm. The left panels show enclosed energy (EE) as a function of f-ratio. The right panels show the effective f-ratio of a beam that captures a certain percentage of the total light (EE). Data is for the FBP300330370 fiber, 17m in length.

the spectrograph optics would need to be $f/3.2$.

2.2.4.1 Grit-size and f-ratio Dependence

The primary result of the experiment can be seen in figure 2.4, which shows FRD curves at one wavelength (551 nm) and at all of the different end-polish levels and f-ratios. As expected, the effects of FRD improve as grit size decreases, but only to a point. There is steady improvement in output beam quality between 60 μm and 15 μm, a sharp improvement between 15 μm and 5 μm, and almost no improvement between 5 μm and 0.5 μm.

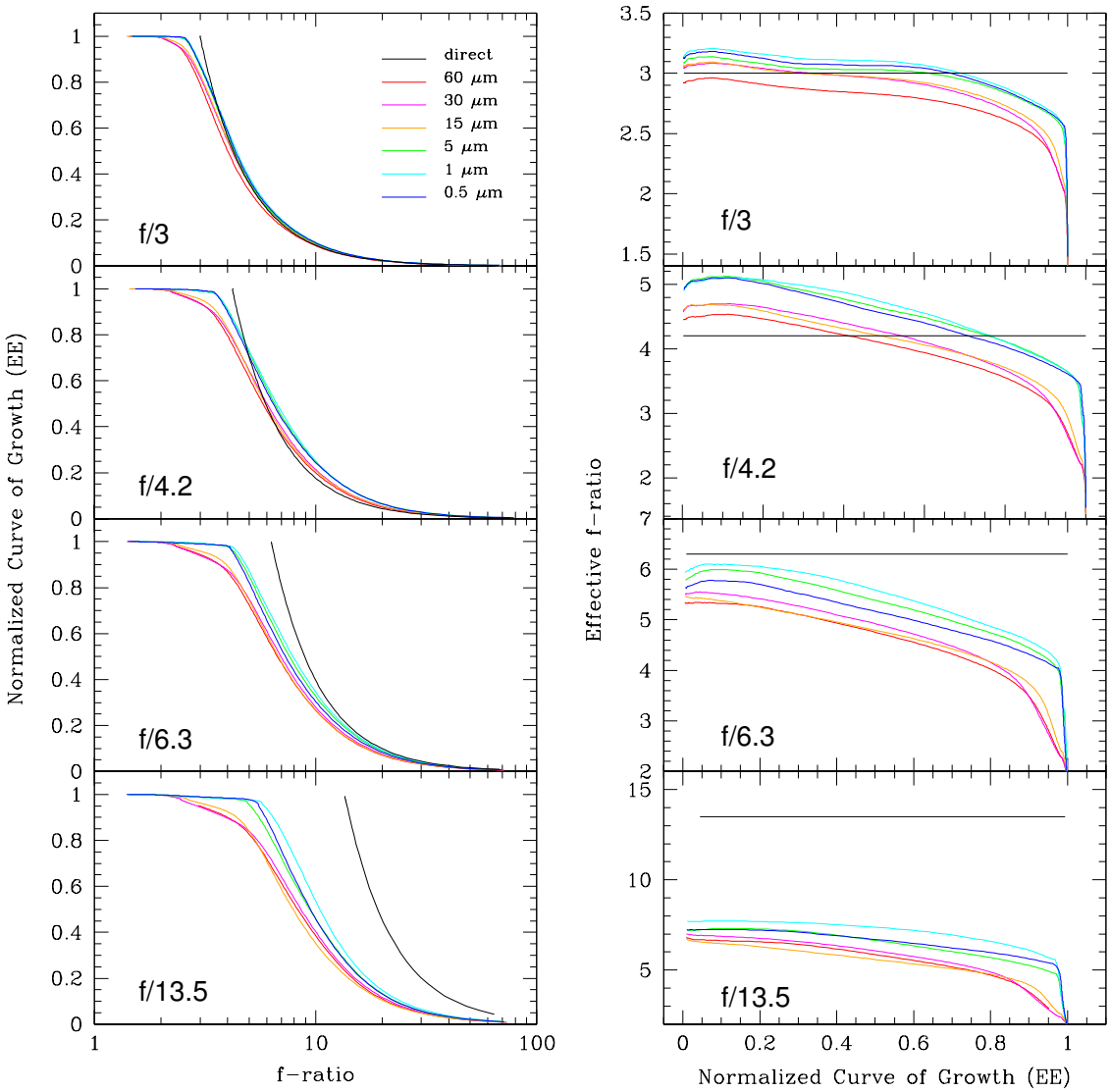

Figure 2.4 Dependence of FRD on polish grit size at 551 nm and all f-ratios measured for 17m of FBP300330370 fiber.

It is also worth noting that for certain combinations of input f-ratio and polish level there is a radius (output f-ratio) within which there is relatively *more* light in the fiber beam than in the direct beam. The explanation is straightforward: FRD scatters light from each input angle into both larger and smaller output angles. If the width of the scattering profile increases towards smaller angles (see §2.3) then more light is scattered out of these

angles compared to larger angles. However, for a uniform input beam larger input angles contain more luminosity (because they contain larger annular areas) and so the amount of light scattered in from large angles will exceed the amount of light scattered out from small angles despite the wider scattering profile at small angles. In this case the fiber beam will have relatively more light at smaller angles than the direct beam, as seen in the plots for $f/3$ and $f/4.2$. Conversely, there is some sufficiently large output angle that has significant scattering contributions from angles where there is no light in the input beam. At these output angles, the COG drops below the ideal beam, as observed.

It is well known that FRD changes with changing input f-ratio, increasing with slower beams Ramsey (1988), as seen in Figure 2.4. For beams slower than $f/6.3$ the scattering becomes so large that the output beam never contains more light than the input beam for any angle.

2.2.4.2 Wavelength Dependence and Total Throughput

Previous tests for a wavelength dependence on FRD have been split between results that suggest there is such a dependence (Carrasco & Parry 1994; Gloge 1972), based on what would be predicted by a micro-bend origin, and results that point to no wavelength dependence (Bershady et al. 2004; Schmoll et al. 2003). Figure 2.5 shows FRD curves for all filters at $f/4.2$ and $f/6.3$ and 0.5 μm and 60 μm polish levels. The data suggest that at a fine polish level (0.5 μm) the amount of scattering caused by FRD does *not* depend on the wavelength of the input light. However, at 60 μm we do see some wavelength dependence to the FRD curves, which must therefore be caused by surface scattering (see figure 2.6).

We also find that the total throughput of the fiber depends on fiber polish. Figure 2.6 shows the total throughput as a function of grit size for all three wavelengths and $f/6.3$. The total throughput is defined as the asymptotic (in output angle) fiber beam

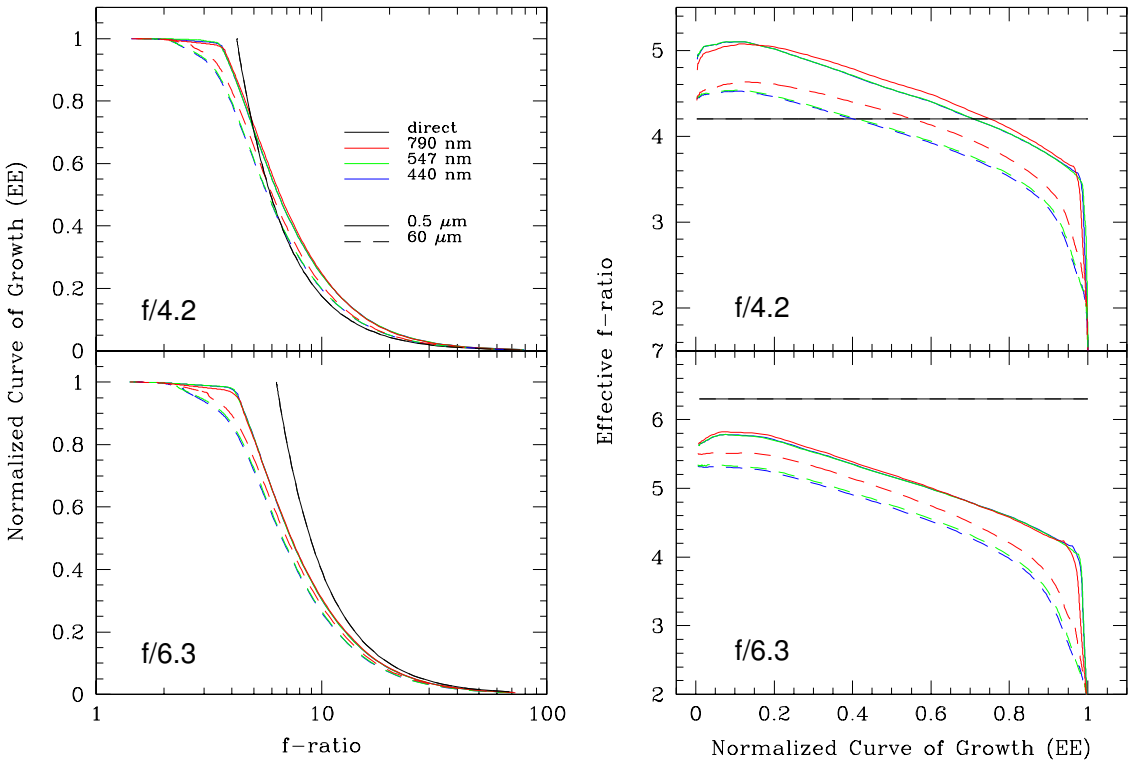

Figure 2.5 Wavelength dependence of FRD at 0.5 and 60 μm polish grit at $f/4.2$ and $f/6.3$ for 17m length FBP300330370 fiber.

counts referenced to the same measurement of the direct beam. From the manufacturer's specifications we expect the fiber attenuation to depend on wavelength. Polymicro reports attenuations of 20 dB/km at 440 nm, 10 dB/km at 551 nm, and 5 dB/km at 790 nm, and we also expect a 3.43% light loss from each air-silica interface (input and output faces). Thus, in the case of an ideal, 17 m long fiber we expect a throughput of 85.6%, 89.3%, and 91.2% for 440 nm, 551 nm, and 790 nm, respectively. These values are plotted as horizontal dashed lines in figure 2.6. Any additional losses are likely due to surface scattering.

We also find a polish dependence on the color of the transmission. As seen in the right panel of figure 2.6, the throughput gains are greater at shorter wavelengths as the surface-polish improves, as would be expected from a surface-scattering phenomenon.

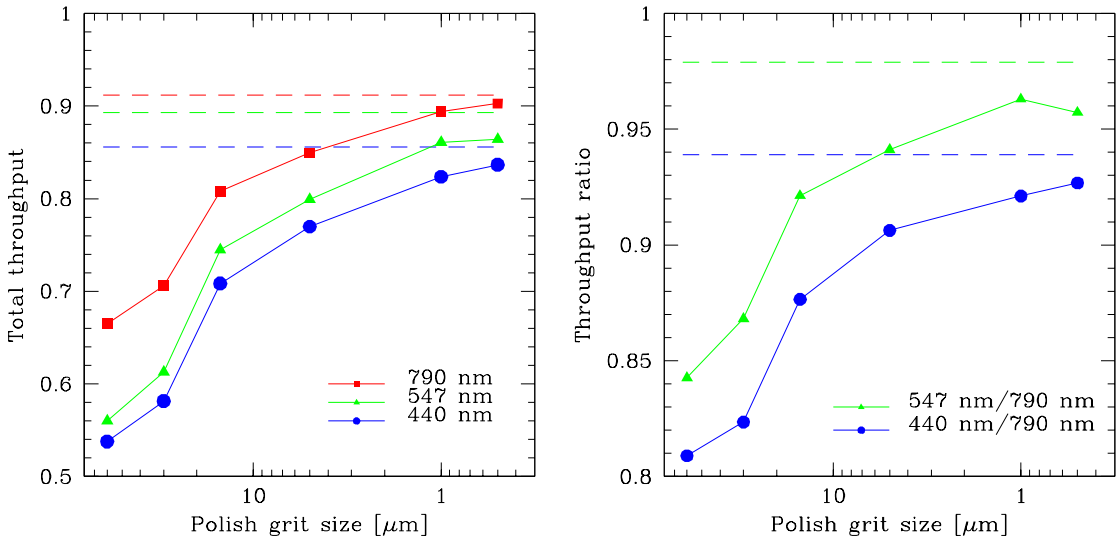

Figure 2.6 Total throughput as a function of polish grit for three different wavelengths (left), and the relative increase in 440 nm and 551 nm referenced to 790 nm (right). Dashed lines show the values expected from the product specifications. This is measured for a 17m length of FBP400440480 fiber.

2.3 Angle Dependence

2.3.1 Experiment

We are also interested in the dependence of FRD on the light input angle. The direct beam injection method reported in §2.2.2 injects a full cone of light into a fiber, i.e., the input beam contains rays incident on the fiber face from normal up to half of the vertex angle of the cone. To probe FRD effects at single, discrete input angles (essentially an annular cone) we use an experiment similar to the laser injection method of Carrasco & Parry (1994) and Haynes et al. (2011), but modified so that the far field fiber output is imaged on to an opaque screen rather than through a translucent screen. This was done to eliminate ring blurring that occurs when imaging through a translucent object of finite thickness.

We also needed to ensure that the imaging screen was far enough away from the

output fiber face. The output images consist of a ring with a radius corresponding to the laser input angle and a thickness that varies depending on the amount of FRD present at that particular input angle. We expect each ring to have an inherent width equal to the diameter of the fiber, but this width is in a collimated beam while any FRD scattering results in a slightly diverging beam. With this in mind, the far field images were recorded at a far enough distance from the fiber output face that the FRD smearing width described by Carrasco & Parry (1994) and Haynes et al. (2011) (calculated to be $\sim 2.6^\circ$ for our fiber) dominated the ring width. At the distance chosen the 300 μm core of the fiber subtends $\sim 0.06^\circ$ on the screen. Unfortunately, our direct-imaging approach requires the fiber output and camera to be off-axis (due to physical constraints), resulting in elliptical ring images. Significant effort was expended to model the geometric distortion caused by this method; our analysis software does an excellent job of removing the distortion to produce circular rings.

Data were taken at input angles of $\pm 17^\circ$ ($\sim f/1.6$) in increments of 0.5°. For simplicity we use the FWHM of the ring profile as a first-order measure of for the amount of FRD, ignoring here the intricacies of the profile shape (Haynes et al. 2011; Carrasco & Parry 1994).

2.3.2 Results

Figure 2.7 shows how the amount of "smearing" caused by FRD (ring width) varies with different input beam angles. Angles below 4° are not plotted; future reports of this experiment will measure ring widths in the regime where ring-width exceeds ring radius.

The results in figure 2.7 show that FRD effects are very large at small angles, as expected, and decrease with increasing angle until leveling out at $\sim 10^\circ$, which is within a few degrees of the numerical aperture (12.7°). It is possible to extend the ring measurements

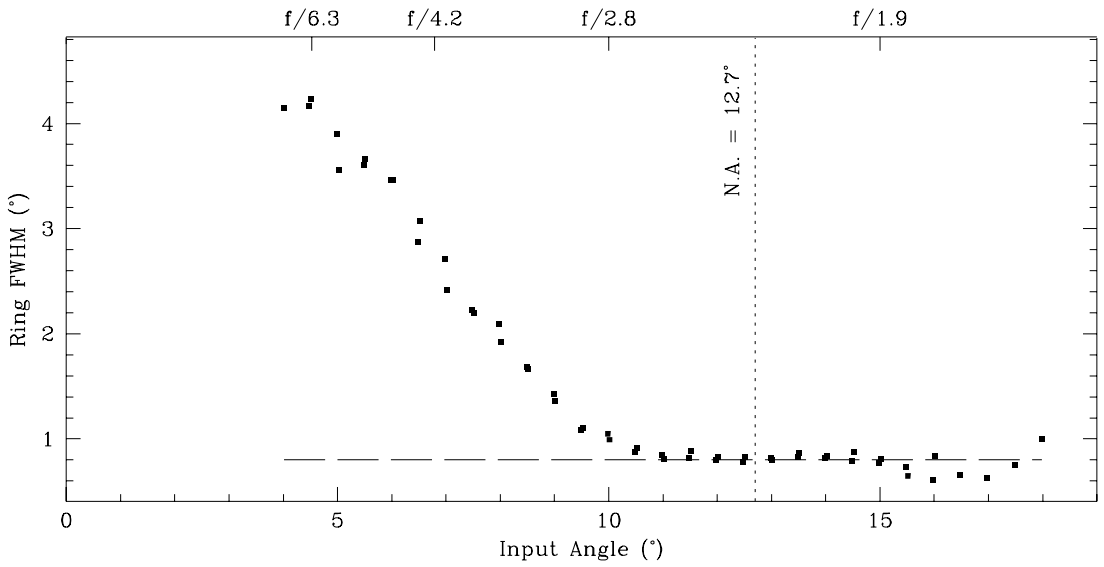

Figure 2.7 Smearing due to FRD (ring width) as a function on input angle. The vertical dotted line marks the numerical aperture of the fiber specified by the vendor. The horizontal dashed line represents a best fit to the micro-bend model of Carrasco & Parry (1994) over the full angular range of our data adopting $D = 1.15 \times 10^{-6}$ m^{-1}. This value of D is constrained by a best-fit of the micro-bend model to our data in the range of 10 to 18 degrees.

to angles above the numerical aperture. While the throughput decreases in this regime, the FRD appears to remain fairly constant.

We have compared these trends to predictions of the micro-bend model presented in Carrasco & Parry (1994). We find a micro-bend parameter of $D = 1.15 \times 10^{-6}$ m^{-1} provides the best fit to our data (plotted in figure 2.7). This is a lower limit on the value of D for this fiber. An upper limit on the value of D comes from matching the micro-bend model to our widest ring (4°), from which we find $D < 2.0 \times 10^{-5}$ m^{-1}. For this range of D, our measurements are in an angular regime where the micro-bend model predicts a ring width nearly constant in angle. The fact that our data show a non-constant ring-width indicates that this micro-bend model is not a good description of the data and therefore not likely the physical origin of FRD.

Our results are also important because they indicate just how strongly FRD is dominated by light entering the fiber at smaller angles with respect to the fiber optical axis. In astronomical applications, fibers are typically fed by on-axis optical systems with central obstructions from secondary and/or field-corrector optics. From an entropy standpoint, i.e., information gathering-power per unit cost, the central rays obscured are the least valuable. Consequently, wide-field survey-telescopes (e.g., SDSS, York et al. 2000; Gunn et al. 2006), which are fast and have relatively large central obstructions, are ideally suited to fiber coupling. Further analysis of data like that in Figure 7 will allow us to quantify this statement.

2.4 Summary

Two experiments to measure the amplitude of FRD as a function of wavelength, surface polish, and light-injection angle have been carried out and described. The primary results are:

1. A component of FRD is attributable to the end-polish on fiber surfaces, however this appears to be a second-order effect relative to the impact of light-injection angle (beam speed) slower than $f/3$. FRD decreases with polishing down to finer grit sizes, but not significantly below grit-sizes of 5 μm.

2. Total throughput (light emerging at all angles) also depends on end-polish, with a wavelength dependence that indicates the increase in throughput is simply a reduction in surface-scattering. The most significant gains occur for polishing that proceeds down to 5 μm grit, although for most astronomical applications at low light-levels polishing down to the finest grit is measurably advantageous.

3. The amount of FRD does **not** depend on wavelength, as found now in several

experiments. This is in contrast to the predictions of micro-bend theory for FRD's origin (Carrasco & Parry 1994).

4. FRD is dominated by light entering the fiber at smaller angles (in our case $< 10°$), as is well known. Measurements here allow us to quantify this statement in detail. The amplitude and angular dependence of FRD also do not agree with predictions from micro-bend theory.

This work was supported by NSF grants ATI-0804576 and AST-1009471.

References

Angel, J. R. P., Adams, M. T., Boroson, T. A., & Moore, R. L. 1977, ApJ, 218, 776

Avila, G. 1998, in Astronomical Society of the Pacific Conference Series, Vol. 152, Fiber Optics in Astronomy III, ed. S. Arribas, E. Mediavilla, & F. Watson, 44

Bershady, M. A., Andersen, D. R., Harker, J., Ramsey, L. W., & Verheijen, M. A. W. 2004, PASP, 116, 565

Carrasco, E., & Parry, I. R. 1994, MNRAS, 271, 1

Crause, L., Bershady, M., & Buckley, D. 2008, in Presented at the Society of Photo-Optical Instrumentation Engineers (SPIE) Conference, Vol. 7014, Society of Photo-Optical Instrumentation Engineers (SPIE) Conference Series

de Oliveira, A. C., de Oliveira, L. S., Dos Santos, J. B., et al. 2011, MNRAS, 413, 3003

Gloge, D. 1972, Appl. Opt., 11, 2506

Gunn, J. E., Siegmund, W. A., Mannery, E. J., et al. 2006, AJ, 131, 2332

Haynes, D. M., Withford, M. J., Dawes, J. M., Lawrence, J. S., & Haynes, R. 2011, MNRAS, 414, 253

Ramsey, L. W. 1988, in Astronomical Society of the Pacific Conference Series, Vol. 3, Fiber Optics in Astronomy, ed. S. C. Barden, 26–39

Schmoll, J., Roth, M. M., & Laux, U. 2003, PASP, 115, 854

York, D. G., Adelman, J., Anderson, Jr., J. E., et al. 2000, AJ, 120, 1579

Chapter 3

∇Pak and HexPak: A Variable-pitch, Dual-head IFU for the WIYN 3.5m Bench Spectrograph

When the going gets weird, the weird turn pro

Raoul Duke

A version of this chapter has previously appeared in
Ground-based and Airborne Instrumentation for Astronomy IV. Proceedings of the SPIE
Wood, et. al. 2012. Volume 8446, article 84462W

Abstract

We describe the design, construction, and expected performance of two new fiber integral field units (IFUs) — HexPak and ∇Pak— for the WIYN 3.5m Telescope Nasmyth focus and Bench Spectrograph. These are the first IFUs to provide formatted fiber integral field spectroscopy with simultaneous sampling of varying angular scales. HexPak and ∇Pak are in a single cable with a dual-head design, permitting easy switching between the two different IFU heads on the telescope without changing the spectrograph feed: the two heads feed a variable-width double-slit. Each IFU head is comprised of a fixed arrangement of fibers with a range of fiber diameters. The layout and diameters of the fibers within each array are scientifically-driven for observations of galaxies: HexPak is designed to observe face-on spiral or spheroidal galaxies while ∇Pak is optimized for edge-on studies of galaxy disks. HexPak is a hexagonal array of 2.″9 fibers subtending a 40.9 arcsec diameter, with a high-resolution circular core of 0.″94 fibers subtending 6" diameter. ∇Pak is a 39 by 55 arcsec rectangular array with rows of fibers of increasing diameter from angular scales of 1.″9 to 5.″6 across the array. The variable pitch of these IFU heads allows for adequate sampling of light profile gradients while maintaining the photon limit at different scales.

3.1 Introduction

HexPak and ∇Pak are two new formatted fiber optic integral field units (IFUs) for the WIYN 3.5m telescope Bench Spectrograph[1]. These two IFUs are unique because they are the first formatted fiber IFUs to include multiple fiber diameters within the same fiber head. Including multiple fiber diameters allows each of these IFUs to simultaneously sample different angular scales within the same observation. The smaller fibers can gather light from higher surface brightness regions (e.g. the core or midplane of a galaxy disk) while the larger fibers can collect light from fainter, more diffuse regions (e.g. larger scale heights or scale radii of a disk), thereby enabling high S/N measurements to be obtained simultaneously at a range of spatial positions.

The two IFUs share the same cable and "foot" for mounting onto the WIYN Bench Spectrograph. Sharing the same cable minimizes the total volume required for routing within the WIYN telescope in an already over-filled system. Sharing the same foot results in a unique dual-slit design, allowing the two heads to be exchanged at the telescope without requiring changes to the spectrograph system. HexPak has a high-resolution core of fibers three times smaller in diameter than the surrounding fibers. As a hexagonal array with a circular, high-resolution core, HexPak is tailored for studies of radially-distributed, diffuse light sources, such as face-on galaxy disks, spheroidal galaxies, or star clusters. The ∇Pak head consists of five different fiber sizes, arranged in rows to form a gradient of fiber diameters from one edge of the array to the other. It is designed for integral field spectroscopy of edge-on galaxies, making it well-suited for studying extra-planar gas and

[1]The WIYN Observatory is a joint facility of the University of Wisconsin-Madison, Indiana University, Yale University, and the National Optical Astronomy Observatory.

stars in spiral galaxy disks.

Including multiple fiber diameters comes at a cost, however. In the case where the system spectral resolution is limited by the slit width, this will result in a varying spectral resolution, inversely proportional to the fiber diameter. In this case the maximum resolution will change by a factor of 3 for ∇Pak and 3.1 for HexPak, increasing from the largest to the smallest fibers. However, the smallest reimaged fiber sizes will have contributions from optical aberrations from the spectrograph. As a result, we expect the achievable resolution to increase only by a factor of 2–2.5 for HexPak.

The science impact of changing spectral resolution depends on the specific application. For example, the velocity dispersion of stars is expected to increase with scale height above the disk midplane in edge-on disk galaxies. For the study of stellar velocity dispersions in spheroidal or face-on disk galaxies, as another example, it would be advantageous to *increase* spectral resolution with radius, since systems become dynamically colder moving outward. This is opposite what these instruments deliver. On the other hand, at lower surface brightness the limits of S/N prevent useful information from being obtained at high spectral resolution, and in this sense these instruments provide a practical balance between signal and resolution. As we describe below, ample sky fibers are included for all fiber sizes to ensure excellent sky subtraction.

This instrument follows in the legacy of the excellent WIYN fiber IFUs DensePak (Barden et al. 1998) and SparsePak (Bershady et al. 2004, 2005). The primary impetus behind this project was the increased throughput and image quality of the newly redesigned WIYN Bench Spectrograph (Barden et al. 1994; Bershady et al. 2008; Knezek et al. 2010). In the process an opportunity arose to rebuild the decommissioned DensePak IFU. The fiber from DensePak is being reused for the larger fibers in the new HexPak array, and most of the hardware in the cable "foot" housing that terminates the cable in the spectrograph

room at WIYN is reused from the DensePak cable. HexPak contains additional fibers that were newly purchased for this project. ∇Pak is made entirely using new fiber. Additionally, all the cabling and head mount hardware is newly constructed.

In §3.2 we detail the key science drivers that served as a design target for the instrument, as well as describe the design challenges inherent in the design of formatted IFUs with multiple fiber diameters. We detail the construction process in §3.3 and summarize the project in §3.4.

3.2 Design

3.2.1 Science drivers

These IFUs are designed for studying nearby galactic stellar populations, the ISM of other galaxies, and stellar and gas kinematics of nearby galaxies. Science drivers that influenced the design of the IFUs include: probing the vertical structure of spiral disks using stellar and gas kinematic tracers; studying the kinematics and abundances of diffuse ionized gas in edge-on and face-on spiral galaxies; understanding the origin of winds in starburst galaxies; measuring the rate of galactic outflows in normal spirals; and connecting the properties of galaxy cores to the secular evolution of their parent galaxies for E+A galaxies, QSO/AGN hosts, and pseudo-bulges.

3.2.2 Head design

The primary limitations on the overall head size result from technical limitations in the telescope and spectrograph system. The maximum number of fibers is limited simply by the maximum allowable slit length. The overall field of view is limited by the IFU mount on the telescope. The IFU heads mount into the WIYN Fiber-Optic Echelle (WIFOE) port on the telescope. The WIFOE port limits the overall head mount to a 1in circular

diameter. Accounting for mounting hardware, this limits the overall physical IFU head size to approximately a square 0.5in×0.5in, corresponding to a maximum field of view (FOV) of $119'' \times 119''$ at the WIYN plate scale of $9''.374$/mm. Packing fibers and head mount fixturing make the usable FOV somewhat smaller than this, as shown later.

Each IFU head design presented a unique challenge for packing the fibers together to form the heads. The main problem we needed to overcome was one of "circle packing": what is the best way to arrange the fibers (represented as circles as viewed along the optical axis of the system) so that we maximize the focal plane filling factor in a compact region while achieving our target scientific capability? To our advantage, the problem of circle packing has been relatively well-studied in the field of geometry. For a single diameter, the highest density packing arrangement is a hexagonal lattice arrangement as used in both DensePak and the SparsePak array on WIYN, which results in a packing density of $\pi/\sqrt{12} \approx 0.907$ (Steinhaus 1999). Circle packing becomes markedly more difficult when including more than one circle diameter in the packing, as each of these new IFU heads does. Our conceptual goal for these IFUs was to enable the simultaneous sampling of varying surface brightness levels in the same IFU observation. To that end, the challenges of circle packing were central to our ability to design these IFU heads in a way that achieved our scientific goals yet were within our ability to fabricate. In the following sections we describe the challenges we have overcome to develop scientifically-useful head designs that were also feasible to construct.

3.2.2.1 HexPak

The HexPak IFU head is designed to study objects with radial surface brightness profiles (e.g. face-on galaxy disks, spheroidal galaxies). As the name suggests, HexPak is a hexagonal fiber array, based on a hexagonal lattice arrangement. As a result, the larger-

diameter HexPak fibers are arranged in the most compact manner possible. The fiber diameter for the hexagonal region was set by the diameter of the pre-existing DensePak fibers. These fibers have core diameters of 310μm and full outer diameters measured to be 405μm. At the plate scale of the WIYN focal plane the cores of these fibers span 2.″8 on the sky. The design goal for the HexPak head was to have a hexagonal region of fibers in an annulus around a high-spatial resolution fiber core, necessitating two different fiber diameters. There are only nine possible compact[2] packings of two circle diameters in a plane (Kennedy 2006). Of these, only one is particularly relevant to the science goals of HexPak. This packing involves replacing one larger circle with an array of seven smaller circles (with a diameter ratio of $\sim$0.386) while retaining the hexagonal lattice arrangement of the other large circles (see Figure 1.e Kennedy 2006).

[2]A packing is "compact" if, for every circle C that is tangent to a series of circles C_1,C_2,...,C_n, circle C_i is tangent to circle C_{i+1} for $i = 1, 2, \ldots, n$.

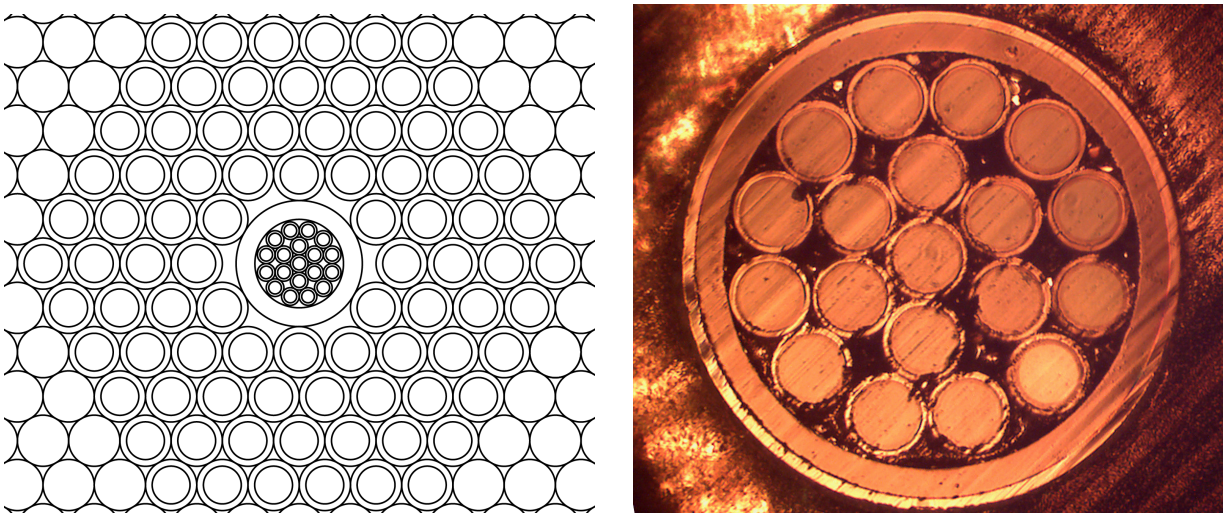

Figure 3.1 *Left:* Detail of the HexPak science fibers. Fiber core regions are not shown for packing fibers. The region depicted is approximately 0.18in×0.15in centered on the hexagon. *Right:* Prototype of the HexPak core packing. The fibers and capillary were glued into a 0.25in brass ferrule and ground to an even length in order to observe the quality of the packing. This face has not been well-polished and does not represent our final target level of surface polish.

The main flaw in this design as it pertains to our design goals is that the seven smaller circles *must* be surrounded by larger circles to maintain a compact packing. Stated differently, this arrangement dictates that the high-resolution core of HexPak be no larger than the diameter of one large fiber. The reason behind this is that the largest radius occupied by the seven smaller fibers is larger than the radius of the one fiber which was removed. Adjacent packings of seven small fibers would therefore overlap each other. This means that this packing arrangement would allow for higher spatial sampling of no larger than a $2\farcs8$ diameter region, but we felt a larger region would more closely meet our science goals. In order to achieve a larger high-resolution core, we realized that this particular compact packing can be reversed by instead replacing seven circles with one larger circle. This reversal ultimately led to the final design.

For the final HexPak head design we have replaced the central seven $2\farcs8$ fibers in the hexagon with a glass capillary tube. The outer diameter of this tube is such that it packs compactly to the surrounding fibers, and the inner diameter of the tube leaves a large, circular profile in which we can pack small fibers. Our final task was to determine how to densely pack a moderate number of fibers inside this new circular aperture. In order to determine an efficient packing within this aperture, we once again turned to the study of circle packing. A sub-field of circle packing investigates the most efficient methods for packing circles of a given diameter into one circle of a larger diameter. Kravitz (1967) presents empirically-derived optimal packings of circles into a circular container. For a diameter ratio of $\sim$0.206, it is possible to pack 19 small circles into one larger circle. This final design of all the HexPak object fibers can be seen on the left in Figure 3.1.

It was prohibitively expensive to fabricate a form for a custom diameter capillary draw just a few inches in length, so in practice our chosen diameter (and the diameters of the fibers in the core) was limited to stock sizes. In the case of HexPak, our chosen glass

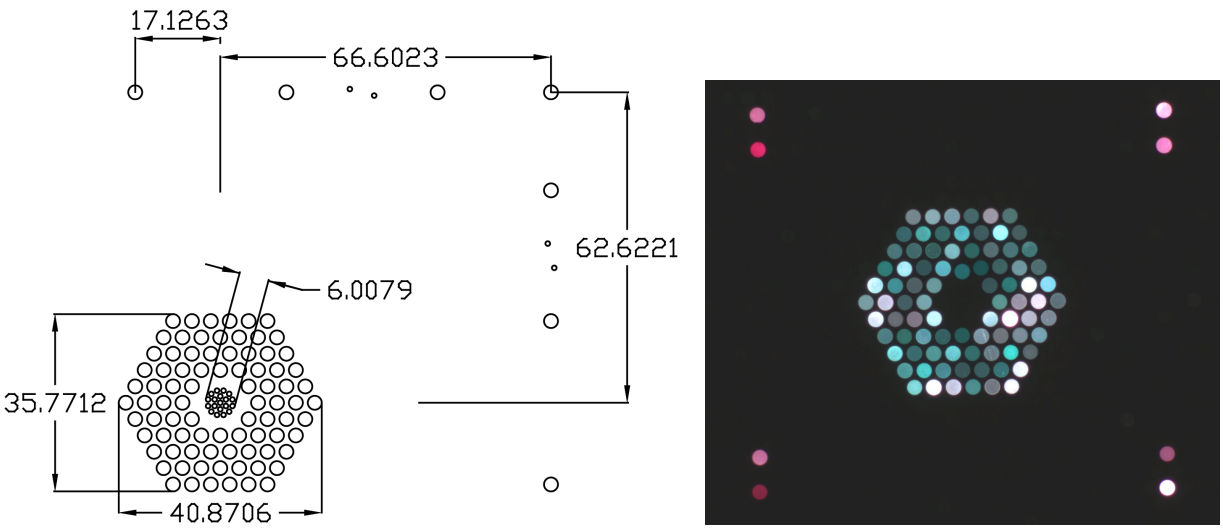

Figure 3.2 *Left:* Head design for the HexPak IFU. All displayed values are in units of arcseconds. The two different fiber diameters are 2.″8 and 0.″94 on the sky. Only the active fiber core regions are shown. *Right:* An image of an early prototype of the HexPak head design. The center of the hexagonal region contains a hypodermic needle as a placeholder for the capillary with small fibers. No small fibers are in the hypodermic shown here. The ends of the fibers were colored with marker to easily differentiate object fibers (green) from sky fibers (red).

capillary was purchased from Polymicro Technologies[3] and has a specified inner diameter of 750μm. This capillary inside diameter corresponds to a core fiber outer diameter of about 154μm. The closest stock fiber outer diameter from Polymicro was 140μm (100μm or 0.″94 core diameter), resulting in the final design of 19 0.″94 fibers packed in the center of the hexagon. One sacrifice we make in using stock sizes is that there is a 2–3″ gap between the core fibers and the larger fibers in the hexagonal region. The necessary outer diameter to fill the space of seven 405μm OD fibers is 1,050μm, but this capillary has an outer diameter of 850μm. This amount of undersizing is problematic for the packing arrangement. We manually thickened the pieces of capillary used in the head by applying thin coatings of spray paint to the tubes until we reached the desired diameter.

Although the results from Kravitz (1967) are empirical (and therefore may not be

[3]Polymicro Technologies, 18019 N. 25th Avenue, Phoenix, AZ 85023–1200, (602) 375–4100

compact) and our chosen fibers are slightly undersized, the amount of extra space in the packing arrangement is at an appropriate level to allow for mechanical tolerances. We have successfully assembled two prototypes of this packing and have high confidence that this will be viable in the final head assembly. The right side of Figure 3.1 shows one of these prototypes after being glued and roughly polished.

Our final head design is shown in Figure 3.2. The array design has 114 total fibers. Of these, the main science fiber region consists of 84 fibers with 2.″8 diameters contained within the outer hexagonal region and 19 fibers with 0.″94 diameters spanning the central 6″ diameter of the hexagon. The capillary tube housing the 0.″94 fibers creates an annular gap 2–3″in radius between the core fibers and the outer hexagonal region. The array also has 11 total sky fibers, seven with 2.″8 diameters and four with 0.″94 diameters. The sky fibers are placed along the edges of the array opposite the science fibers to maximize the separation between the object and sky sampling regions. The sky fibers lie between 45″ and 75″ from the *edge* of the hexagon. The HexPak head design employs nearly 1,000 short (3in) packing fibers to fill the space in between the science fibers and the sky fibers, similar to the scheme used for SparsePak. The packing fibers also create a roughly rectangular exterior head profile. An early prototype of the HexPak design is also shown in Figure 3.2. This prototype shows an earlier revision in sky fiber arrangement and contains no small fibers in the core of the array.

Bershady et al. (2004) found that focal ratio degradation[4] (FRD) increases at the edge of the SparsePak array. They suggest several possible causes, including stress incurred when releasing the head from its mold and pressure introduced by the head-mount clamp. Regardless of the cause, they recommend leaving at least a 1.2mm buffer region at the outside of the head in order to protect the active fibers from these potential stresses. The

[4]Focal ratio degradation is a decrease in focal ratio of a beam as it passes through a fiber.

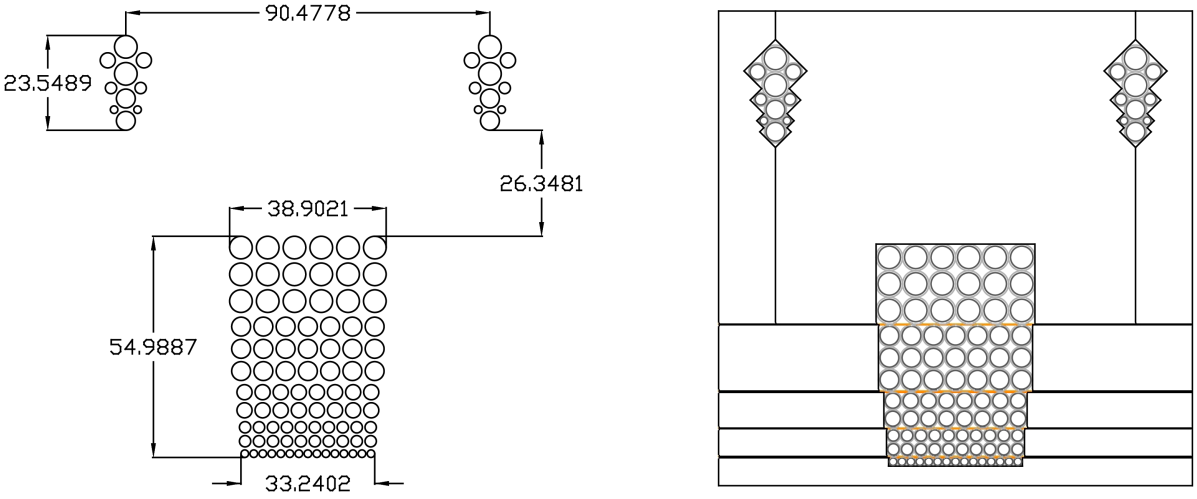

Figure 3.3 *Left:* Fiber layout for the ∇Pak IFU. All displayed values are in units of arcseconds. The different fiber diameters are 1.″9, 2.″8, 3.″7, 4.″7, and 5.″6 on the sky. Only the active fiber core regions are shown. *Right:* Detail of the ∇Pak head mount. The darker gray circles are the active fiber cores, the lighter gray circles are the full O.D. of the fibers, and the orange lines represent 25μm-thick plastic dividing layers. The full exterior profile measures 0.5in×0.5in.

"packing fiber" buffer in the HexPak head is four large fibers, or about 1.6mm, which we expect will alleviate FRD increases at the edge of the array.

3.2.2.2 ∇Pak

∇Pak is designed to study objects that exhibit linear gradients in surface brightness (e.g. edge-on galaxy disks, linear outflows). Therefore, the desired fiber arrangement in the head is linear rather than approximately circular as it is in HexPak. The design goal was to approximate layered pseudo-slits of increasing slit width, accomplished by using stacked rows of fiber, with fiber diameters increasing between rows. There is no compact packing of two different circle diameters that allows for each fiber size to be arranged into linear, contiguous rows. Circle packing theory did not show obvious solutions for this problem, so we settled on a design that uses five physically separated fiber regions, each containing only a single fiber diameter. This design is shown on the left in Figure 3.3. Our final design includes a total of 110 fibers composed of five different fiber core diameters: 200μm,

300μm, 400μm, 500μm, and 600μm. Respectively, these fibers span angular diameters of 1.″9, 2.″8, 3.″7, 4.″7, and 5.″6 at the WIYN focal plane. In order to successfully accommodate five different fiber diameters within the same packing arrangement, we have designed a layered head mount.

This head mount fixturing represents one of the largest engineering challenges we have overcome. In order to get each row of fibers to remain parallel to each other, fibers of different diameters could not touch. This is a result of there being no compact packing of two different fiber diameters that allows for parallel rows. This meant that it would be impossible to use short packing fibers in the ∇Pak head. After numerous iterations, we ultimately designed a layered head mount that is assembled in stages, one fiber-diameter region at a time. The final head mount design can be seen on the right in Figure 3.3. Each set of fibers of a given diameter is contained by aluminum walls, precisely machined to the height of each fiber region. The head is then assembled by layering subsequent stacks of these segments on top of one another. All of the parts of the fixture are held together as an assembly using small dowel pins that run the full height and width of the assembly. The main cavity was cut out as an assembly using a wire electric discharge machining (EDM) process to ensure the best possible alignment between adjacent fiber regions. The ∇Pak head block cavity was cut using a 0.004in diameter wire, allowing for a minimum corner radius of 0.002in (50μm), small enough to ensure the smallest fibers fit into place.

The dimensions of the entire head block are 0.5in$\times$0.5in. Each region of fibers containing a single fiber diameter is separated from its neighbors by a thin layer of plastic shim stock 0.001in (25.4μm) thick. Although this adds a gap between each region of fibers, the on-sky angular size of the plastic layer is very small (0.″24), which we deemed acceptable. We have successfully designed and assembled two prototype ∇Pak head assemblies and we are confident that this design is feasible.

The resulting array design consists of five stacked blocks of fibers arranged into one or more rows, with the fiber core diameter increasing from 200μm to 600μm between each block of fibers. The entire block of science fibers includes 90 fibers and covers an area on the sky roughly $35'' \times 55''$. The array also has two regions of sky fibers for simultaneous sky measurements. Each sky fiber region contains two fibers of each fiber diameter included in the science fiber region. The fibers in ∇Pak are arranged in a square lattice rather than in a hexagonal lattice, reducing the effective filling factor within each fiber region. This yields a packing density of only $\pi/4 \approx 0.785$. The advantage of this arrangement is that the pseudo-slits within each region are vertically aligned and are offset only in one dimension on the sky.

Since the entire ∇Pak head mount assembly is composed of aluminum parts, no short packing fibers are used in its design. The design does, however, place active fibers within 1.2mm of the edge of the head, inside the prescribed minimum buffer distance. However, we believe FRD edge effects should be negligible due to the use of a stronger buffer material (aluminum in this case) and the fact that at no point during assembly is any part of the ∇Pak head released from a mold.

3.2.3 Slit design

∇Pak and HexPak both terminate in the same "foot" housing in a dual-slit configuration. The slit block uses a custom design that modified the SparsePak slit block design. The slit block assembly is made from two separate aluminum plates, each specifically designed to create a pseudo-slit for one of the IFUs. Each pseudo-slit was created by cutting 'v'-grooves into the slit block. The groove size, placement, and spacing is designed to match the varying number and sizes of fibers in each IFU pseudo-slit. A schematic of the slit block assembly is shown in Figure 3.4. For mechanical reasons, the fibers are aligned to be tan-

gent to the optical center line of the slit, rather than being aligned by their centers. The 'v'-grooves were precision-cut into the slit block using a wire EDM process like that used for the ∇Pak head mount fiber cavity, but with a smaller 0.002in diameter wire, resulting in a minimum corner radius of approximately 0.001in (25μm). This radius is smaller than the smallest fiber outer radius (measured to be about 71μm) ensuring that even the smallest fibers will sit nicely into the grooves.

We have set the fiber core edge-to-edge spacing at 291μm to minimize cross-talk while maximizing the number of fibers in the slit. Bershady et al. (2004) found that 400μm was the ideal edge-to-edge spacing of fiber cores in the slit in terms of the trade-off between cross-talk and packing density (i.e. total number of fibers). However, this determination was made using the old Bench Spectrograph system which was upgraded in 2008 (Bershady et al. 2008). With improved image quality and detector sampling as a result of the upgrade, we estimate we can reduce the fiber spacing by $\sim$ 25% without introducing significant amounts of cross-talk between fiber channels.

The fiber arrangements in the slit are informed by their locations within the head design. In HexPak, the hexagonal region is divided into six equal wedges, each containing 14 fibers. The fibers within each wedge are located in the same region of the slit, with fibers near the core of the array being located in the center of the slit segment. Each wedge section in the slit is separated from the adjacent wedge sections by a sky fiber, allowing sky sampling across the entire slit length. Three wedges and associated sky fibers are located on each end of the slit, separated by all of the 0.″94 fibers. The 0.″94 fibers are located in the center of the slit, with the associated 0.″94 sky fibers being located on either side of the 0.″94 object fibers. The ∇Pak slit is sorted by fiber diameter. Within each diameter region, each fiber row in the head is placed contiguously in the slit, with sky fibers evenly distributed as separators between rows.

We also slightly modified the standard Bench Upgrade design for the "toes" of the cable in order to negate vignetting of the light exiting the fiber slit. The toes house the slit block and have open chambers for inserting blocking filters, slit masks, and a back-illumination mirror. These chambers each have an aperture through which the exit beam must pass in order to reach the spectrograph collimator. We performed a vignetting analysis to determine the maximum fiber slit width and slit length that could pass unvignetted through the toes. Bershady et al. (2004) show that, due to FRD, 99% of the energy in an $f/6.3$ input beam (the WIYN focal ratio) exiting the fibers is contained within an $f/4$ output beam. Therefore, as long as an $f/4$ beam could pass through the toes without being blocked, we could consider light losses from the toes to be negligible. The SparsePak design for the toes allowed for a maximum slit length of 79.8mm under this vignetting requirement. This number informed the fiber-to-fiber spacing for our final slit design, resulting in an overall slit length of 76.6mm. The maximum allowable slit width for an $f/4$ beam was 1.23mm, or a 615μm beam displacement from slit center. Our largest fiber has a 600μm core diameter with approximately 55μm of cladding and buffer in radius. Each half of the slit block also has a 25μm plastic divider at slit center, a requirement of our slit block construction process. In total, the maximum beam displacement from slit center is about 680μm, too large for the standard design for the toes. As a result, we modified the design and increased the width of one critical aperture in the toes such that the maximum allowable displacement from slit center is 927μm.

3.3 Construction and Status

The design and construction of the SparsePak cable served as the starting point for this instrument. Technical details of SparsePak fabrication are available in the Appendix section of Bershady et al. (2004). In this section we focus primarily on detailing the

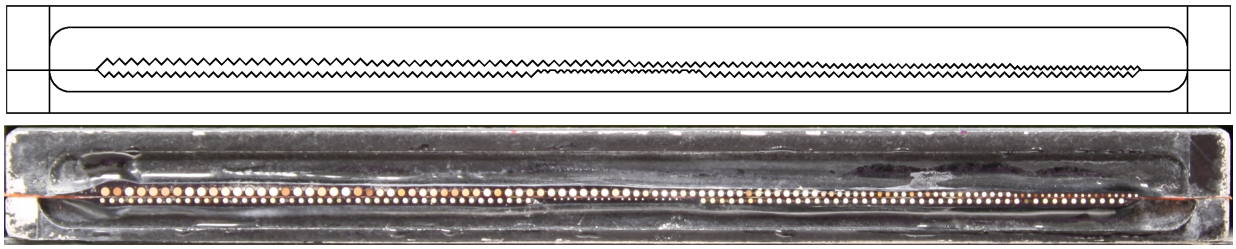

Figure 3.4 *Top:* A schematic view of the slit block without fibers. Both halves of the slit block assembly are shown. The bottom set of grooves is the HexPak slit and the upper set of grooves is the ∇Pak slit. *Bottom:* An image of the slit face in its current state. The top row of fibers are ∇Pak, arranged by decreasing diameters. The bottom row of fibers are HexPak, with the 0.″94 fibers situated between the 2.″8 fibers. Brightness differences between fibers are largely due to surface irregularities in the unpolished head end. Color differences are simply due to some fibers pointing at different parts of the lab. The two 0.001in-thick plastic shim stock dividers are seen as a thin orange line separating the two slits. The shown view spans 3.562in×0.312in.

important features unique to this instrument and noting significant departures from the SparsePak design.

At the present time, construction is complete on all cabling and the entire spectrograph feed assembly (the foot). Polishing of the fiber slit is nearly complete, and final gluing and polishing of the IFU heads are scheduled to conclude in June–August 2012.

3.3.1 Fiber optics

The 91 2.″8 fibers that compose the hexagonal region and its associated sky fibers are re-purposed from the DensePak IFU. They have a specified active core diameter of 310μm and a measured total O.D. (including cladding and buffer) of approximately 405μm. Barden et al. (1998) states that the DensePak fibers are similar to the Hydra FIP-type "red-optimized" fibers. The 23 0.″94 fibers forming the high-resolution core and associated sky fibers were purchased new from Polymicro Technologies. These new fibers are FBP-type broad-spectrum optical fiber with excellent throughput for optical wavelengths. The fibers have silica cores with silica cladding and are designed to have excellent throughput across

the visible spectral window and into the near-infrared. The diameter specification (given as core:clad:buffer, in microns) is 100:120:140. This new fiber is very similar to the fiber used in SparsePak and therefore we expect similar throughput performance from the core HexPak fibers.

Throughput testing for SparsePak showed a roughly 20% improvement in throughput compared to the DensePak fibers, after accounting for differences in fiber diameter and collected solid angle (Bershady et al. 2005). However, most of the light loss in the DensePak cable was likely due to vignetting in the original design of the fiber cable toes, before the Bench Upgrade. With our modified version of the standard Bench Upgrade toes, we expect these fibers to have comparable performance to the SparsePak fibers in the red (> 4000Å; the FBP-type fibers have better transmission properties below 4000Å compared to the FIP-type fibers).

The ∇Pak IFU consists entirely of new FBP-type broad-spectrum optical fiber from Polymicro Technologies. The fibers have specified diameters (given as core:clad:buffer, in microns) of 200:220:240, 300:330:370, 400:440:480, 500:550:590, and 600:660:710. This fiber is very similar to the fiber used in SparsePak and therefore we expect similar throughput performance from all the ∇Pak fibers.

3.3.2 Cabling

Each fiber is individually housed in a PTFE tube for protection and strain relief. The PTFE tubes for the 310μm HexPak fibers were also re-used from the DensePak cable. All of the newly-purchased fiber is housed in new PTFE tubing from Zeus, Inc[5]. As a design decision to reduce the radial cable size, the new PTFE tubes have "light-weight wall" thicknesses (0.006in in radius). This has proven troublesome due to the relative lack

[5]Zeus, Inc., 3737 Industrial Blvd., Orangeburg, SC 29118, (800) 526–3842

of radial strength and rigidity in the wall compared to thicker-walled tubing. The very thin walls of these tubes are prone to kinking which threatens the integrity of the fibers they serve to protect. We recommend, at minimum, "thin wall" PTFE tubes ($\gtrsim$0.01in).

The PTFE tubes terminate at each end of the cable in metal shear clamps. The foot-end shear clamp contains an array of approximately 9×27 holes in a three-element aluminum clamp. The elongated design of this clamp serves to transform the circular bundle of fibers into a rectangular shape approximating the slit arrangement. The head-end shear clamps are a similar three-element design and function in a similar fashion to the foot shear clamp. The hole pattern in the head end shear clamps is roughly hexagonal in order to accommodate the circular fiber bundle and to approximate the fiber layout of the HexPak head.

The fibers and their PTFE tubes are encased in 75 feet of flexible metal conduit. The conduit housing the shared length of the cable consists of approximately 57 feet of 2in ID IE30 and IE50[6] interlocking stainless steel exhaust hose. This conduit retains flexibility for handling while providing strength and durability for the length of cable that will be enclosed within the telescope structure.

The remaining 18 feet of the cable is housed in two separate lengths of 1.25in ID flexible aluminum standard electrical conduit. Each length contains the remaining length of fiber for one of the IFU heads. The lightweight construction and smaller diameter of this conduit allows for ease of handling for mounting the IFU heads into the telescope's Nasmyth port. These two lengths of conduit are completely covered in polyolefin and PVC heat-shrink tubing for additional rigidity and abrasion resistance. The smaller lengths of conduit are joined to the larger, stainless steel conduit through a custom-built merge

[6]Penflex, Corp., 105B Industrial Drive, Gilbertsville, PA 19525, (800) 232–3539

collector from the automotive industry[7].

The conduit for each IFU head contains two custom-designed low-profile rotation couplers. Each coupler has 180° of rotation about the optical axis, allowing each IFU head to rotate a full 360° with the telescope instrument port rotator. The two rotation couplers are spaced approximately 12in apart along the cable to ensure that the full rotation is distributed along a sufficient length to avoid fiber stress.

3.3.3 Fiber slit

For gluing the fiber ends into the slit grooves, we fabricated custom metal fixturing to bend the fibers 90° in the foot and hold them with clearance to mount the slit blocks. We used EPO-TEK[8] 354 heat-curing optical epoxy to bond the fiber ends to the slit block. The gluing fixture held each fiber in its respective slit position and allowed us to seat all the fibers simultaneously. We used a thin sheet of plastic to cover the exposed fiber and epoxy and held the fibers in place using an aluminum pressing block while the epoxy cured. We glued each slit block separately and then constructed the final assembly from the two completed halves. The two halves are pinned together to ensure accurate, repeatable positioning between the two slit halves.

3.3.4 Fiber heads

As tested with SparsePak and our HexPak and ∇Pak test head assemblies, we will use the same EPO-TEK 354 heat curing epoxy for assembling the IFU heads. The HexPak head is assembled one row of fibers at a time, using short packing fibers to fill in the spaces around the active fibers. The $0\farcs94$ fibers are pre-assembled into their capillary tubes and then placed into the final assembly during the gluing process. For constructing the HexPak

[7]Specialty Design Products, Inc., 11252 Sunco Drive, Rancho Cordova, CA 95742, (888) 778–3312

[8]Epoxy Technology, Inc., 14 Fortune Drive, Billerica, MA 01821, (978) 667–3805

head, we follow a design and process used for SparsePak, based on a concept from S. Barden (*private communication*). We will assemble the fibers in a micrometer-driven vice with the vice channel width set precisely to the width of the head. We will then use a precisely-machined tamping tool, just slightly narrower than the width of the head, to pack the fibers into the channel mold. The mold and the tamping tool are sprayed with a PTFE mold release[1] prior to gluing.

The ∇Pak head is assembled one fiber region at a time, with all fibers of a single diameter being assembled at the same time. The assembly is cured after each additional region is assembled. In contrast to the HexPak construction, no vice is used for ∇Pak. The head mount parts are machined to the precise cavity width to hold the fibers for each region, requiring only a pressing plate to ensure the fibers remain seated in the cavity while curing. The pressing plate is coated in PTFE mold release as a precaution and separated entirely from the epoxy by the plastic dividing layers, so at no point are the fibers released from a cured mold. This should alleviate any additional FRD introduced through fiber stresses when releasing the mold, as seen in SparsePak.

3.3.5 Polishing

We will polish the optical surfaces of the fiber slit and each of the fiber heads in order to minimize light losses and FRD as the light passes through the cable. We are using an UltraPol[2] 1200 model lapping machine with 8in diameter silicon carbide and aluminum oxide lapping disks. The lapping disks span a range of grit sizes, starting from 70μm for the grinding phase to 0.3μm for the final polishing phase. Our laboratory testing shows that FRD is minimized for surface roughness $< 5\mu$m. Our target surface roughness is

[1]Miller–Stephenson Chemical Company, Inc., 55 Backus Ave., Danbury, CT 06810, (203) 743–4447

[2]ULTRA TEC Manufacturing, Inc., 1025 E. Chestnut Avenue, Santa Ana, CA 92701, (877) 542–0609

$< 0.5\mu$m. See Eigenbrot et al. in these proceedings for a full description of our FRD and surface polish testing. At the time of this writing, the entirety of the slit was polished at a 5μm level and ready to proceed to 1μm grit disks, followed by 0.3μm grit. An image of the slit in this state is shown in Figure 3.4.

3.4 Summary

We are in the final construction phase of two new fiber optic IFUs, ∇Pak and HexPak. These IFUs will be the first formatted fiber IFUs to utilize multiple fiber diameters within the same IFU head. By including multiple fiber diameters these IFUs will greatly expand the spectroscopic capabilities of the WIYN 3.5m telescope, providing the ability to sample varying spatial scales within the same observation with the highly versatile Bench Spectrograph. This will enable observations simultaneously spanning a wide range in surface brightness to be optimized for the photon limit at spectral resolutions between $1000 < \lambda/\Delta\lambda < 30{,}000$.

HexPak is designed to observe axi-symmetric surface brightness profiles with a $36'' \times 41''$ hexagonal region sampled by $2\farcs8$ fibers and a $6''$diameter high-resolution core sampled by $0\farcs94$ fibers. ∇Pak is optimized for linear surface brightness gradients, with a stacked pseudo-slit design spanning $39'' \times 55''$ using fibers ranging from $1\farcs9$ to $5\farcs6$ in diameter. Each of these IFUs presented unique challenges for successfully incorporating multiple fiber diameters within the same fiber head. We have described two methods for overcoming these challenges, one for radial arrangements of fibers and one for linear arrangements. Our solutions optimize the packing fraction of science fibers while also achieving regular and precise placement and configuration of fibers within each IFU.

References

Barden, S. C., Armandroff, T., Muller, G., et al. 1994, in Proc. SPIE, Vol. 2198, Instrumentation in Astronomy VIII, ed. D. L. Crawford & E. R. Craine, 87–97

Barden, S. C., Sawyer, D. G., & Honeycutt, R. K. 1998, in Proc. SPIE, Vol. 3355, Optical Astronomical Instrumentation, ed. S. D'Odorico, 892–899

Bershady, M., Barden, S., Blanche, P.-A., et al. 2008, in Proc. SPIE, Vol. 7014, Ground-based and Airborne Instrumentation for Astronomy II, 70140H

Bershady, M. A., Andersen, D. R., Harker, J., Ramsey, L. W., & Verheijen, M. A. W. 2004, PASP, 116, 565

Bershady, M. A., Andersen, D. R., Verheijen, M. A. W., et al. 2005, ApJS, 156, 311

Kennedy, T. 2006, Discrete and Computational Geometry, 35, 255

Knezek, P. M., Bershady, M. A., Willmarth, D., et al. 2010, in Proc. SPIE, Vol. 7735, Ground-based and Airborne Instrumentation for Astronomy III, 77357D

Kravitz, S. 1967, Mathematics Magazine, 40, 65

Steinhaus, H. 1999, Mathematical Snapshots (Dover)

Chapter 4

Vertical Population Gradients in NGC 891 I. Instrumentation and Spectral Data

If you save your breath I feel a man like you can manage it.

Tuco, The Ugly

A version of this chapter, with elements from Chapter 1 is currently in preparation to for submission to ApJ

Abstract

We have undertaken a study of the vertical and radial stellar population gradients in the edge-on spiral galaxy NGC 891. We compare gradients measured in integrated star-light to those known for the Milky Way disk from studies of resolved stars. Our optical spectroscopic measurements between 3850 and 6850 Å extend spatially from the disk midplane up to 2.6 kpc in height and out to a radius of 12 kpc on both the receding and approaching sides of the galaxy. Data were acquired with ∇Pak, a variable-pitch fiber integral field unit (IFU) on the WIYN telescope designed specifically to sample vertical gradients in edge-on galaxies. We describe the laboratory and on-sky performance of ∇Pak as well as modifications to the standard observational and analysis procedures to calibrate data taken with this unique IFU. The IFU itself has a mean throughput of 80% at 5500 Å. To achieve an estimated precision of 10% in light-weighted mean age and metallicity, we define a set of spatial apertures in radius and height in which spectra are binned to achieve a signal to noise of $\sim$20 Å^{-1}. We use spectral indices to measure age, metallicity, and abundance. Metallicities are found to be in the range from 0.2 to 2.5 $Z_{\odot}$, with abundances between solar and +0.3 dex. Metallicity and abundance gradients prove difficult to measure from indices alone for stellar populations with a broad range of ages. However, we find a clear transition from young ($< 3 - 5$ Gyr) to old (> 7 Gyr) stellar populations at 0.4 kpc, roughly the scale height of the thin disk. We also find a slight trend towards younger populations at larger radii, consistent with an inside-out disk formation scenario. The vertical age gradient in NGC 891 is in remarkable qualitative agreement with a model for disk heating tuned to studies of the Milk Way's solar cylinder.

4.1 Introduction

In this paper we present a detailed, spectroscopic study of stellar populations in the nearby, edge-on galaxy NGC 891. We measure these populations in integrated starlight mapped over much of the visible stellar disk in both radius and height. The importance of looking at NGC 891 as well as other nearby edge-on disks is several fold. First, it allows us to expand the census of spiral disks beyond the Local Group, particularly for a geometric projection that allows us to examine the spatial gradients in both radius and height more directly than in either M31 or the MW. Second, NGC 891, while historically called out as a nearby MW analog, clearly has some properties that are exceptional, such as a large HI scale height ($\sim$1 kpc Oosterloo et al. 2007), consistent with an extended dust layer (Howk & Savage 2000). Measurements of vertical and radial population gradients in NGC 891 will provide a better picture of the range of such gradients in MW-like systems, pointing to the range and multiplicity of disk formation and assembly scenarios of MW-like galaxies.

As a benchmark for what we might expect to see in terms of AVMα-R (the Age, Velocity, Metallicity, enhancement relation) in the integrated light of an external, edge-on galaxy, we focus simply on age and velocity (AV-R, where velocity, i.e., velocity dispersion is rendered in equivalent height given relevant dynamical assumptions) and ask: If NGC 891 has a similar star-formation history and AV-R as the MW's solar cylinder, what would the integrated light look like if observed edge-on? In answering this question our intent is to demonstrate the essence of our experimental design, namely a method to measure disk dynamical stratification rates by using stars as chronometers.

To estimate the vertical distribution of the stellar spectral energy distribution we construct a simple model where stars in disks (i) form at some rate at the mid-plane with

a scale-height and velocity dispersion comparable to the gas; and then (ii) are dynamically stratified through some secular process over time. We adopt a constant star-formation rate (SFR), a total age of 11 Gyr[1], the "heating" model for the solar cylinder of Aumer & Binney (2009), and assume the dynamics are such that σ_z^2/h_z is constant at late times, which is roughly what is observed in the MW disk near the sun (σ_z is the vertical stellar velocity dispersion and h_z is the corresponding scale-height, i.e., σ_z^2/h_z is proportional to the surface mass-density of the disk). We also adopt the stellar population synthesis models of Bruzual & Charlot (2003) but note that in the spectral range of interest here the choice is unimportant. By coupling elements (i) and (ii) to stellar population synthesis models it is then possible to compute the vertical distribution of star light.

By adopting this simplified model to represent what we might see for the projected vertical distribution of integrated starlight of an edge-on galaxy like NGC 891 we are in effect assuming the SFR and dynamical stratification are constant with radius. This assumption, despite the apparent radial constancy of disk thickness observed over many radial scale-lengths in external galaxies, at some level must be incorrect. Certainly we know there is flaring in gas layers with radius as well as gradients in the total and specific SFR. In a companion paper we discuss details about assumptions of the gas-layer thickness between NGC 891 and the MW, radial variations in the gas-layer thickness and heating rate, relative sensitivity to the star-formation rate versus the heating rate, as well the general problem of heating models' inability to match the thick disk. The simplifications adopted here allow us to look at what appear to be the primary observational consequences of dynamical stratification on vertical trends in the spectral energy distributions of galaxies; this simple model is likely to capture the interplay of stellar evolutionary time-scales and dynamical

[1]This is a reasonable match for the total age of the MW disk and the star-formation formation rate over the past few Gyr based on analysis of stars in the solar cylinder (e.g., Pilyugin & Edmunds 1996).

stratification that dominate the younger and intermediate-age disk components in the MW (Bird et al. 2013).

We illustrate the spectrophotometric rendering of our simple model in Figure 4.1. This example shows how the spectra of integrated star-light would appear as a function of height above the disk mid-plane for a dynamical stratification rate self-similar to what is seen in the MW solar cylinder. Inspection shows that at roughly $z \approx 0.4$ kpc there is a rapid transition in the stellar population. Here, the spectrum evolves from Balmer-absorption to metal-absorption dominance on the time-scale of A/F main-sequence stellar lifetimes (∼0.5 Gyr). The break-height where this occurs is relatively insensitive to star-formation history; spectroscopic line-strengths are reddening independent, and line-of-sight attenuation from

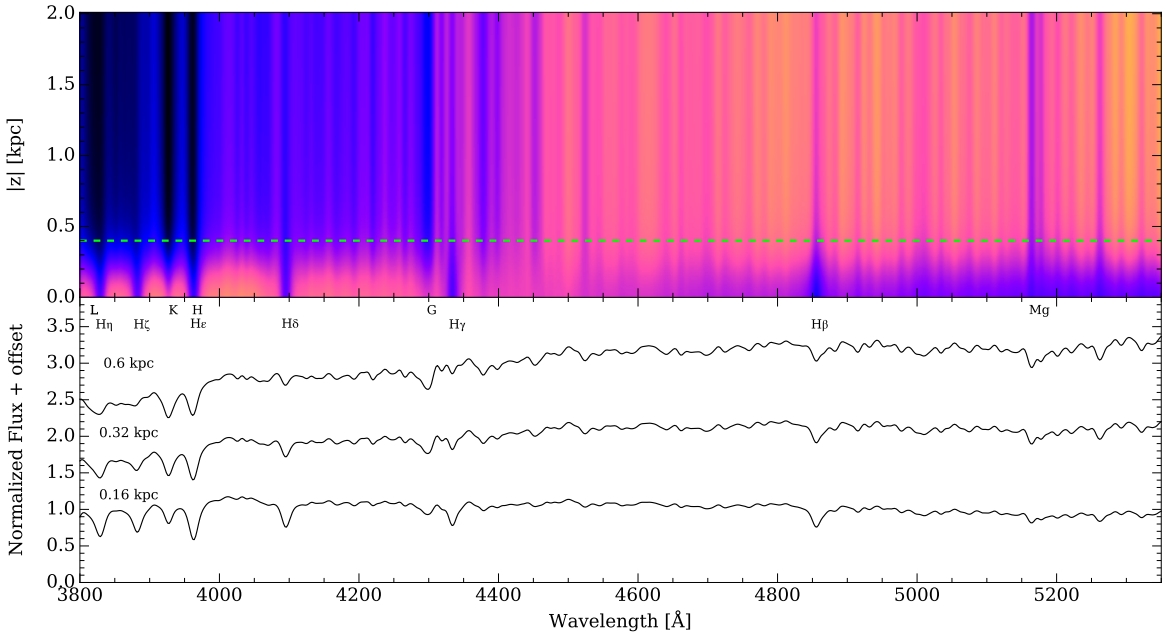

Figure 4.1 Example of spectrophotometric index change with height and stellar population. Spectra are from a model with a fast-rotating (200 km s^{-1}) disk with a constant star-formation rate and a MW-like disk-heating rate, rendered at a spectral resolution of 200 km s^{-1} (σ). *bottom:* Note the transition from Balmer-line to metal-line dominance between 0.32 and 0.6 kpc. *top:* The same model spectra plotted with height and color-coded by normalized intensity. The transition between Balmer-line and metal-line dominated populations is clear in Hδ_A and Ca H&K. The green line shows the same transition in NGC 891 at 0.4 kpc as discussed in §4.6.

dust at this expected break-height is not prohibitive for detection. Consequently, measuring the break height yields a constraint on the dynamical stratification rate on these time-scales. The transition is best detected in spectra covering the 4000 Å region, and can be measured easily even with low-resolution spectrophotometry.

Our first-order objective is to determine if we can detect and measure a spectral break height in the disk of NGC 891, and if so, how it compares to the this simple model for the MW solar cylinder. The height and width over which the spectral break occurs yields a constraint of AV-R, or the dynamical stratification rate at late times. While this model may be qualitatively correct for the solar neighborhood and NGC 891, it is well worth verifying if the observed gradients are constant with projected radius. It has been suggested from the simulations of Martig et al. (2014) that the young, star-forming disk flares at every epoch, likely for dynamical reasons perhaps related to the flaring of atomic and molecular gas at the current epoch. Recent measurements suggest such flaring is seen in MW stars (Ness et al. 2016). We will probe for a similar flaring in NGC 891, manifest as a change in break height with radius. While differential extinction effects cannot be ignored when interpreting line-of-sight depths of our observations, we will use Doppler tomography in Chapter 5 (see for example, Kregel & van der Kruit 2005) to increase the fidelity of our measurements.

Our higher-order objective is to probe whether the spectrophotometric data farther above the mid-plane enables us to extend constraints on the dynamical stratification over longer time frames commensurate with the old thin and thick disks. While the implementation is beyond the scope of the present work, the detection of metallicity and abundance gradients in both radius and height provides a mapping of AVMα-R in external galaxies, and, via the appropriate chemo-dynamical model, constraints on the dynamical stratification for disk stars over most of the star-formation history of the galaxy.

In this paper we describe the custom fiber integral field unit (IFU) we built to make measurements of vertical population gradients in nearby, edge-on disks (Section 4.2). Our observations of NGC 891 with this IFU are described in section 4.3. The data reduction and calibration procedures, particularly those specific to this first variable-pitch IFU, are given in section 4.4. The resulting spectral maps are binned based on a signal-to-noise (S/N) criterion determined by astrophysically motivated requirements on determining age and metallicity in the integrated light of stellar populations. The requirements are determined via modeling in Section 4.5. Spectral diagnostics are measured for these binned spectra to examine of the trends in age, metallicity and abundance with radius and height in Section 4.6. These give a qualitative picture of the population gradients in NGC 891, as projected along the line of sight. A synopsis of the results from this paper are given in Section 4.7.

4.2 The ∇Pak Variable-Pitch IFU

4.2.1 Design

The ∇Pak integral field unit (IFU) is mounted on the WIYN[2] Bench Spectrograph (Barden et al. 1994; Bershady et al. 2008; Knezek et al. 2010) and makes up one half of the novel HexPak/∇Pak IFU system (Wood et al. 2012), a pair of IFUs that have unique fiber configurations and share a common slit. The fiber geometry of ∇Pak is optimized for observations of edge-on galaxies; five different fiber sizes are arranged in a rectangular gradient pattern that allows for efficient observations of objects with significant surface brightness gradients on scales of roughly an arcminute (Figure 4.2). A list of fiber diameters can be found in Table 4.1. The increase in fiber size across the array corresponds

[2]The WIYN Observatory is a join facility of the University of Wisconsin-Madison, Indiana University, the University of Missouri-Columbia, and the National Optical Astronomy Observatory.

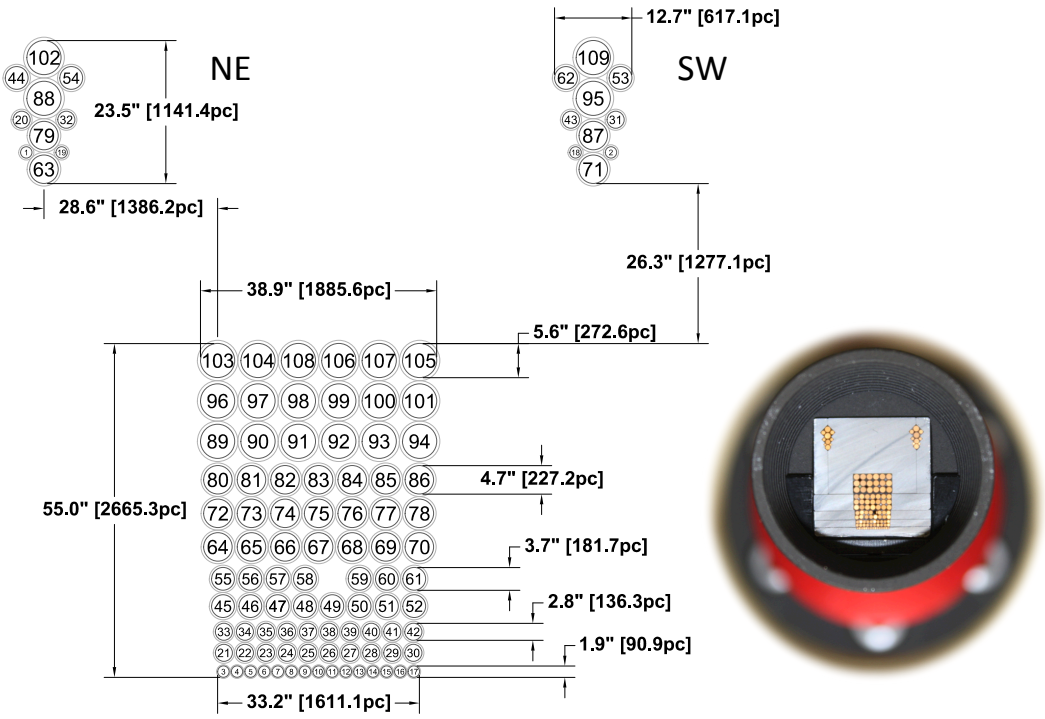

Figure 4.2 ∇Pak IFU on the WIYN 3.5m Telescope. Distances are in arcseconds and in kpc for a distance of 10 Mpc. The inset image shows the completed IFU in its mounting bracket. Note aluminum fixture and absence of packing fibers.

to equal signal-to-noise (S/N) per unit wavelength in the source or background-limit for light distributions with e-folding scales of 26 to 50 arcsec. This corresponds to vertical scale-heights of 1.3 to 2.4 kpc at a distance of 10 Mpc, comparable to the thickest possible disk components in NGC 891. In practice, the complex vertical structure of stars and dust in galaxy disks such as NGC 891's make the S/N optimization imperfect. This instrument design, by attempting to achieve similar signal-to-noise per exposure in all fibers, maximizes mapping efficiency at the cost of reduced spatial and spectral resolution in the larger fibers at larger scale-heights. This trade-off is sensible given the increased e-folding scale of the disk away from the mid-plane, and the commensurate expectation of large velocity dispersions.

The physical layout of ∇Pak consists of a main array and two groups of offset sky

fibers. The main array is a 55 arcsec high stack of pseudo slits with increasing slit-width and fiber diameters (Figure 4.2). The fibers used are broad spectrum, stepped index, fused silica fibers (Polymicro FBP) with core diameters between 200 μm and 600 μm (corresponding to 1.″87 to 5.″62 at the WIYN $f/6.3$ focal plane). The non-active (i.e., cladding and buffer) portion of each fiber takes up an additional 20% of each fiber's physical diameter. The pseudo-slits are grouped into blocks that contain all the fibers of the same size. The blocks were assembled sequentially from small to large fiber sizes to build up the entire stack. Each block is mechanically bounded by precision layers of aluminum and located with pins. The smallest fibers have only one row (or pseudo-slit) that is 33.2 arcsec in length; the two largest fibers sizes have three rows each, with a maximum pseudo-slit length of 38.9 arcsec; while the intermediate sizes have two rows. After a block has been assembled, glued and cured, it is separated from the next block by a plastic shim that is 25.4 μm (0.″24) thick; this separation is a key component of the assembly and curing process. While the scientific design of ∇Pak required a non-optimal fiber packing arrangement, the total

Table 4.1. ∇Pak Fiber Diameters

(μm)	spatial (pixels)	spectral [a] (pixels)	(arcsec)	(pc [b])
200	4.64	4.36	1.87	90.9
300	6.96	6.55	2.81	136
400	9.28	8.73	3.75	182
500	11.6	10.9	4.69	227
600	13.9	13.1	5.62	273

[a]Assuming the anamorphic factor in Table 4.2

[b]Assuming a distance of 10 Mpc to NGC 891.

packing efficiency (defined as light-gathering area divided by total area) of the main array is roughly 55%.

The sky fibers of ∇Pak occupy two sub arrays that are offset 26.″3 vertically and 28.″6 horizontally on either side of the main array. On NGC 891 this places the sky fibers 1.3 kpc above the top of ∇Pak and ∼ 3.8 kpc from the plane of the galaxy, far above measurable flux from the galaxy (Rand et al. 2011). The sky fibers were assembled separately in machined blocks that are mechanically attached to the main array. The entire IFU was polished as a single, assembled unit. The polishing process was similar to what was undertaken for SparsePak (Bershady et al. 2004).

∇Pak does not have any packing fibers. Instead, the physical layout is established with a custom-built aluminum fixture, as described above and in (Wood et al. 2012). Based on the results of §4.2.3 we do not think the lack of buffering fibers causes a significant loss of performance. However, the use of aluminum, and in particular the aluminum shim material comprising the walls of the pseudo-slit layers is not optimal for optical polishing, with deleterious effects noted in §4.2.3. A lesson learned is that the fabrication ease, efficiency, and low machining cost of aluminum does not out-weigh the superior performance of suitable stainless steel, invar or ceramics, which we would recommend for future builds. In contrast, for example, the stainless steel ferrules used in MaNGA in SDSS-IV (Bundy et al. 2015) provided outstanding fixturing for obtaining good optical finish on the polished fibers (Drory et al. 2015). We note that the challenges with the aluminum fixture for ∇Pak was not an issues for HexPak which, like its predecessors DensePak (Barden et al. 1994) and SparsePak (Bershady et al. 2004) consisted of an entirely fused-silica array.

Further details of the design and construction of HexPak/∇Pak, including cable design, fabrication and commercial product descriptions for specific components can be found in Chapter 3 (a reprint of Wood et al. 2012). Notable are the dual-slit assembly

that sits inside a standard Bench Spectrograph fiber "foot," as well as the rotation couplers that ease handling while minimizing stress-inducing torsion on the fibers during telescope rotator motion.

4.2.2 Mechanical Performance

Despite best effort and extensive testing to develop best practices, the mechanical alignment of the ∇Pak fibers has some noticeable imperfections. In Appendix A we provide a high-resolution image (Figure A2) of the as-built fiber array to document this. The irregularities are particularly notable for the 400 μm ($3\farcs75$) fiber pseudo-slits for which some fibers have offsets from their idealized location (Figure 4.2) by as much as $0\farcs5$. The other pseudo-slits have internal and relative alignment to other pseudo-slits that we estimate are accurate at the $0\farcs1$ - $0\farcs2$ level. Table D1 provides the idealized fiber locations corresponding to Figure 4.2. These should suffice for almost all applications except the most demanding that for whatever reason require very high precision relative astrometry. Overall, the final IFU has good-to-excellent mechanical regularity.

4.2.3 Optical Performance

The IFU face and slit were both polished to a 0.5 μm grit level to mitigate throughput losses caused by surface scattering (Eigenbrot et al. 2012). Material from the aluminum fixture was seen to form deposits on the fiber faces, with some performance degradation that we summarize here and detail in Appendix A.

Laboratory measurements of throughput and focal-ratio degradation (FRD) in the Johnson V band revealed distinct performance gradients across the array. Some of the throughput variations are likely due to polish imperfections from aluminum residue. However, we find FRD systematically decreases with larger fiber size, with a small upturn

for the largest fibers. Unfortunately we cannot separate systematic performance differences for different fiber core sizes from differences in the handling and assembly process. We also find, not surprisingly, that FRD correlates to first order with throughput, but that there is a bimodal distribution in transmission and FRD which indicates several processes at work in determining fiber performance.

Overall, the throughput, defined for an $f/6.3$ fiber input from the telescope and the $f/4$ out speed matching the Bench Spectrograph collimator, has a maximum of 90% and a minimum of 50% at 5500 Å. The mean throughput for all fibers is 80%, with means by fiber size of 70, 81, 84, 83, and 79%, from small to large. Means for sky fibers are comparable, within a percent. We compared our lab measurements to the relative throughput from dome-flats measurements once ∇Pak was installed on the telescope. This comparison shows that the on-telescope *relative* performance is the same, indicating throughput variations are intrinsic to the cable and not the spectrograph, consistent with expectations for the performance of the upgraded Bench Spectrograph (Bershady et al. 2008; Knezek et al. 2010).

One of the 3.″75 fibers (between fibers 58 and 59 as marked in Figure 4.2) fractured during polishing. The fracture is close to the surface and likely could be polished out; this was deemed impractical to pursue due to the indeterminate fracture depth and the risk of exceeding the finite gluing length. The fracture leaves 10% of the fiber face intact and transmitting, but for practical purposes this fiber is considered not usable and ignored in all astrometry tables. A close-up image of the ∇Pak fibers that shows polishing imperfections and the broken fiber can be found in Figure A2. Despite these imperfections, the final IFU has good transmission performance.

4.2.4 Installation

Final construction of ∇Pak was completed in September 2013. HexPak/∇Pak were then installed at WIYN during November 2013. The 25 m of cabling that contain the IFUs are routed from the Bench Spectrograph room, up through the central bearing of the azimuth drive, out of one of the telescope forks, and onto a tray designed to hold the SparsePak cable. During observations one of the IFU heads is plugged into the the WIFOE[3] port, which provides common IFU access to the IAS[4] on one of WIYN's nasymth ports. During cable routing a section of cabling developed a hole that was the result of bend stress causing the helical wrapping of the cable to come undone. This hole was repaired on site and is located just within the fork on the observing floor. Fibers were not damaged, and the cable integrity has been deemed acceptable for the life of ∇Pak.

During installation we confirmed that both the HexPak and ∇Pak slits occupy the same focal plane, which allows the heads to be switched at the telescope end without the need to adjust the Bench Spectrograph. We also adjusted the precise location of the HexPak, ∇Pak, and SparsePak (Bershady et al. 2005) fiber faces so that they share a common focus in the port. The common focus locations at both ends of the fiber cable allow users to switch between HexPak and ∇Pak in only a few minutes during the night, which allows great flexibility in scheduling multiple programs on the same night.

In addition to access for the WIYN IFUs the WIFOE port has a pellicle and camera that allow observers to see an image of the IFU fibers overlaid on the view from the telescope focus. To resolve the smallest fibers in HexPak/∇Pak the existing WIFOE camera was

[3]WIYN Indiana Fiber Optic Echelle

[4]Imaging Acquisition System

replaced with an Allied GigE GT3300 CCD with a default resolution of 0.″258/pixel[5].

4.3 Observations

Observations of NGC 891 were obtained over two runs in November and December of 2014. Data were collected with the ∇Pak IFU, coupled to the WIYN Bench Spectrograph.

4.3.1 Spectrograph Configuration

For both runs the spectrograph was configured identically and set up to cover as far blueward of the 4000Å-break as practically possible while reaching as far red as Hα. The scientific motivation for this large baseline was to capture Ca H&K (3934,3968 Å; this also includes Hϵ), the G-band (∼4304 Å), MgI (∼5175 Å), and the upper Balmer series (at least

[5]more information can be found at `http://www.wiyn.org/Instruments/WifoeCameraInterface.pdf`

Table 4.2. Spectrograph Setup

Parameter	Value	Units
Grating Name	400@4.2	-
Order	1	-
Grating Angle	21.53	deg.
Camera-Collimator Angle	30.00	deg.
Anamorphic factor	0.941	-
$\lambda_{\rm min}$[a]	3372	Å
$\lambda_{\rm max}$[a]	7640	Å
Dispersion at 5500 Å[b]	2.079	Å/pix

[a]Formal wavelength range; values used for analysis are between 3850 and 6650Å as described in the text.

[b]For 2× binning in the spectral dimension.

up to Hδ), all important diagnostics for stellar populations; to provide a measure of the continuum slope to determine reddening independent of stellar age; and to have additional checks on the extinction as derived from the ratio of Hα/Hβ emission line fluxes (i.e., the Balmer decrement).

Achieving such a broad wavelength range that extends to the blue with the Bench Spectrograph is challenging. This is due primarily to the decreasing transmission of the spectrograph optics and fibers and decreasing CCD quantum efficiency below 4500 Å. In addition, as a single beam spectrograph with all-refractive optics, the ability to focus over a broad wavelength range extending to the blue is limited, despite the ability to tilt the detector to compensate for chromatics. Lastly, the grating suite is not optimal. Two 600 l/mm gratings are just able to capture from, e.g., 3800-6650 Å, which would enable us to just capture the Fraunhofer L-band and Hη features between 3810-3840 Å in the blue, and the redder [NII] line at 6584 Å in the red. Unfortunately these gratings are blazed too far to the red to provide adequate overall efficiency in the blue.

We used engineering time to test alternative spectrograph configurations with improved performance in the blue. As we show in Appendix B, compared to the best alter-

Table 4.3. Program Targets

Name	Type	α	δ	epoch
NGC 891 P1	object	02:22:29.7	+42:19:17.2	2000
NGC 891 P2	object	02:22:32.5	+42:20:26.0	2000
NGC 891 P3	object	02:22:37.6	+42:22:38.3	2000
NGC 891 P4	object	02:22:30.1	+42:21:33.7	2000
NGC 891 P5	object	02:22:26.8	+42:18:07.9	2000
NGC 891 P6	object	02:22:40.4	+42:23:57.0	2000
BD 284211	flux standard	21:48:57.1	+28:37:48.0	1950
Feige 110	flux standard	23:17:23.5	-05:26:22.0	1950

native 600 l/mm grating, the very low (blue) blaze of the 400@4.2 grating yields better performance below 4500 Å (a factor of 2 increase in total system efficiency at 4000 Å), and broader wavelength coverage, albeit with a 37% lower spectral resolution. Because of the importance of the blue spectral region, we chose this grating for our observations. The detailed configuration provided in Table 4.2.

While our spectrograph configuration covers between 3372 and 7640 Å (the blaze wavelength is 3496 Å) on the detector, in practice the useful blue limit of the data is roughly 3850 Å due to the sharp decline in system efficiency. This captures Hζ and sufficient pseudo-continuum to define a break amplitude (e.g., D_n4000; Balogh et al. 1999). The Fraunhofer L-band and Hη features between 3810-3840 Å are clearly visible in the highest signal-to-noise data, while the strong FeI blends in the 3700-3750 Å region and the Balmer break (3646 Å) are not detected. At the red end of our wavelength range defocus becomes a serious problem and fiber traces begin to blend significantly. This defocus, and the rise of strong atmospheric OH features, sets the usable red limit to 6650 Å; this still captures Hα and [NII] lines.

4.3.2 Targeting

We observed NGC 891 with 6 pointings of ∇Pak spanning a radial range between $\sim$0.8 kpc $< |r| <$ $\sim$10 kpc, as given in Table 4.3. We chose pointings covering both approaching and receding sides of the galaxy because of the known asymmetry in star-formation and orientation of what appears to be a two-armed spiral (Xilouris et al. 1999; Schechtman-Rook et al. 2012). In particular, the approaching side appears to have significantly more Hα emission and visible star-formation (Rand et al. 1990; Howk & Savage 2000; Kamphuis et al. 2007b), with the spiral arm closer along the line of sight. Kamphuis et al. (2007a) claim the star-formation asymmetry based on Hα emission is over-estimated

due to differential attenuation effects, but nonetheless the 24μm emission indicates at least a 30% difference in current star-formation on the two projected halves of the galaxy. Furthermore, the HI distribution is also asymmetric, with an extension to larger radii at lower column-density on the receding side (Swaters et al. 1997; Oosterloo et al. 2007), although a similar asymmetry has not been detected in CO (Scoville et al. 1993) possibly because of lack of depth or coverage. Throughout this paper we use a sign convention where radius is negative corresponding to the approaching (NE) side and positive corresponding to the receding (SW) side.

To probe the known radial variations in disk components of NGC 891 on both sides of the disk while continuously sampling in $|r|$, pointings are staggered across the two sides of the galaxy. The inner two ∇Pak pointings (P2 and P4), on opposite sides of the center, sample within the *inner* truncation of the thin and super-thin disk components, as reckoned by Schechtman-Rook & Bershady (2013); this region is dominated by a thickened, vertically

Table 4.4. Summary of Observations

Pointing	Date (UT)	r (kpc)	Integration (min) Nightly	Total
1	2014 Nov 20	4.4	210	···
	2014 Nov 21	···	60	270
2	2014 Nov 21	0.8	210	···
	2014 Nov 22	···	60	270
3	2014 Nov 23	−6.4	330	330
4	2014 Nov 24	−2.3	270	270
5	2014 Dec 20	8.1	270	···
	2014 Dec 22	···	270	540
6	2014 Dec 21	−10.0	240	···
	2014 Dec 23	···	120	···
	2014 Dec 24	···	180	540

exponential layer with a similar scale-height to the thick-disk seen in the outer radial regions. This inner region displays bar-like x-shaped isophotes, and the extended luminosity is not that of a classical bulge. P1, P3, and P5 sample the region of the super-thin disk. The outermost ∇Pak pointing, P6, probes the region beyond which there appears to be a super-thin disk as reckoned by NIR broad-band photometry (Schechtman-Rook et al. 2012), i.e., beyond the outer truncation of the super-thin disk.

Figure 4.3 shows our ∇Pak pointings related to the results of Schechtman-Rook & Bershady (2013), Figure 4.4 contains a pointing map, and a summary of observations can

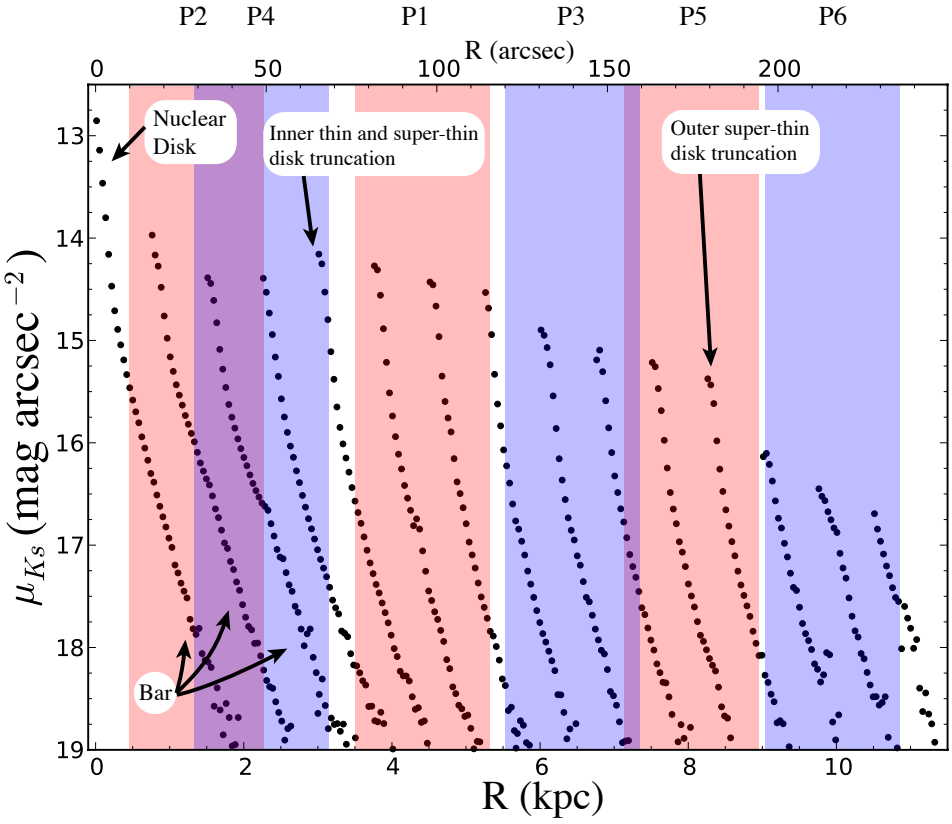

Figure 4.3 Comparison of our ∇Pak pointings to attenuation-corrected K-band light profiles measured by Schechtman-Rook & Bershady (2013). Important morphological features from that work are labeled with arrows. Shaded regions show the radial extent of each ∇Pak pointing. Positive values of radius (receding) are red and negative radius values (approaching) are blue. The innermost ∇Pak pointings were chosen be within the inner disc truncation visible in the density profiles.

be found in Table 4.4. Ideally we would have observed both the southern vertical half of the extended disk as well as the northern vertical half. However, our pointings cover the full inner 0.5 kpc of the disk mid-plane in height and we anticipate vertical asymmetries between the two halves of the galaxy at larger heights are modest compared to radial variations on the approaching and receding sides.

All individual exposures for NGC 891 were 30 min in duration. This exposure time was chosen so that the dominant random error in the measured counts is caused by photon shot-noise from the sky and galaxy flux, and not detector read-noise. To further beat down the read-noise all exposures were binned 2x2 before readout, which still allowed for adequate sampling of the smallest fibers (∼2 pixels full width at half maximum in both the spectral and spatial dimensions). The total integration time for each pointing varies with radius and are based on the requirement of the MaNGA survey (Bundy et al. 2015) to measure absorption line indices sensitive to age and metallicity. This S/N limit is roughly 50 per resolution element. In practice the complex structure of NGC 891 lowers this limit, but, as shown in §4.5.1, a S/N of 50 is larger than required for full-spectrum SSP fitting.

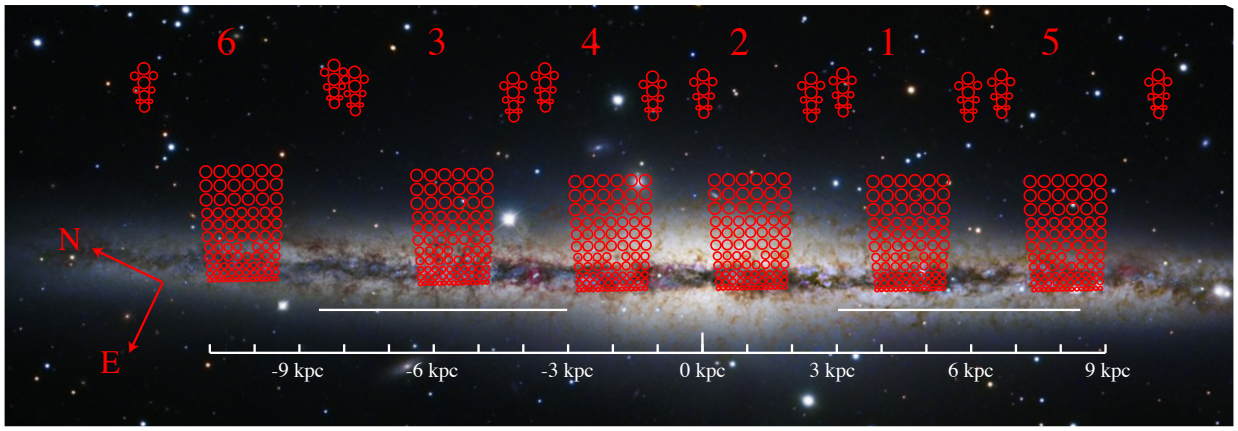

Figure 4.4 NGC 891 ∇Pak pointings (Table 4.3) overlaid on combined Subaru (V band)/West Mountain Observatory (R,G,B) image. The horizontal white lines denote the extent of the super-thin disk reported by Schechtman-Rook & Bershady (2013). *Image credit:* Robert Gendler, NAOJ, HST/NASA, BYU (Michael Joner, David Laney). In this orientation the approaching side is to the left.

Some extra time left at the end of our program was used to increase the observation time (and therefore S/N) of the outermost pointings (5 and 6) where the signal was expected to be lowest.

For all ∇Pak observations the PA offset was 295.79° (East of North), which is slightly offset from perfectly perpendicular to the disk of NGC 891. This offset allows each fiber to occupy a unique location in z, but is small enough to not affect the differential light-gathering power unique to ∇Pak.

4.3.3 Calibration Data

In addition to on-sky galaxy exposures we took bias, dark, dome-flat, CuAr arc lamp, and standard star exposures for use during data reduction. Standard star and other calibration exposures were short enough (< 2 min) that dark current was not a significant source of noise for these frames. Unfortunately, for the longer exposures the elevated dark current of the Lincoln Labs STA1 (SN 5644) CCD currently used on the Bench requires accurate dark-frame subtraction for any work approaching sky-limited surface-brightness levels. Dark frames were 30 minutes long (i.e., the length of a single object exposure) and taken during the day, between nightly observations.

Due to tight scheduling at WIYN we were only able to observe dome flats and arc lamps at the beginning of each night. Comparisons of these frames across nights (and even from month-to-month) show that the Bench Spectrograph is stable following 30 minutes from a dewar fill. Once-a-night calibration frames are adequate for accurate data reduction so long as the spectrograph configuration is not changed.

The presence of multiple fiber sizes in ∇Pak required modifications to the standard calibration procedure for dome flats and standard stars. In particular, two sets of dome flats at different exposures are needed: one set with a short (1 sec.) exposure time to

avoid saturating the largest fibers, and one set with a longer (4 sec.) exposure time to get enough signal in the smallest fibers. These two sets are combined during data reduction as described in §4.4.1.2.

Once during each of the observing runs a set of blank sky observations was recorded during twilight (i.e., sky flats). Due to the challenging nature of flat observations described above these flats were not deemed suitable for use during data reduction, but we are optimistic that further investigation and experimentation with sky flats can yield success for future ∇Pak programs.

Nightly observations were made of two standard stars taken from the IDS Photometric Standards catalog, listed in Table 4.3, and were made ∼2 times per star per night. The ∇Pak fibers have a broad range of sizes, which, at the smallest, are insufficient to capture the entire PSF. Further, because of atmospheric refraction, the amount of light lost in the smaller fibers varies with wavelength. While scanning the stars across the fibers at the parallactic angle would eliminate wavelength-dependent effects, the available telescope software was not up to this task. Consequently, we chose to use only the largest (5.″62 diameter) fibers for standard star observations. Each set of standard star observations used 2-4 fibers so that over the course of the entire observing program all of the 5.″62 fibers had been used to observe the standard stars. Application of these observations to flux calibrating the NGC 891 observations is described in §4.4.2.

4.4 Data Reduction and Calibration

4.4.1 Image processing and spectral extraction

Basic reduction (overscan correction, bias/dark subtraction) was done with IRAF's CCDPROC package. Cosmic rays were cleaned with the CRUTIL package. Spec-

tral extraction, wavelength calibration, and flux calibration were done with the HYDRA package. The multiple fiber sizes in ∇Pak required modifications to the standard DOHYDRA procedure for flat-field generation, sky-subtraction, and flux calibration. A detailed walkthrough and discussion of these modifications can be found at `www.astro.wisc.edu/~eigenbrot/GradPak`; we summarize the important points below.

4.4.1.1 Wavelength Calibration

Uncertainties in the wavelength solution in the blue (<4500 Å) are the dominant source of uncertainty in determining the line-of-sight doppler shift of the observed spectra. As shown in Chapter 5, these velocities are important for determining the line-of-sight depth of our spectroscopic observations, which requires velocity precision better than the spectral resolution of our data. The reason for the wavelength calibration uncertainty at short wavelengths is the combined dearth of strong spectral features in the CuAr arc-lamp and the sensitivity fall-off in the fibers, spectrograph optics, grating and CCD. The number of good spectral lines that can be fit from the available arc-lamps between 4130 Å and 7300 Å is 33.

To characterize the uncertainties in the wavelength calibration, we measure the centers of Solar Ca H&K absorption (from zodiacal or atmospheric scattering) and three HgI emission lines (atmospheric scattering from terrestrial sources, e.g., Tucson) present in our data (before sky subtraction). In all of our data exposures the foreground (zodiacal plus atmospheric) signal dominated over the flux from NGC 891 to the point where discrimination between Solar Ca H&K and Ca H&K in NGC 891 was not necessary.

For each night of observation all wavelength-calibrated object frames are combined to improve S/N (especially relevant for measurements of absorption lines) before line centroids are measured with IRAF's FITPROFS routine. For each line measured the average offset

from the known center across all ∇Pak fibers is taken as an indication of the accuracy of the wavelength solution at that particular wavelength. The standard deviation of the measured centers across all ∇Pak fibers is a measure of the precision of the wavelength solution at a particular wavelength.

Accordingly, Figure 4.5 shows the estimated accuracy and precision for each of the 10 nights of NGC 891 observations. At wavelengths > ∼4000 Å our wavelength solution is both

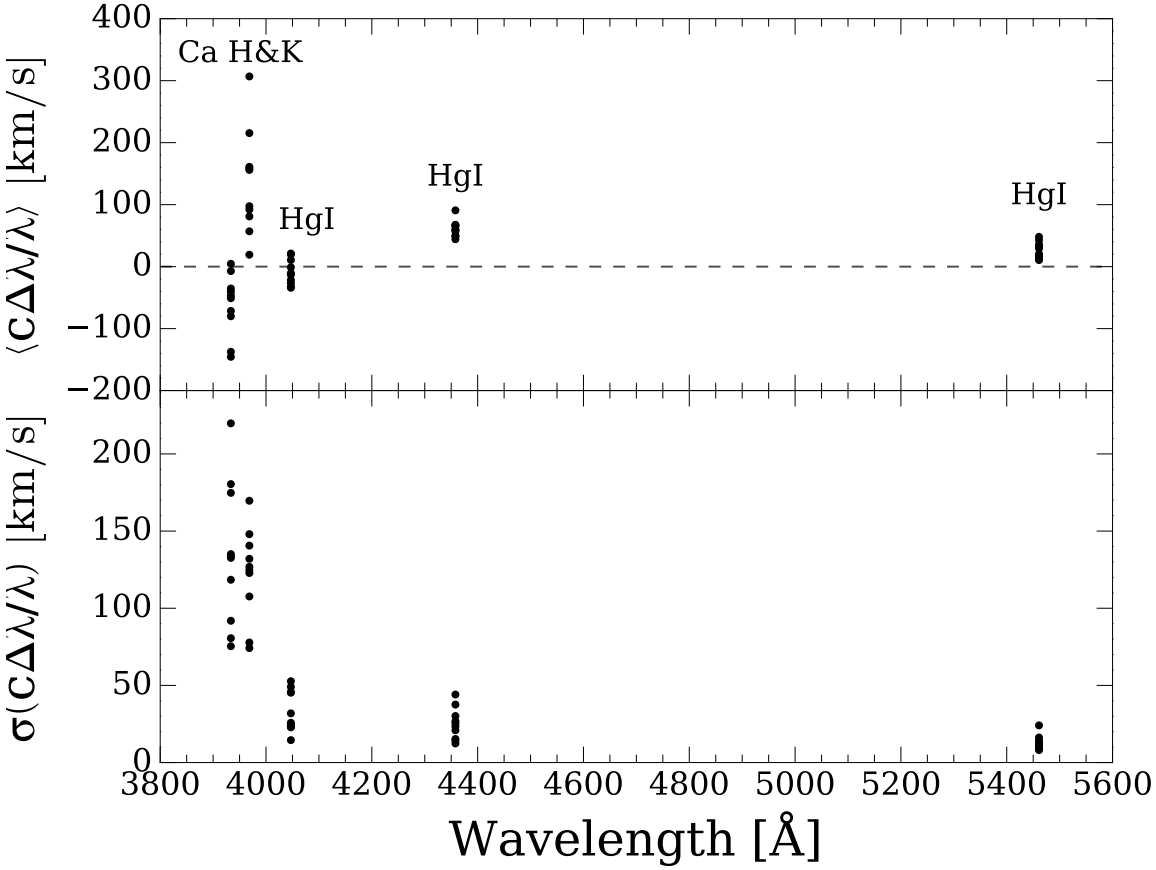

Figure 4.5 Estimated accuracy and precision of the wavelength solution in the blue region of the spectrum based on measurements of known foreground features (HgI emission at 4047, 4358 and 5461 Å from terrestrial light pollution, and Solar Fraunhofer H&K lines from Ca) in our sky spectra. Each point corresponds to a measurement of a line from an individual night of NGC 891 observations. *top:* The mean offset in km $^{-1}$ between measured line centers and the known values, averaged over all ∇Pak fibers. *bottom:* The standard deviation of the measured line centers in km s^{-1}, computed across all ∇Pak fibers.

accurate and precise to within ∼50 km s^{-1}. Below 4000 Å (where the wavelength solution is determined via extrapolation of the CuAr lamp line data) we measure a systematic offset of ∼120 km s^{-1} with a comparable value for the random error. We therefore report an upper limit on the uncertainty in our wavelength solution to be 120 km s^{-1} at 4000 Å, while noting that for most wavelengths this is an overestimation. The RMS uncertainty reported by the wavelength fitting routine is ∼90 km s^{-1}, which is likely a more accurate estimate of the uncertainty for the wavelength region covered by arc lines (4130 Å$< \lambda <$ 7300 Å). Even in the worst case we are able to calibrate wavelengths to a higher precision than the spectral resolution (see §4.4.3), which varies from 180 to 570 km s^{-1} at 4000 Å (depending on fiber size). Thus, accurate measurements of velocity based on χ^2 fitting of absorption lines (as done in Chapter 5) is possible with our data.

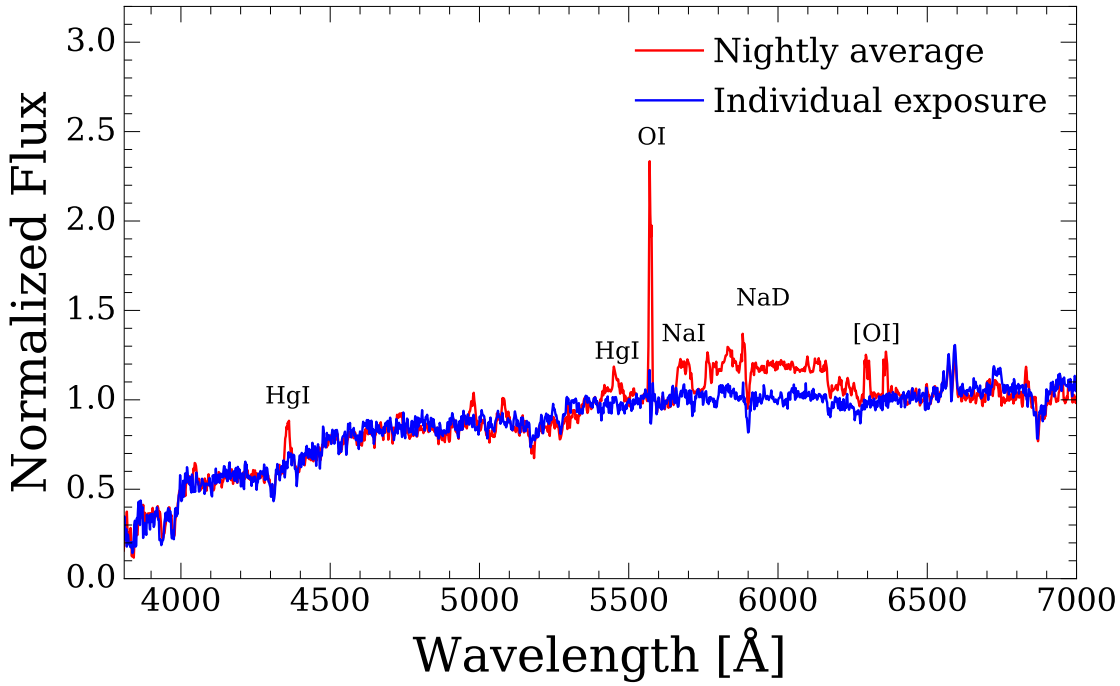

Figure 4.6 Example of large sky-subtraction residuals from November 21st, 2014. The red spectrum shows fiber 80 after sky subtraction using a sky spectrum that is the average across the whole night. The blue spectrum shows the same fiber after sky subtraction using only the sky fibers from the same exposure.

4.4.1.2 Flat Fields

The combination of spectrograph setup and the multiple fiber sizes in ∇Pak required two different dome flat exposure times: a short exposure (1 s) to avoid saturating the largest fibers, and a long exposure (4 s) to get adequate signal in the smallest fibers. Both sets of dome flat exposures were run through CCDPROC, combined, and had their apertures extracted independently by DOHYDRA. The so-called "extraction" produces a one-dimensional data vector (spectrum) for each fiber. In both cases the extraction used fiber traces computed from the 1 s flat for all data because we found that saturated large fibers in the 4 s flats introduced errors in the extraction process while the low signal in small fibers at 1 s was still adequate for tracing purposes. In practice, traces using the 4 s or 1 s are very similar, as confirmed by the intermediate-size fibers that have good signal without being saturated. This is expected given the fact that the two exposure sets were taken right after each other over a short period of time.

Once the two flats had their apertures extracted, the resulting spectra were scaled to the same exposure time and stitched together into a "master" flat where the $1\farcs87$ and $2\farcs81$ fibers were taken from the 4 s flat and the $3\farcs75$, $4\farcs69$, and $5\farcs62$ fibers were taken from the 1 s flat. This master flat was used in all subsequent reduction of the on-sky data.

During the exercise of establishing this pipeline we discovered a lag in the shutter time that affects exposures shorter than ∼7 s. The WIYN Bench Spectrograph CCD has a linear slide shutter that has opening and closing times that are not equal. Because the shutter moves along the wavelength dimension of the CCD the effect of this inequality is to add an artificial spectral signature. The magnitude of this signature varies with exposure time, with the largest deviation measured as ∼20% at 1 s. We removed this spectral mismatch

between the 1 s and 4 s flats by normalizing all fibers in the 4 s flat to the mean spectrum of the 1 s flat. While this method still introduces the shutter spectrum present in the 4 s flat this spectrum is constant across all fibers and is thus removed during flux calibration.

4.4.1.3 Sky Subtraction

Each fiber size in ∇Pak has 4 dedicated sky fibers, as illustrated in Figure 4.2. Sky subtraction was performed on a fiber-size basis using different beam numbers for each fiber size in HYDRA's SKYSUB routine. Since there are multiple sky fibers, rejection of contaminated sky fibers was possible, as indeed was required (see Figure 4.4 for P6, P4, P1).

The data from the night of November 21st, 2014 (P1) showed strong variation in sky intensity across the course of the night. This variation did not subtract well when using a sky spectrum averaged across the whole night. In particular, the region between atmospheric NaI emission at 5684 Å and the broad high-pressure sodium feature around 5900 Å often left strong residuals when using a nightly average for the sky spectrum. Accurate sky subtraction was achieved by computing the average sky spectrum on an exposure-by-exposure basis and combining individual object exposures *after* sky subtraction. For consistency across the observing program the data for all nights was sky subtracted in this way. Figure 4.6 shows representative before-and-after spectra illustrating this issue.

4.4.2 Flux Calibration

As discussed in §4.3.3 atmospheric refraction limited our standard star observations to only the 5.″62 fibers. On each night the same two standard stars were observed in multiple 5.″62 fibers and a flux calibration was computed using the ONEDSPEC package. Time

constraints in our observing program limited the range of airmasses available for standard star observations and for this reason we could not compute an extinction curve for our data. We instead used the KPNO extinction curve provided in ONEDSTDS[6].

To zeroth order we expect the spectral response of all the ∇Pak fibers to be the same because they are made of the same material and are all from the same foundry run (Wood et al. 2012). In reality the ∇Pak fibers come from different draws, were handled differently during construction, and have different degrees of termination quality. Consequently, there are throughput variations not only between fiber sizes, but also within fiber sizes, as illustrated in Figure A1. Throughput characteristics vary across the ∇Pak

[6]http://stsdas.stsci.edu/cgi-bin/gethelp.cgi?onedstds

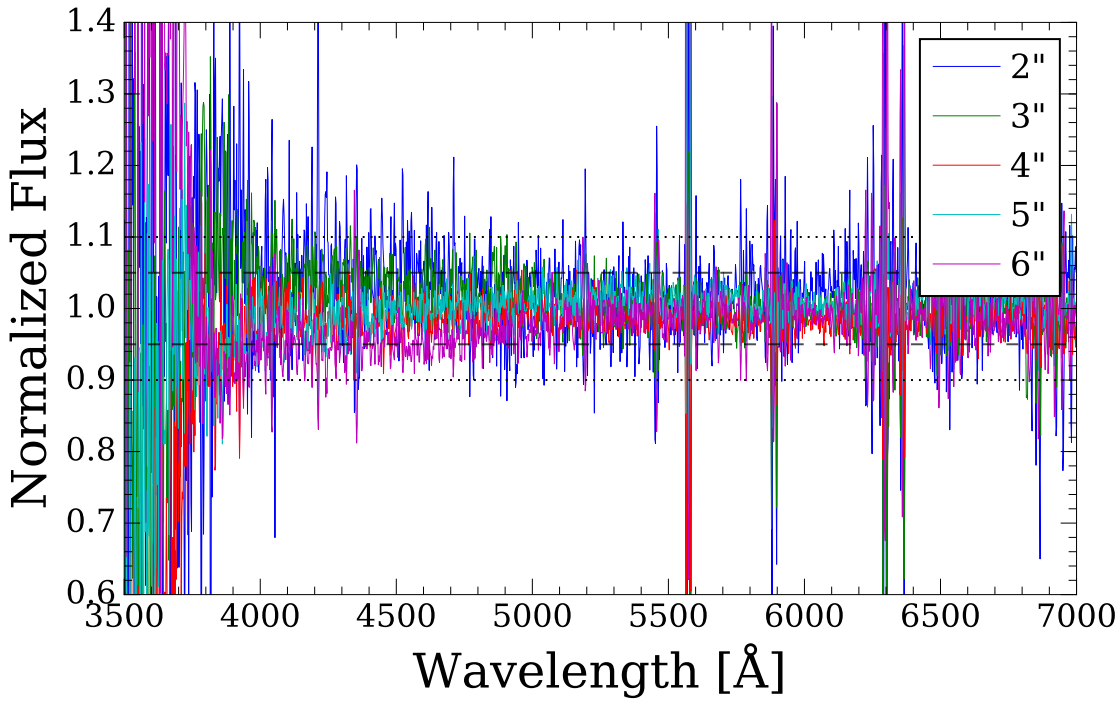

Figure 4.7 Flux calibration test for all fiber sizes when using standard star data from only 5.″62 fibers. Data are taken from a single galaxy exposure reduced through flux calibration, but not sky-subtracted. Each line represents the average of all 4 sky fibers for a given fiber size and all lines are normalized by the mean of all sky fibers. The dashed and dotted lines show deviations at the 5% and 10% level, respectively.

array. In particular, the total throughput and focal ratio degradation are worse for the smallest fibers. The throughput variations are expected to be relatively grey (wavelength independent), but variations in FRD can lead to different, wavelength dependent losses within the spectrograph. Because the flat-field screen uniformly illuminates the array, the flat-fielding process should remove all of these relative variations.

To assess the effects of using flux standards taken in a single fiber size to calibrate the entire ∇Pak IFU we compared flux calibrated sky spectra for all fiber sizes. The data came from a single exposure of P3 (see Figure 4.4) where none of the sky spectra appeared to be outliers due to source contamination from foreground stars or background galaxies. All sky fibers were flux calibrated using data from the $5\farcs62$ fibers, and then the 4 sky fibers of each size were averaged together. Figure 4.7 shows the average spectrum for each fiber size, normalized to the mean of *all* sky fibers. At wavelengths greater than 4000 Å the sky spectra are consistent between fiber sizes to within 5%. Below 4000 Å the flux calibration varies by up to $\sim$20% due to low signal to noise at these wavelengths.

To account for night-to-night offsets in extinction (caused by, e.g., high cirrus clouds) we scaled each individual exposure so that all exposures in a particular pointing have the same average flux in the region 4500 Å $\leq \lambda \leq$ 5500 Å. Within a single night this scaling was always less than $\sim$3%, but between nights it could vary by a factor of up to 2 in cases where a night had poor observation conditions (high humidity, persistent clouds, etc.). The final spectra for each pointing are an average of individual exposures weighted by the square of the inverse of their deviation from the mean pointing flux in the range 4500 Å $\leq \lambda \leq$ 5500 Å.

4.4.3 Instrumental Line Profile

The optical distortions of the WIYN Bench Spectrograph results in an instrumental line profile that varies with wavelength and field location along the fiber slit for a fiber of a given size. The delivered line profile in the spectral dimension (the instrumental dispersion) is a convolution of this distortion with the anamorphically demagnified fiber image. Consequently the different fiber sizes in ∇Pak cause the spectral line profile to be a different function of wavelength for each fiber size. We refer to this value as $\sigma_{\rm inst}$, reported in units of km s^{-1}.

To account for the variations in $\sigma_{\rm inst}$ in our later fitting of model spectral energy distributions, we first measured the width of arc-lamp emission lines across our entire wavelength range for all fibers. Widths for each arc line were measured for every fiber,

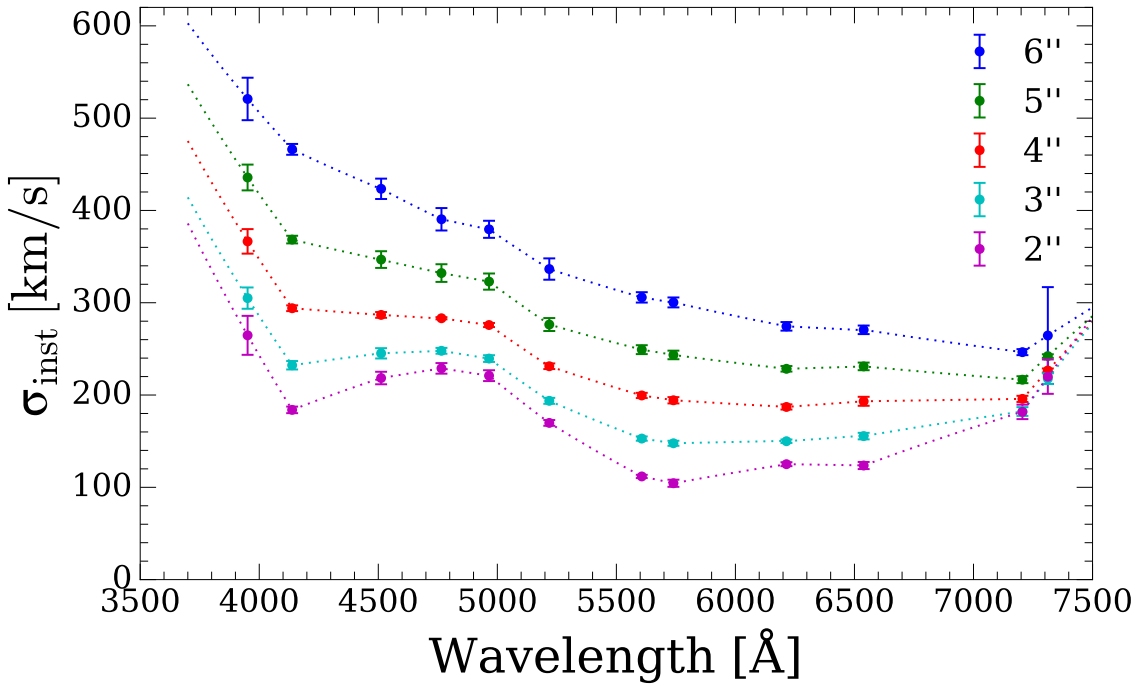

Figure 4.8 Instrumental resolution as measured from CuAr arc-lamps are plotted as points; the interpolated and extrapolated dispersion functions used in spectral modeling is shown by the dotted lines.

and then averaged for all fibers of the same size, weighted by poisson noise in each fiber. Arc lines with low signal-to-noise were combined together in groups over narrow wavelength ranges to improve the signal and assigned a new wavelength weighted by the signal-to-noise of the component lines. This was particularly important in the far blue where the lines were few and often weak.

These data were interpolated to create dispersion functions, $\sigma_{\mathrm{inst},i}(\lambda)$, for each fiber size, i. Past the blue and red ends of the region covered by arc lines (4130 Å$< \lambda <$ 7300 Å) the dispersion functions are extended with linear extrapolation. The line-width data and resulting instrumental dispersion functions can be found in Figure 4.8. Note the hat-shaped profile seen for the smallest fibers, characteristic of the typical compromise focus value chosen for the all refractive Bench Spectrograph system. For larger fiber sizes the resolution is dominated by the geometric fiber diameter and the changes in the grating dispersion with wavelength.

4.5 Signal to Noise and Spatial Binning

4.5.1 Signal-to-Noise threshold for spectral bins

Despite ∇Pak's design, clumpiness in the distribution of dust and star-light result in different signal-to-noise ratios (S/N) in each fiber. Co-adding spectra ("binning") from adjacent fibers enables us to homogenize S/N and hence the precision on age and metallicity inferred from spectral fitting, but at the expense of spatial resolution. We have attempted to optimize the spectral binning by defining a critical S/N threshold to achieve a *precision* of 10% in age and metallicity. In the absence of other mitigating effects, this precision is ample to detect the vertical age break in a MW-like heating model and to determine the break height to within 50 pc because the predicted gradient in light-weighted mean

age is very steep near the mid-plane. At this level of precision, systematic effects in the interpretation of the break height, e.g., due to inaccuracies of our estimated line-of-sight depth or model assumptions about star-forming history become dominant. In what follows we define S/N in pixel units, where each pixel samples roughly 2 Å.

Accordingly, the critical S/N threshold was determined using an idealized Monte Carlo simulation of model galaxy spectral energy distributions (SED) with known star formation histories and chemistries (and therefore known ages and metallicities). We have ignored systematic errors in, e.g., flux calibration or between the model libraries and stellar evolutionary tracks and reality, although we address issues with stellar libraries and evolutionary tracks in Chapter 5. While other studies have undertaken similar analyses we stress the importance of this modeling exercise to be undertaken on any data set distinct

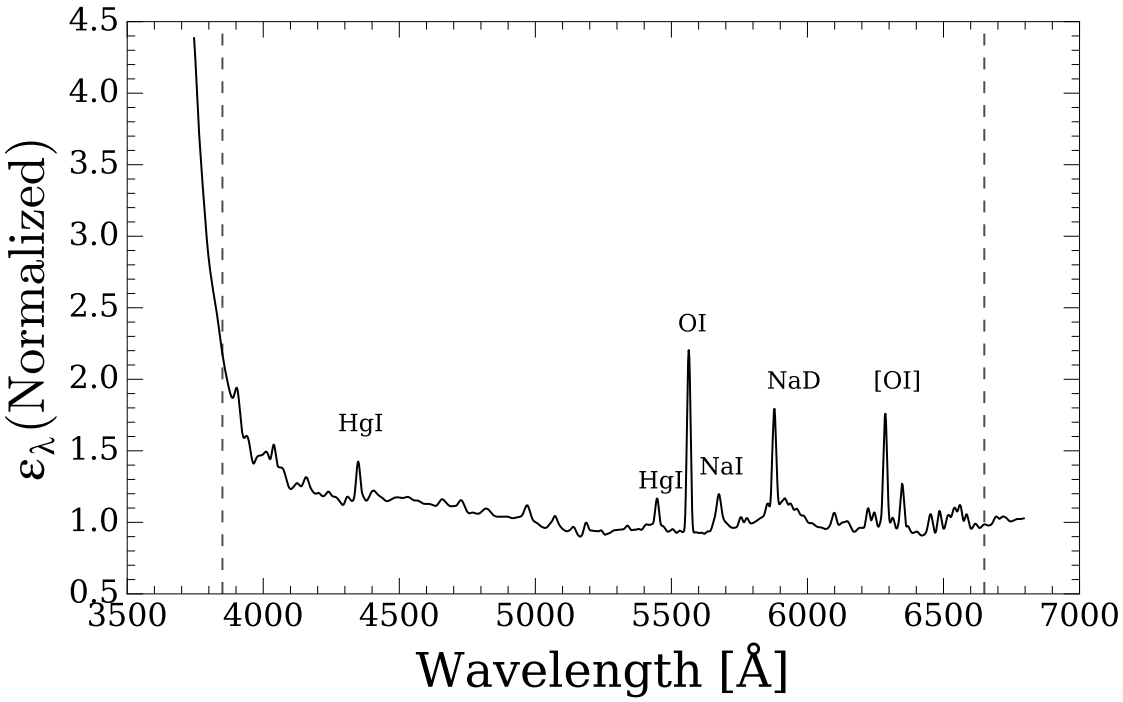

Figure 4.9 Characteristic noise vector used to construct noisy galaxy models, as described in §4.5, here normalized between 5450 Å $\leq \lambda \leq$ 5550 Å. Vertical dashed lines correspond to used spectral range in analysis.

in wavelength range and error vector.

4.5.2 Monte Carlo Simulations

Model galaxy spectra were constructed using the method outlined in Appendix C with star-formation e-folding time-scales τ_{SF} = 0.1, 1, 2, 4, and 10 Gyr and a total age of $\tau_{\rm form}$ = 12 Gyr. All model galaxies were constructed from mono-metallicity SSPs with a metallicity of 0.4 $Z_{\odot}$ and had extinction dictated by the model of Charlot & Fall (2000) with $A_V = 1.63$ (an optical depth τ_V of 1.5, close to the median we find in Chapter 5 from full spectral fitting). The spectral resolution of the models was set to 210 km s^{-1} to match the characteristic resolution of the data at 5500 Å. For each model galaxy noise was added to produce spectra with S/N = 3, 5, 7, 10, 15, 20, 30, 40, and 60. We define S/N for both our galaxy observations and Monte Carlo models as $\mathrm{S/N} = \Sigma_\lambda \left(f_\lambda/\epsilon_\lambda\right)/N$ where f_λ is the measured flux, ϵ_λ is the corresponding error vector, and the sum is over N pixels in a specified band pass. For our tests we choose the bandpass to be 5450 Å $\leq \lambda \leq$ 5550 Å, but we note that the choice of bandpass only scales the derived S/N thresholds by a constant related to the SED of our galaxy/models. Provided the bandpass used to compute the S/N threshold is the same as that used to bin the data the specific choice of bandpass is irrelevant.

For observed galaxy data the quantities f_λ and ϵ_λ are the result of the reduction described in section 4.4. For the model galaxies the shape of ϵ_λ was based on the spectral noise structure of our data. To compute ϵ_λ we average together the error vectors from *all* fibers across all pointings. We then fit a smooth function to this average to remove high-frequency variations. The result in Figure 4.9 captures the general trend of how ϵ_λ varies with wavelength in our data.

For each combination of τ_{SF} and S/N we generate 30 Monte Carlo noise realizations

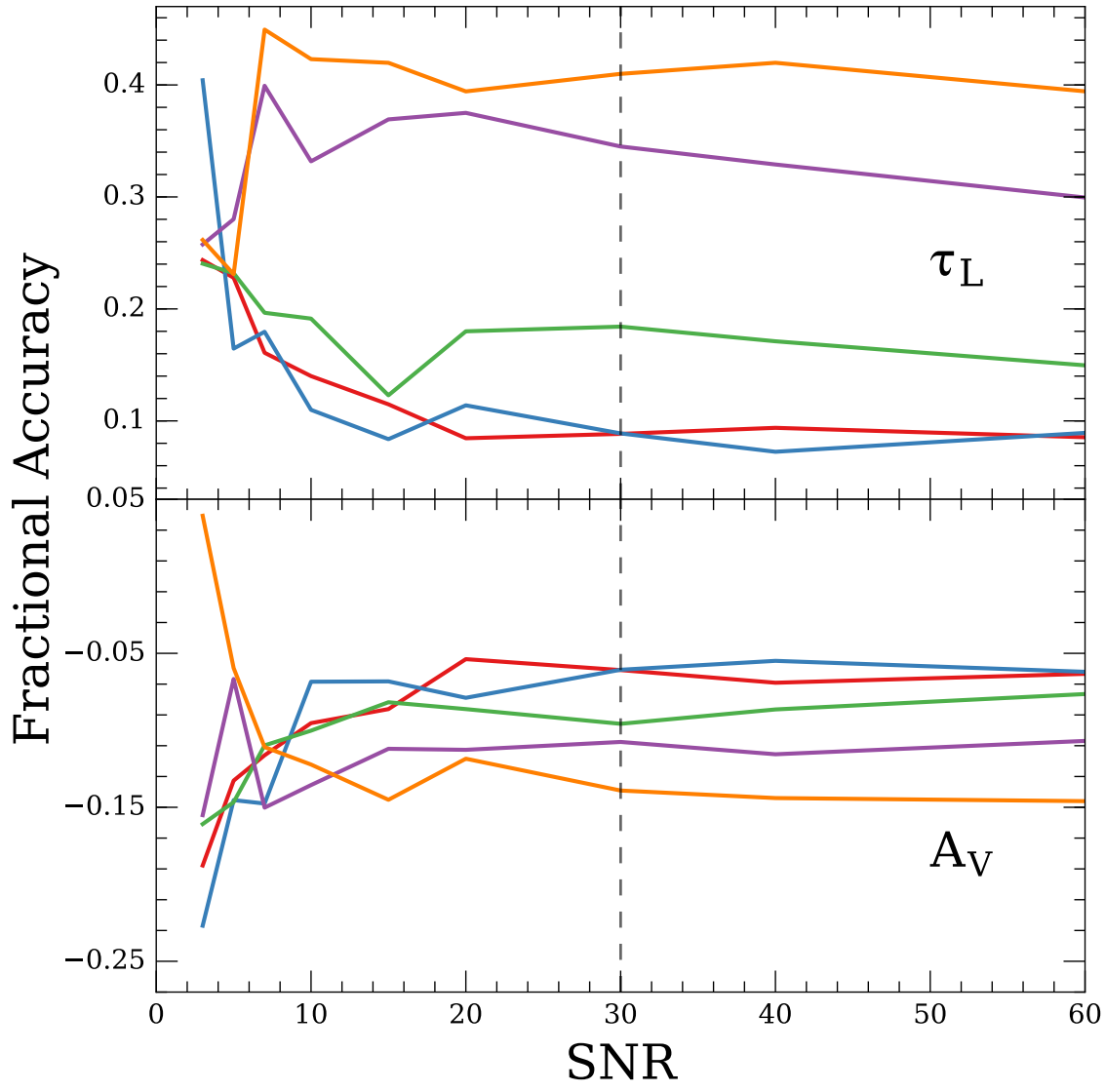

Figure 4.10 Systematics in fit parameters caused by degeneracies in star formation history as a function of S/N per pixel (each pixel samples ~ 2Å). Fractional accuracy is defined as $1 - X_{\rm fit}/X_{\rm model}$, where $X = \tau_L$ in the top panel, and $X = A_V$ in the bottom panel. Models adopt a solar-metallicity smoothly declining star-formation rate governed by an e-folding time-scale τ_{SF}, while the fit has no restrictions on the SFH or metallicity. Colors correspond to different values of τ_{SF} as given in Figure 4.11. Vertical dashed lines at S/N=30 pix^{-1}) are for reference.

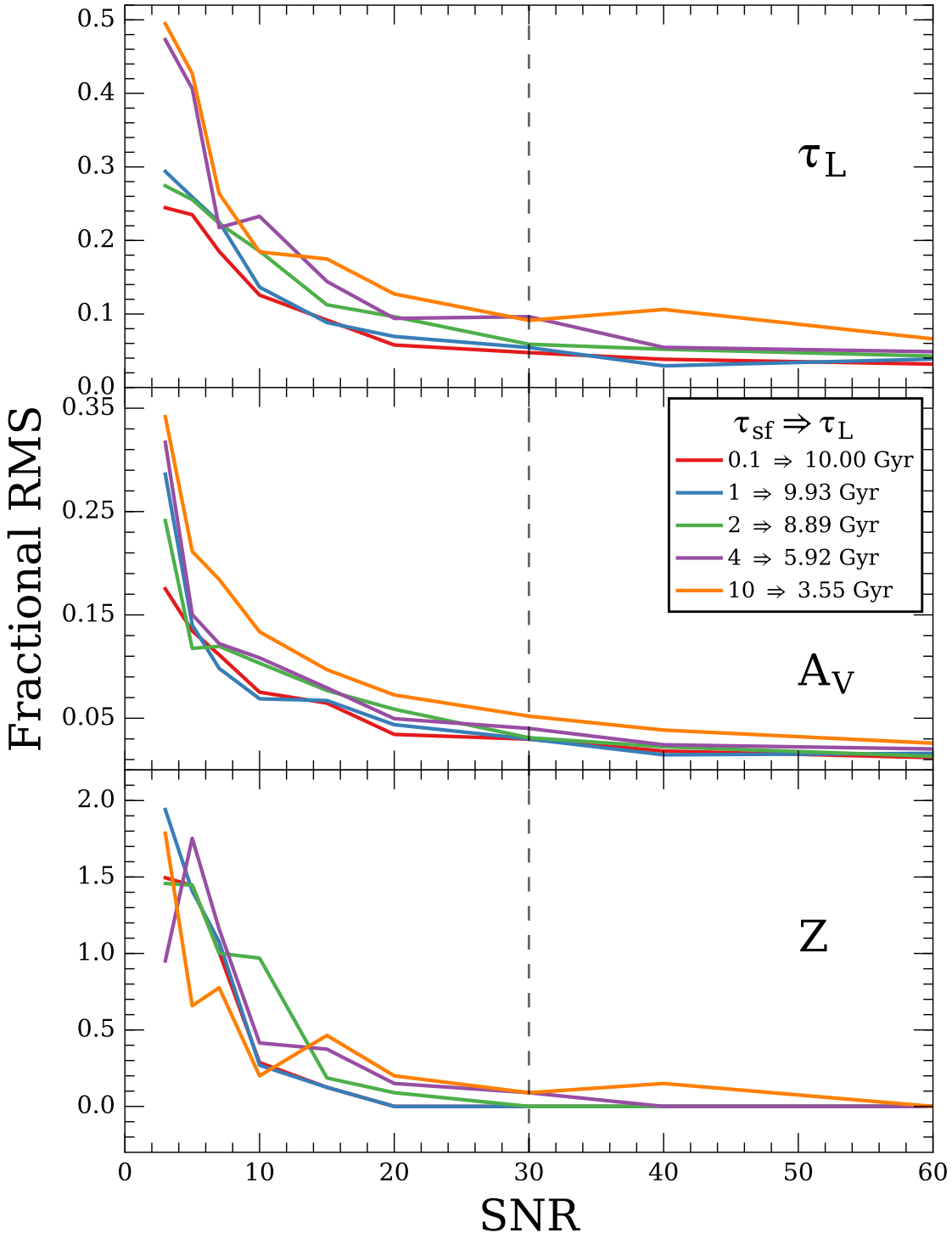

Figure 4.11 Precision of recovered parameters as a fraction of S/N per pixel for different model input values of mean light-weighted age (τ_L, top), extinction (A_V, middle), and metallicity (Z, bottom). Precision is estimated as the root-mean-square deviation of the fitted values from the mean of the 30 Monte Carlo noise realizations. Colored lines correspond to results for model spectra described in Figure 4.10, as indicated in the key. Model values of τ_L for each τ_{SF} assuming a formation epoch 12 Gyr in the past are also specified. Vertical dashed lines at S/N = 30 pix^{-1} indicate our precision criterion largely driven by τ_L.

(while still maintaining the same S/N) which produce 30 versions of the same galaxy that differ only by stochastic variations. Once the model galaxies are constructed they are fit using the same method described in Chapter 5. In short, a Levenberg-Marquardt minimization routine is used to fit a superposition of SSPs taken from the models of Bruzual & Charlot (2003) in the same 10 age bins used by Tremonti et al. (2004) (in Gyr: 0.005, 0.025, 0.1, 0.286, 0.64, 0.904, 1.434.2.5, 5, and 10). The result of each fit is a set of SSP weights and a single value for extinction A_V, assuming the extinction model of Charlot & Fall (2000) (i.e., the same extinction model used to construct the model galaxies). In both the models and the fitting, we have made the simplifying condition that the same value for the extinction and the extinction law is applicable to all age stellar populations; to do otherwise is beyond the scope of this analysis.

When assessing the accuracy and precision of each S/N level we directly compare the known model A_V to the fit A_V, and we use the mean light-weighted age (τ_L, Equation C.10 in Appendix C, as measured between 5450 Å $\leq \lambda \leq$ 5550 Å)[7] as a proxy for the SSP weights. This substitution allows us make a quantitative assessment of the *precision* of our fits but comes with some important caveats concerning *accuracy* that we consider in detail in Chapter 5, and summarize here.

In the broadest terms τ_L is known to be degenerate with the detailed star formation history (SFH); in our models we assume a smooth, exponentially declining star-formation rate parameterized by τ_{SF} but a different SFH could yield a very similar spectrum with a significantly different τ_L. Because we do not impose a specific SFH during the fitting process, our fit values of τ_L are likely to be systematically offset from the input model

[7] This band-pass for defining τ_L is between and narrowly missing terrestrial and airglow lines of HgI and OI. However, since the measurement is made from and referenced to the models, night-sky contamination is not relevant.

values.

More specifically, we find that any model with a smoothly varying prescription of the SFH (specifically the τ_{SF} model outlined in Appendix C) gives a generally poor description of our galaxy spectra and also yield measurements of τ_L that are offset from the best fitting models with unconstrained star formation histories. We highlight these systematics in Figure 4.10.

Fits with unconstrained SFH report values of τ_L that are offset by as much as 40% from the true values of τ_{SF} model galaxies. The maximum offsets occur at the largest values of τ_{SF}, i.e., approaching a constant star-formation rate where all SSP ages are well represented in the integrated spectrum. This suggests systematics may be driven by degeneracies caused by similarities between the 10 SSPs used during fitting. In Chapter 5 we explore methods to reduce the number of SSPs used (and therefore the number of free parameters) using the statistical methods presented by Mosby et al. (2015).

Despite these caveats τ_L can still provide a useful diagnostic for the purpose of assessing S/N. The assumption of a particular star formation history (or lack thereof) in both model creation and spectral fitting introduce systematic offsets that are independent of the S/N in the spectra at *high* S/N (Figure 4.10). In other words, a change in S/N does not change the underlying SFH (and therefore τ_L) of the model galaxy, nor does it change the assumed SFH used during fitting (in this case, none). When determining a useful S/N we are only concerned with the precision in derived quantities that is caused by noise in the spectra.

To estimate uncertainties in determining metallicity, separate fits were performed using mono-metallicity SSP input libraries with metallicities of 0.005, 0.02, 0.2, 0.4, 1 and 2.5 $Z_{\odot}$. The final "fit" value of metallicity was then taken to be the metallicity of the fit with the lowest value of χ^2_{ν}. The assumption of mono-metallicity stellar populations is probably

unrepresentative of NGC 891, even on a spatially resolved scale, but this simplification provides a good estimate of the uncertainties in recovering the metallicity of the model in the presence of random noise.

Figure 4.11 shows the results of our S/N Monte Carlo simulations. In the limit where S/N $\rightarrow \infty$ the scatter (rms) in the fit parameters tends to 0. We choose our "best" S/N to ensure we just achieve our 10% precision requirements on τ_L, A_V, and Z. Based on our simulations, the requirement is driven by τ_L, and indicates S/N ≥ 30. At this S/N the rms in all quantities begin to asymptote; any further increase in S/N yields only marginal gains in precision at the cost of real losses in spatial resolution.

For subsequent analysis we bin individual ∇Pak fibers to S/N ≥ 30. To ensure at least one bin at all heights and to avoid mixing fibers of different spectral resolutions (i.e., different sizes) we construct bins starting at the left-most (NE) fiber in each row and adding fibers to the bin until the S/N ≥ 30 or there are no more fibers left in the row. The flux in each bin is the average of all fibers in that bin, weighted by the individual S/N^2. This method can produce bins with S/N ≤ 30 (e.g., if there are not enough fibers left in a row to achieve S/N ≥ 30), but in practice the number of underfilled bins is $\sim$2 per pointing. In most cases these underfilled bins have S/N ≥ 25.

A complete list of our data apertures (i.e., the final spectra) can be found in Table E1. The "notes" column identifies apertures that are excluded from further analysis for various, data-quality reasons. The "bad" flag indicates that the wavelength solution appears to be wrong by more than $\sim$100 km s^{-1}, usually at the extreme blue end of the spectrum, and some spectra features do not match their known locations. The "ugly" flag is applied to spectra that, despite an adequate S/N, appear to be overly noisy and of poor quality. Both the "bad" and "ugly" flags are applied manually examining each individual spectrum.

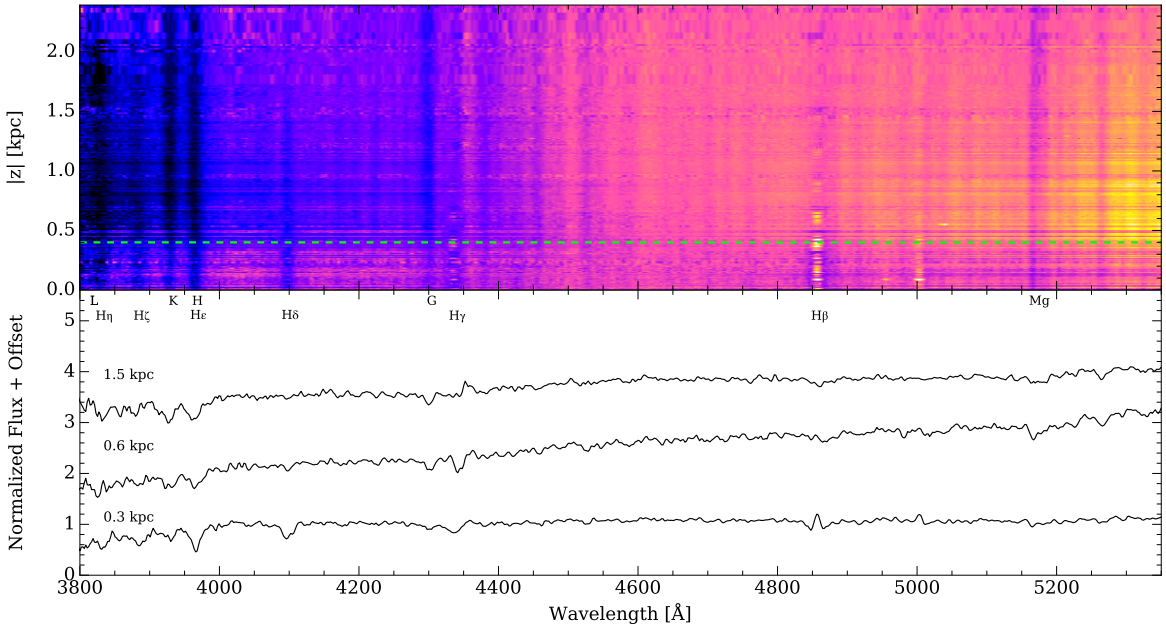

Figure 4.12 Same as Figure 4.1, but for the ∇Pak data from NGC 891. Top: Normalized galaxy spectra at different heights, color-coded by intensity (see text for a description of how this image was made). The horizontal line marks the age break at 0.4 kpc described for Figure 4.13. Bottom: Representative spectra at three different heights (labeled). Prominent spectral features are labeled at the boundary between the two panels.

4.6 Results and Discussion

4.6.1 Vertical Trends

The almost perfectly edge-on nature of NGC 891 allows unambiguous determination of vertical trends in our spectra. Figure 4.12 presents our data for direct comparison to Figure 4.1. This was made by sorting spectra from all apertures by height, regardless of radius, and then interpolating them onto a regular grid to form a linear scale in kpc. The grid spacing (8 pc) was chosen for cosmetic reasons to keep the interpolation from being apparent except at the largest heights. As with the model spectra in Figure 4.1, the individual spectra were first normalized by their mean value.

The transition from young, Balmer-dominated spectra to old, metal-dominated

spectra is clear at 0.4 kpc, as highlighted by the bottom panel. At 0.3 kpc Balmer absorption dominates, but at larger heights strong Ca H&K and G band absorption indicate the presence of older populations. The amazing match between Figures 4.1 and 4.12 is even more remarkable given that the MW heating model used in Figure 4.1 includes no information about NGC 891 and is simply tuned to observations from the Solar Cylinder.

This first-blush qualitative comparison has visceral appeal, and demonstrates the vertical trends in stellar populations seen in the MW (as described in §4.1) are manifest in NGC 891. However, the comparison lacks quantitative rigor. Our primary interest is to quantify the comparison and determine to what extent these trends also depend on radius. In particular, the precise location of a sharp vertical transition from Balmer-line to metal-line dominated spectra can be used to calibrate how disk stars are vertically stratified in phase space as a function of age and radial location. This in turn can be interpreted in terms of time-scales for dynamical heating or gas-cooling models, and the extent to which vertical age gradients in spiral disks are ubiquitous and quantitatively similar or distinct.

Disentangling age from metallicity, and metallicity from abundance is fraught with degeneracies, particularly in complex stellar populations observed in integrated star-light. In an edge-on galaxy like NGC 891, there is the additional complication of projection effects compounded with extinction that is patchy, but also changes broadly with height and radius. Chapter 5 undertakes to model all of these complexities, but here we are interested in using simple spectral indices, the measured value of which are model-independent and insensitive to redenning. These indices allow us to we probe for vertical *age* transitions and their radial trends while at the same time bounding (providing priors on) the age and metallicity of the more complicated modeling we later undertake.

4.6.2 Spectral Indices

4.6.2.1 Definitions

We focus our attention on the spectral indices defined in Table 4.5. The first two entries have primary sensitivity to age, while the remainder are primarily sensitive to metallicity, and, in combination, to abundance. Because the age-sensitive indices have varying degrees of dependence on metallicity and vice versa, index combinations are required to disentangle these effects, as well established in the literature, particularly for older stellar populations, as we cite in what follows.

The strength of Balmer absorption has long been used as a mostly metallicity-insensitive measure of population age because it depends primarily on the main-sequence turn off temperature instead of the red giant branch temperature. In other words, strong Balmer absorption is produced by young, hot main-sequence stars with lifetimes of < 100 Myr, regardless of metal content. Worthey & Ottaviani (1997) find that, of the Balmer absorption lines, Hβ is the least sensitive to metallicity (due to a lack of adjacent metal lines that impact the continuum) and, given its relative strength, is the

Table 4.5. Spectral Index Definitions

Index Name	On-Band		Blue Continuum		Red Continuum	
	Center (Å)	Width (Å)	Center (Å)	Width (Å)	Center (Å)	Width (Å)
$D_n(4000)$	-	-	3900	100	4050	100
Hδ_A	4103.9	38.8	4060.7	38.1	4144.8	32.5
Mgb	5176.4	32.5	5152.0	18.8	5198.9	15.0
Fe_{5270}	5265.7	40.0	5240.7	15.0	5301.9	32.5
Fe_{5335}	5332.1	40.0	5310.3	11.3	5358.4	10.0

most sensitive to age. However, contamination from nebular emission is problematic, with increasing contamination for the lower-order Balmer lines. All of our spectra show strong signs of Hα emission and in some apertures Balmer lines have negative equivalent widths as high as Hγ. The traditional trade between age sensitivity (i.e., *insensitivity* to metallicity variations) and systematics due to nebular emission is to use Hδ_A (Worthey & Ottaviani 1997) as an age indicator, which in fact has long been used in extragalactic studies of mixed stellar populations (e.g., Couch & Sharples 1987). In Chapter 5 we develop a model for Balmer emission and find that applying an emission correction correction shifts Hδ_A by only -0.4 ± 0.3 Å, which is roughly 10% of the dynamic range in Hδ_A across the age transition found in §4.6.3.

The break at 4000 Å can also be used to estimate the age of stellar populations, albeit with a larger sensitivity to metallicity. This break is caused by an increase in opacity resulting from ionization of metal lines; young stars are hot enough to put metals into high ionization states and the thus the total opacity is low. As temperature decreases more of the metals occupy lower ionization states that are suitable for absorption and the opacity increases. Beyond a certain limit, very cool stars (i.e., M stars) are unable to even singly ionize the neutral atoms and the amplitude of the break decreases. Thus the 4000 Å break traces population age (specifically related to the temperature of the red giant branch), but also depends on the population metallicity, although not as strongly (see Bruzual A. 1983, and Figure 4.13 here). The metal line that contributes most to the 4000 Å break is Ca K at 3933 Å, which causes the magnitude of the break to also exhibit a weak dependence on abundance. To measure the 4000 Å break we use the narrower-band definition of Balogh et al. (1999) primarily because our flux calibration deteriorates blueward of 3800 Å (Figure 4.7), and we adopt the nomenclature, $D_n(4000)$, of Kauffmann et al. (2003).

We also define composite indices to determine metallicity and α-enhancement in our

populations. In particular, Thomas et al. (2003) find that

$$[\mathrm{MgFe}] = \sqrt{\mathrm{Mg}b(0.72 \times \mathrm{Fe}_{5270} + 0.28 \times \mathrm{Fe}_{5335})} \tag{4.1}$$

is almost totally insensitive to changes in abundance and is therefore a good tracer of the total metallicity in a stellar population. They also note that, when plotted against Mgb, Fe_{5270}, Fe_{5335}, and Fe_{5408} are all fairly sensitive to changes in abundance. We choose to use $\langle \mathrm{Fe} \rangle = (\mathrm{Fe}_{5270}+\mathrm{Fe}_{5335})/2$, because these two Fe indices are slightly better calibrated than Fe_{5408} (Thomas et al. 2003) and have been have been used in other important studies (e.g., Trager et al. 2005, 2008; Trager & Somerville 2009).

The reported "indices" are equivalent widths defined as

$$EW = \left(1 - \frac{F_I}{F_C}\right) \Delta_\lambda, \tag{4.2}$$

where F_I and F_C are the average fluxes in the index and continuum bands, respectively and Δ_λ is the width of the index bandpass defined in Table 4.5. The value of F_C is computed by linearly interpolating the flux computed in the red and blue continuum bands to the center of the index band. In the case of $D_n(4000)$ the reported value is simply the ratio of the average flux in the red continuum band to the average flux in the blue continuum band. Table F1 reports our measured values for all apertures defined in Table E1.

Recognizing the wisdom of Balogh et al. (1999) we caution that the absolute values of our measured indices do not correspond to physical quantities. The specific conditions of our data (e.g., spectral resolution, sampling, signal-to-noise, etc.) can, and will, affect the derived index values. The reader is thus warned away from comparing our results in an absolute sense to those of other studies unless they are careful to match to our spectral sampling and resolution as described in Section 4.3.

4.6.2.2 Model Grids

To aid interpretation of the indices defined above we construct a set of fiducial galaxy models from the SSP basis set of Bruzual & Charlot (2003) on a grid of metallicity and age. However, unlike most previous applications, we do not use the SSPs themselves as the reference. For each model we again assume an exponentially declining star formation rate starting 12 Gyr in the past, as described in Appendix C, and construct galaxies with τ_{SF} = -1, -3, -9, 13, 5, 3 and 1 Gyr. These models have corresponding mean, light-weighted ages of τ_L = 0.3, 0.7, 1.3, 2.8, 4.7, 7.2, and 11.2 Gyr, respectively, as measured between 5450 Å $\leq \lambda \leq$ 5550 Å. Each model is constructed from mono-metallicity SSPs ranging from 0.005, 0.02, 0.2, 0.4, 1, to 2.5 $Z_{\odot}$. Because we do not have the ability to vary abundance in our models (as done, for example, by Trager et al. 2008) all models have solar abundance.

The model galaxies are degraded to match the spectral resolution and sampling of our ∇Pak data before having indices measured in exactly the same way as the data. In Figures 4.13 - 4.15 we contrast index measurements in three different height bins: $z < 0.4$ kpc, $0.4 \leq z < 1$ kpc, and $1 \leq z < 2.6$ kpc. Since the fiber size, and hence the instrumental resolution, is correlated with height (z), we suitably modify our models for the mean resolution in each vertical bin. Respectively, for $D_n(4000)$ we adopt 294, 392, and 470 km s^{-1}; for $H\delta_A$ we adopt 241, 344, and 428 km s^{-1}; and for Mgb we adopt 200, 258, and 313 km s^{-1}. Since ⟨Fe⟩ is a combination of Fe_{5270} and Fe_{5335}, we adopt (189, 179), (245, 250), and (298, 303) km s^{-1}, respectively, for this index pair. The general effect of decreased spectral resolution is to compress the dynamic range in the index value as a function of age and metallicity. Particularly, because the dynamic range in index values also decreases at low ages (where our instrumental resolution is highest) we bring the models forward to the data instead of correcting the data to some fiducial (e.g., Lick) resolution. This maximizes

the rendered information content of the indices.

In Chapter 5 we demonstrate that the location of a galaxy in both the age and metallicity index planes is highly sensitive to the assumed star formation history. Furthermore, we find that a τ_{SF} model for star formation is likely not representative of our data from NGC 891. Despite these shortcomings, our fiducial grid is still useful for assessing relative trends in metallicity and age, but we caution the reader not to strictly interpret the absolute values of these quantities because they are predicated on specific star-formation models.

4.6.3 Age Gradients

We use Hδ_A and $D_n(4000)$ as our primary age indicators. As noted by Hamilton (1985) these two indices are generally anti-correlated and are useful, when combined, as an estimator of population age because of their sensitivity to different star-formation timescales. Historically, Hδ_A has been used with $B-R$ color (e.g., Couch & Sharples 1987) to discriminate between different star-formation scenarios involving bursts, but Balogh et al. (1999) has shown that $D_n(4000)$ works as a suitable alternative to color, as one might expect based on the correlations shown in Hamilton (1985). In essence, $D_n(4000)$ is a narrow-band color intermediate in the wavelength range spanned by $U-B$. Because of its relatively narrow band-pass it is more immune from extinction effects, say, than broad-band colors.

Figure 4.13 shows these measurements grouped into three radial and three vertical bins. The radial bins are chosen to sample the region within the inner truncation of the super-thin disk ($|r| < 3$ kpc), the super-thin disk itself (3 kpc $\leq |r| < 8$ kpc), and beyond the outer super-thing disk truncation (8 kpc $\leq |r|$) (Schechtman-Rook & Bershady 2013). Vertical bins were chosen to illustrate the stratification seen in stellar

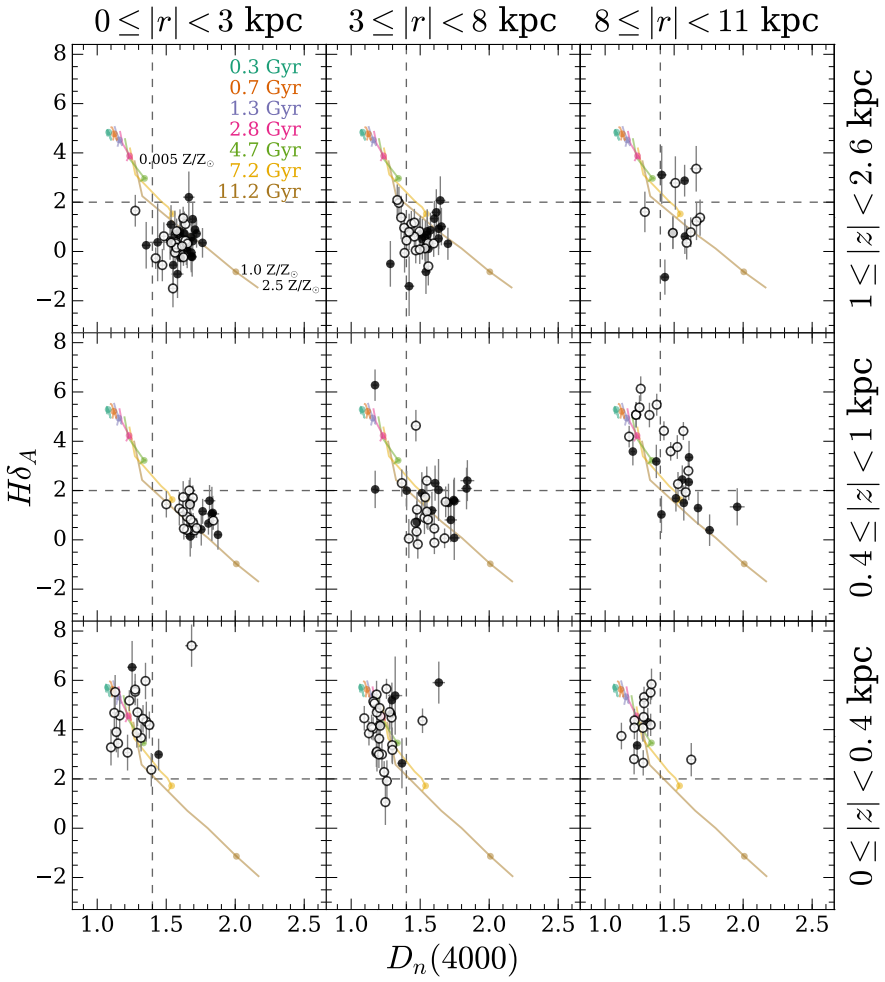

Figure 4.13 Spectral indices Hδ_A and $D_n(4000)$ for all good apertures in NGC 891 as a function of projected radius and height. Rationale for radial and vertical bins is provided in the text. Open symbols are for apertures on the approaching side, while filled circles are for apertures the receding side. Color-coded isochrones, labeled by their mean, light-weighted age at 5550 Å are based on models with exponentially declining star-formation and a total age of 12 Gyr, as described in §4.6.2.2; these are shown to highlight trends in age and the dependence of these indices on metallicity. The extreme values of metallicity are shown at the ends of the oldest isochrone in the top-left panel; solar metallicity for each isochrone is marked with a filled circle in all panels. The model values are adjusted for the mean instrumental resolution of each vertical bin as described in the text. Dashed lines are fiducial to highlight trends in age.

populations: below 0.4 kpc stellar light is dominated by young populations with strong Balmer absorption, but above this height we see old populations with weak Balmer absorption and a correspondingly strong $D_n(4000)$ break.

Again, as we saw in the comparison of Figures 4.1 and 4.12, the results in Figure 4.13 for the vertical age gradients are qualitatively consistent with the basic heating model tuned to the MW solar cylinder presented in §4.1. Our MW heating model predicts this transition to occur at roughly the scale-height of the old, thin disk with the exact value depending on the assumed star-formation history and how the scale-height is measured (e.g., band-pass and number of components). We can begin by assuming the star-formation histories are comparable for the two galaxies. In NGC 891 we find a sharp transition from young to old stellar populations at 0.4 kpc. This is very close to the vertical exponential scale-height for a single component stellar disk fit to the broad-band light profile; Xilouris et al. (1999) find values of ranging from 0.34 to 0.43 kpc from the K to B bands, accounting for attenuation. For comparison, the super-thin and thin disk components measured in the near-infrared K (Schechtman-Rook & Bershady 2013) band are 0.16 and 0.47 kpc, respectively. It is reasonable to presume that the super-thin and thin components correspond to the young and old thin disks in NGC 891.

Radial age gradients are minimal at low heights, but above the midplane we see evidence for younger stars at larger radii, particularly on the approaching side where there is an excess of Hα, as discussed in Section 4.3. This gradient is most pronounced for 0.4 kpc $\leq |z| <$ 1 kpc but is visible even at the largest heights. Discounting the azimuthal asymmetry for a moment (here projected onto radius on either side of the center), this radial trend is indicative of inside-out disk formation combined with disk flaring as seen in simulations of MW-like disks (e.g., Martig et al. 2014). There is ample evidence in today's massive disk galaxies that such a scenario may indeed be viable. For example, in the MW

and NGC 891 there is evidence for gas flaring in atomic and molecular gas (e.g., Scoville et al. 1993; Yim et al. 2011, for NGC 891). There also is recent evidence for stellar flaring in the MW (Ness et al. 2016) as seen for age-dated giant stars from APOGEE (Majewski et al. 2015). In the $z \sim 1$ galaxy population there is also ample evidence of inside-out disk formation based on Hubble Space Telescope studies (e.g., Nelson et al. 2015), even for MW-like masses (e.g., van Dokkum et al. 2013). This growth pattern appears to be part of a broader trend (in time and galaxy type) of size evolution (e.g., Shibuya et al. 2015), although the interpretation is challenging given the complexity of present day mass-size relations seen, e.g., by Lange et al. (2015) in the GAMA survey. Nonetheless, spatially resolved spectroscopic maps of nearby galaxies clearly show age gradients in disks, with the outer parts of disks being younger in a light-weighted sense (Sánchez-Blázquez et al. 2014; González Delgado et al. 2015). What we are able to resolve here, for the first time in a massive spiral galaxy external to the MW, is the *vertical* structure of these radial gradients.

Now considering the azimuthal asymmetry in star-formation and spiral arm projection, it is clear that this asymmetry is reflected in the vertical and radial gradients in the mean stellar age as reckoned in a light-weighted sense with the indices in Figure 4.13. At the very least this should provide a cautionary reminder that interpreting the radial and vertical gradients of spectral indices in terms of specific scenarios (e.g., disk flaring and inside-out growth) is necessary but perhaps not sufficient proof of the scenario's plausibility. In particular, the role of projection, especially in the context of the spiral arms and extinction, needs to be accounted for (cf the relative excess of Hα vs 24μ emission, as discussed in Kamphuis et al. 2007a). We will show elsewhere that differential SFH as a function of radius (where the outer portions of disks are younger but not thicker) can also lead to *apparent* flaring in integrated star-light of a constant-thickness disk. While star counts can certainly distinguish between flaring and radially modulating SFH scenarios,

for galaxies beyond the reach of resolved stellar populations, stellar kinematics is likely the only recourse to resolve different physical scenarios.

The model grid in Figure 4.13 also highlights the degeneracy between age and metallicity. Each colored line corresponds to an isochrone of a given mean light-weighted age with varying values of metallicity. As age increases the metallicity dependence in Hδ_A and $D_n(4000)$ also increases. At an age of $\sim$11 Gyr these indices can vary by almost the entire dynamic range of our data just by assuming a different value for metallicity. This age-metallicity degeneracy is somewhat ameliorated by considering a reduced range of metallicity (between 0.2 and 2.5 $Z_\odot$) (which, as we will show in §4.6.4 and Chapter 5, is plausible). Moreover, despite these degeneracies there is still a clear distinction between "young" and "old" populations across the vertical cut at 0.4 kpc; it is the actual age of this cutoff that depends on metallicity.

4.6.4 Metallicity and Abundance Gradients

Figure 4.14 shows how metallicity (traced by [MgFe]) varies in the same bins defined in §4.6.3 and Figure 4.13. Since [MgFe] is also age sensitive, we plot it versus Hδ_A. Guided by the fiducial grid described in §4.6.2.2 we do not see significant trends in metallicity with radius or height. The preponderance of apertures are well described by metallicities in the range of $0.2 < Z/Z_\odot < 2.5$.

The lack of discernible gradients is perhaps unsurprising given the precision of the measurements and the small dynamic range of the indices, particularly for young ages. There are also line-of-sight effects to consider as well. For example, there is a weak trend toward slightly higher metallicities at intermediate heights. This may appear counter-intuitive, but it may well reflect the confluence of negative vertical and radial metallicity gradients and the fact that as we move above the mid-plane the deprojected radii become

smaller as extinction diminishes. In other words, all else being equal, young stars formed near the center of a galaxy have higher metallicity than young stars forming at large radii. Thus, at low heights where we cannot see far into the disk we expect to find young populations with low metallicity, but as height increases we can detect light from smaller radii where the metallicity is on average higher.

Age gradients with height are again apparent in Figure 4.14, as too is the possible

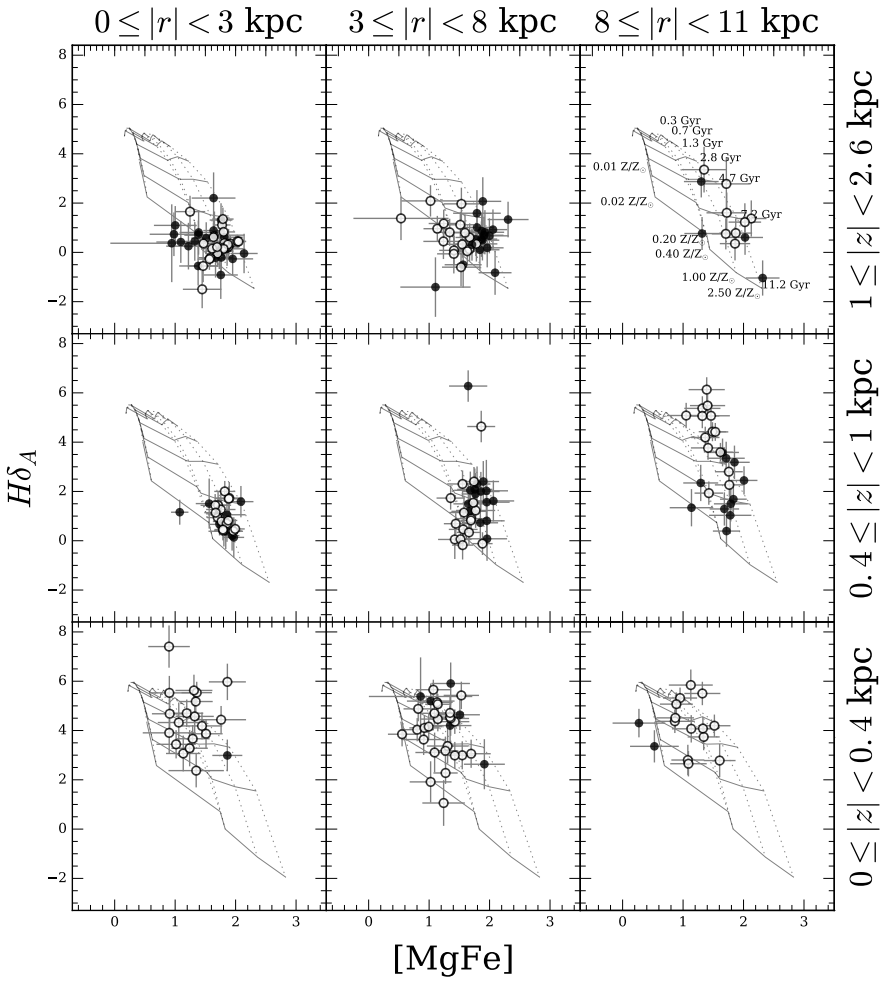

Figure 4.14 Spectral indices Hδ_A and [MgFe] for all apertures as a function of projected radius and height. Symbols, bins in radius and height, and models are the same as in Figure 4.13. Lines of constant mean light-weighted age (isochrones, solid lines) and lines of constant metallicity (isofers, dotted lines) for the models are labeled in the top-right panel. The model values are adjusted for the mean instrumental resolution of each vertical bin as described in the text.

flaring of young stars in the outer disk, particularly on the approaching side. What is also readily apparent is an asymmetry in the metallicity on the two sides of the galaxy at intermediate radii. The receding side of the galaxy, where there is less evidence for flaring, appears to be more metal rich. This enhancement is most evident at intermediate and large heights, i.e., for the older stars. This may also be a line-of-sight depth effect in the sense that we are seeing farther in to the disk on the receding side where, for a given height, metallicity is higher.

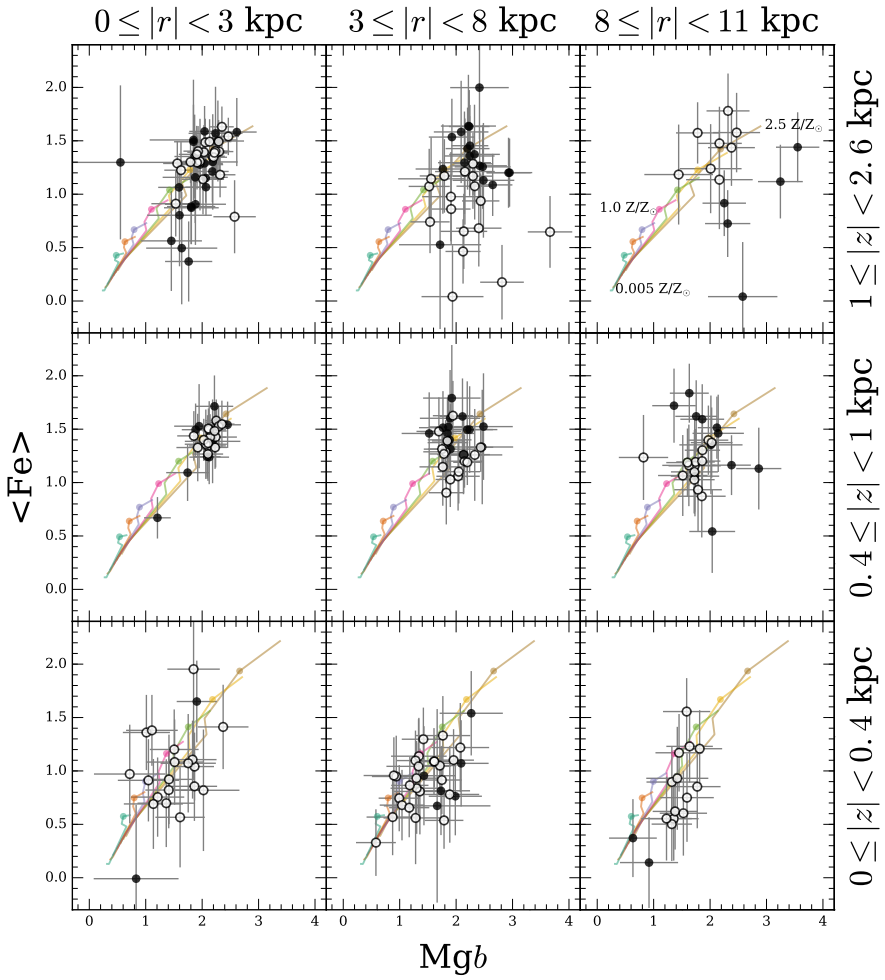

Figure 4.15 Spectral indices ⟨Fe⟩ and Mgb for all apertures as a function of projected radius and height. Symbols, bins in radius and height, and model grid (including color-coding for age) are the same as in Figure 4.13. The model values are adjusted for the mean instrumental resolution of each vertical bin as described in the text.

In Figure 4.15 we examine how abundance changes in our data with radius and height. Based on the results of Thomas et al. (2003) (specifically their Figure 4) we note that populations with different abundance will occupy different loci in the Mgb vs $\langle$Fe$\rangle$ plane, with higher abundance populations at smaller values of $\langle$Fe$\rangle$ and slightly larger values of Mgb. In general, increasing overall metallicity moves points diagonally upward in this plot.

The differences in metallicity seen at intermediate radii and larger heights in Figure 4.14 appear to not have associated abundance gradients. There is some evidence for enhanced abundances at low heights, and again at the largest heights. At intermediate heights, where the errors are also the smallest, the abundances appear to be very close to solar.

4.7 Summary

We set out to measure vertical population gradients in NGC 891, motivated to determine if the long-known vertical age gradients in our solar neighborhood are seen in another spiral galaxy with comparable rotation speed and morphology as the Milky Way. The advent of large spectroscopic surveys of Milky Way stars has renewed interest in the age and metallicity gradients seen in the Milky Way. Studies using these surveys (e.g., Bovy et al. 2012; Hayden et al. 2014, 2015) are establishing the relationships between age, velocity (height), metallicity and compositional abundance of stars in unprecedented detail and accuracy, but only for one galaxy. Recent measurements have established the age-velocity-metallicity relationship in M31's disk (Dorman et al. 2015). In this context we have undertaken to make the first comprehensive determination of both vertical and radial population gradients in integrated light for a massive spiral galaxy outside of the Local Group.

To aid detailed studies of nearby galaxies like NGC 891 we constructed a unique fiber

integral field unit for the WIYN telescope's Bench Spectrograph called ∇Pak. ∇Pak is part of a pair of variable-pitch IFUs that share a common cable and spectrograph mount; the other IFU is called HexPak, described elsewhere. The ∇Pak instrument is optimized to measure vertical gradients in edge-on galaxies like NGC 891. In this chapter we have detailed the primary attributes of this instrument relevant for astronomical observations, and we have presented laboratory and on-telescope calibration of its performance. The unique design of this instrument required novel construction methods that had some impact on its performance. In particular, the choice of an aluminum fixture for ∇Pak resulted in a sub-optimal polish for some fibers that induced throughput losses (Appendix A), however, the over-all performance of the IFU is quite high with a mean throughput of 80%.

The multi-pitch nature of ∇Pak also required modifications to the standard IFU data reduction routines, specifically flat-field and absolute flux calibrations. We have shown (§4.4) that these modifications do not significantly affect the quality of the final data product. In fact, in the absence of atmospheric dispersion correction, the presence of very large (6" diameter) fibers makes it possible to flux-calibrate ∇Pak data very accurately in both a relative and absolute sense (∼5%), as we have demonstrated.

We have obtained spectroscopic observations of NGC 891 covering the wavelength range from 3370 to 7640 Å, with high-quality data in the range from 3800 to 6700 Å. Spectral resolution varies with wavelength and fiber size in the range from 100 to 500 km s^{-1}; at 5200 Å the range is 180 to 350 km s^{-1}. Our spectroscopic maps span continuously from the galaxy mid-lane to heights of 2.6 kpc, and sample projected radii from 0.25 to 11 kpc from the center on *both* sides of the disk. With these data we see clear trends in age with both projected radius and height.

As a preliminary step in quantifying these age trends, and possible trends in metallicity and abundance, we undertook measurement of well-known spectroscopic indices

including $D_n(4000)$ and the Lick indices associated with Mgb, <Fe>, and [MgFe]. We have compared these to standard, solar-abundance, SSP-based galaxy models brought forward to the resolution of the data and constructed for a range of on-going star-formation. Our primary findings are:

1. There is a clear transition with height above NGC 891's disk midplane between young and old populations at 0.4 kpc (roughly the broad-band exponential scale-height), consistent with models of heating of the stellar disk in the Milky Way's Solar cylinder.

2. For $|z| > 0.4$ kpc there is a trend towards younger populations at larger projected radii, consistent with an inside-out formation history in NGC 891. The trend also suggests a flaring of the young stellar disk at radii beyond 8 kpc, which happens to be where Schechtman-Rook & Bershady (2013) found an outer break in the super-thin (presumably star-forming) disk.

3. Beyond 8 kpc in radius and between 0.4 kpc $\leq |z| < 1$ kpc there is a a clear asymmetry in age between the two sides of the galaxy. The approaching side, where there is more Hα emission, appears younger. The extent to which this is an m=1 asymmetry rather than a differential line-of-sight depth effect due to the (m=2) geometric arrangement of dust trailing stars and gas in spirals arms (as argued by Kamphuis et al. (2007a) on the basis of 24μm emission) is not yet clear. The gist of the argument against lopsided variations would be that the young-disk flaring between heights of 0.4 to 1 kpc is not as clearly seen on the receding side because these young stars are in a spiral arm projected behind a relative thick dust layer. This suggests that better quantification of line-of-sight depth is needed to accurately interpret this asymmetry in the variation in vertical structure *within* NGC 891's disk.

   Secondary findings include there is little evidence for mean metallicities outside the

range of 0.2-2.5 $Z_{\odot}$ or abundances outside the range of 0 to +0.3 dex of solar values. Changes in metallicity and abundance are more difficult to quantify with these small sets of indices, particularly given the relatively young ages at low heights. There is a hint that metallicity increases slightly at intermediate heights, but we caution this may be modulated by projection effects due to a negative metallicity gradient with radius and increasing line-of-sight depth with height. There is evidence for metallicity differences at the *same* height (above 0.4 kpc) and *projected* radius (between 3 and 8 kpc) on either side of the galaxy. Again, this may be a projection effect due to different line-of-sight depths along the two halves of the galaxy, and in that sense it may be related to the asymmetry seen in age versus height beyond 8 kpc. However, if there is indeed a negative radial metallicity gradient this would require the line-of-sight depth for older stars to be somewhat larger on the receding side, which is plausible given they will not be preferentially in spirals arms.

We stress that all of these measurements are *light*-weighted by the very virtue of their observational nature, and hence are sensitive to star-formation history (as we would like), and line-of-sight depth. The latter is a considerable complication for edge-on galaxies, and must be overcome for a detailed picture of the location of different stellar populations in NGC 891 to emerge. The index measurements reported above provide powerful qualitative measurements of the general trends in stellar populations in NGC 891, but a detailed quantitative assessment is hampered by degeneracies in age and metallicity (see, for example, Figure 4.13). In Chapter 5 we employ full spectra fitting, guided by the results from these indices, to reduce this degeneracy and make better quantitative measurements of the population age as a function of both radius and height. These measurements include extinction estimates and, critically, kinematic estimates line-of-sight depth to our data in an effort to de-project our radial measurements. What is robust from these preliminary measurements, however, is the presence of vertical age gradients in NGC 891 that appear

much like what we see in the Milky Way's disk.

We thank Guy Worthey for contributing his models of simple stellar populations as a function of age, metallicity and abundance. We thank Eric Hooper, as Interim WIYN Director, and Charles Corson for helping make the ∇Pak installation possible; gift funds from the Department of Astronomy made this shipping and travel possible. This research was directly supported by the U.S. National Science Foundation (NSF) ATI-0804576, AST-1009471 and AST-1517006.

References

Aumer, M., & Binney, J. J. 2009, MNRAS, 397, 1286

Balogh, M. L., Morris, S. L., Yee, H. K. C., Carlberg, R. G., & Ellingson, E. 1999, ApJ, 527, 54

Barden, S. C., Armandroff, T., Muller, G., et al. 1994, in Proc. SPIE, Vol. 2198, Instrumentation in Astronomy VIII, ed. D. L. Crawford & E. R. Craine, 87–97

Bershady, M., Barden, S., Blanche, P.-A., et al. 2008, in Proc. SPIE, Vol. 7014, Ground-based and Airborne Instrumentation for Astronomy II, 70140H

Bershady, M. A., Andersen, D. R., Harker, J., Ramsey, L. W., & Verheijen, M. A. W. 2004, PASP, 116, 565

Bershady, M. A., Andersen, D. R., Verheijen, M. A. W., et al. 2005, ApJS, 156, 311

Bird, J. C., Kazantzidis, S., Weinberg, D. H., et al. 2013, ApJ, 773, 43

Bovy, J., Rix, H.-W., Hogg, D. W., et al. 2012, ApJ, 755, 115

Bruzual, G., & Charlot, S. 2003, MNRAS, 344, 1000

Bruzual A., G. 1983, ApJ, 273, 105

Bundy, K., Bershady, M. A., Law, D. R., et al. 2015, ApJ, 798, 7

Charlot, S., & Fall, S. M. 2000, ApJ, 539, 718

Couch, W. J., & Sharples, R. M. 1987, MNRAS, 229, 423

Dorman, C. E., Guhathakurta, P., Seth, A. C., et al. 2015, ApJ, 803, 24

Drory, N., MacDonald, N., Bershady, M. A., et al. 2015, AJ, 149, 77

Eigenbrot, A. D., Bershady, M. A., & Wood, C. M. 2012, in Proc. SPIE, Vol. 8446, Ground-based and Airborne Instrumentation for Astronomy IV, 84465W

González Delgado, R. M., García-Benito, R., Pérez, E., et al. 2015, A&A, 581, A103

Hamilton, D. 1985, ApJ, 297, 371

Hayden, M. R., Holtzman, J. A., Bovy, J., et al. 2014, AJ, 147, 116

Hayden, M. R., Bovy, J., Holtzman, J. A., et al. 2015, ApJ, 808, 132

Howk, J. C., & Savage, B. D. 2000, AJ, 119, 644

Kamphuis, P., Holwerda, B. W., Allen, R. J., Peletier, R. F., & van der Kruit, P. C. 2007a, A&A, 471, L1

Kamphuis, P., Peletier, R. F., Dettmar, R.-J., et al. 2007b, A&A, 468, 951

Kauffmann, G., Heckman, T. M., White, S. D. M., et al. 2003, MNRAS, 341, 54

Knezek, P. M., Bershady, M. A., Willmarth, D., et al. 2010, in Proc. SPIE, Vol. 7735, Ground-based and Airborne Instrumentation for Astronomy III, 77357D

Kregel, M., & van der Kruit, P. C. 2005, MNRAS, 358, 481

Lange, R., Driver, S. P., Robotham, A. S. G., et al. 2015, MNRAS, 447, 2603

Majewski, S. R., Schiavon, R. P., Frinchaboy, P. M., et al. 2015, ArXiv e-prints, arXiv:1509.05420

Martig, M., Minchev, I., & Flynn, C. 2014, MNRAS, 442, 2474

Mosby, G., Tremonti, C. A., Hooper, E. J., et al. 2015, MNRAS, 447, 1638

Nelson, E. J., van Dokkum, P. G., Förster Schreiber, N. M., et al. 2015, ArXiv e-prints, arXiv:1507.03999

Ness, M., Hogg, D. W., Rix, H.-W., et al. 2016, ApJ, 823, 114

Oosterloo, T., Fraternali, F., & Sancisi, R. 2007, AJ, 134, 1019

Pilyugin, L. S., & Edmunds, M. G. 1996, A&A, 313, 783

Rand, R. J., Kulkarni, S. R., & Hester, J. J. 1990, ApJ, 352, L1

Rand, R. J., Wood, K., Benjamin, R. A., & Meidt, S. E. 2011, ApJ, 728, 163

Sánchez-Blázquez, P., Rosales-Ortega, F. F., Méndez-Abreu, J., et al. 2014, A&A, 570, A6

Schechtman-Rook, A., & Bershady, M. A. 2013, ApJ, 773, 45

Schechtman-Rook, A., Bershady, M. A., & Wood, K. 2012, ApJ, 746, 70

Scoville, N. Z., Thakkar, D., Carlstrom, J. E., & Sargent, A. I. 1993, ApJ, 404, L59

Shibuya, T., Ouchi, M., & Harikane, Y. 2015, ApJS, 219, 15

Swaters, R. A., Sancisi, R., & van der Hulst, J. M. 1997, ApJ, 491, 140

Thomas, D., Maraston, C., & Bender, R. 2003, MNRAS, 339, 897

Trager, S. C., Faber, S. M., & Dressler, A. 2008, MNRAS, 386, 715

Trager, S. C., & Somerville, R. S. 2009, MNRAS, 395, 608

Trager, S. C., Worthey, G., Faber, S. M., & Dressler, A. 2005, MNRAS, 362, 2

Tremonti, C. A., Heckman, T. M., Kauffmann, G., et al. 2004, ApJ, 613, 898

van Dokkum, P. G., Leja, J., Nelson, E. J., et al. 2013, ApJ, 771, L35

Wood, C. M., Bershady, M. A., Eigenbrot, A. D., et al. 2012, in Proc. SPIE, Vol. 8446, Ground-based and Airborne Instrumentation for Astronomy IV, 84462W

Worthey, G., & Ottaviani, D. L. 1997, ApJS, 111, 377

Xilouris, E. M., Kylafis, N. D., & Papamastorakis, J. 1999, in ESA Special Publication, Vol. 427, The Universe as Seen by ISO, ed. P. Cox & M. Kessler, 993

Yim, K., Wong, T., Howk, J. C., & van der Hulst, J. M. 2011, AJ, 141, 48

Chapter 5

Vertical Population Gradients in NGC 891

II. Spectral Analysis

Science is magic that works

Kurt Vonnegut

A version of this chapter is currently in preparation to for submission to ApJ

Abstract

We report the results of applying full-spectrum fitting methods to IFU data from NGC 891. The edge-on nature of NGC 891 allows us to use line centroid velocity measurements to deproject on-sky radii and get a fully 3D picture of the location of our data in this galaxy. Our data are fit using a set of only 4 SSPs chosen, through statistical methods, to be a basis set for much larger SSP libraries. We attempt to refine the standard χ^2 metric to make it more sensitive to spectral regions that encode information about age and metallicity, but find that this greatly increases uncertainty in our fits. Full spectral fits produce measurements of age, metallicity, and extinction as a function of height and radius in NGC 891. Examining trends in this phase space we determine that the disk of NGC 891 formed inside-out as a superposition of mono-aged flared disks (i.e., each subsequent disk flares at a larger radii). We also identify two distinct epochs in the enrichment history of the disk: before 6 Gyr ago the metallicity content of the galaxy increased with time, but since 6 Gyr the metallicity has been decreasing, likely an indication that pristine gas is currently infalling onto the disk of NGC 891.We are also able to make rough estimates about the star formation history of NGC 891.

5.1 Introduction

In Chapter 4 we used a focused set of spectral line measurements to show that the signature of disk heating in NGC 891 matches observations of the Milky Way (e.g., Bovy et al. 2012; Hayden et al. 2015) with startling accuracy. Near the midplane of NGC 891 ($|z| < 0.4$ kpc) spectra have strong Balmer absorption features, indicative of young stellar populations, while above 0.4 kpc there is a sharp transition to spectra dominated by metal absorption, notably Ca H&K, MgI, and Fe. Secondary results include detection of a negative age gradient with radius, which could be the signature of an inside-out formation history similar to that seen in the Milky Way (Bovy et al. 2012; Hayden et al. 2015), and a potential flare in the star-forming disk beyond $\sim$8 kpc.

These results represent important new information about NGC 891 (and, by extension, Milky Way-like disk galaxies), but they do not take advantage of the full wealth of information contained in our data. Specifically, the index measurements presented in Chapter 4 consider each spectral feature in isolation (or, at best, in relation to one other feature) and ignore the fact that *every* spectral channel encodes information about the underlying astrophysics. By construction, the data taken by ∇Pak and described in Chapter 4 are of sufficiently high signal-to-noise (S/N) that using the entire spectrum can yield physical insights beyond what can be measured by line indices alone.

In this chapter we extend our previous results by using full-spectral fitting to measure age, metallicity, and extinction (our three "quantities of interest") as a function of radius and height in NGC 891. As discussed in Chapter 1 full spectrum fitting requires an SSP basis set, which in turn depends on stellar template library, IMF, and stellar isochrones. In §5.5 we explore a range of different SSP libraries and methods for mixing them together to

form a full model galaxy. The primary reason for this exploration is a desire to understand and quantify uncertainties that arise from astrophysical degeneracies in the SSP libraries. It is well known (O'Connell 1976; Aaronson et al. 1978; Worthey et al. 1994; Gil de Paz & Madore 2002) that stars of different metallicities and ages can have spectral shapes that are very similar. This similarity poses a challenge to interpreting the results of a full spectrum fit to a mix of SSPs; it is very difficult to know which of the many similar SSPs represents the "correct" astrophysical reality. Confounding this issue further is the fact that the presence of dust also affects the final galaxy spectrum. The result is a complex covariance between age, metallicity, and extinction (i.e., dust).

Some modern fitting codes, like FIREFLY (Wilkinson et al. 2015) or STEKMAP (Ocvirk et al. 2006), attempt to circumvent the impact of dust by first removing low-order information from both the model SSPs and galaxy data. The advantage of this method is that, by effectively removing the continuum shape, the goodness-of-fit is driven primarily by the strength of stellar absorption lines[1]. Ironically this is a step towards focused spectral index measurements like those employed in Chapter 4, albeit one with a much larger set of lines and all the advances of modern computing behind it. However, this increased focus on absorption lines requires sacrificing information contained in the continuum shape and, perhaps more importantly, ignores degeneracies that exist between, e.g., extinction and age.

In this chapter we use a somewhat simple method to perform the galaxy fits, as described in §5.3.1. The strength of our astrophysical interpretation comes from our relatively high S/N data (see Chapter 4) and our understanding and quantification of the uncertainties in our fits (§5.7).

[1] In §5.6 we make our own attempt to increase the power contained in strong spectral lines, with limited success.

In addition to its importance as a nearby Milky Way analog, NGC 891 offers a unique perspective as one of the few galaxies close enough for detailed study that is also perfectly edge-on. This orientation allows for unambiguous measurements of vertical trends, but also provides an opportunity to measure a fully three dimensional picture of stellar populations. Unlike face-on disk galaxies, edge-on disk galaxies have a clear and strong velocity structure along the line of sight that is caused by the rotation of the galaxy. The detailed kinematic structure of NGC 891 is known (Swaters et al. 1997; Kregel & van der Kruit 2005; Oosterloo et al. 2007) and we can leverage this knowledge to determine the true location of measured data within the galaxy. In principle a detailed study of the kinematics (i.e., line shape) of an edge-on galaxy like NGC 891 could yield a very detailed picture of the that galaxy's line of sight (LOS) structure (what we call "doppler tomography"), but in this work we are restricted by spectral resolution to simply measuring line centroids.

The following chapter is organized as follows: in §5.2 we briefly describe the data of Chapter 4, which is used in this work. §5.3 details further analysis needed to ready the data for SSP fitting, along with our general fitting methodology. In §5.4 we use velocity information to determine the true, 3D location of our data in NGC 891, and in §5.5 we discuss a range of different SSP libraries and motivate our final choice of library used for fitting. An attempt to improve the precision of our fits by modifying χ^2 is shown in §5.6 while in §5.7 we quantify both fitting and systematic uncertainties present in our analysis. Finally, §5.8 presents a new view of the phase-space of NGC 891 as revealed through our full spectrum fits and we summarize this work in §5.9.

5.2 Data

The data used in this paper were recorded using ∇Pak (Wood et al. 2012) on the WIYN[2] telescope Bench Spectrograph (Barden et al. 1994; Bershady et al. 2008; Knezek et al. 2010). In Chapter 4 we detail the observational methodology, data reduction, and spectral coadding used to produce the spectra that will be used in this work. Briefly, spectra were extracted and reduced primarily using standard IRAF tasks with some custom modifications to account for the unique nature of ∇Pak. The individual fibers were then coadded to produce "aperture" spectra that have signal to noise $\geq$ 30 px^{-1} ($\sim$20 Å^{-1}). We refer the reader to Chapter 4 and Appendix E for an in-depth discussion of all of these steps and tables listing the details of each aperture (location, constituent fibers, etc.).

5.3 Basic Analysis

To quantify uncertainties in our full spectrum galaxy fits we will test different methods of fitting spectra and interpreting the results. In this section we describe the basic, high-level methodology that is common to all fitting methods. We also detail preparatory analysis that is required before these methods can be applied to our data, namely determining the velocity of each aperture and correcting for Balmer emission.

5.3.1 SSP fitting methodology

Our fitting method involves minimizing differences between measured NGC 891 spectra and synthetic galaxy spectra constructed from the superposition of simple stellar populations (SSPs, see §5.5). Fits are performed with MPFITFUN[3] (Markwardt 2009),

[2]The WIYN Observatory is a join facility of the University of Wisconsin-Madison, Indiana University, the University of Missouri-Columbia, and the National Optical Astronomy Observatory.

[3]available at `http://purl.com/net/mpfit`

an IDL implementation of the MINPACK Levenberg Marquardt minimization algorithm (Morè 1978). The model galaxy spectra are defined as

$$g(\lambda) = R(\lambda, \tau_V) \sum_{i,j} M(\Delta t_i, Z_j) f(\lambda, \Delta t_i, Z_j), \tag{5.1}$$

where $f(\lambda, \Delta t_i, Z_j)$ is the spectrum of an SSP with metallicity Z_j formed over time interval Δt_i, $M(\Delta t_i, Z_j)$ quantifies the strength of the contribution of each SSP, and $R(\lambda, \tau_V)$ governs the total extinction in the galaxy. All of our SSPs are normalized to 1 $M_\odot$ so the strength of each SSP is simply

$$M(\Delta t_i, Z_j) = \int_{\Delta t_i} \psi(t, Z_j) dt, \tag{5.2}$$

where $\psi(t, Z_j)$ describes the mass of stars formed at time t with metallicity Z_j (i.e., the star formation rate). In other words, $M(\Delta t_i, Z_j)$ is the total mass in stars formed during the time interval, Δt_i, associated with a particular SSP. The extinction, $R(\lambda, \tau_V)$, is parametrized by a single variable, τ_V and, importantly, does not depend on SSP age (t_i) or metallicity (Z_j). In §5.3.3 we discuss the details of $R(\lambda, \tau_V)$ and the limitations of this simplification. During fitting the free parameters are the SSP weights ($M(\Delta t_i, Z_j)$) a single extinction term ($\tau_{\rm V,cont}$), and the systematic velocity.

For each aperture our primary values of interest are the age, metallicity, and extinction. We measure extinction directly as $A_V = 1.086\ \tau_{\rm V,cont}$, but age and metallicity depend on assumptions made during fitting (i.e., priors in the SSP library) and during subsequent analysis.

As shown in Equation 5.2 the fit weights describe the integral of a particular star formation history (SFH), but it is useful to reduce a SFH down to single values for age and metallicity. To do this we define a pair of light-weighted quantities. The mean, light-weighted age is

$$\tau_L = \frac{\sum_{i,j} W_{L,i,j} \times t_i}{\sum_{i,j} W_{L,i,j}} \tag{5.3}$$

where t_i is the age associated with each SSP and W_L is the "light weight", defined as

$$W_{L,i,j} = M(\Delta t_i, Z_j) \sum_k S(\lambda_k) R(\lambda_k, \tau_V) f(\lambda_k, \Delta t_i, Z_j), \tag{5.4}$$

where $S(\lambda_k)$ defines a bandpass over which the light weight is computed. We set $S(\lambda_k)$ to be flat over 5450 Å $\leq \lambda \leq$ 5550 Å and zero everywhere else. The choice of t_i depends on assumptions about the SFH and in this work we make the simple assumption that star formation is constant across the lifetime of each SSP (Δt_i) so that t_i is simply the midpoint of each Δt_i. In §5.7.2 we discuss and quantify the systematics that arise from such an assumption. We note that Equation 5.4 also describes a conversion from mass-weights (i.e., $M(\Delta t_i, Z_j)$) to light-weights that is simply a constant that is independent of the specific mix of SSPs (but does depend on the overall extinction).

Similarly to τ_L we also define the mean, light-weighted metallicity as

$$Z_L = \frac{\sum_{i,j} W_{L,i,j} \times Z_j}{\sum_{i,j} W_{L,i,j}}. \tag{5.5}$$

5.3.2 Velocities

The systemic velocities of our model galaxies do not depend on the shape of the spectra (i.e., the SSP mix) and thus we can reduce the number of free parameters in our SSP fits by measuring the velocities once and then keeping them fixed for all subsequent analysis. The velocity values we use are a combination of velocity estimates from two sources: the "fit" velocities that result from SSP fitting, and velocities measured from the centers of bright emission lines.

5.3.2.1 Fit velocities

During full spectrum fitting the velocity can be a free parameter of the model, and this fit provides the first estimate of the velocity of each aperture. The first step is to

run a fully unconstrained fit where all SSP weights, the velocity, and the extinction are allowed to vary (see §5.3.1). This produces a "best fit" only in the sense that the resulting model spectrum matches the data well in a χ^2 sense; to determine velocities the details of the astrophysical assumptions behind each model are unimportant. The reported fit uncertainties on these velocities is on the order of $\sim$10 km s^{-1}, depending on ∇Pak fiber size (see Chapter 4), which is slightly better that 10% of the instrumental resolution (again, depending on fiber size).

Once the "best fit" spectrum is determined we run a second iteration of the fitting routine with the SSP weights and extinction fixed to the best fit values. This keeps the shape of the model spectrum the same and causes χ^2 minimization to be driven only by the velocity offset between the model and the data. When fitting these velocities we used only the range of wavelengths that lie within the region spanned by arc lamp lines (4100 Å $\leq \lambda \leq$ 6600 Å). This avoids wavelengths that could be affected by extrapolation of the wavelength solution (see Chapter 4). In the majority of apertures this "refined" velocity was within $\sim$10 km s^{-1} of the original fit velocity, which is similar to the precision of the fits and indicates that this second iteration is perhaps not necessary.

The results of these fits produce what we call the "fit velocities". The final fit values were found to be stable to a wide ($\sim$100 km s^{-1}) range of starting velocity values. These velocity fits are driven mainly by regions of the spectrum that deviate significantly from the continuum level, which in our case are the Balmer absorption series, the MgI absorption band, and the G band. Many apertures show moderate to strong Hα emission, but we masked this feature (and [OIII]) during fits because our model SSPs do not have nebular emission. For this reason the χ^2 velocities can be though of as the "stellar" velocity values.

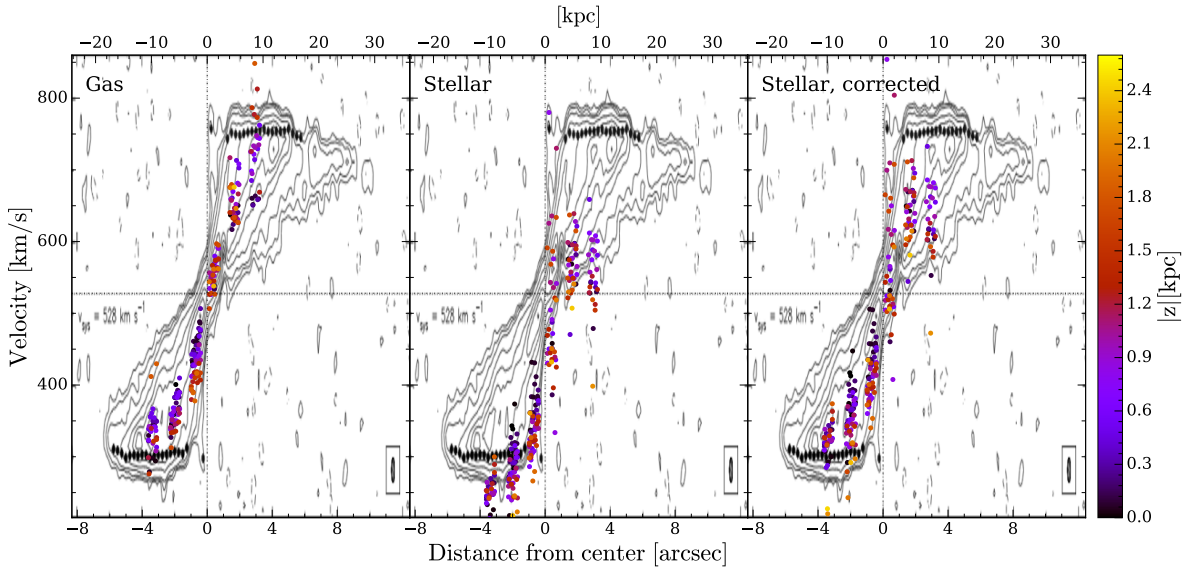

Figure 5.1 Comparison of HI velocity envelope (from Swaters et al. (1997)) to *left:* measured Hα centroids, *middle:* best fit velocities from SSP models, and *right:* best fit stellar velocities with a constant offset to minimize median difference between gas and stars.

5.3.2.2 Emission line velocities

As a check on the velocities found above we also measure the velocity of nebular emission lines, namely Hα. Centroids were computed using the IRAF task FITPROFS which allows us to deblend the Hα, [NII] complex. We focus only on the Hα velocities, which are then compared to known HI velocities from Swaters et al. (1997), as shown in the left panel of Figure 5.1. We call the velocities measured in Hα "gas velocities".

The center panel of Figure 5.1 shows the "stellar velocities" compared to known HI velocities and our measured Hα velocities. Clearly there is a systematic offset between the stellar and gas velocities and we find that this offset is constant in magnitude and sign across both sides of the galaxy. This fact rules out an offset caused by asymmetric drift (Binney & Tremaine 1987). Furthermore, many of the stellar velocities are unphysical in the sense that they lie outside of the HI envelope. We therefore conclude that this offset is caused by systematic measurement uncertainty (likely arising from uncertainty in our

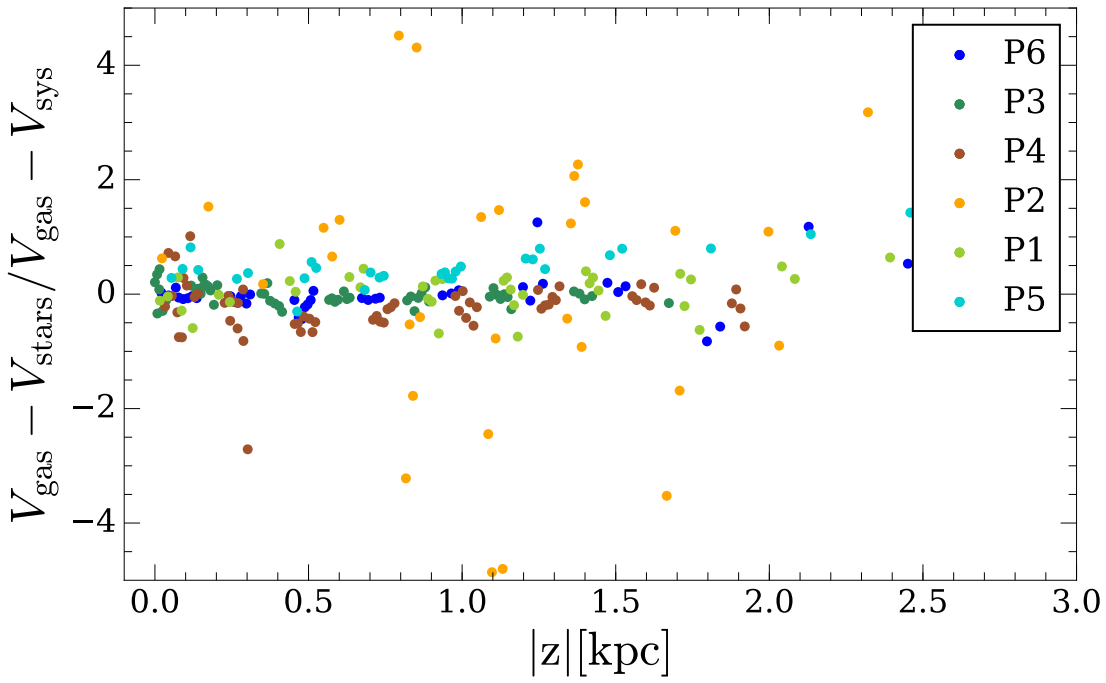

Figure 5.2 Difference between stellar and gas velocities after applying a constant 74 km s^{-1} offset to the stars. A median of 1 corresponds to no average offset between the two population *across both sides of the galaxy.*

wavelength solution) and compute a constant velocity "correction" that is applied to the stellar velocities. This offset is computed to minimize the median difference between stellar and gas velocities. While we do expect the stellar tangential speed to lag behind the gas the fact that we measure both sides of the galaxy means, the median difference between gas and stars should be, to first order, zero.

Figure 5.2 shows the relation between stellar and gas velocities after applying an offset of 74 km s^{-1}. This offset minimizes the global difference between gas and stellar velocities across both sides of the galaxy. Based on these results, the final velocity of each aperture is fixed as the velocity measured during χ^2 fitting ("stellar velocity") plus a constant offset of 74 km s^{-1}. The right hand panel of Figure 5.1 shows the final velocities used. We note that the systematic correction of 74 km s^{-1} is within the total uncertainty in our velocity

as dictated by uncertainties in the wavelength solution (120 km s^{-1}, see Chapter 4).

5.3.3 Extinction Model

During all steps of full spectral fitting (§5.3.1) we assume the extinction model of Charlot & Fall (2000), which is described by

$$R(\lambda) = e^{-\tau_{\rm V,cont}\left(\lambda/5500\ \mathring{\rm A}\right)^{-0.7}}. \tag{5.6}$$

This model has a steeper slope than a simple foreground dust screen, but the authors show it accurately reproduces the ratio of far-infrared to ultraviolet luminosities, the ratio of Hα to Hβ luminosities, the Hα equivalent width, and the ultraviolet spectral slope of nearby starburst galaxies. We retain the functional dependence of $\tau \propto \lambda^{-0.7}$ and define two normalizations, one for gas emission and one for stellar continuum. Thus, the total optical depth to a particular species is either

$$\tau_{\rm cont}(\lambda) = \tau_{\rm V,cont}\left(\frac{\lambda}{5500\ \mathring{\rm A}}\right)^{-0.7} \tag{5.7}$$

or

$$\tau_{\rm em}(\lambda) = \tau_{\rm V,Balmer}\left(\frac{\lambda}{5500\ \mathring{\rm A}}\right)^{-0.7}, \tag{5.8}$$

where $\tau_{\rm V,cont}$ and $\tau_{\rm V,Balmer}$ are the normalization factors for stellar continuum and gas emission, respectively.

As described in §5.3.1, $\tau_{\rm V,cont}$ is a free parameter of the SSP models that essentially measures the slope of the continuum. To measure $\tau_{\rm V,Balmer}$ (which we need to compute emission corrections a la §5.3.4) we use the ratio of measured Hα/Hβ flux and compare it to the expected value of 2.86 from Osterbrock (1989), assuming case B recombination in a 10^4 K gas. Under these assumptions, and given the extinction law in equation 5.8, we compute

$$\tau_{\rm V,Balmer} = 4.84 \ln\left(\frac{\rm H\alpha/H\beta}{2.86}\right). \tag{5.9}$$

The Hα and Hβ line fluxes were measured using the IRAF task FITPROFS which allows us to deblend the Hα/[NII] emission feature. Before fitting the emission lines a "best fit" galaxy model is subtracted. As in §5.3.2 the detailed astrophysics of the best fit model are unimportant; we only require that the model accurately match the stellar continuum so that it can be subtracted from the data. Once the continuum is subtracted the data are smoothed with a 3 pixel ($\sim$350 km s^{-1}) wide moving average. To mitigate the impact of bad continuum fits the centroid fitting window is constrained to be only $\sim 4\sigma$ wide, where σ is the average spectral width (standard deviation) of bright sky emission lines.

The relative strength of the two [NII] lines in the Hα/[NII] complex is governed by quantum mechanics and we expect the flux ratio $[\mathrm{NII}]_{6585}/[\mathrm{NII}]_{6549} = 3$. When measuring the H$\alpha$/[NII] lines, however, we often find $[\mathrm{NII}]_{6585}/[\mathrm{NII}]_{6549} > 3$, which indicates that the line fit is attributing some of the $[\mathrm{NII}]_{6549}$ flux to Hα and causing the Hα flux to be overestimated. This is likely due to an incorrect de-blending of the Hα and $[\mathrm{NII}]_{6549}$ lines. We correct for this effect by using the flux of $[\mathrm{NII}]_{6585}$ as a "calibration" flux (reasonable given its isolation, away from blending issues of Hα and $[\mathrm{NII}]_{6549}$) and define an Hα correction,

$$\Delta\mathrm{H}\alpha = [\mathrm{NII}]_{6549} - \frac{[\mathrm{NII}]_{6585}}{3}, \tag{5.10}$$

which is added to the measured Hα flux.

As mentioned above, measuring Hα and Hβ emission requires first correcting for Hα and Hβ absorption present in the stellar continuum. In practice the entire process is iterative because fitting SSPs accurately requires accurate emission corrections (§5.3.4), which, in turn, requires accurate extinction values. We find that the measured Balmer fluxes and derived emission corrections are stable after only a single iteration.

5.3.4 Emission Corrections

Many of our apertures show moderate to strong Balmer emission that is not present in the SSP libraries underlying our galaxy models and therefore must be subtracted before accurate analyses can be made. To do this we construct a model spectrum containing only emission from Hα, Hβ, Hγ, Hδ, and Hϵ.

The basic idea is to first construct a model galaxy produced from fits where the cores of the Balmer lines were masked. These fits will be good first guesses of the stellar continuum in the absence Balmer emission. We then use these fits to remove the stellar continuum and isolate this emission. Then the two strongest emission lines (Hα and Hβ) can be used to construct a model containing emission from the higher-order lines. Based on the results of Osterbrock (1989), and assuming case B recombination in a 10^4 K gas, the ratios of fluxes for the Balmer series is 1 : 0.350 : 0.164 : 0.087 : 0.056 (Hα: Hβ: Hγ: Hδ: Hϵ), thus if we know the flux in a single Balmer line we can construct a model containing all of these Balmer lines. In our emission models the width of each line is dictated by the instrumental resolution measured at the line location (see Chapter 4), with apertures made from different sized ∇Pak fibers having different widths.

This idealized Balmer emission model is then extincted using Equation 5.9 based on the value of $\tau_{\rm V,Balmer}$ as measured in section 5.3.3. To minimize the impact of aberrant extinction calculations we compute a height-dependent $\tau_{\rm V,Balmer}$ by fitting a line to the data from all apertures (and thus from all radii), as shown in Figure 5.3. From these data it is clear that the radial dependence to the vertical trend in $\tau_{\rm V,Balmer}$ is minimal so our grouping of all radii is valid. We find for NGC 891

$$\tau_{\rm V,Balmer}(z) = -0.91z + 4.15, \tag{5.11}$$

which allows us to compute the extinction in our Balmer emission models at any height

above the midplane.

Finally, the emission model is scaled so the Hα flux matches the Hα flux measured in each individual aperture. The data spectra are then corrected by subtracting the corresponding emission model. Figure 5.4 shows an example of a spectrum with strong Hβ emission before and after subtracting the Balmer emission model.

In many apertures the blending of the Hα/[NII] complex causes imperfect subtraction in this region (as it should, our emission model does not contain [NII] emission), and in subsequent analysis we do not fit (i.e., mask) data within $\pm$500 km s^{-1} of Hα (which includes both [NII] lines). In addition to Hα/[NII] we mask other strong sources of nebular emission ([OIII]$_{4959}$, [OIII]$_{5007}$, and S2) and sky lines with strong residuals ([OI]$_{6300}$, NaD, and OI$_{5577}$).

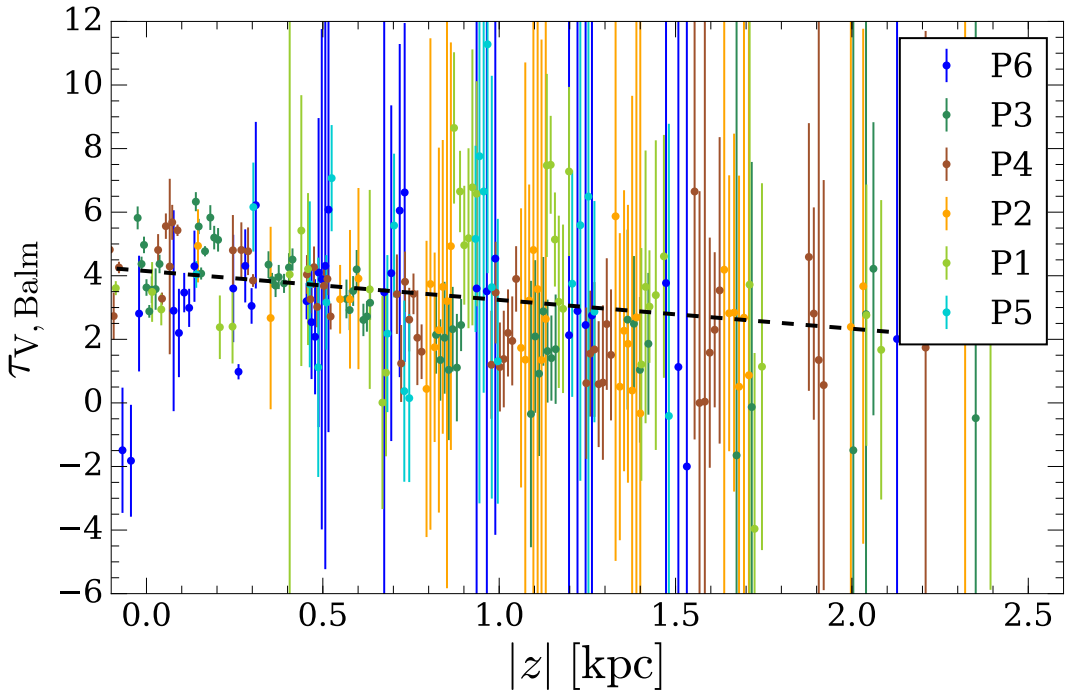

Figure 5.3 Measured values of $\tau_{\mathrm{V,Balmer}}$ as a function of distance from the midplane. The error bars show the uncertainties reported by IRAF from 100 Monte Carlo noise iterations. The black shows a linear fit described in Equation 5.11.

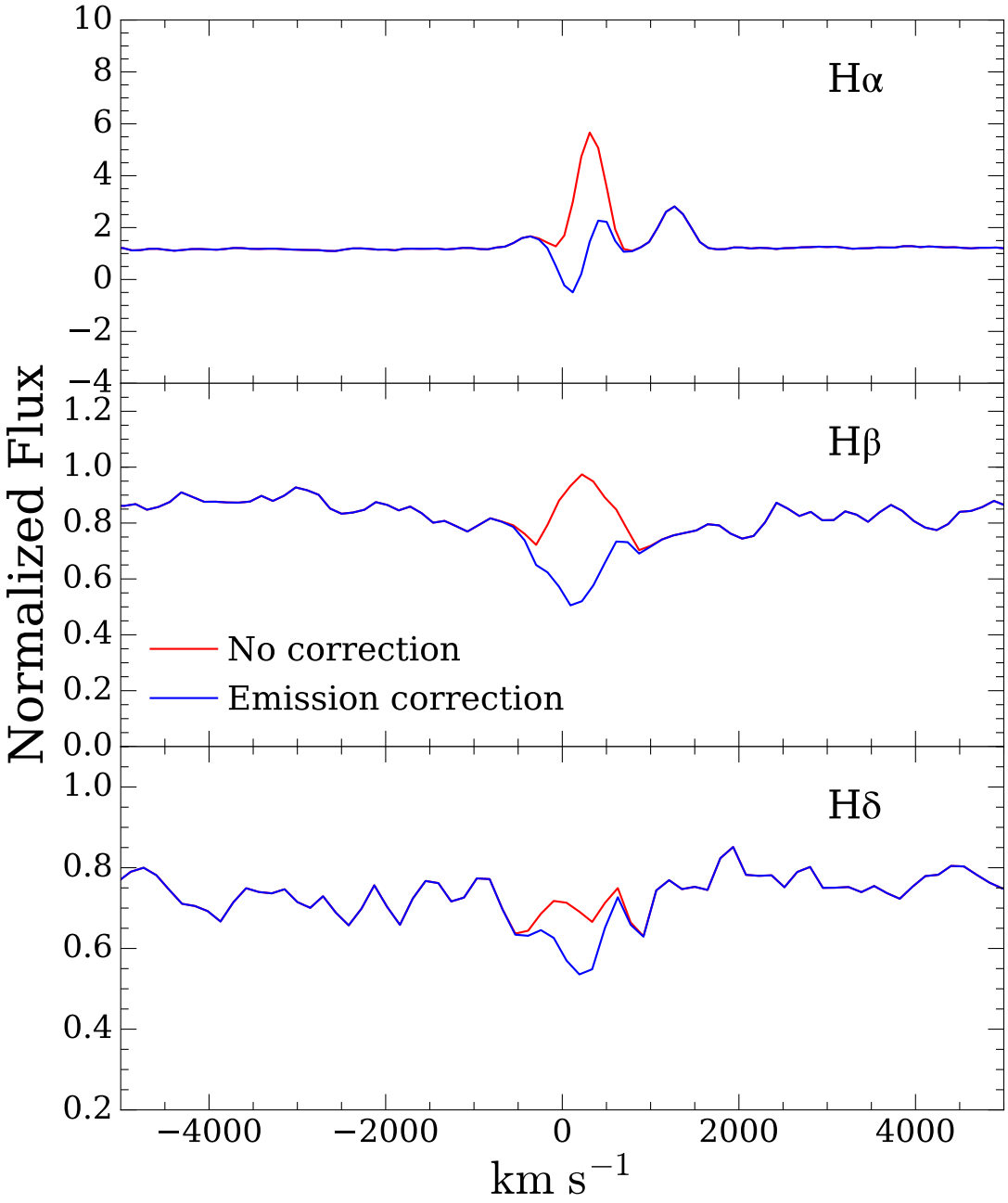

Figure 5.4 An example of Balmer emission correction. The red and blue spectra show an aperture with strong Balmer emission (aperture P4.6) before and after the Balmer emission model described in §5.3.4 is applied.

As mentioned above, the best-fit, extinction-value, emission-model analysis steps are interconnected and at least one iteration is required to find the "final" values.

5.4 Line of Sight Depths

To report our quantities of interest as a function of height and true, galactic radius we need to deproject our measured radii into radii defined with respect to the true center of NGC 891. This deprojection relies on understanding the average line-of-sight (LOS) depth to the emitting material in each ∇Pak aperture. This LOS depth can be computed from the measured tangential velocity in each aperture.

In the absence of any attenuating material (i.e., dust) the maximum velocity measured in each aperture will be the tangential speed of the galaxy at any given radius and height, which, to first order, is well approximated by the circular speed of the galaxy. In reality, however, when looking through an edge-on disk with high attenuation the measured velocity

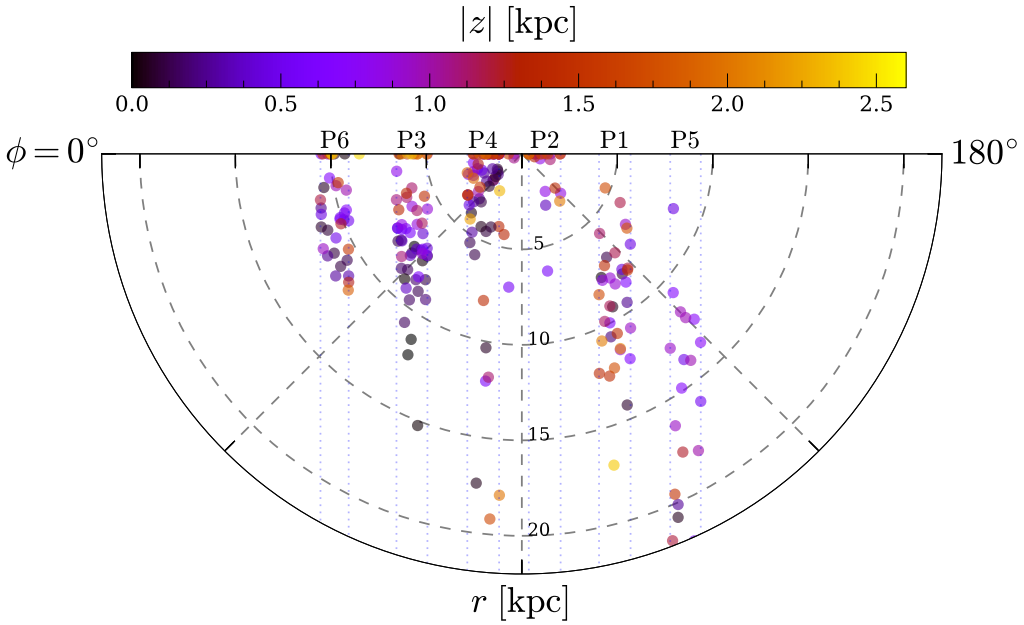

Figure 5.5 Map of the physical location of average emission from each aperture, as determined by a velocity-based LOS depth calculation (equations 5.12). The vertical dotted lines show the boundaries of the ∇Pak pointings described in 4.

is the projected velocity of emitting material along the entire sight-line, which will become opaque before reaching the tangent point. Thus, by comparing the measured velocity to the known circular velocity at a given radius we can determine the LOS depth to the emitting material.

Under the assumption that all material in the galaxy rotates at the circular speed the relation between measured and circular velocity comes from simple geometry. Given a measured projected radius and velocity, $r_{\rm proj}$ and $V_{\rm obs}$, respectively, the effective location of the emitting material in cylindrical coordinates centered on the galaxy is

$$\phi = \cos^{-1}\left(\frac{V_{\rm obs}}{V_{\rm c}}\right) \tag{5.12}$$

$$r = r_{\rm proj}\frac{V_{\rm c}}{V_{\rm obs}}, \tag{5.13}$$

where $V_{\rm c}$ is the circular velocity. Due to the nearly perfect edge-on nature of NGC 891 the projected radius, $r_{\rm proj}$, can be measured directly as the on-sky distance from the galaxy center. Measurements of $V_{\rm obs}$ are described in §5.3.2.

To compute V_c we construct a simple model rotation curve using circular velocities derived from envelop-fitting the HI data of Swaters et al. (1997). We also include the height-dependence on circular speed reported by Oosterloo et al. (2007). These measurements of the circular speed are based on collisional particles (i.e., gas) and are therefore not perfect estimates for the circular speed of the stars, which will lag the gas slightly due to asymmetric drift. However, in the absence of measurements of the true, stellar circular speed the gas velocities make an acceptable approximation. Our rotation curve for NGC 891 is thus

$$\begin{aligned} V_{\rm c}(r_{\rm proj}, z) = (-15.79\ {\rm km\ s^{-1}})\left(\frac{z}{\rm kpc}\right) \\ + \begin{cases} (68.2\ {\rm km\ s^{-1}})\left(\frac{r_{\rm proj}}{\rm kpc}\right) & r_{\rm proj} < 3.3\ {\rm kpc} \\ 225\ {\rm km\ s^{-1}} & r_{\rm proj} \geq 3.3\ {\rm kpc}. \end{cases} \end{aligned} \tag{5.14}$$

Figure 5.5 shows each aperture in its velocity-derived cylindrical coordinate. We define the approaching side of the galaxy ($r_{\rm proj} < 0$) to be at $\phi < 90°$ and the receding side to have $\phi > 90°$. With this view the large-scale structure of NGC 891 becomes clear; sight-lines to the receding side of NGC 891 probe the back of a spiral arm, where Kamphuis et al. (2007) identifies a higher concentration of dust, and as a result our measurements do not sample very far into the disk. Conversely on the approaching side we see the leading edge of a spiral arm, which has less dust due to ongoing star formation. On the approaching side of the galaxy there is also a clear trend that we see farther into the disk at larger heights, which is consistent with dust occupying a disk with a surface density that decreases with height.

5.5 SSP Basis Sets

Generating synthetic spectra that fit our data in a χ^2 sense is not very difficult or illuminating. A "good" fit is good only in the sense that a collection of SSPs was added together with a set of weights (Equation 5.1) that reproduce the spectrum of our galaxy with a reasonable degree of accuracy. Degeneracies between SSPs that have different underlying ages or metallicities but similar spectra (and therefore can contribute equally to "good" fits) make an accurate recovery of SFH, age, and metallicity difficult. To maximize the amount of information we get from full-spectrum fits we need to use an SSP library that a) produces "good" fits, and b) minimizes internal degeneracies to increase the precision on derived parameters (i.e., SFH, age, metallicity, and extinction).

In this section we explore different methods of combining information from SSPs with different ages and metallicities (§5.5.1). We then discuss a statistically motivated way to reduce the number of free parameters in our fits (§5.5.2) and examine systematic differences between different SSP libraries (§5.5.3). The final SSP library used for analysis of NGC

891 is discussed in §5.5.4.

Before any analysis, all model SSPs are degraded to match the spectral resolution of our data. As discussed in Chapter 4 this resolution is a function of both ∇Pak fiber size and wavelength.

5.5.1 Variations in Treating Metallicity and Extinction

The first class of SSPs used all come from Bruzual & Charlot (2003) (hereafter BC03) and use the the same 10 age bins used by Tremonti et al. (2004) (in Gyr: 0.005, 0.025, 0.1, 0.286, 0.64, 0.904, 1.434.2.5, 5, and 10). Within these ages we also explored six metallicities (0.005 $Z_\odot$, 0.02 $Z_\odot$, 0.2 $Z_\odot$, 0.4 $Z_\odot$, 1 $Z_\odot$, and 2.5 $Z_\odot$).

Using this basis set we tried three different mixing/fitting methods, described below.

5.5.1.1 Mono-Metallicity SSPs

The most basic libraries we used are 10 SSPs corresponding to the ages listed above all at a single metallicity. To probe different metallicities we construct a single library for each of the six metallicities listed above and run separate fits for each one. The final "best" metallicity value in each aperture is then determined to be the mono-metallicty fit with the lowest χ^2_ν value. Assuming that all the separate metallicity fits represent the same underlying photon distribution (i.e., NGC 891) and therefore sample from the same χ^2 distribution (one that contains the "correct" model) we can compute a confidence limit in metallicity space by considering $\Delta\chi^2$. Here $\Delta\chi^2$ is simply the difference in χ^2 for each metallicity from the metallicity with the lowest χ^2 value. Following the example of Wall & Jenkins (2003), the probability that a best fit with value $\chi^2 = \chi^2_i$ comes from the same

distribution (and is therefore a valid fit) as a model with $\chi^2 = \chi^2_{\rm min}$ is[4]

$$\alpha(\Delta\chi^2, k) = \int_0^{\Delta\chi^2} \frac{t^{(k-2)/2} e^{-t/2}}{2^{k/2}\Gamma(k/2)} dt \tag{5.15}$$

where $\Delta\chi^2 = \chi^2_i - \chi^2_{\rm min}$, k is the number of free parameters, and Γ is the gamma function. Equation 5.15 is simply the cumulative distribution function of the χ^2 distribution.

Once the probabilities have been computed we reject any metallicities with $\alpha < 0.68$. The final reported age is then the average of τ_L over the remaining metallicities, and a good estimate of the τ_L uncertainty caused by degeneracy in metallicity is the corresponding standard deviation.

One drawback of this fitting method is that SSPs of all ages are forced to have the same metallicity. Additionally, while different apertures are allowed to have different metallicities, the metallicity resolution is constrained to the grid of metallicities defined in Bruzual & Charlot (2003).

5.5.1.2 Multi-Metallicity SSPs

To address the metallicity issues mentioned above we next explored an SSP library that sampled all SSP ages and metallicities *simultaneously*. In other words, each age bin of stars is allowed to contribute flux from an arbitrary combination of SSPs at different metallicities; instead of fitting 10 ages six times (one for each metallicity) we now fit 60 SSPs (10 ages times 6 metallicities) all at once. The reported metallicity is the the mean, light-weighted metallicity described in Equation 5.5.

Unlike the mono-metallicity libraries our multi-metallicity SSP library allows for a more physically realistic picture of NGC 891, one in which each location in the galaxy is a superposition of stellar populations with different formation ages and metallicities.

[4] $\Delta\chi^2$ and Equation 5.15 do *not* correspond to reduced χ^2. In practice all of our fits have the same number of degrees of freedom so this distinction is irrelevant.

This additional information comes at a cost, however; 60 free parameters (plus one for the extinction) can lead to degeneracies that severely dilute our ability to precisely interpret the results of our fits.

Figure 5.6 shows an example of the age/metallicity parameter space spanned by this method. We find that 60 SSPs generally over-constrain the spectral fitting and only ∼5 SSPs contribute significant flux. To further investigate these degeneracies we constructed a test basis set that contained only 3 of the 60 SSPs described above: 5, 904, and 1000 Myr SSPs all at solar metallicity. We then compared the distributions of best-fit, reduced χ^2 values resulting from fitting 60 SSPs to fits using only 3 SSPs. As shown in Figure 5.7 these two χ^2_ν distributions look remarkably similar and a 2-sample KS test confirms that

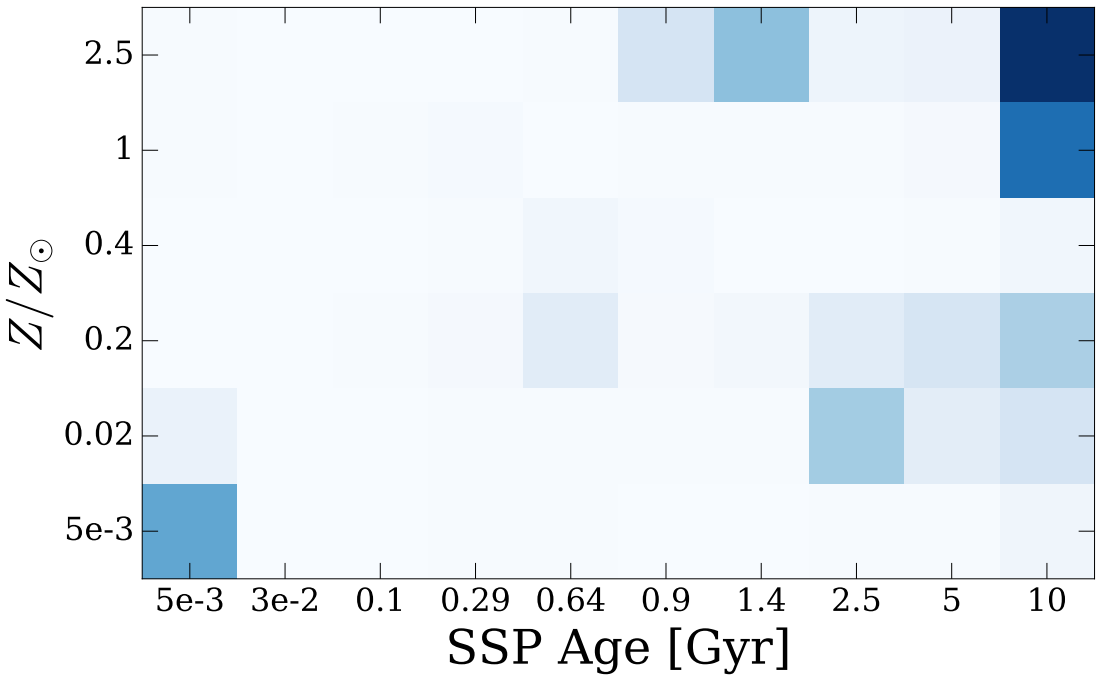

Figure 5.6 SSP light weights across all apertures in all pointings for the multi-metallicity SSP basis set. Each square shows the light weight, $W_{L,i,j}$, for SSP age t_i and metallicity Z_j, averaged across all 261 apertures. Before averaging each aperture is normalized to the same total flux so that the darkness of the box represents a true comparison of the relative contributions of each SSP across the all apertures.

they are drawn from the same distribution with $p > 0.99$.

This result confirms the claim that 60 SSPs over-constrain our fits, but doesn't' provide a satisfying resolution; the choice of the three SSPs used in the comparison was largely arbitrary and similar results can be obtained regardless of the specific SSPs used. In other words, we lack the ability to downselect from 60 SSPs in a physically or statistically motivated way. In §5.5.2 we argue that a downselection based on diffusion k-means can solve this problem.

5.5.1.3 Multi-Extinction SSPs

In the above cases we apply a single extinction parameter to all SSPs within an aperture, however models of dust in galaxies often prescribe separate extinctions for

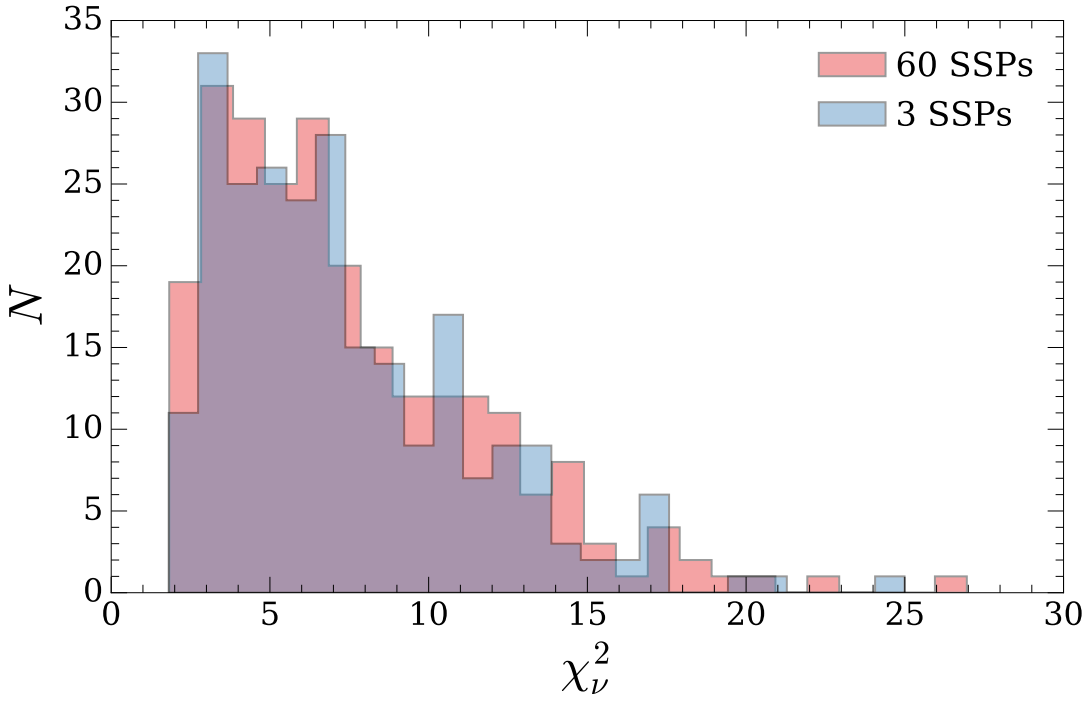

Figure 5.7 Distribution of best-fit χ^2_ν values for the full, multi-metallicity basis set described in §5.5.1.2 (*red*) and a artificially down-selected basis set containing only 5, 904, and 1000 Myr SSPs at 1 $Z_\odot$ (*blue*). A 2-sample KS test indicates these two distributions come from the same underlying distribution with $p > 0.99$.

different age populations. In a basic example (Charlot & Fall 2000) stars younger than 30 Myr are still shrouded in an HI envelope and therefore experience more attenuation of their light. We can simulate this type of behavior by allowing each SSP to have its own value of $\tau_{\mathrm{V,cont}}$ so that Equation 5.1 becomes

$$g(\lambda, Z) = \sum_i R(\lambda, \tau_{V,i}) M(\Delta t_i, Z) f(\lambda, \Delta t_i, Z). \tag{5.16}$$

This raises the number of fit parameters from 11 (10 $M(\Delta t_i, Z)$ values and 1 $\tau_{\mathrm{V,cont}}$) to 20 (10 $M(\Delta t_i, Z)$ and 10 $\tau_{\mathrm{V,cont},i}$).

In practice this library produced fits that failed to converge on reasonable timescales (days) and was abandoned. We note, however, that the reduction in parameters provided by the method discussed in the next section might make this problem tractable. Future work will investigate the resurrection of a multi-extinction SSP mix.

5.5.2 Diffusion K-Means BC03 SSPs

An attractive way to address the issues arising from a large SSP library (e.g., degeneracies and hence lack of precision in fit parameters) is to simply reduce the total number of SSPs used (e.g., Tremonti et al. 2004; Cid Fernandes et al. 2005; Tojeiro et al. 2007). The diffusion k-means (DFK) method of Mosby et al. (2015) (hereafter M15) directly achieves this reduction of parameter space in a statistically and physically motivated way. M15 take all 107 solar metallicity BC03 SSP templates and place them in a three-dimensional diffusion space (a reduction from the > 1000 wavelength channels) through a process called *diffusion mapping*. During this mapping M15 only consider wavelengths in the range 3600 Å $\leq \lambda \leq$ 8500 Å, which fully covers the wavelength range of our ∇Pak data. The templates are then grouped into bins based on how close they lie in this diffusion space, which essentially groups the templates based on similarities in their spectra shape. The result is 4 broad age bins that capture important differences between different aged

populations. The age range of these bins is shown in Table 5.1 and we refer to them as Young (Y), Intermediate 1 (I1), Intermediate 2 (I2), and Old (O).

It is important to note that M15 find that simply using the median BC03 SSP from within a DFK bin does not produce a basis set that is more precise than the full set of BC03 templates. The spectrum associated with each DFK bin must be an average of all the spectra within that bin and thus the DFK basis set constitutes a set of spectra that are different than the standard BC03 templates. These averages are weighted by the time interval straddled by each of the input BC03 spectra and the weights used in M15 and in this work assume a constant star formation across each DFK bin.

Figure 5.8 shows a comparison between the SSP templates used in §5.5.1 (taken from Tremonti et al. (2004)) and the reduced, DFK templates. It also highlights the evolutionary scatter in each DFK bin: the O bin is old enough that there is almost no change in spectral shape across the entire age range. The I1 and I2 bins, on the other hand, cover a wide range in spectral shape but are still represented well by their single, averaged DFK spectra.

Despite being based on purely statistical methods (i.e., diffusion k-means), the age groupings of the final bins roughly correspond to important timescales in stellar evolution. The Young bin corresponds to the very brightest O and B stars that have strong UV flux

Table 5.1. Diffusion k-means bins

DFK group	M15[a] label	Age range
1	Y	0.9-5.2 Myr
2	I1	5.5-404 Myr
3	I2	453.5-5750 Myr
4	O	6000-13500 Myr

[a]Mosby et al. (2015)

and prominent Balmer absorption. Intermediate 1 covers B, A, and F stars that have the strongest Balmer absorption. Intermediate 2 covers timescales where the main sequence turn-off transitions from A stars to late F stars and the total flux has major contributions from giant branch and thermally pulsating asymptotic giant branch stars. Finally, the Old bin contains F and G stars with strong metal lines and very little spectral evolution over the bin. It is important to note that M15 do artificially adjust the limits of the oldest two bins to account for the fact that star formation histories are rarely constant over 10 Gyr.

One of the current limitations of this method is that the diffusion k-means grouping has so far only been performed on solar metallicity SSPs. To constrain metallicity we construct composite metallicity libraries in the style of both §5.5.1.1 and §5.5.1.2 using the exact same SSP groupings described in Table 5.1. The resulting analysis is the same as for

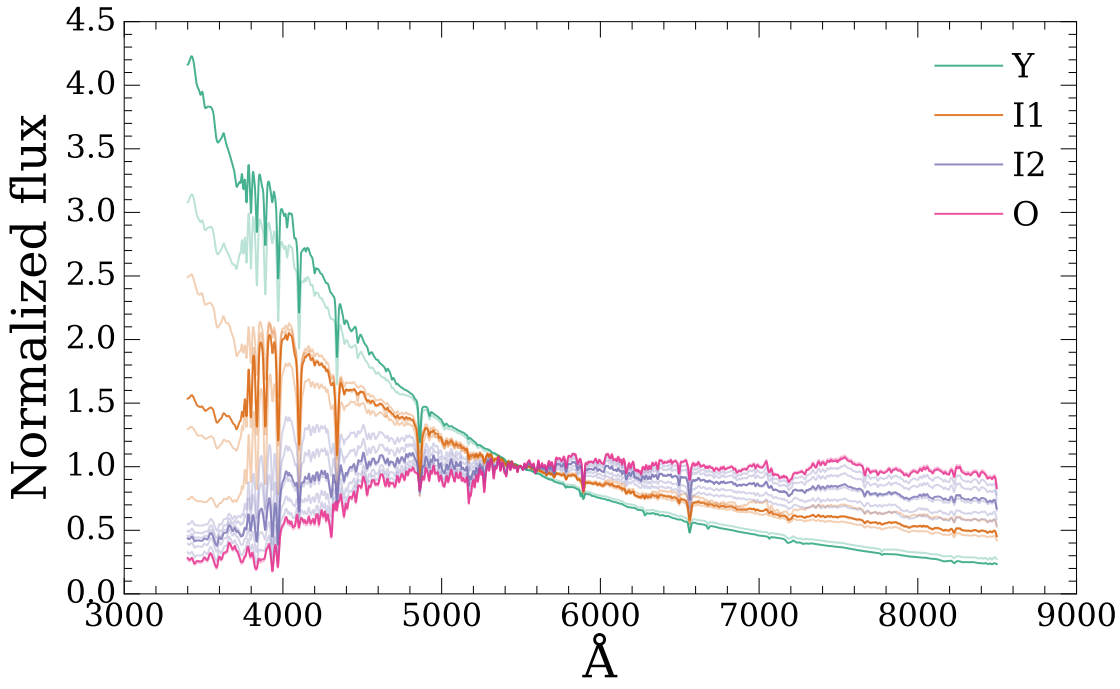

Figure 5.8 The set of BC03 SSPs used in §5.5.1 (lightly shaded) and the reduced basis set that results from applying diffusion k-means (solid). The colors correspond to the final groupings in diffusion K-means space (defined in Table 5.1). Figure adapted from M15.

those sections. In this sense the DFK grouping only reduces the size of the age dimension of SSP parameter space; we still need to deal with uncertainties in the choice of metallicity and degeneracies between age and metallicity.

5.5.3 Alternative SSP templates

The SSPs of Maraston & Strömbäck (2011) (hereafter MA11) offer an appealing, modern alternative to the BC03 SSPs. Namely, they avoid the known issues with Balmer absorption in the Stelib library (Groves et al. 2011) by using the MILES stellar libraries (Vazdekis et al. 2010; Falcón-Barroso et al. 2011). MA11 also use the fuel consumption theorem (Renzini & Voli 1981; Buzzoni 1989; Maraston 2005) to address problems that arise from using isochrones (as do BC03) to simulate the rapid changes in phase that occur at the tip of the RGB, the AGB, and the RGB bump.

To make as fair a comparison as possible the MA11 models were first grouped into the same diffusion k-means bins as the BC03 models (the consequences of using a DFK grouping from a different set of models will be ignored for the time being). This decision comes with one major caveat; the MA11 models do not extend to the youngest ages sampled by BC03. The youngest MA11 age is 6.5 Myr, which is *older* than the youngest bin found by M15. For this reason our MA11 basis set does not have a "Young" SSP and thus consists of only 3 SSPs for each metallicity.

Figure 5.9 shows a comparison between the MA11 and BC03 SSP basis sets at 1 $Z_{\odot}$. The differences in the shapes of these two basis sets have important implications for the interpretation of the SSP fitting results. In particular, the difference between the two models in the blue end decreases with SSP age; the I2 MA11 SSP has less flux than the I2 BC03 SSP by a larger difference than the I1 SSPs. At the oldest SSP age the MA11 model actually produces slightly more flux than the BC03 model. Because of this trend

the MA11 require more mass at younger ages to match the same spectrum as the BC03 basis. Thus we expect the derived τ_L values for the MA11 basis set to be lower than those derived using BC03 SSPs.

In addition to the lack of young ages, the age resolution of MA11 is much less than BC03. Compared to BC03's 107 age bins the MA11 have at most 50 age bins (for solar metallicity) and sometimes as few as 14. To assess whether this limited age sampling affects the diffusion k-means averages we rebinned the BC03 diffusion k-means spectra from a sample of BC03 spectra down-selected to match the age bins of the MA11 models. Figure 5.10 shows a comparison of the MA11 and BC03 DFK models; down-selecting the BC03 models does not appreciably affect the final, averaged DFK spectra.

Ultimately, we choose not to use the DFK'd MA11 models, but this is primarily due

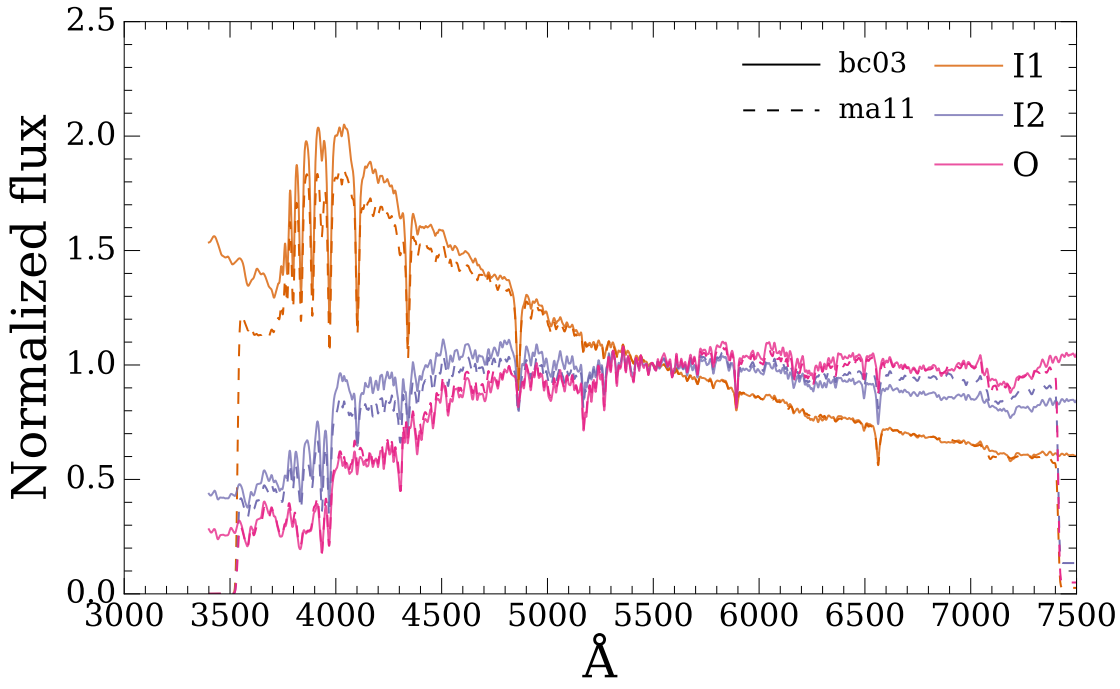

Figure 5.9 Comparison of diffusion k-means BC03 and MA11 models. Colors correspond to DFK age bins, as defined in Table 5.1. The solid and dashed lines are the BC03 and MA11 basis sets, respectively. Note that the MA11 basis set lacks the youngest age bin and does not extend redward of ∼7500 Å

to the fact that our DFK bins are constructed specifically for the BC03 data set. The omission of MA11 models from subsequent analysis is not a statement about the quality of the models themselves. We strongly warn the reader away from making a robust comparison between the models of BC03 and MA11 based on our analysis precisely for the reason that our DFK binning was tailored for the BC03 models. Future work in the area of diffusion k-means should be able to easily produce a separate set of DFK basis spectra for the full MA11 model set.

5.5.4 The final choice of SSP basis set

We choose the BC03 DFK template set as our primary SSP library because it is statistically motivated, reduces the number of fit free parameters (which also reduces computation time), and approximates important epochs in stellar evolution. We do note,

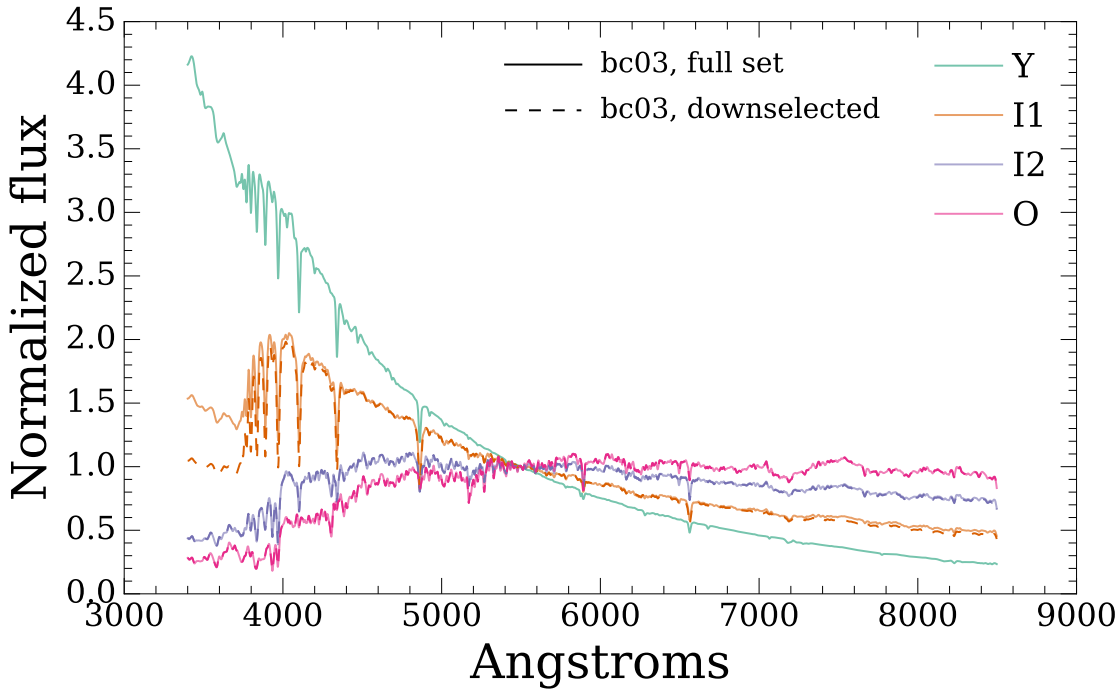

Figure 5.10 The effect of downselecting the BC03 ages to match the age grid of the MA11 models. This down-selection reduced the number of input SSPs from 107 to 50. Note that the MA11 age grid does not contain the youngest age bin.

however, that the DFK bins presented in M15 are designed for very low signal to noise data and therefore may reduce the number of SSP templates beyond what is strictly necessary for our data. In particular the I2 DFK bin covers a very wide range in stellar evolution and future work might show that it can be split into multiple bins.

We modify the solar metallicity basis set defined by M15 to consider multiple metallicities using the same method described in §5.5.1.2; each age bin is allowed to contribute light from an arbitrary number of SSPs with different metallicities. Thus the full set contains 24 separate SSPs: six metallicities each in the four age bins described by M15. We find, however, that SSPs with metallicity below 0.2 $Z_\odot$ are both statistically unrepresentative of our galaxy spectra and astrophysically implausible given the expected rapid chemical enrichment time-scales that result in a minimal contribution from super metal-poor populations to the integrated light.

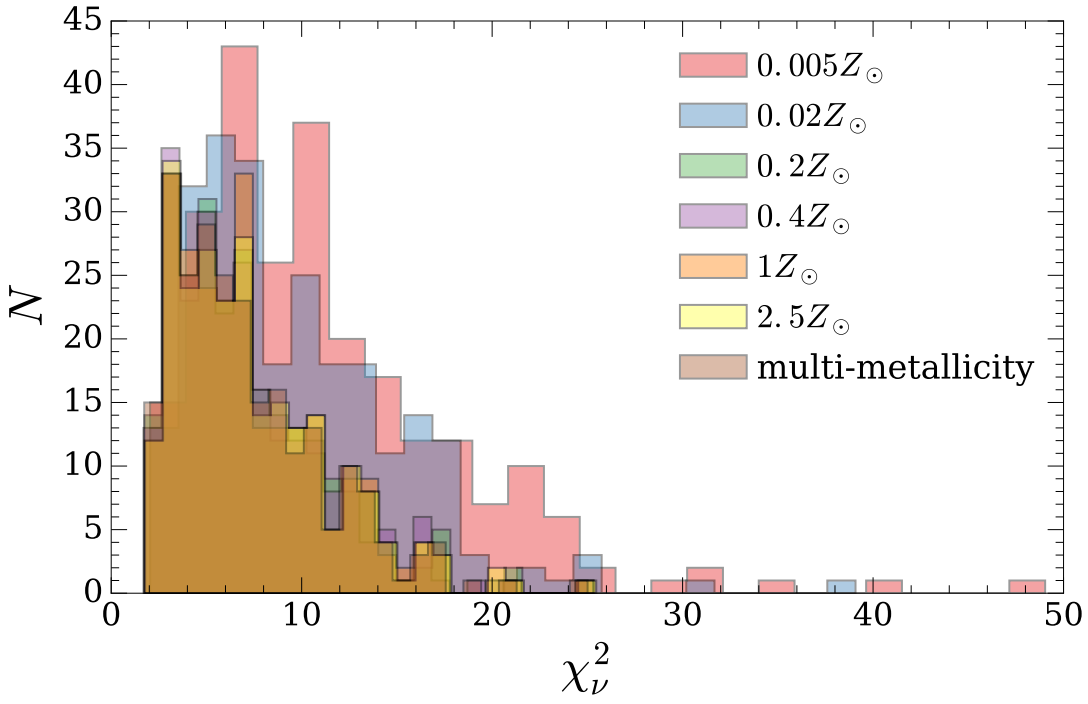

Figure 5.11 Histograms of best-fitting χ^2_ν values for all 261 apertures using both mono-metallicity and multi-metallicity DFK SSP library sets.

To test this assertion we construct mono-metallicity DFK basis sets in the same metallicity bins listed in §5.5.1.1 and fit them to our data. We then compare the distributions of goodness-of-fit (i.e., χ^2_ν) between the different metallicities and can identify fits that are statistically different from the best fitting model and therefore not likely representative of the true galaxy spectrum.

Figure 5.11 shows the χ^2_ν distributions for all ∇Pak apertures for the mono-metallicity DFK basis sets and our final choice of SSP basis set ("multi-metallicity"). The two lowest mono-metallicity SSP sets (0.005 and 0.02 $Z_\odot$) produce spectral fits that occupy a different locus in χ^2_ν and are worse than all other metallicities. A 2-sample KS test confirms that these two metallicities are not part of the same distribution as the other mono-metallicity basis sets with $p \ll 0.001$. Conversely, all other mono-metallicity basis sets are drawn from the same underlying distribution with $p > 0.8$, in the worst case, and it is therefore difficult to justify, in a statistical sense, choosing a single metallicity over another.

Figure 5.11 also shows that our final, multi-metallicity basis set (with only $Z \geq 0.2$ $Z_\odot$) produces fits of comparable quality to the mono-metallicity fits ($p > 0.8$). Thus we cannot say that our multi-metallicity basis set provides a statistical improvement over any one mono-metallicity basis set. The advantage, however, of the final basis set is in the physical insight gained by creating a more realistic physical model of the galaxy. Using a multi-metallicity SSP set also allows us to check if astrophysically reasonable age-metallicity relations come out of our analysis *without* having to assume age/metallicity priors (as is done in mono-metallicity basis sets). In other words, both mono and multi-metallicity basis sets will be subject to degeneracies between age and metallicity, but we can only quantify these degeneracies (§5.7.1) with a multi-metallicity basis set.

Finally, Figure 5.12 shows an example of the best fit in one of our apertures (pointing 6, aperture 9). This example is typical for most apertures in our data set; the data has

relatively high signal/noise and is well fit by the superposition of our final SSP basis set.

5.6 A Smarter χ^2

The algorithms used for full-spectrum fitting are designed to minimize the χ^2 difference between some model spectrum and our observational data. In this χ^2 calculation each wavelength channel is given a weight equal to the inverse of the poisson noise propagation described in section 5.2. This type of weighting benefits from historical momentum and ease of implementation but ignores the fact that certain wavelength regions are astrophysically more important than others for constraining star formation histories. In other words, a traditional χ^2 calculation gives more-or-less equal weight to all wavelength

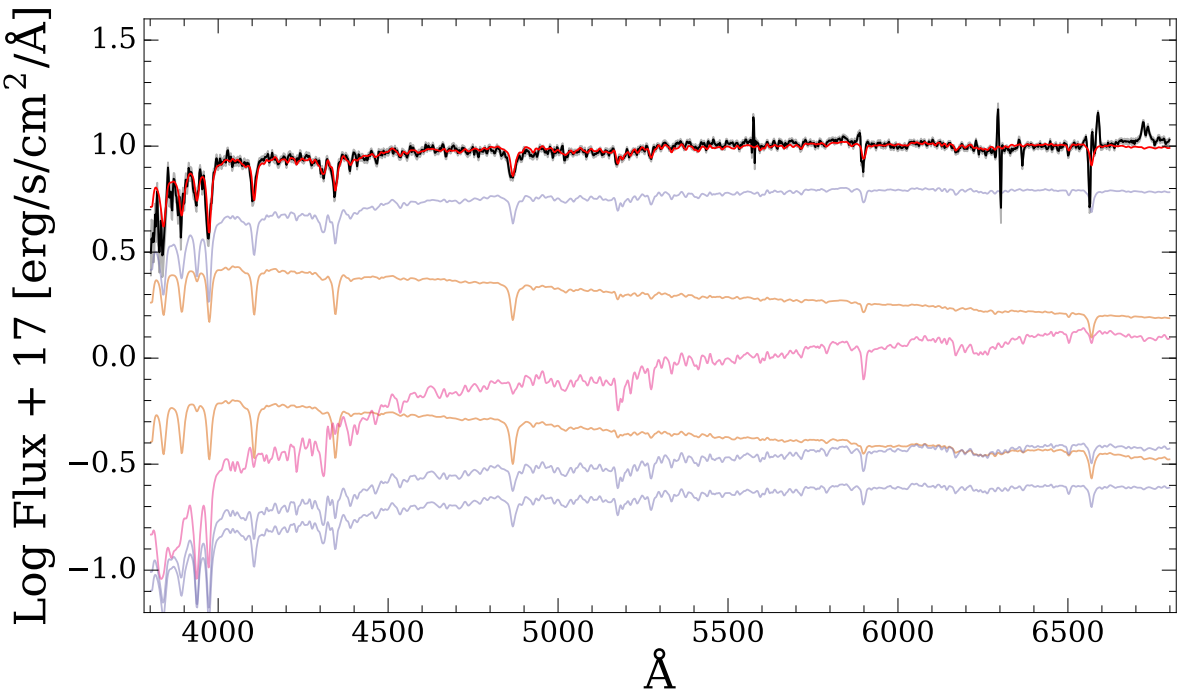

Figure 5.12 Example SSP fit to a single galaxy aperture (P6.9). The black line with gray shading (hard to see) show the measured flux and corresponding uncertainty. Each colored line (besides red) is an SSP from the BC03 DFK basis set described above and the colors are the same as in Figure 5.8. The red line is the superposition of all the individual SSP spectra.

channels despite the fact that some channels are more sensitive to differences in models than others.

To capture this astrophysical importance we compute a weighting spectrum that is applied to χ^2 during full-spectrum fitting. These weights are computed as the root-means-square (RMS) difference between the model basis SSPs and therefore capture how much each wavelength channel changes with different SSPs. For this calculation we use the 0.2 $Z_\odot$, 0.4 $Z_\odot$, 1 $Z_\odot$, and 2.5 $Z_\odot$ mono-metallicity BC03 diffusion k-means SSPs (see section 5.5.2).

Before computing the RMS, each SSP is normalized to have a flat continuum to remove any low-order continuum shape effects from the final weights. This step is important because the continuum shape changes significantly with different metallicities and ages and also because the overall continuum shape in the full-spectrum fits is controlled largely by the extinction parameter, $\tau_{\mathrm{V,cont}}$. The average spectrum across all ages and metallicities is then computed and set as the zero point for computing the final RMS spectrum. This attempt to remove the effects of low-order spectral shape is similar to the method of FIREFLY (Wilkinson et al. 2015).

Figure 5.13 shows the resulting RMS spectrum along with important spectral features. In addition to computing the RMS across all ages and metallicities we also compute RMS spectra across all ages at each metallicity and vice versa. The "total" RMS closely matches the RMS across age, which suggests that age variations cause the majority of the difference between different SSPs. There are also few spectral features that have a high RMS value in *only* age or metallicity, which suggests these weights will struggle to break the age/metallicity degeneracy.

The total RMS spectrum modifies the traditional χ^2 by

$$\chi^2 = \sum_{\lambda} \left(\frac{f(\lambda) - g(\lambda)}{\sigma(\lambda)} \zeta(\lambda) \right)^2, \tag{5.17}$$

where $f(\lambda)$ and $g(\lambda)$ are the data and model spectra, respectively, $\sigma(\lambda)$ is the poisson errors on $f(\lambda)$, and $\zeta(\lambda)$ is the RMS spectrum.

In addition to modifying our full-spectrum fits, the results shown in Figure 5.13 provide insight into the statistically important differences between model spectra. The Balmer series stands out as strong indicators of both age and metallicity, but surprisingly the higher-order Balmer lines (Hδ, Hγ) have more power than Hβ and Hα. This is important because in the absence of an accurate correction for Balmer emission (§5.3.4) these higher order lines are less likely to be contaminated. Beyond the Balmer series Na, Fe, Mg, and G-band absorption also have powerful spikes in the RMS spectrum. Unfortunately the

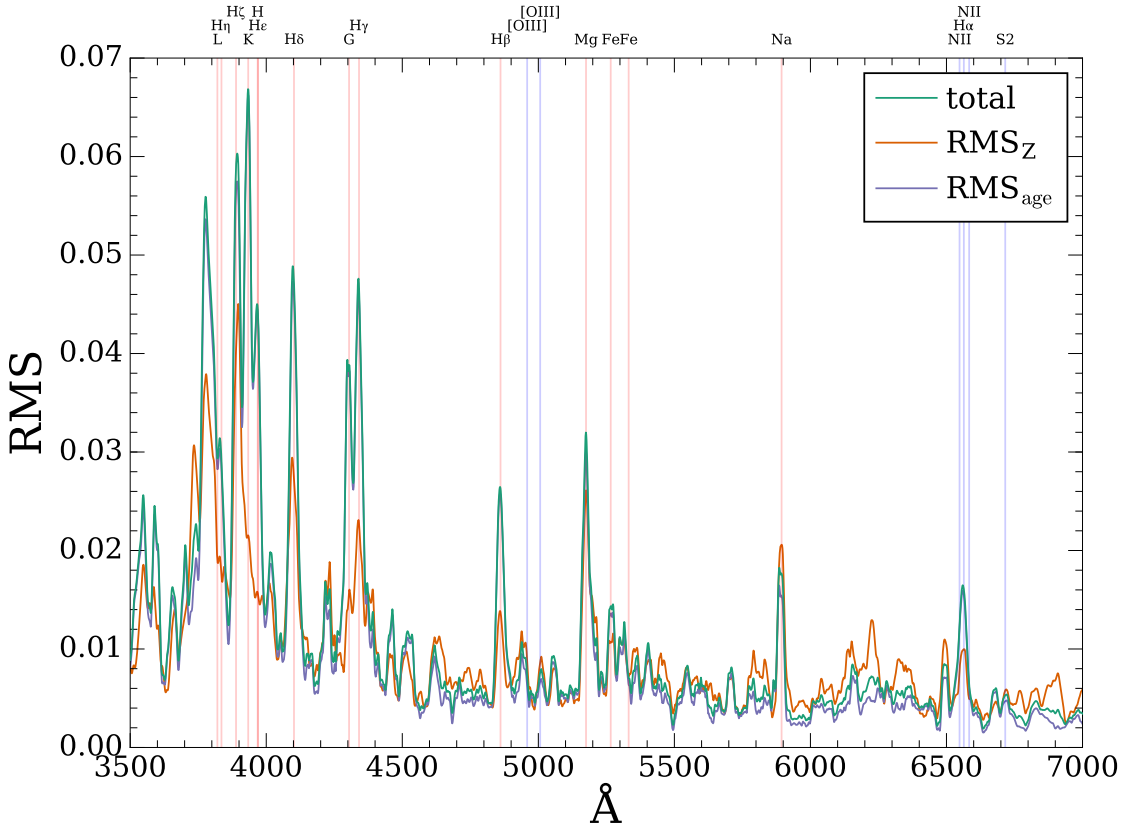

Figure 5.13 The RMS weighting function used to modify our χ^2 fits ($R(\lambda)$ in Equation. 5.17). The total RMS value is computed across all metallicities and ages. RMS_Z is computed across all metallicities and is sensitive to differences between models with different metallicity values. Similarly, $\mathrm{RMS}_{\mathrm{age}}$ is computed across all ages and is therefore more sensitive to model differences as a function of age.

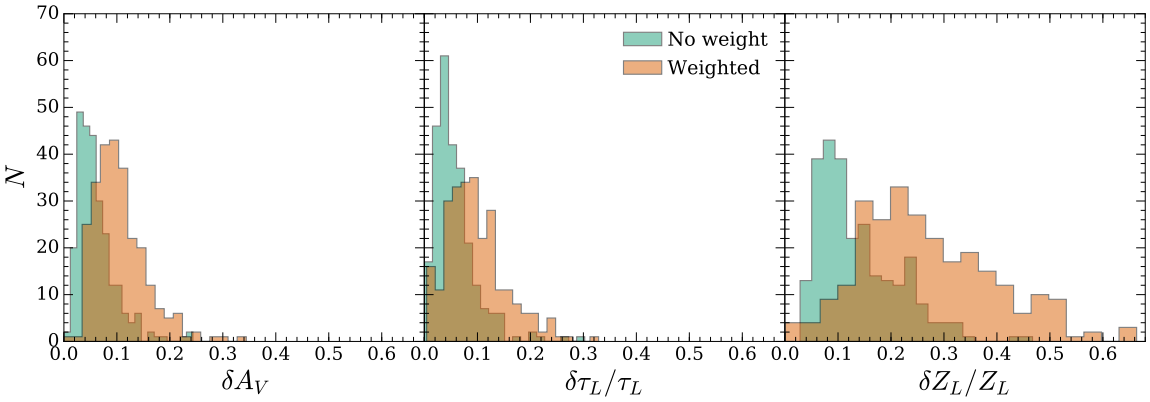

Figure 5.14 Distribution of fitting errors (§5.7.1) for fits using un-weighted and weighted χ^2.

distance to NGC 891 places Na absorption right on top of the NaD sky emission line so it cannot be used in analysis.

In many ways the index/equivalent width measurements common to Astronomy and used in Chapter 4 can be thought of as χ^2 comparisons that are very highly tuned to specific spectral features and therefore are highly dependent on the stellar physics that go into producing the models. In this context it comes as no surprise that the spectral features that differentiate our SSP models are the same features that have been used extensively in the LICK system to assign astrophysical parameters to observations of galaxy and stars.

To assess the benefit of using a weighted χ^2 we compare fitting uncertainties (§5.7.1) produced by un-weighted fits to those produced with weighted fits and find, somewhat surprisingly, that a weighted χ^2 produces significantly less precise fits. Figure 5.14 shows that for all parameters of interest the distribution of fit uncertainties is larger for weighted fits than for un-weighted fits, often by a factor of > 2. This level of uncertainty is unacceptable and it is clear that weighted fits *do not* improve our ability to understand NGC 891. They are therefore abandoned for the remainder of this work. We would like to note, however, that these tests are in no way an exhaustive exploration of the general

concept of weighted χ^2 and we encourage future research in this topic.

5.7 Uncertainties

Uncertainties in our derived parameters (τ_L, Z_L, A_V) come from a number of sources: the precision and accuracy of the data (e.g., random errors and flux calibration, respectively); degeneracies between age, metallicity, and extinction; and systematic uncertainty in our interpretation of the results of the fit. In the context of our DFK basis set, the latter consists of the assignment of the effective age of each template, which then propagates into the mass- or light-weighted mean age and metallicity. In this section we quantify the magnitude of these uncertainties, first looking at the coupling between random errors in the data and covariance in age, metallicity, and extinction.

5.7.1 Stochastic Uncertainty and Covariance

Stochastic uncertainty in (τ_L, Z_L, A_V) that arises during full spectral fitting is driven by two effects: uncertainty in the true shape of our galaxy SED and degeneracies between

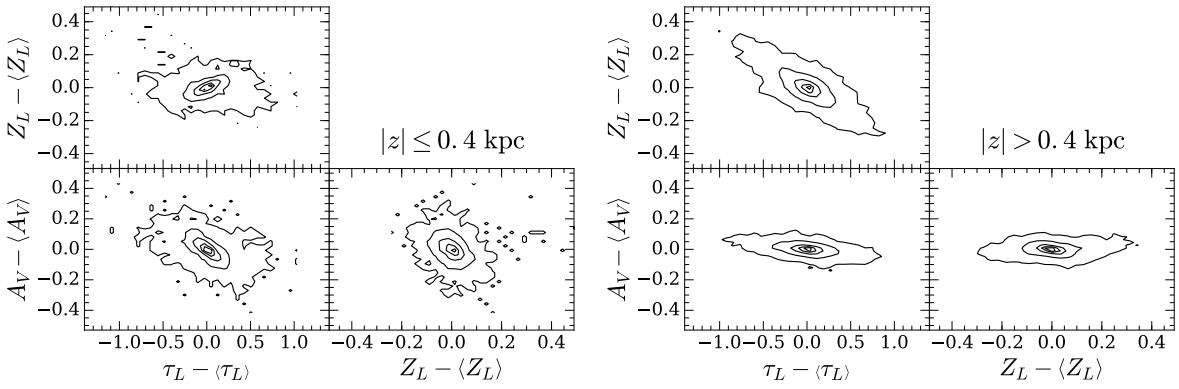

Figure 5.15 Derived parameters for all iterations of the Monte Carlo noise perturbations for all apertures. To remove real differences in values between apertures the values for each aperture are zeroed to the mean of the 100 noise perturbations. *left:* Data for apertures below 0.4 kpc. *right:* Data for apertures above 0.4 kpc. The contour levels are 0.5%, 10%, 40%, 70%, and 90%.

age, extinction, and metallicity. The uncertainty of the SED of NGC 891 is already quantified; it is exactly the error spectrum computed as part of the data reduction described in Chapter 4 and accounts for uncertainty in wavelength calibration, sky subtraction, and flux calibration.

To quantify uncertainties caused by degeneracies in the fit parameters we construct a set of 100 Monte Carlo iterations of each galaxy spectrum. For each iteration the galaxy flux at a specific wavelength, $f(\lambda)$, is perturbed by an amount randomly chosen from a normally distributed set of values with a width equal to the error spectrum computed during data reduction. Thus, the kth Monte Carlo spectrum is $f'_k(\lambda) = f(\lambda) + r(e(\lambda))$, where $r(\sigma)$ represents a normal distribution with width σ and $e(\lambda)$ is the galaxy error spectrum. Each of the $f'_k(\lambda)$ spectra are then fit with the identical method and SSP library (§5.5.4). The "true" value of the fit parameters is then taken to be the mean over all 100 iterations while the total fit uncertainty (i.e., stochastic plus degeneracies) is defined by an ellipse in (τ_L,Z_L,A_V) space that contains 68% of all Monte Carlo iterations (i.e., a 68% phase-space confidence interval). The reported uncertainties for each individual parameter are the projection of the limits of this ellipse onto the specific parameter. These uncertainties are shown in Figure 5.15.

The decision to perform Monte Carlo perturbations on our data rather than the best fit model is similar to the approach taken by PIPE3D (Sánchez et al. 2016), and we feel it yields important information. Namely, it allows us to quantify how any systematic differences between our data and the models couple with random uncertainties in the data. In other words, it fully encapsulates all sources of uncertainty that affect the final fits.

The primary degeneracy in our fit parameters is the well known age/metallicity degeneracy (see, for example, O'Connell 1976; Aaronson et al. 1978; Worthey et al. 1994; Gil de Paz & Madore 2002), whereby a mix of younger, more metal-rich populations can

be spectrally indistinguishable from a mix of older, more metal-poor populations. This correlation is especially relevant to our work given our attempt to simultaneously fit SSPs with multiple metallicities and ages.

Secondary degeneracies exist between extinction and both age and metallicity, the amplitudes of which are dependent on the overall age of the model spectrum. In models with a high fraction of young SSPs extinction is strongly correlated with age. This is due to the fact that the stars dominating the blue-visible portion of the spectrum in these populations are so hot that any metals present will be sufficiently ionized that their contribution to stellar atmospheric opacity is negligible. Thus the only way to change the slope of the continuum is to either vary age or attenuation.

In intermediate-aged populations metal absorption lines make up a key component of the opacity in stellar atmospheres and a higher concentration of metals absorption lines will "redden" the spectrum through increased line-blanketing at bluer wavelengths (see, e.g., Figure 4 in Vazdekis et al. 2010). In this regime there is a strong negative correlation between metallicity and extinction because the model spectrum can be reddened by increasing the strength of these metal lines. The left panel of Figure 5.15 shows this effect in the (A_V, Z_L) plane. As we will see in §5.8.3, below 0.4 kpc most of the measured light comes from intermediate populations where the correlation between A_V and Z_L is strongest.

There is a limit to this effect, however; the very oldest SSPs are cool enough that there is significant metal-line reddening regardless of the overall metallicity (at least within the range of metallicities considered here) and increasing the total metallicity will not appreciably change the shape of the continuum. This effect can be seen in the right panel of Figure 5.15; there is very little correlation between Z_L and A_V in regions dominated by the Old DFK bin.

As shown in Figure 5.15, the majority of apertures our quantities of interest show the expected degeneracies discussed above (negative age/metallicity correlation, negative age/extinction correlation, and negative metallicity/extinction correlation) however there are large group of apertures that exhibit a *positive* correlation between age and metallicity (i.e., increasing the metallicity leads to fits that have older ages). This seemingly backward trend is reasonable (and expected) in the context of how the reddening affects different aged populations. Apertures with a positive age/metallicity relation are concentrated below the age break at 0.4 kpc (Chapter 4) and therefore have a high fraction of total flux contributed by young SSPs (although, importantly, I2 and Old populations still contribute the majority of the light, a la §5.8.3). As discussed above, young SSPs have a continuum shape that is only weakly dependent on metallicity, so reddening is achieved by increasing A_V. Thus, as the fraction of Young SSPs increases more extinction is needed to redden the models to the level of the data. This increase in total extinction (for a given aperture) then requires the I2 and Old SSPs to have lower metallicities to counteract the extinction-induced reddening. This decreases the total metallicity, Z_L, because (as shown in §5.8.3) I2 and Old SSPs still contribute the majority of the light at all points in the galaxy. Thus, the positive age/metallicity correlation at small heights is the result of the fact that metallicity is a

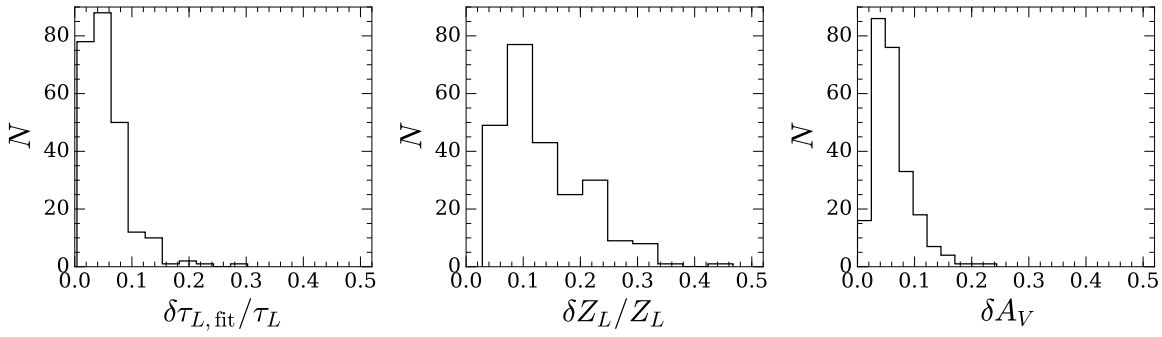

Figure 5.16 Distribution of parameter uncertainties in age, metallicity, and extinction derived from full spectral fitting. The uncertainties are 68% confidence limits on all three parameters simultaneously based on the Monte Carlo perturbations described above.

weighted average that is mostly dominated by older SSPs, and that a single extinction value, A_V, is applied to all SSPs in a particular fit.

The fact that a purely random perturbation of our data results in fits that clearly show the expected astrophysical degeneracies indicates that these degeneracies are the primary source of fitting uncertainty. In other words, uncertainty in our SSP fits is driven mainly by similarities between different model SSPs; random flux errors in a given wavelength channel are only a secondary source of fitting uncertainty.

We compute total fitting uncertainty using the method described above separately for each aperture. The values thus derived constitute all sources of uncertainty that arise from the simultaneous measurement of the three parameters. Figure 5.16 shows the distribution of uncertainties in age, metallicity, and extinction. These uncertainties are on the order of 5% for most apertures, but the distribution of uncertainty in metallicity is broader than either τ_L or A_V and can reach $\sim$30% in the worst cases.

5.7.2 Systematic Uncertainty in DFK Ages

Computing a weighted age (e.g., Equation 5.3) for a superposition of model SSPs requires assigning a specific age to each individual SSP, which, in turn, requires making an assumption about the star formation history (SFH) across the range of ages spanned by the SSP age bin (see Table 5.1). Different SFHs have minimal impact on the youngest SSPs due to their narrow age range, but the oldest SSPs span a range of over 7 Gyr and thus the age assigned to this bin can vary by the same magnitude, depending on the assumed SFH. Because of this, the choice of SFH creates systematic uncertainty in the computed value of τ_L. This uncertainty is primarily a consequence of the fact that old stellar spectra are essentially constant over a large age range. In other words, these old populations do not provide enough information in their spectral shape to yield precisely defined ages.

To quantify this systematic uncertainty we compute τ_L as derived from 100 Monte Carlo SFHs. For each Monte Carlo iteration we assign each DFK bin an age that is randomly selected from a uniform distribution bounded by the limits of the age bin given in Table 5.1. These ages correspond to t_i in Equation 5.3, which allows us to compute a different τ_L for each iteration. It is important to note that t_i is the only quantity that changes between iterations; the specific SSP weights ($W_{L,i,j}$) are held constant at their best fit values. The standard deviation of τ_L across all 100 Monte Carlo iterations quantifies the systematic uncertainty that results from assuming a SFH.

By choosing t_i completely randomly from within the corresponding age bin we allow completely unconstrained SFHs. The drawback of this approach is an almost certain overestimation of the true systematic uncertainty, but the benefit is that we are not required to make assumptions about the general form of the SFH. In this way, our computation captures not only our lack of knowledge about the specific shape of SFH, but also our lack of knowledge about the general form of SFH (e.g., bursty versus smooth).

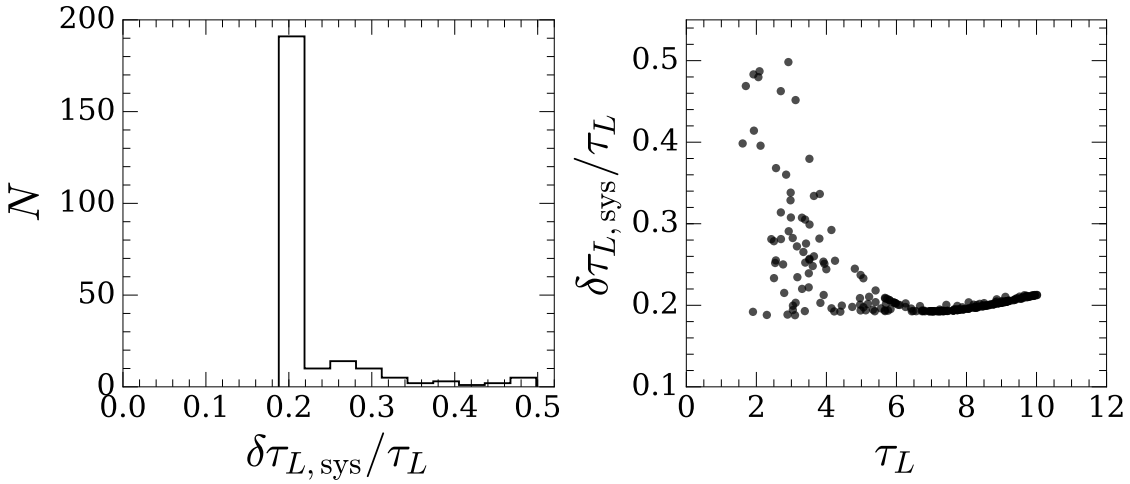

Figure 5.17 *left:* Distribution of systematic uncertainty that arises from assuming a star formation history. The uncertainties are the standard deviation of 100 values derived from a random assignment of ages to the SSP basis set. *right:* The same systematic uncertainties as a function of τ_L.

The left panel Figure 5.17 shows the distribution of systematic uncertainties in τ_L. In the majority of our apertures this uncertainty is $\sim$20%, but there is a tail with high fractional uncertainties that extends up to 50%. As shown in the right panel this tail comes from apertures with $\tau_L < \sim$5 Gyr. As we will see in §5.8.3 I2 and O populations make up the largest contributions to the total light in *all* apertures, even those with a significant fraction of younger populations, and it is these older populations that have the largest systematic uncertainty due the large range of ages they represent. Thus in all apertures the systematic uncertainty is dominated by the presence of old populations. Figure 5.18 shows these uncertainties in the context of the age gradients presented in §5.8.2; the magnitude of these uncertainties still allows us to determine broad, smooth trends over large ranges in height, but it becomes difficult to make statements about the detailed age structure of NGC 891.

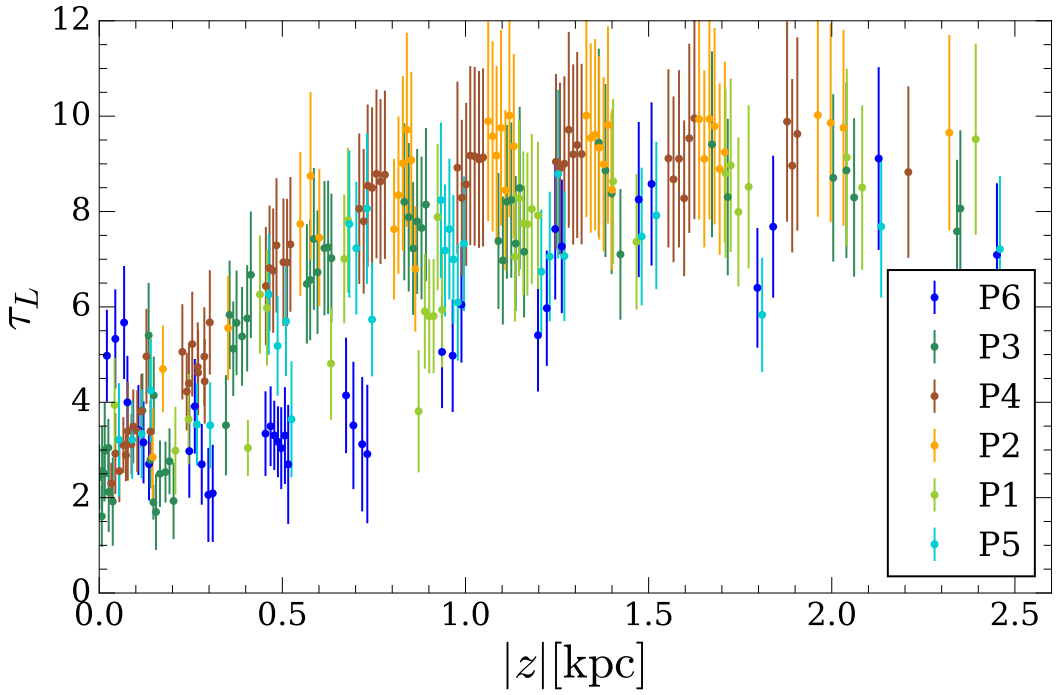

Figure 5.18 τ_L as a function of height above the midplane showing the magnitude of the systematic uncertainties that arise from assuming a star formation history.

Despite this bleak picture, we urge the reader to take solace in the fact that the systematic uncertainties presented above are an extreme upper limit and ignore NGC 891 as a coherent galaxy. In other words, it is unreasonable to assume that the SFH within NGC 891 varies on time scales greater than a dynamical timescale ($\sim$1 Gyr). Thus, when assessing trends in τ_L, Z_L, or A_V we can say with confidence that points near each other in phase space likely come from the same underlying population(s), despite the large systematic uncertainties. It is only on large physical and time scales that these uncertainties become relevant. Furthermore, in §5.8.3 we find evidence that the general form of SFH is mostly invariant over the portion of NGC 891 we measure. For these reasons we choose not to include systematic uncertainties in the final results shown in §5.8, where we draw conclusions about the detailed, small-scale structure of NGC 891. If we were to compare the global results for NGC 891 presented here to other galaxies with potentially different SFH then the systematic uncertainties would be relevant.

5.8 Results

5.8.1 Age and Metallicity

The analysis methods described above allow us to measure τ_L and Z_L as a function of galactic radius and height. This parameter space can yield powerful insights into the history and formation of NGC 891, but first it is useful to examine the distribution of these parameters on a galactic scale, as shown in Figure 5.19. In the left panel we see a roughly tri-modal distribution of τ_L that suggests multiple epochs of star formation in NGC 891. These epochs are centered near 3.5, 5.5, and 8.5 Gyr and we assign age bins to capture these different eras. We choose to split the oldest age bin in two so that our bins are $\tau_L < 4.3$ Gyr, 4.3 Gyr $\leq \tau_L < 6$ Gyr, 6 Gyr $\leq \tau_L < 8$ Gyr and 8 Gyr $\geq \tau_L$.

The distribution of Z_L shown in the right panel of Figure 5.19 also reveals multiple populations. Metallicity is peaked at 0.75 $Z_\odot$, and we choose to break this peak into two bins. Additionally, we define a bin that samples the low-metallicity tail, and two bins that probe the extended, high-metallicity tail. Thus our metallicity bins are $Z_L < 0.5$ $Z_\odot$, 0.5 $Z_\odot \leq Z_L < 0.75$ $Z_\odot$, 0.75 $Z_\odot \leq Z_L < 0.95$ $Z_\odot$, 0.95 $Z_\odot \leq Z_L < 1.3$ $Z_\odot$, and $Z_L \geq 1.3$ $Z_\odot$.

Armed with the global distribution of stellar populations in τ_L and Z_L we can examine where the different ranges defined above exist in NGC 891. Figure 5.20 shows both τ_L and Z_L as a function of radius and height. In the left panel the trends identified in Chapter 4 are immediately obvious: below 0.4 kpc all of the populations are young (< 6 Gyr), the region where $0.4 < |z| \leq 1$ kpc is a transition zone where the age generally increases, and above 1 kpc the light is dominated by the oldest populations.

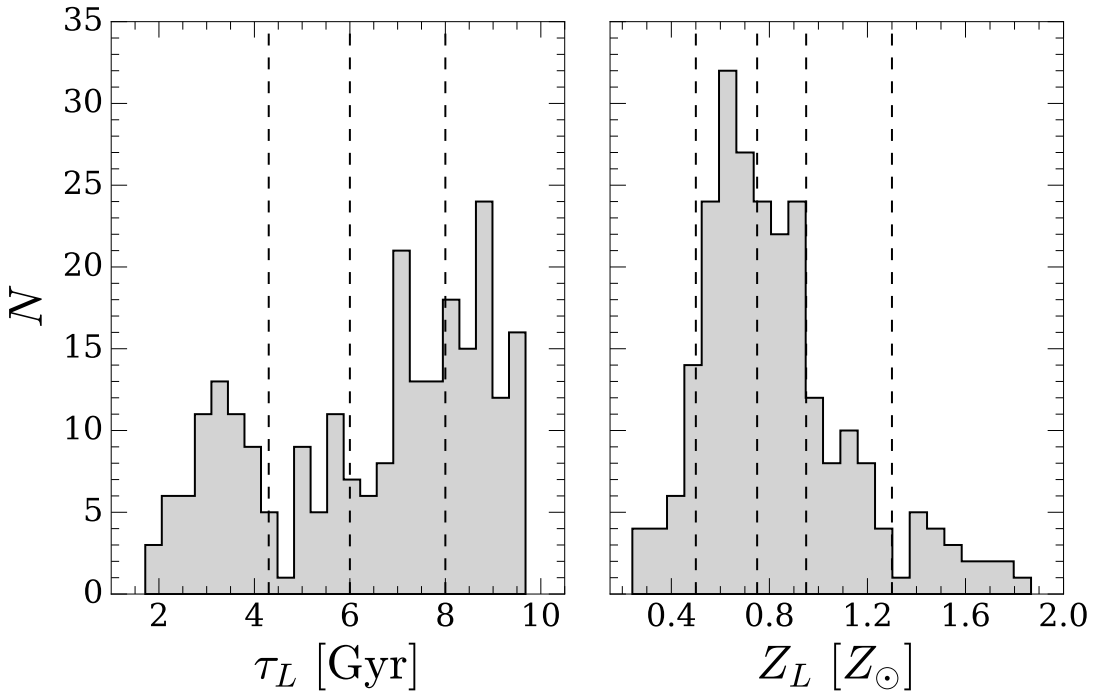

Figure 5.19 Distribution τ_L (*left*) and Z_L (*right*) across all radii and heights in NGC 891. The vertical lines identify cuts in these parameters that are discussed in rest of §5.8.1. They are 4.3, 6.6, and 8 Gyr; and 0.5, 0.75, 0.95, and 1.3 $Z_\odot$ for τ_L and Z_L, respectively

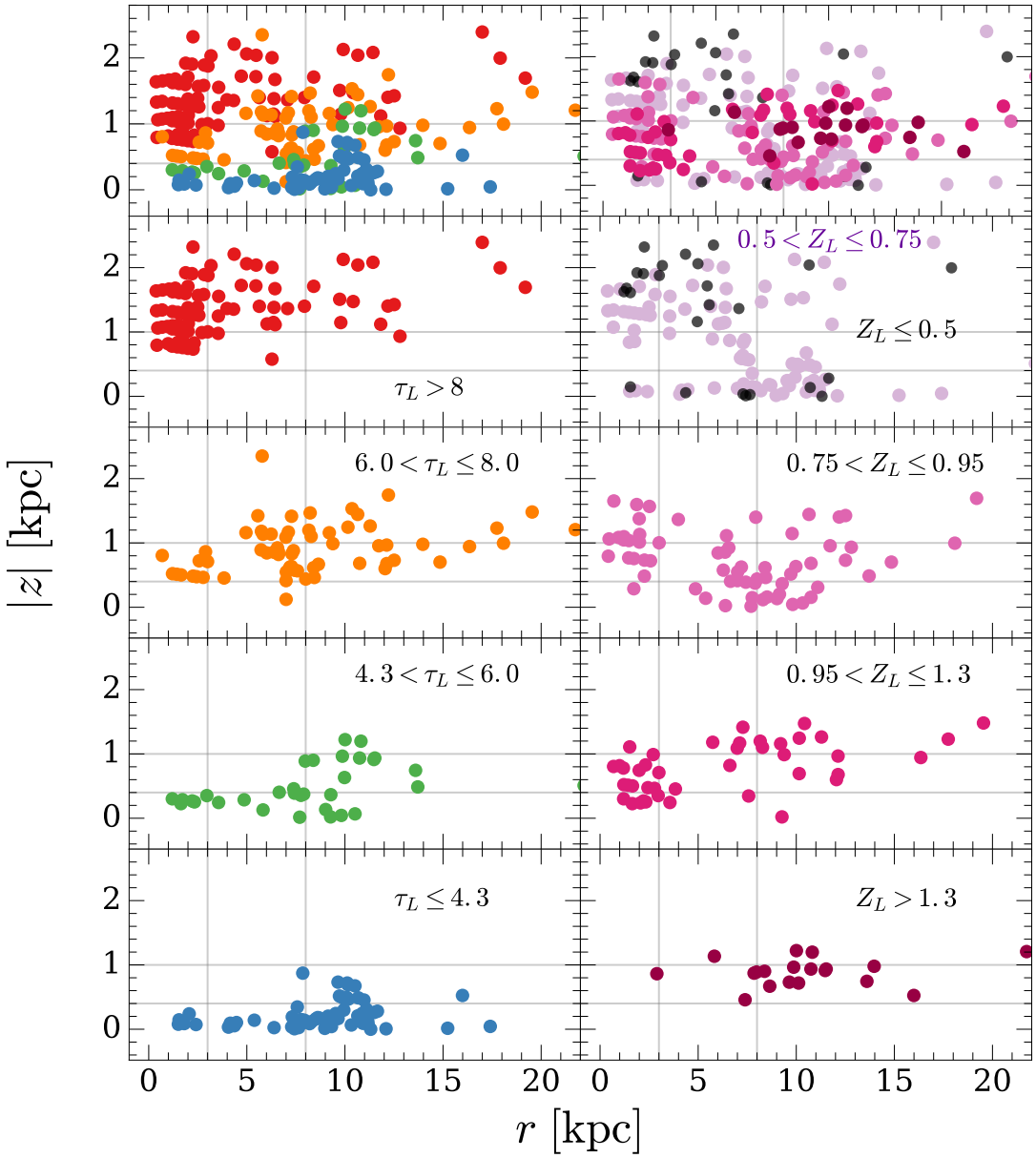

Figure 5.20 Distribution of τ_L (*left*) and Z_L (*right*) in NGC 891 as a function of radius and height. Each parameter is split into the same groups defined in Figure 5.19. Vertical and horizontal dotted lines correspond to the vertical and radial cuts made in Chapter 4, respectively

Examining radial trends in τ_L yields an even more detailed picture. In general, younger ages tend to be more concentrated toward larger radii, which is consistent with the inside-out formation scenario seen in Chapter 4 and the Milky Way (Bovy et al. 2012; Hayden et al. 2015). Furthermore, for each of the age epochs defined above and in Figure 5.20 there is a clear flaring in height at larger radii. What's more, this "flare radius" is larger for more recent epochs of star formation (i.e., increasing galaxy age). In other words, each epoch of star formation forms a flared disk and as the galaxy ages star formation (and the corresponding flare) migrate to larger and larger radii. Thus the galaxy disk as a whole can be thought of as a superposition of flared disks that formed at different times. These results are remarkably consistent with those of Martig et al. (2014), who suggest this pattern can be caused by minor interactions with small satellites and/or radial migration (Minchev et al. 2012). It is worth noting, however, that other studies argue the radial migration does not appreciably affect the vertical structure of galaxy disks (Vera-Ciro et al. 2014).

Trends in Z_L shown in the right panel of Figure 5.20 complement the trends in τ_L. Firstly, the lowest metallicities exist primarily at large heights (although there is a locus of points at small heights and large radii), which matches the general view that the old populations at large heights were formed from pristine gas early in the history of NGC 891. Modifying this simple picture is the fact that the majority of populations with super-solar metallicities also exist at intermediate to large heights. Below $\sim$0.4 kpc most of our data are sub-solar. As discussed below we suspect this trend in metallicity with height is indicative of a transition from galactic self-enrichment to inflow-dominated metallicity suppression.

This transition can be seen in the left panel of Figure 5.21, which reveals two distinct trends in metallicity with height. For populations with $\tau_L > 6$ Gyr metallicity decreases with height, as expected from the simple view that old stars are made from pristine gas

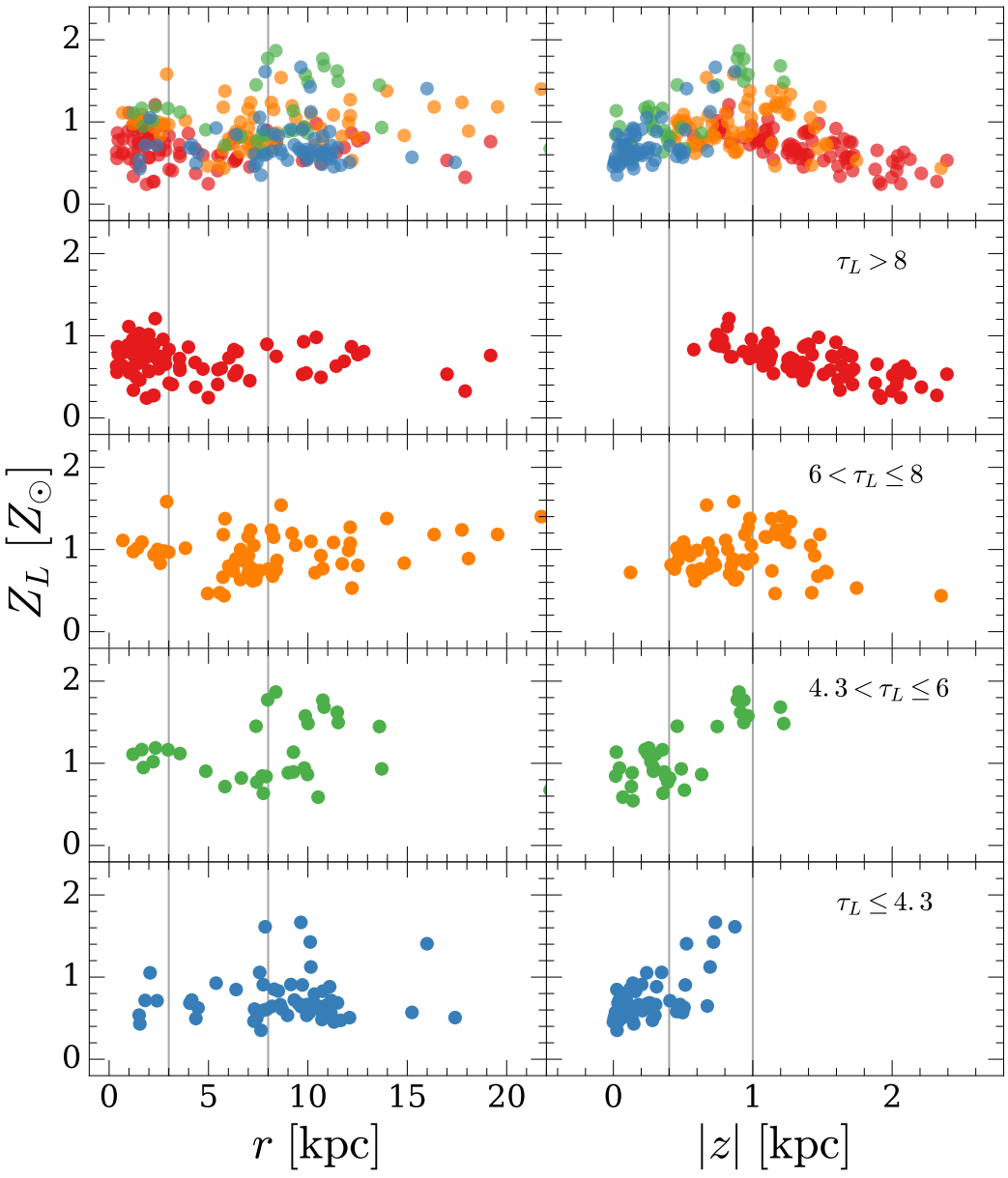

Figure 5.21 Z_L as a function of height and radius. Colors are the same as in Figure 5.20 and correspond to the τ_L cuts shown in Figure 5.19. The vertical lines show the vertical and radial cuts made in Chapter 4.

and exist at large heights. Populations younger that ∼6 Gyr show the opposite trend; here metallicity sharply increases as a function of height. If we consider height to broadly correspond to age (see Figure 5.23) then the following picture emerges: during the first few Gyr of its history NGC 891 was essentially a closed-box; each generation of stars was enriched by the chemical processing of gas by the generations that preceded it. Around 6 Gyr ago, however, low-metallicity gas from outside the galaxy started to infall onto the disk, and as the amount of pristine gas increased the average metallicity of subsequent populations decreased. Thus, the "peak metallicity" of NGC 891 occurred roughly 6 Gyr ago.

Figure 5.22 confirms this enrichment history. At all radii and heights there are two distinct epochs of the enrichment rate, dZ_L/dt: before 6 Gyr the disk of NGC 891 was enriched at a rate of roughly 0.15 $Z_\odot$/Gyr, but since 6 Gyr the infall of pristine gas onto the galaxy has been decreasing the metallicity at about -0.18 $Z_\odot$/Gyr.

In addition to the locus of metal-poor stars at large radii and small heights (i.e., the most recent star formation) in Figure 5.21 we identify a second locus of metal-poor stars at small radii and intermediate heights. In the context of the history proposed above, this second population likely corresponds to the oldest portion of the inner thick disk or pseudo-bulge. This view is strengthened by Figure 5.23, which clearly shows two very different physical locations of populations with $Z_L < 0.5$ $Z_\odot$.

Figure 5.23 also offers another view of the entire scenario presented above. To first order, age increases with height (as expected from Chapter 4) and above 1 kpc the average population age asymptotes to the oldest age (∼10 Gyr). As described in §5.7.2 the specific value of τ_L at the largest heights is dependent on the physical assumptions made when constructing the models (i.e., the first stars in the Universe formed ∼12 Gyr ago), but these assumptions only modulate the actual value; the conclusion that the integrated light

is dominated by the oldest possible populations above 1 kpc is valid regardless of the specific population age.

The enrichment history of NGC 891 is also visible in Figure 5.23. The highest metallicity populations have ages narrowly scattered around $\tau_L \approx 6$ Gyr (bottom panels), which is exactly the age of "peak metallicity" identified above. As metallicity decreases there is an increasing level of bifurcation in age, representing the two epochs of metal-poor star formation: the first, at large heights and small radii, corresponds to the first stars formed in NGC 891. The second, at small heights and large radii, corresponds to recent star formation that is drawing from metal-poor gas that has been infalling onto the disk for the last 6 Gyr.

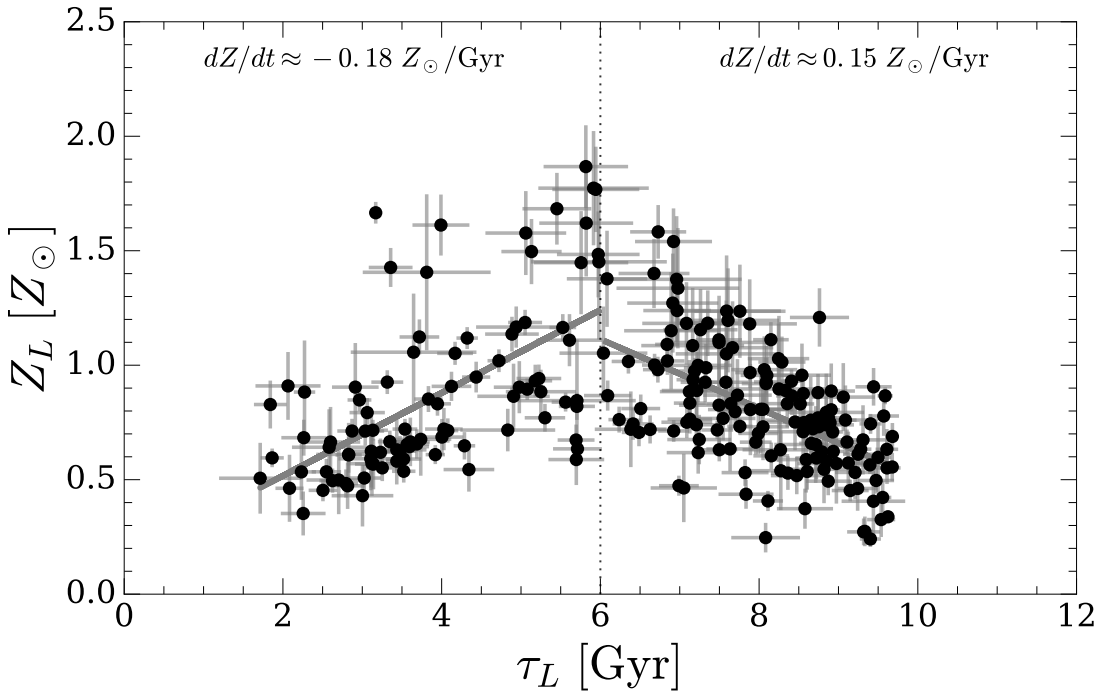

Figure 5.22 Metallicity as a function of population age across all regions of NGC 891. The vertical dotted line denotes "peak metallicity" at 6 Gyr. The solid lines are linear fits to each epoch of enrichment. Note that τ_L corresponds to population age, while dt represents the time *since the formation of the galaxy.*

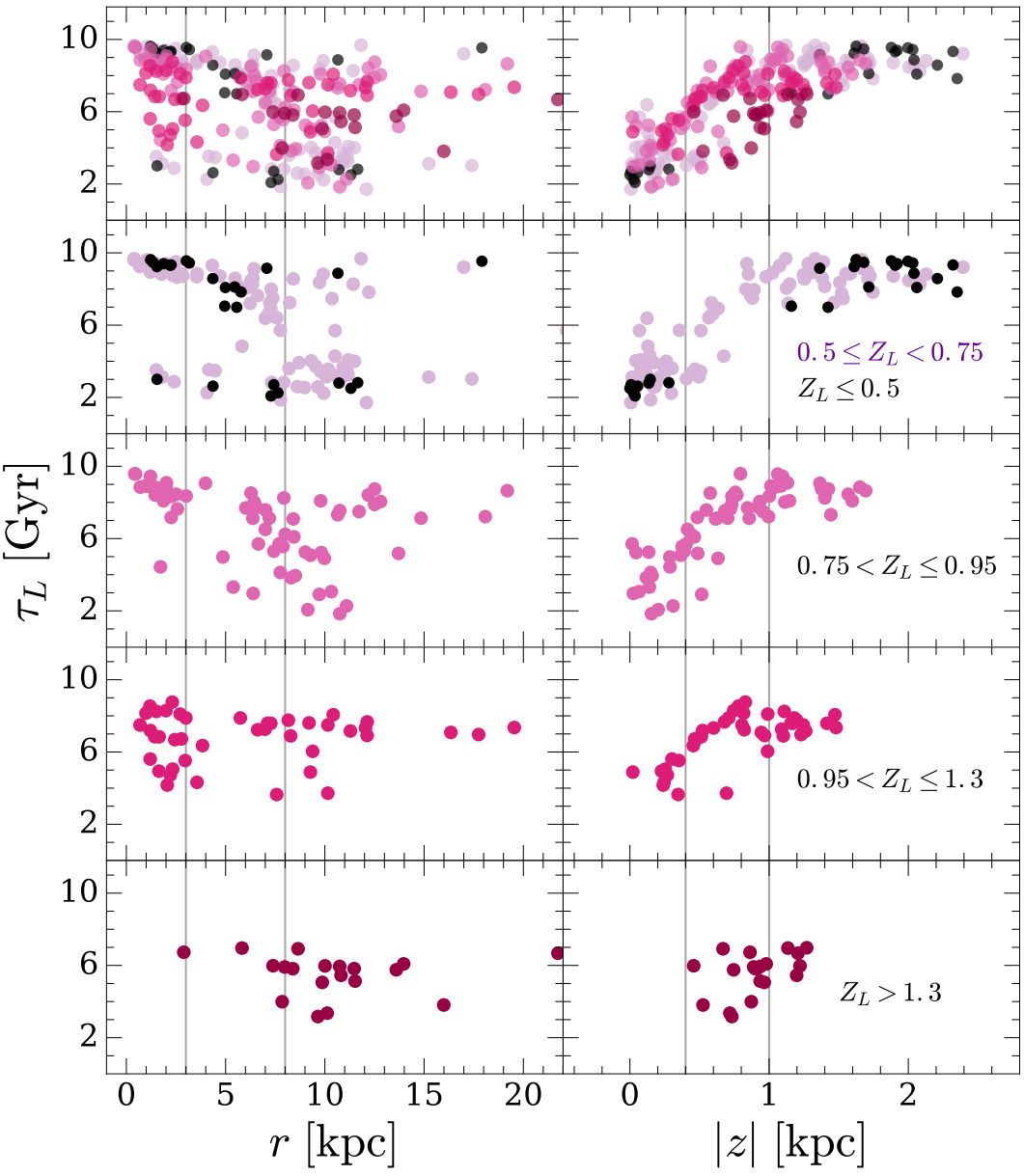

Figure 5.23 τ_L as a function of height and radius. Colors are the same as in Figure 5.20 and correspond to the Z_L cuts shown in Figure 5.19. The vertical lines show the vertical and radial cuts made in Chapter 4.

5.8.2 Features in Phase Space

In the previous section we examined the locations of (essentially) mono-age and mono-metallicity populations in NGC 891. This is a very useful method that leads to powerful results, but it does not paint the full picture. Our analysis techniques (§5.3.1) yield a parameter space consisting of τ_L, Z_L, A_V, radius, and height, and there is information to be gained by considering volumes of populations in this space. Examining NGC 891 in this parameter space reveals three distinct features: (i) a "primary" disk, (ii) a flared extension of the same disk, and (iii) a high-metallicity sequence that exists at large radii, which we call simply "sequence 3". Figures 5.24 - 5.26 show these features and we discuss how we identified them based on three projections of this parameter space below. We note that these features are not distinct from the conclusions drawn about NGC 891 in §5.8.1, rather they present a different view of the same overall picture.

5.8.2.1 τ_L

Figure 5.24 shows the projection of our data into the $\tau_L(r, z)$ volume. As in Figure 5.23, the three broadly defined regions from Chapter 4 are immediately obvious in the top-right panel (i.e., primary disk): below 0.4 kpc all of the populations are young (< 6 Gyr), the region where $0.4 < |z| \leq 1$ kpc is a transition zone where the age generally increases, and above 1 kpc the average population age asymptotes to the oldest age ($\sim$10 Gyr). As described in §5.7.2 and §5.8.1 the specific value of τ_L can modulate with assumed SFH, but the fact that the integrated light is dominated by the oldest possible populations above 1 kpc is true regardless.

Xilouris et al. (1999) fit a single stellar disk to broad band photometric profiles of NGC 891 and find a scale height of 0.38 - 0.43 kpc from K to B bands. In this context it is plausible that our primary disk roughly corresponds to this single stellar disk.

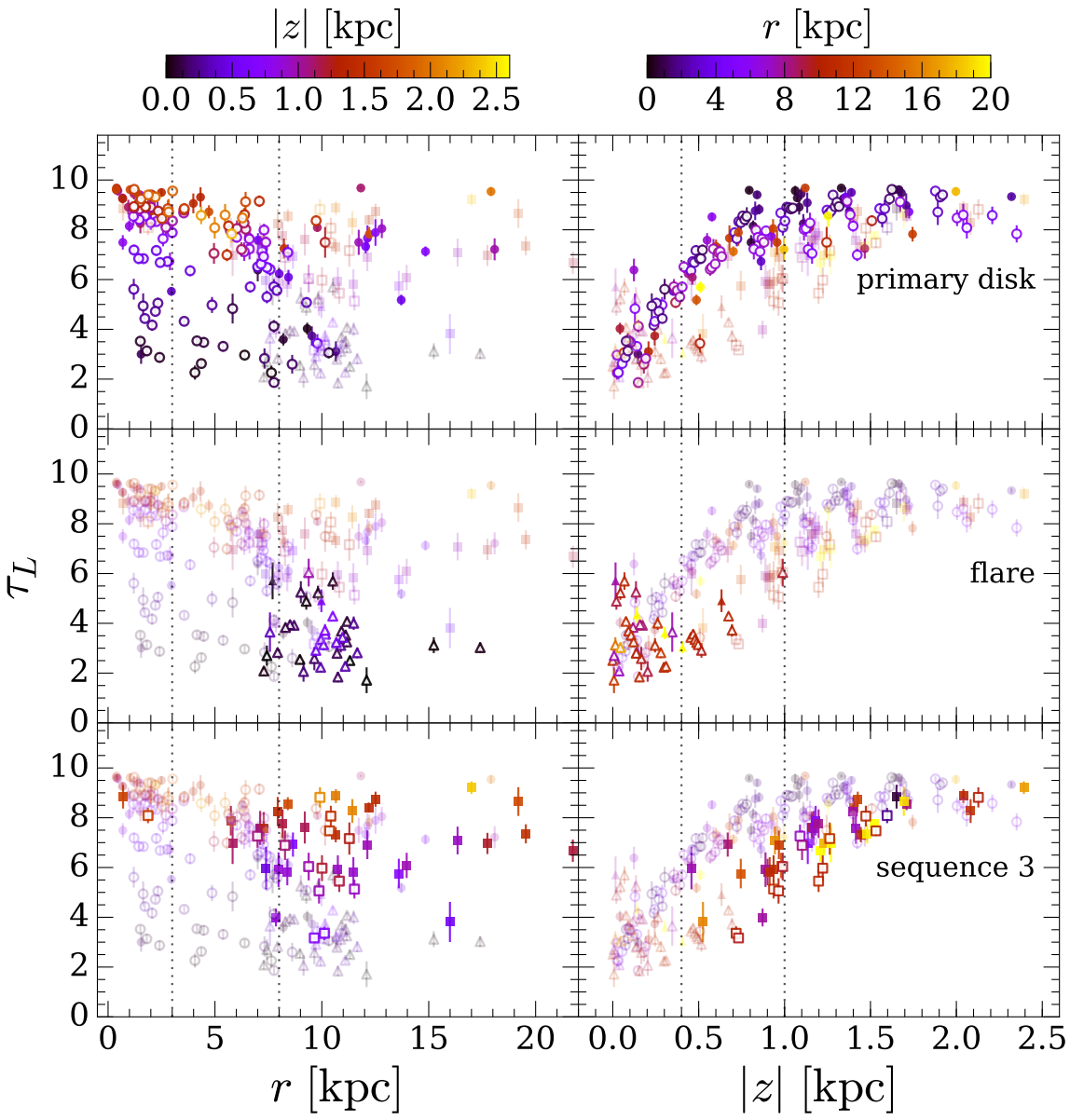

Figure 5.24 τ_L as a function of true radius (*left*) and height (*right*). On each side the points are color coded by the opposite position parameter. Open and filled circles correspond to the approaching ($r_{\rm proj} < 0$) and receding ($r_{\rm proj} \geq 0$) side of NGC 891, respectively. Vertical dotted lines correspond to the radial and vertical cuts used in Chapter 4 and Figure 5.27. The three rows show the exactly the same data, but shaded to highlight the feature identified in the right-hand labels.

However, more recent studies of NGC 891 (Schechtman-Rook et al. 2012; Schechtman-Rook & Bershady 2013, 2014) have refined this single-disk model to include three distinct disk components: super-thin, thin, and thick with scale heights (in K_S band) of 0.16, 0.47, and 1.44 kpc, respectively. In this view it is likely that the smooth transition from young to old ages seen in the upper-left panel of Figure 5.24 is a result of the superposition of these different disk components and thus our primary "disk" encapsulates substructure beyond our measurement capabilities. Furthermore, the primary disk also does not extend much beyond $r = 8$ kpc, which is where Schechtman-Rook & Bershady (2013) identify a truncation in their super-thin disk

Radial trends in τ_L reveal detailed substructure in NGC 891. The top-left panel of Figure 5.24 confirms that, in the primary disk at a given radius, older populations occupy larger heights, but it is also clear that the maximum age at these large heights decreases slightly with increasing radius. This can be seen as confirmation of the inside-out formation of mono-age flares with increasing radii seen in §5.8.1 and proposed by Martig et al. (2014). In this scenario the oldest stars at larger radii tend to be younger than their inner-disk counterparts, exactly as seen in Figure 5.24.

The middle row of Figure 5.24 highlights a flare in NGC 891. At low heights it occupies the same τ_L space as the primary disk, but as height increases the ages stay relatively young compared to the main disk. Importantly almost all of the apertures belonging to this sequence exist at radii beyond 8 kpc, which is one of the main reasons we identify this feature as a flared extension of the star forming disk. Such a flare would be manifest as an increase in scale height with radius and thus the star-forming disk would extend to larger heights at large radii. Given this simplistic picture, and assuming the star-forming disk extends to roughly 1 scale height at all radii we can roughly estimate that at radii > 8 kpc flaring has increased the scale height by roughly a factor of two (up to $\sim$0.8 kpc).

In the context of the work of Martig et al. (2014) the flare identified here is not unique; it merely corresponds to the most recent epoch of star formation. In other words, it is the mono-age flare that is at the largest radii and therefore most visible.

The bottom row of Figure 5.24 shows the high-metallicity "sequence 3". It exists only at heights above 0.4 kpc and mostly beyond $r = 8$ kpc and is made up of stellar populations that are generally younger than the stars from the primary disk in the same (r, z) locations. That said it is clear that many of the apertures in sequence 3 contain a significant amount of light contributed by Old population stars and the slightly lower age at large heights is most likely indicative of an increased contribution from I2 populations.

5.8.2.2 A_V

In Figure 5.25 the three morphological features mentioned above are identified in the $A_V(r, z)$ volume. The primary disk (top row) shows slightly increasing extinction with height below $\sim$0.4 kpc followed by a roughly exponential decrease with height above $\sim$0.4 kpc. These results lend further proof to the conclusion that the region below 0.4 kpc is the location of current star formation, which requires regions of optically thick dust and gas. Above 0.4 kpc the older stars are likely to be smoothly distributed in a way that is uncorrelated with the dust. Thus at the heights where old stars dominate we measure a reasonable estimate of some mean extinction along a significant line of sight. At low heights the dust is patchy, very dense, and correlated with younger stars so our line of sight is likely to be abruptly truncated at some relatively short line of sight. Hence the stars we *do* see have relatively little extinction, which explains the lower extinction values below 0.4 kpc.

Above 0.4 kpc the general decline in A_V is consistent with the simple morphological view of exponentially decreasing surface density in edge-on galaxies. The rate of decline shown in Figure 5.25 indicates the scale height of attenuating material is $\sim$0.6 kpc, which is

significantly larger than either Xilouris et al. (1999) or Schechtman-Rook et al. (2012), who find a vertical dust scale height of 0.3 and 0.24 kpc in the V and K_S bands, respectively. It is important to note, however, that both of these studies find a wavelength dependence on extinction that is steeper than the model of Charlot & Fall (2000) used in our model galaxies (see §5.3.3). Our prescription of extinction therefore requires larger normalization

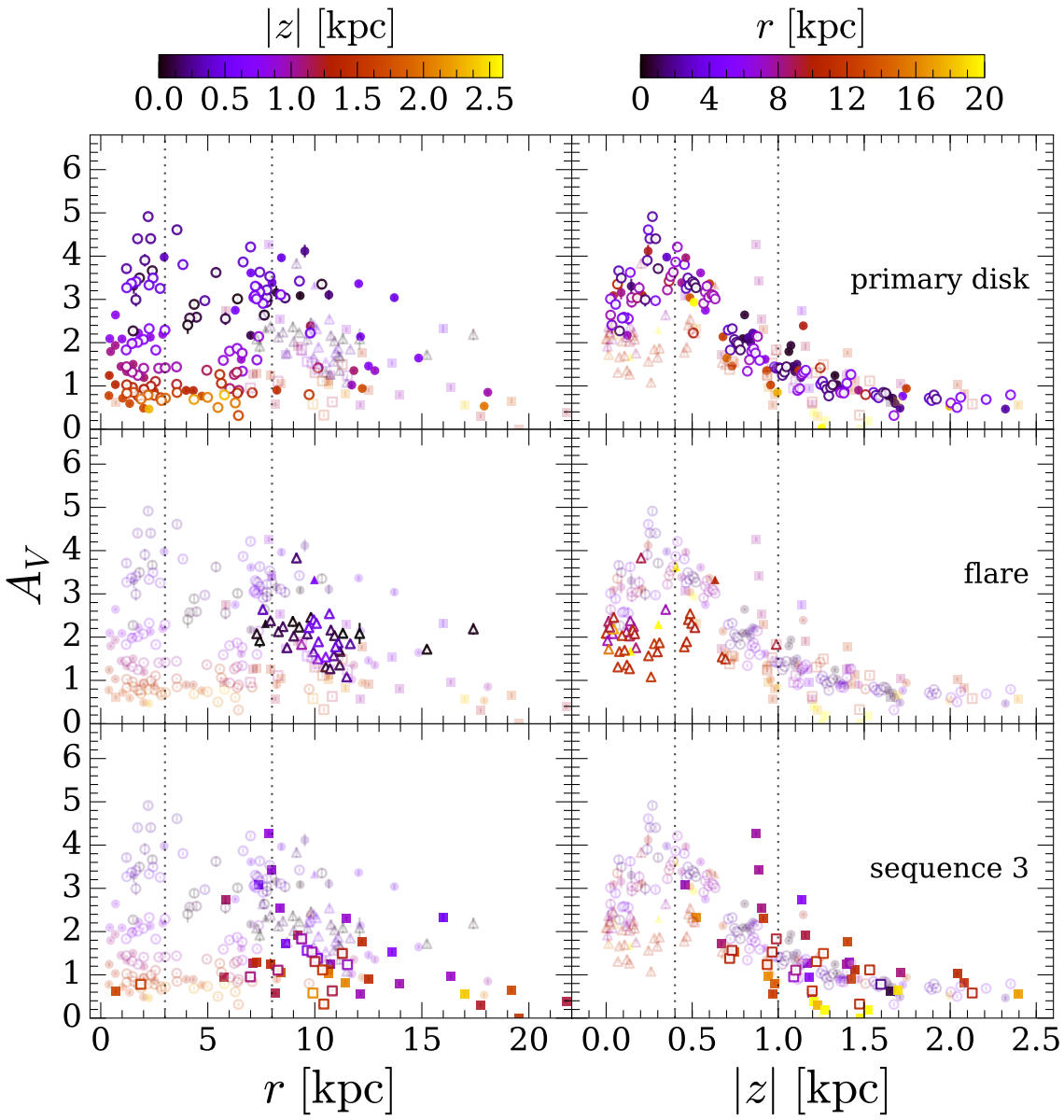

Figure 5.25 A_V as a function of true radius (*left*) and height (*right*), plotted in the same style as Figure 5.24

values (A_V) to achieve the same level of extinction which makes direct comparison of our data to the conclusions of Xilouris et al. (1999) or Schechtman-Rook et al. (2012) difficult.

The middle row of Figure 5.25 shows that flared extension of the primary disk has systematically lower extinction than the main disk. In a flared disk with a roughly constant total dust fraction an increase in scale height at large radii (i.e., the flare) would cause the dust surface density to decrease at these larger radii, which is consistent with the lower values of A_V seen in the data corresponding to the flare.

Sequence 3 does not stand out very much in the $A_V(r, z)$ planes. It shows extinction values that are generally consistent with the other morphological features that exist at smaller radii, albeit with more scatter (bottom right panel of Figure 5.25). This is a clue that sequence 3 might not be a separate entity from the primary disk, but rather an extension along a different axis of parameter space of the same populations seen in the disk.

5.8.2.3 Z_L

Finally, Figure 5.26 shows Z_L as a function of location in NGC 891 and highlights the discriminatory power of metallicity in identifying the three morphological features mentioned above. The primary disk shows slightly negative correlations between metallicity and radius. This view is consistent with measurements from the Milky Way (Bovy et al. 2012; Hayden et al. 2014) and with the conclusions of Chapter 4.

The metallicity trend with height, however, increases slightly up to about 0.6 kpc at which point it decreases with increasing height. This turn over height corresponds to the epoch where pristine gas began to infall onto the primary disk and lower the metallicity of more recently formed stars (as seen in Figure 5.21).

The middle row of Figure 5.26 shows strong evidence that the flare identified in

previous sections comes from the same underlying distribution as the primary disk. At all radii and heights in the $Z_L(r, z)$ volume the flare points are essentially indistinguishable from those of the primary disk. The flare exists in a different (r, z, A_V) location, but its ages and, importantly, metallicity are consistent with the same populations seen in the disk. Once again, this is consistent with the view that the primary disk is a superposition

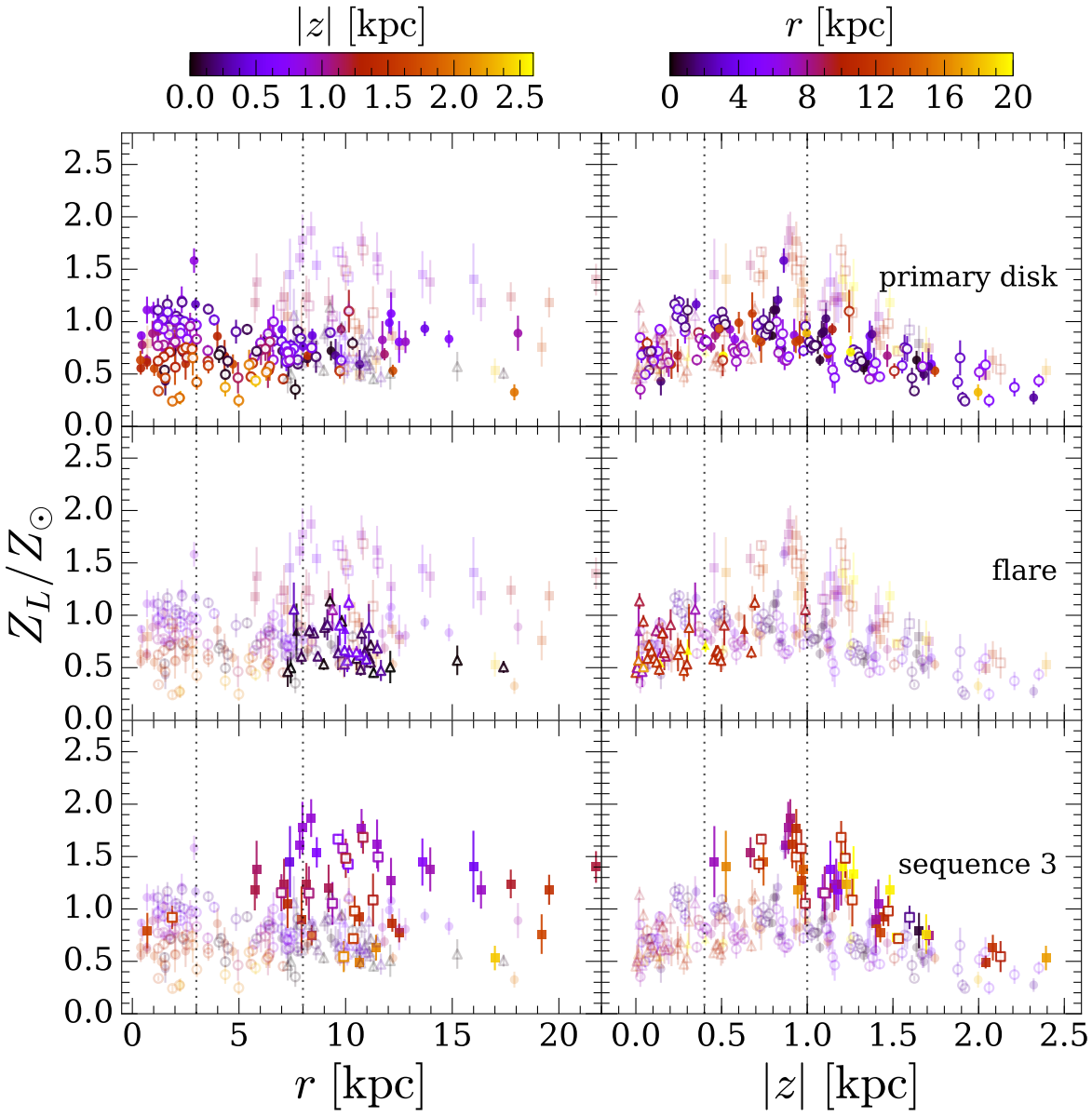

Figure 5.26 Z_L as a function of true radius (*left*) and height (*right*), plotted in the same style as Figure 5.24

of mono-age flared disks; the "flare" is simply the most recent epoch of star formation.

Sequence 3 is perhaps most visible as a high-metallicity sequence in the $Z_L(r, z)$ volume, as shown in the bottom row of Figure 5.26. At all radii and heights it occupies a locus that has larger values of Z_L than either the primary disk or the flare (which are the same in terms of metallicity). With this view it is possible that sequence 3 is in fact the portion of NGC 891's disk that formed during "peak metallicity" around 6 Gyr ago (see §5.8.1). In this context the results of Figure 5.24 take on new meaning; sequence 3 has ages mostly between 6 and 8 Gyr, which is exactly when NGC 891 was at its maximum level of enrichment. Thus sequence 3 is not a distinct population of stars, but instead a snapshot of the disk from the era just before extragalactic gas began to suppress metallicity in NGC 891.

5.8.3 Star Formation History

A primary benefit of full-spectrum SSP fitting is that it allows us to fit and measure the star formation history (SFH) for every aperture in our data set. As discussed in §5.7.2 the mean, light-weighted age (τ_L) is a convenient proxy for SFH, but requires an assumed SFH for the models used to fit our galaxy data. To avoid these assumptions we can examine the integral of the SFH multiplied by the flux of each SSP, which is identical to the light-weights found during SSP fitting (see §5.3.1 and Equation 5.3).

By examining trends in this pseudo-SFH space we are able to completely free our interpretation from the systematic uncertainties discussed in §5.7.2. In other words, the uncertainties in the results presented below only stem from degeneracies inherent in the SSP template library and fitting process.

Figure 5.27 shows these values in the same grid of radius and height used in Chapter 4 (although now the radius values are the true, cylindrical values a la §5.4). From

these data we can see the same general trend found in Chapter 4 and above: younger populations predominantly exist below 0.4 kpc. There are also small contributions from young populations above 0.4 kpc at the largest radii, which confirms the idea that NGC 891 built up from a superposition of flared disks with increasing "flare radii".

Above 0.4 kpc (and even below this for $r < 8$ kpc) the I2 populations contribute more

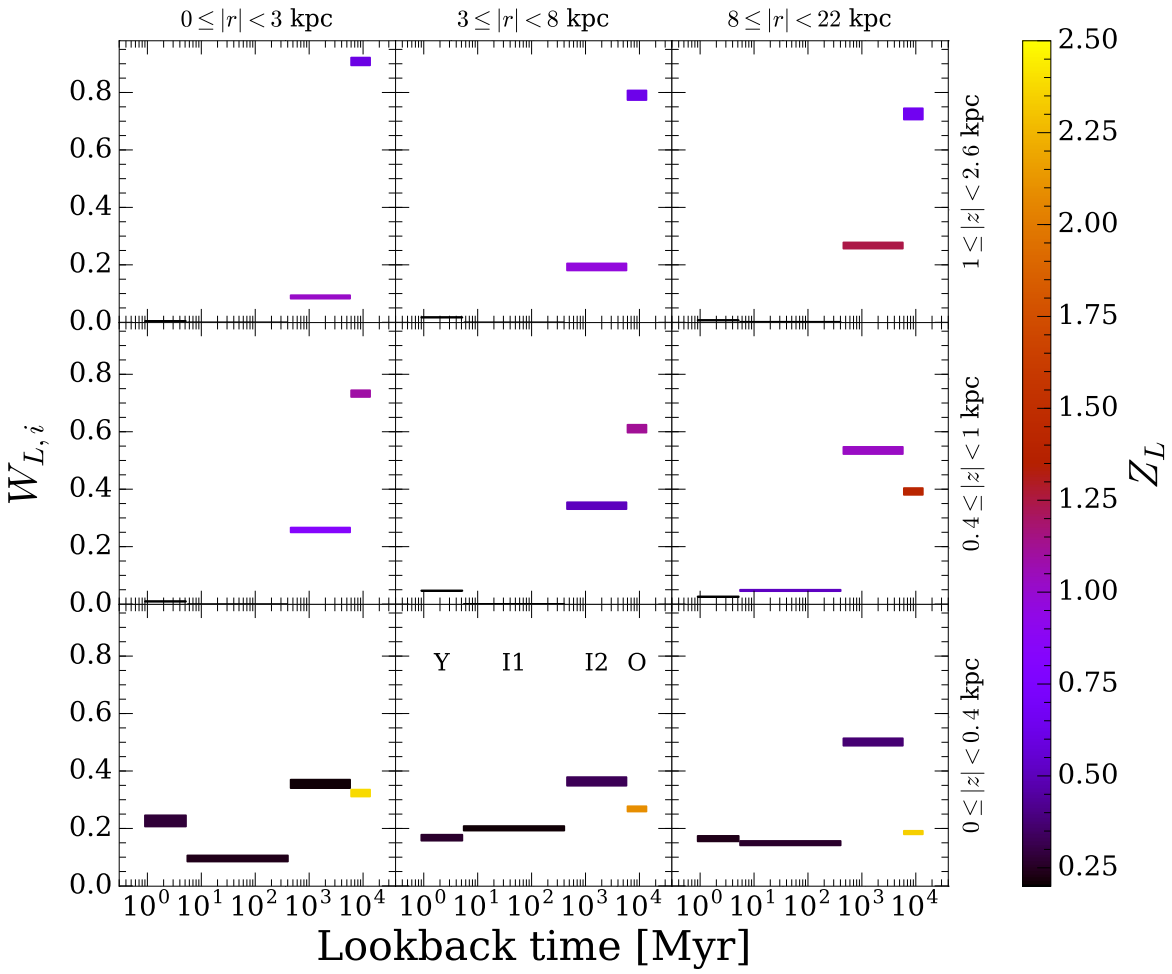

Figure 5.27 Fractional light-weight (Equation 5.4) for each DFK age bin as a function of radius and height. The radial and height bins shown are the same as used in Chapter 4 and highlight the different components of NGC 891 described in the text. The horizontal extent of each bar spans the range of ages covered by each SSP and the vertical width of each bar corresponds to the fitting uncertainty of each weight computed using the same method detailed in §5.7.1. Each weight is color coded by the average Z_L in the particular (r, z) bin.

to the total light at larger radii, with a corresponding decrease in the contribution from Old populations. This trend is broadly consistent with an inside-out view of star formation in NGC 891. Such a formation scenario (which we also see in Chapter 4) predicts a higher fraction of young and intermediate aged stars at large radii, exactly as seen in Figure 5.27.

Finally, the metallicity color-coding in Figure 5.27 is consistent with the enrichment history presented in §5.8.1. The youngest populations (which only contribute appreciable light at low heights) are metal poor because they are formed from pristine material that has recently fallen onto the disk of NGC 891 (see also Figure 5.21). At these low heights the most metal-rich population is the Old population, and indeed it is these populations that have the largest values of Z_L anywhere in NGC 891. This suggests that the Old populations at low heights correspond to the youngest limit of the Old DFK age bin, which is exactly the age of "peak metallicity" discovered in §5.8.1 ($\sim$6 Gyr).

We also see that the metallicity of the Old population decreases with height (at all radii) while the metallicity of the younger populations increases with height. Once again, this beautifully illustrates the enrichment history presented above; the Old population formed during the "closed-box" period in NGC 891's history, where older stars (i.e., stars at larger heights) formed from pristine gas. Star formation more recent than 6 Gyr (i.e., anything besides the Old population), however, occurred during a time when metal-poor gas from outside of NGC 891 caused *younger* stars (i.e., those at lower heights) to have lower values of metallicity.

5.9 Summary

We have used full-spectrum SSP fitting to measure trends in τ_L, Z_L, and A_V with both radius and height in NGC 891. To mitigate the impact of degeneracies between these quantities we downselect the full BC03 SSP template library in two ways: limiting the

range of metallicity values used, and reducing the age resolution of the template library. We limit the range of allowed metallicities to be $Z \geq 0.2\mathrm{Z}_{\odot}$ and show in §5.5.1.2 that SSPs with lower metallicity produce model galaxies that; a) are statistically worse than higher metallicities, in a χ^2 sense, and b) result in the astrophysically implausible situation of very old super-solar metallicity stars combined with very young super metal poor stars.

The age resolution of our SSP template libraries is reduced using the statistically motivated method of diffusion K-means (M15), which accounts for the fact that there is very little difference in spectral shape between old SSPs over a range of roughly 5 Gyr. We find that this limited basis set still accurately reproduces our observed galaxy spectra (§5.5.4).

While these steps do reduce the magnitude of degeneracies between τ_L, Z_L, and A_V these degeneracies are still the dominant sources of uncertainty in our fit parameters. However they are typically on the order of $\sim$10%, which still allows us to measure trends in these quantities with radius and height. We also find two distinct regimes of degeneracy between τ_L and Z_L; for intermediate and old populations these two quantities are negatively correlated (as expected from e.g., O'Connell (1976); Aaronson et al. (1978); Worthey et al. (1994); Gil de Paz & Madore (2002)) but for young populations τ_L and Z_L are positively correlated, indicating that older populations have higher metallicities. This correlation is caused by the interplay between all three of our fit parameters, as discussed in §5.7.1, underlining the importance of parameter covariance in understanding fit uncertainties.

While we use τ_L as a proxy for star formation history we caution that any single metric of age (including τ_L) requires assumptions about the underlying star formation history that will introduce systematic offsets into the results. We quantify the magnitude of this systematic uncertainty and find it to be, in a worst case scenario, $\sim$20%. It is important to note, however, that for studies of a single galaxy a worst-case scenario (which

assigns a completely random star formation history to each location in the galaxy) is a large overestimation. On time scales greater than one dynamical time we expect the the galaxy to be relatively well mixed which causes the average SFH to be relatively constant and thus the systematic uncertainties discussion in §5.7.2 will not apply. At large radii the dynamical timescale of NGC 891 is roughly 1 Gyr, which means the systematic uncertainties in the I2 and O DFK bins are greatly mitigated by mixing of stars within the galaxy.

The light weights shown in Figure 5.27 suggest an even more optimistic picture, in which the SFH is relatively constant across all of NGC 891. While the specific weights do change with r and z, the general *trends* for each DFK bin are the same at all radii and heights. For example, the strength of the I2 population increases with radius at all heights and the strength of the O population decreases with radius at all heights. In other words the qualitative similarity in the light weights (a proxy for the SFH) seen in Figure 5.27 indicates that the underlying star formation rate does not vary *in shape* by large amounts across large regions of NGC 891. Thus uncertainties that arise from assuming a star formation history (i.e., §5.7.2) only effect systematics on a galactic scale; within NGC 891 these systematics contribute negligibly to the total uncertainty.

Our 3-dimensional view of NGC 891 is enhanced by deprojecting the observed, projected radii to cylindrical radii based on kinematic measurements of stellar populations. Thus armed with fully 3D information about the location of our stellar populations we examine their distribution in $(r, |z|, \tau_L, Z_L, A_V)$ space and find:

1. Confirmation of the results from Chapter 4. Namely Young populations exist only below 0.4 kpc, age increases from 0.4 - 1 kpc, and saturates above 1 kpc.

2. The picture of inside-out galaxy formation seen in Chapter 4 is enhanced by the view that each generation of stars forms a flared disk, with later generations forming disks

with larger radii. This view is similar to the prediction of Martig et al. (2014); the galaxy disk is a superposition of flared disks that formed with increasing radii.

3. Two distinct epochs in the enrichment history of NGC 891. During the first few Gyr of its life NGC 891 existed in more of a closed-box state; from an initial seed of pristine gas each generation of stars formed from gas enriched by the generations before it at roughly a rate of 0.15 $Z_\odot$/Gyr. However, about 6 Gyr ago new, metal-poor gas from outside the galaxy started to fall onto the disk of NGC 891. This new gas lowered the metallicity of stars formed in the last 6 Gyr and the indication is that metallicity will continue to decrease in the future. This rate of decrease is about -0.18 $Z_\odot$/Gyr.

4. Three groupings of stellar populations in the $(r, |z|, \tau_L, Z_L, A_V)$ parameter space: a primary disk, a flared extension of the disk, and a metal-rich sequence at large radii and heights. These groupings are *not* distinct features in NGC 891. Instead they are the consequence of the formation and enrichment history present above. The primary disk is the main disk of the galaxy and is composed of multiple mono-age, flared disks that increase in radius with galactic age. The "flare" at large radii is corresponds to the most recent batch of star formation. The third sequence is the portion of the disk that formed during peak metallicity, $\sim$6 Gyr ago.

Despite the advances presented here there is ample opportunity for future studies to improve upon our work and methods. In particular, our treatment of systematic uncertainties is incomplete and we do not address potential sources of systematics in our calculation of either A_V or Z_L. Our fit values of A_V are dependent on the extinction model assumed (i.e., Charlot & Fall 2000), but beyond that we do not parametrize extinction with separate normalization parameters for populations younger and older than $\sim$10 Myr, as recommended by Charlot & Fall (2000). Furthermore we have not tested how our results

might change when using other common models (e.g., Calzetti et al. 1994).

Systematics in Z_L likely arise from our simplistic treatment of how populations with different metallicities mix together (i.e., we take a straight average of Z). We also note that the specifics of chemical evolution are often highly dependent on the SSP template library used and we have only used one model (BC03) in this work.

We also note that the use of diffusion k-means to down-select the SSP library of Bruzual & Charlot (2003) has not been rigorously tested for effects of metallicity (M15 only consider solar metallicity SSPs). Furthermore, when the DFK spectra are constructed from a weighted average of SSPs we assume a constant star formation across each DFK bin, which very likely introduces systematics in the DFK spectra and ultimately our derived parameters. Finally, the choice of 4 DFK bins was primarily motivated by M15's use of very low S/N data. It is possible that using only 4 DFK bins under-represents the full wealth of information contained in our relatively high S/N data. Specifically, the current I2 DFK bin spans a large range of stellar evolutionary time scales and could likely be split into finer bins, which would allow one to leverage SSP models that offer sophisticated treatment of the late phases of stellar evolution (e.g., MA11)

We would like to thank Greg Mosby for making his diffusion k-means work available to us and answering our numerous question. Discussions with Marsha Wolf inspired many of the techniques used above. This research was directly supported by the U.S. National Science Foundation (NSF) AST-1517006.

References

Aaronson, M., Cohen, J. G., Mould, J., & Malkan, M. 1978, ApJ, 223, 824

Barden, S. C., Armandroff, T., Muller, G., et al. 1994, in Proc. SPIE, Vol. 2198, Instrumentation in Astronomy VIII, ed. D. L. Crawford & E. R. Craine, 87–97

Bershady, M., Barden, S., Blanche, P.-A., et al. 2008, in Proc. SPIE, Vol. 7014, Ground-based and Airborne Instrumentation for Astronomy II, 70140H

Binney, J., & Tremaine, S. 1987, Galactic dynamics

Bovy, J., Rix, H.-W., Liu, C., et al. 2012, ApJ, 753, 148

Bruzual, G., & Charlot, S. 2003, MNRAS, 344, 1000

Buzzoni, A. 1989, ApJS, 71, 817

Calzetti, D., Kinney, A. L., & Storchi-Bergmann, T. 1994, ApJ, 429, 582

Charlot, S., & Fall, S. M. 2000, ApJ, 539, 718

Cid Fernandes, R., Mateus, A., Sodré, L., Stasińska, G., & Gomes, J. M. 2005, MNRAS, 358, 363

Falcón-Barroso, J., Sánchez-Blázquez, P., Vazdekis, A., et al. 2011, A&A, 532, A95

Gil de Paz, A., & Madore, B. F. 2002, AJ, 123, 1864

Groves, B., Brinchmann, J., & Walcher, C. J. 2011, ArXiv e-prints, arXiv:1109.2597

Hayden, M. R., Holtzman, J. A., Bovy, J., et al. 2014, AJ, 147, 116

Hayden, M. R., Bovy, J., Holtzman, J. A., et al. 2015, ApJ, 808, 132

Kamphuis, P., Holwerda, B. W., Allen, R. J., Peletier, R. F., & van der Kruit, P. C. 2007, A&A, 471, L1

Knezek, P. M., Bershady, M. A., Willmarth, D., et al. 2010, in Proc. SPIE, Vol. 7735, Ground-based and Airborne Instrumentation for Astronomy III, 77357D

Kregel, M., & van der Kruit, P. C. 2005, MNRAS, 358, 481

Maraston, C. 2005, MNRAS, 362, 799

Maraston, C., & Strömbäck, G. 2011, MNRAS, 418, 2785

Markwardt, C. B. 2009, in Astronomical Society of the Pacific Conference Series, Vol. 411, Astronomical Data Analysis Software and Systems XVIII, ed. D. A. Bohlender, D. Durand, & P. Dowler, 251

Martig, M., Minchev, I., & Flynn, C. 2014, MNRAS, 442, 2474

Minchev, I., Famaey, B., Quillen, A. C., et al. 2012, A&A, 548, A127

Morè, J. 1978, in Lecture Notes in Mathematics, Vol. 630, Numerical Analysis, ed. G. Watson (Springer Berlin Heidelberg), 105–116

Mosby, G., Tremonti, C. A., Hooper, E. J., et al. 2015, MNRAS, 447, 1638

O'Connell, R. W. 1976, ApJ, 206, 370

Ocvirk, P., Pichon, C., Lançon, A., & Thiébaut, E. 2006, MNRAS, 365, 74

Oosterloo, T., Fraternali, F., & Sancisi, R. 2007, AJ, 134, 1019

Osterbrock, D. E. 1989, Astrophysics of gaseous nebulae and active galactic nuclei

Renzini, A., & Voli, M. 1981, A&A, 94, 175

Sánchez, S. F., Pérez, E., Sánchez-Blázquez, P., et al. 2016, Rev. Mexicana Astron. Astrofis., 52, 21

Schechtman-Rook, A., & Bershady, M. A. 2013, ApJ, 773, 45

—. 2014, ApJ, 795, 136

Schechtman-Rook, A., Bershady, M. A., & Wood, K. 2012, ApJ, 746, 70

Swaters, R. A., Sancisi, R., & van der Hulst, J. M. 1997, ApJ, 491, 140

Tojeiro, R., Heavens, A. F., Jimenez, R., & Panter, B. 2007, MNRAS, 381, 1252

Tremonti, C. A., Heckman, T. M., Kauffmann, G., et al. 2004, ApJ, 613, 898

Vazdekis, A., Sánchez-Blázquez, P., Falcón-Barroso, J., et al. 2010, MNRAS, 404, 1639

Vera-Ciro, C., D'Onghia, E., Navarro, J., & Abadi, M. 2014, ApJ, 794, 173

Wall, J. V., & Jenkins, C. R. 2003, Practical statistics for astronomers, Cambridge Observing Handbooks for Research Astronomers (Leiden: Cambridge Univ. Press)

Wilkinson, D. M., Maraston, C., Thomas, D., et al. 2015, MNRAS, 449, 328

Wood, C. M., Bershady, M. A., Eigenbrot, A. D., et al. 2012, in Proc. SPIE, Vol. 8446, Ground-based and Airborne Instrumentation for Astronomy IV, 84462W

Worthey, G., Faber, S. M., Gonzalez, J. J., & Burstein, D. 1994, ApJS, 94, 687

Xilouris, E. M., Kylafis, N. D., & Papamastorakis, J. 1999, in ESA Special Publication, Vol. 427, The Universe as Seen by ISO, ed. P. Cox & M. Kessler, 993

Chapter 6

Conclusion

Take it from me, there's nothing like a job well done. Except the quiet enveloping darkness at the bottom of a bottle of Jim Beam after a job done any way at all.

Hunter S. Thompson

NGC 891 offers a unique opportunity to perform stellar population analysis and compare the results to our detailed understanding of the distribution of stars in the Milky Way. In this way it occupies an important bridge between the Milky Way and surveys that offer a large sample size, but a smaller spatial resolution. The closeness and nearly totally edge-on nature of NGC 891 also allows for unambiguous determination of finely sampled vertical gradients in stellar population, which makes it a perfect test-case for theories concerning the origin of disk stratification seen in the Milky Way.

To take advantage of the information available in NGC 891 I helped design and construct HexPak/∇Pak, a pair of fiber IFUs for the WIYN telescope. In Chapter 3 I detail the design and fabrication of these instruments. The important features of HexPak/∇Pak are:

1. HexPak has a standard hexagon shape made mostly of fibers with an on-sky diameter of $2\farcs8$. It also has a high resolution core of 18 $0\farcs94$ fibers that make it ideally suited for studies of face-on galaxies or any bright object where high spatial resolution is desired.

2. ∇Pak is roughly rectangular in shape and has five different fiber sizes ranging from $1\farcs87$ - $5\farcs62$. The regions of different size are arranged in a gradient that is optimized to measure roughly exponentially decreasing surface brightness at roughly 10 Mpc; a similar S/N per fiber can be achieved in a single exposure. ∇Pak is ideally suited for observations of objects with a large dynamic range in brightness where spectral resolution can be sacrificed for observing efficiency.

3. At the spectrograph input the slits of HexPak and ∇Pak share a foot and focal plane. This allows observers to swap between the two IFUs with zero modifications to the Bench Spectrograph.

4. The head fixtures of HexPak and ∇Pak, while physically separate, share a common focal plane in the WIYN IAS. This further eases the transition between the two IFUs; in practice an observer can switch between HexPak and ∇Pak during an observing run in roughly 10 minutes.

During the conception and construction of HexPak/∇Pak I researched ways to improve the optical performance of fiber-based instruments, mainly through the mitigation of FRD. In Chapter 2 I detail my experiments, which are broadly applicable to all fiber optic systems, and find:

1. FRD is dominated by light entering the fiber at smaller angles (i.e., closer to the axis of light propagation).

2. A secondary component of FRD is attributable to the end-polish of fiber surfaces. FRD decreases with polishing down to finer grit sizes, but not significantly below grit-sizes of 5 μm.

3. Total throughput also depends on end-polish, with a wavelength dependence that indicates the increase in throughput is simply a reduction in surface-scattering. The most significant gains occur for polishing that proceeds down to 5 μm grit, although for most astronomical applications at low light-levels polishing finer than this level is measurably advantageous.

4. The amount of FRD does **not** depend on wavelength.

Chapter 4 details the first set of results from a program that measures stellar populations in NGC 891 with ∇Pak. In this chapter I detail challenges in data acquisition/reduction caused by the unique nature of ∇Pak, but also present methods that largely eliminate any negative impact on the resulting data.

I also describe the observing program that is designed to cover NGC 891 out to large heights and radii. The design of ∇Pak is ideally suited to a program of this nature and allows for efficient collection of high-quality data.

I then use the well known and characterized LICK spectral index system to identify separate stellar populations in NGC 891 and find:

1. There is a clear transition with height above NGC 891's disk midplane between young and old populations at 0.4 kpc (roughly the broad-band exponential scale-height). This is consistent with models of heating of the stellar disk in the solar cylinder.

2. For $|z| > 0.4$ kpc there is a trend towards younger populations at larger projected radii, consistent with an inside-out formation history in NGC 891. The trend also suggests a flaring of the young stellar disk at radii beyond 8 kpc.

3. Beyond 8 kpc in radius and between 0.4 kpc $\leq |z| < 1$ kpc there is a a clear asymmetry in age between the two sides of the galaxy. The approaching side, where there is more Hα emission, appears younger. This can be explained by spiral structure in NGC 891; on the approaching side of the galaxy we see the leading edge of a spiral arm that has very recent/ongoing star formation. Our sight-lines to the receding side of the galaxy, however, look onto the trailing edge of another arm that is obscured by high concentrations of dust.

Finally, in Chapter 5 I employ the power of full-spectrum fitting to get a detailed and quantitative view of stellar populations in NGC 891. To confidently interpret the results of this method I need to understand the interplay between all of the fit parameters, namely the well known degeneracies between age, metallicity, and extinction. Furthermore, assumptions about the star formation history in NGC 891 can introduce large systematics in our results.

The degeneracies between age, metallicity, and extinction are exacerbated by SSP template libraries that constitute a large set of individual SSPs with little thought to the astrophysical similarities that exist over a wide range of age and metallicity values. In other words, most SSP template libraries have many SSPs that, while assigned different age or metallicity values, have very similar spectra. To mitigate these degeneracies I employ diffusion k-means to create a new SSP basis set that greatly reduces the number of SSP templates while still preserving important astrophysical features. With this new SSP basis set I estimate the uncertainty in fit parameters caused by degeneracies between the model spectra to be roughly 10% for age and extinction and ∼20% for metallicity.

I also quantify the systematic age uncertainty that arises from assuming a star formation history during the interpretation of the fitting results. In the worst case these uncertainties are ∼20%, but I argue that the worst case (totally random star formation on small physical scales) is unrealistically pessimistic for our data. NGC 891 is a coherent galaxy, and over long timescales (∼1 Gyr) the star formation history should be relatively the same across the entire galaxy. Thus the systematic uncertainties do not apply when comparing detailed structure within NGC 891; they are only important when comparing NGC 891 to other galaxies that may have different star formation histories.

With an understanding of uncertainties in my results I identify details in the structure and formation history of NGC 891. Namely,

1. The picture of inside-out galaxy formation seen in Chapter 4 is enhanced by the view that each generation of stars forms a flared disk, with later generations forming disks with larger radii.

2. Two distinct epochs in the enrichment history of NGC 891. During the first few Gyr of its life NGC 891 existed in a somewhat closed-box state; from an initial seed

of pristine gas each generation of stars formed from gas enriched by the generations before it. However, about 6 Gyr ago new, metal-poor gas from outside the galaxy started to fall onto the disk of NGC 891. This new gas lowered the metallicity of stars formed in the last 6 Gyr and the indication is that metallicity will continue to decrease in the future.

3. Three groupings of stellar populations in the $(r, |z|, \tau_L, Z_L, A_V)$ parameter space: a primary disk, a flared extension of the disk, and a metal-rich sequence at large radii and heights. These groupings are a consequence of the formation and enrichment history presented in the previous point. The primary disk is the main disk of the galaxy and is composed of multiple mono-age, flared disks that increase in radius with galactic age. The "flare" at large radii is corresponds to the most recent batch of star formation. The third sequence is the portion of the disk that formed during peak metallicity $\sim$6 Gyr ago.

This work constitutes one of the first detailed, resolved studies of stellar populations in a nearby galaxy, and as such lays the groundwork for future studies. In particular, the methods outlined here could easily be applied to other nearby, edge-on galaxies. This thesis provides a robust set of tools, from instruments to data reduction and analysis methods, that will allow future astronomers to rapidly expand our view of stellar populations and disk formation.

The work presented in this thesis was directly supported by the U.S. National Science Foundation (NSF) grants ATI-0804576, AST-1009471, and AST-1517006.

Appendix A

∇Pak Performance Testing

Before installation all of the ∇Pak fibers were tested for throughput performance using the Wisconsin Test Stand (Bershady et al. 2004; Crause et al. 2008; Eigenbrot et al. 2012). This stand is a double-differential imaging comparator. It consists of an input stage that reimages an illuminated aperture through a controllable aperture at an intermediate pupil, and an output stage that consists of a collimator that places the output pupil from the reimager or fiber output onto a CCD detector. The experiment consists of measuring the input beam differentially between a straight-through configuration and the collimated fiber output. During the entire process the stability of the filtered input beam is monitored with a photo diode.

Tests were performed in the Johnson V band with an input beam set to match the WIYN input beam of $f/6.3$ without the 17% central obstruction of the telescope. The total throughput ($T_{\rm tot}$) is defined as all of the fiber-output light captured by the CCD (roughly corresponding to $f/2.2$, compared with the fiber numerical aperture of $f/2.3$) divided by the all of the light from the input beam captured by the same CCD. This gives a good indication of the total transmission through the fiber, but ignores the effects of FRD on the delivered throughput on the Bench Spectrograph due to the optical stops therein. FRD

describes the tendency for fibers to increase the entropy in an optical beam; light injected into a fiber at a particular f-ratio emerges at a smaller (faster) f-ratio (Angel et al. 1977).

The primary impact of FRD is from light loss from obstructions inside the Bench Spectrograph as detailed in Bershady et al. (2004) and Bershady et al. (2005). With the upgrade (Bershady et al. 2008) the low-order gratings and camera objective are sufficiently near the pupil and are of sufficient size that the limiting stop is from the collimator. The camera objective does begin to vignette for off-axis fields point in wavelength and pseudo-slit position, but for operational purposes we consider the on-axis field point for defining throughput losses due to FRD. The collimator accepts light up to $f/4$ with only minimal obstruction, and is completely unobstructed at $f/4.4$, while the optical design (in terms of aberrations) is optimized for $f/5$.

To characterize the impact of FRD on the the delivered throughput we define the quantity

$$T_4 = \frac{F_{\rm out}(f < f/4)}{F_{\rm in}(f < f/6.3)}, \tag{A.1}$$

where $F_{\rm in}$ and $F_{\rm out}$ represent flux from the the input and fiber output beams, respectively. T_4 is essentially a throughput measurement that accounts for the impact of FRD, and should be representative of how the fibers will perform as part of the WIYN/Bench system. We compute comparable quantities for output f-ratios of $f/4.5$ and $f/5$. The throughput in each of these apertures, as well as the total throughput are included in Table D1 as $T_{\rm tot}$, T_4, $T_{4.4}$, T_5.

Figure A1 contains throughput measurements for all of the active ∇Pak fibers. Throughput losses caused by FRD are spatially coherent and are larger on the top and left (North and East) side of the IFU. This is likely due to surface scattering at the IFU face (Eigenbrot et al. 2012) caused by an uneven polish. Figure A2 shows evidence of this variable polish in the two sky fiber groups; the SW sky group show significantly worse

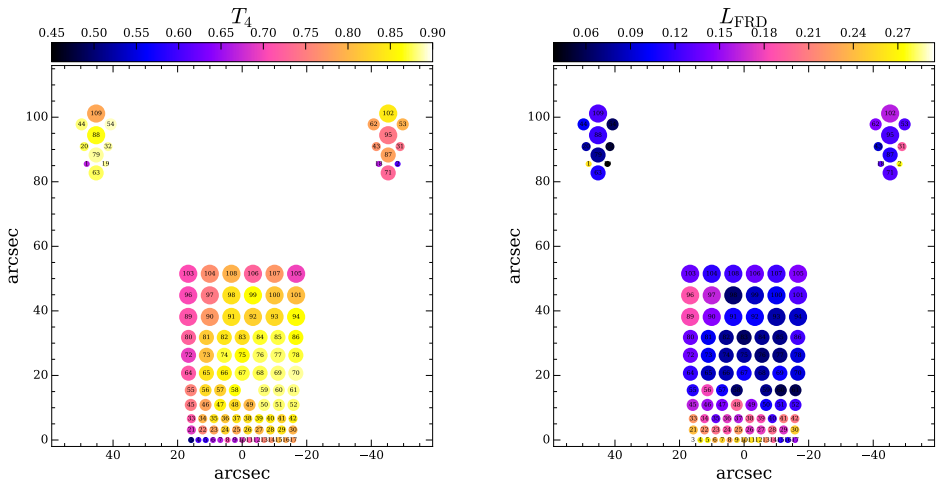

Figure A1 Maps of laboratory measurements of the ∇Pak IFU performance. Throughput ($T_{\rm FRD}$, Equation A.1) is shown in the left-hand panel, while throughput losses ($L_{\rm FRD}$, Equation A.2), is shown in the right-hand panel. Performance values are given in the color scale at the top of each panel.

polish than the NE group and has a correspondingly lower throughput. It is important to note that the FRD losses do *not* appear to be caused by edge fibers pushing against the aluminum structure, as evidenced by the relatively high throughput seen on the left side of the IFU. This is consistent with previous studies (Bershady et al. 2004) that suspected removal from an IFU molding fixture to be the primary cause of stress-induced FRD. Variations in polish quality appears to be caused by detritus from the aluminum fixture.

As a check on the lab measurements of T_4 we also compare total fiber transmission recorded during the observing program described in §4.3. For these measurements a stitched dome flat (see §4.4.1.2 was used as a good approximation of a uniform illumination at the fiber input. The total light transmitted by each fiber is computed by adding together all wavelength channels for each fiber after the data were spectrally extracted. Figure A3 shows are comparison between lab (T_4) and on-telescope performance. "Counts" in this figure are from dome-flats combined as described in §4.4.1.2), and are the sum across all wavelengths of the extracted fiber traces. As expected from Figure A1 the highest throughputs are

found in the middle of the array, with a gradual drop off in performance towards the end of the slit. The right panel of Figure A3 shows a tight correlation between our lab measurements and the on-sky performance. This shows that stresses during installation and the performance of the Bench Spectrograph only cause a ±5% rms modulation in the throughput compared to what was measured in the lab.

We also measure the magnitude of FRD experienced by each fiber. Because FRD represents a scattering of input light to larger output angles a comparison between throughput at two different output f-ratios gives an approximation of the severity of FRD in each fiber. We define

$$L_{\mathrm{FRD}} = 1 - \frac{T_5}{T_4}, \tag{A.2}$$

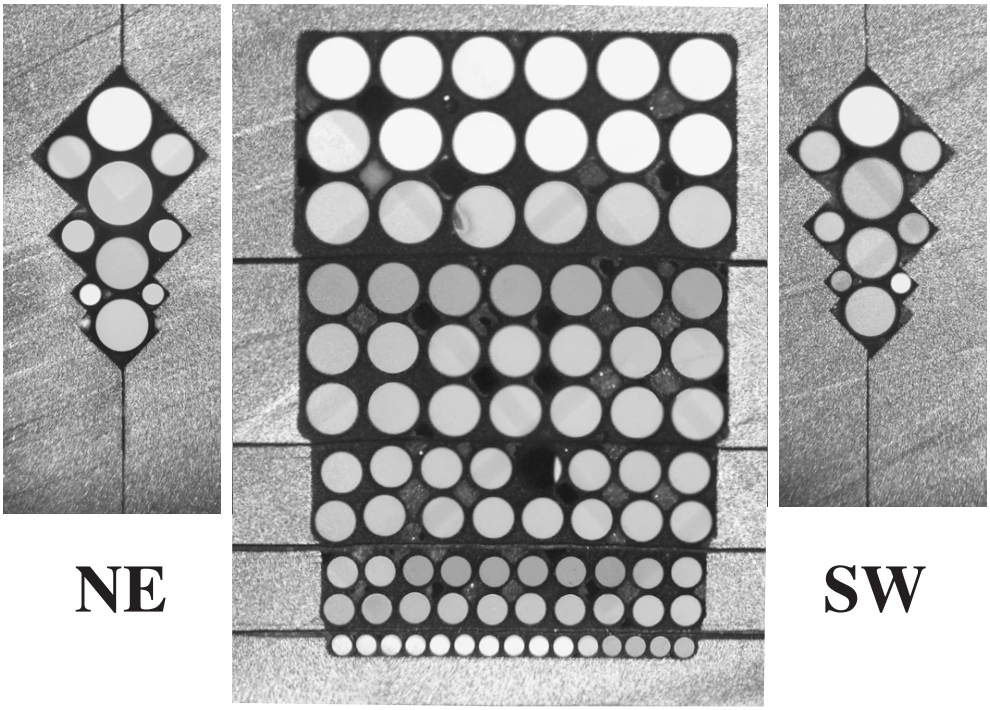

Figure A2 Detail of ∇Pak fiber face after polishing. The 25.4 μm (0.″24) shims between each block fiber-size group are visible in the central array. The hole in the 5th fiber row from the bottom is a fiber that was broken during polishing. The two sky-fiber groups, not shown to scale, have locations marked in Figure 4.2. The 200 μm (1.″87) sky fibers are not visible in this image due to imperfect illumination conditions at the slit end when this picture was taken.

which quantifies the amount of light scattered to smaller f-ratios (larger angles) than $f/5$ as a measure of the severity of FRD experienced by each fiber.

Table D1 contains measurements and Figure A1 shows a map of $L_{\rm FRD}$ for each ∇Pak fiber. Figure A4 compares this quantity with T_4. We find that fibers with low T_4 also tend to have high FRD losses ($L_{\rm FRD}$), which indicates that FRD is a significant source of throughput loss in the ∇Pak and Bench Spectrograph system. However this is relatively more pronounced for smaller fiber sizes, as seen in the bifurcation in the right-hand panel of Figure A4. Smaller fibers tend to suffer from larger amounts of FRD, which may have been caused in ∇Pak due to handling-induced stresses; these fibers were more likely to bend and tangle during construction. The corollary is that lower throughput in larger fibers isn't always the result of increased FRD.

A complete set of measurements showing FRD losses as a function of output f-ratio

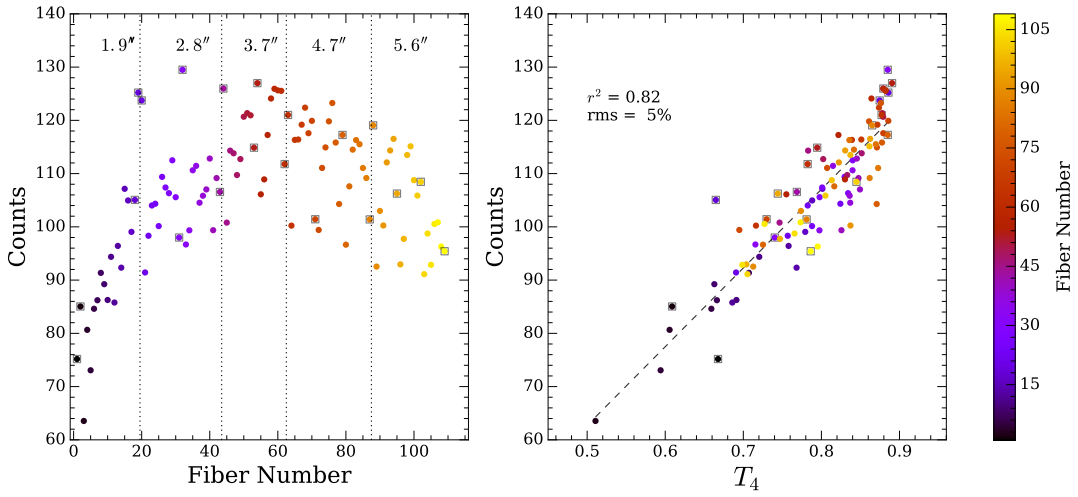

Figure A3 Left: Relative fiber transmission measured *in-situ* on the WIYN Bench Spectrograph. Vertical lines demark transition between different fiber sizes, as labeled. Right: Comparison between the *in-situ* performance and T_4, as measured in the lab after construction. The dashed line represents a linear regression to the data with given correlation coefficient and scatter. Points are color-coded by fiber number (slit position), and sky fibers are marked with black squares.

for each fiber can be found in the supplemental materials online at `www.astro.wisc.edu/~eigenbrot/PAK`.

References

Angel, J. R. P., Adams, M. T., Boroson, T. A., & Moore, R. L. 1977, ApJ, 218, 776

Bershady, M., Barden, S., Blanche, P.-A., et al. 2008, in Proc. SPIE, Vol. 7014, Ground-based and Airborne Instrumentation for Astronomy II, 70140H

Bershady, M. A., Andersen, D. R., Harker, J., Ramsey, L. W., & Verheijen, M. A. W. 2004, PASP, 116, 565

Bershady, M. A., Andersen, D. R., Verheijen, M. A. W., et al. 2005, ApJS, 156, 311

Crause, L., Bershady, M., & Buckley, D. 2008, in Proc. SPIE, Vol. 7014, Ground-based and Airborne Instrumentation for Astronomy II, 70146C

Eigenbrot, A. D., Bershady, M. A., & Wood, C. M. 2012, in Proc. SPIE, Vol. 8446, Ground-based and Airborne Instrumentation for Astronomy IV, 84465W

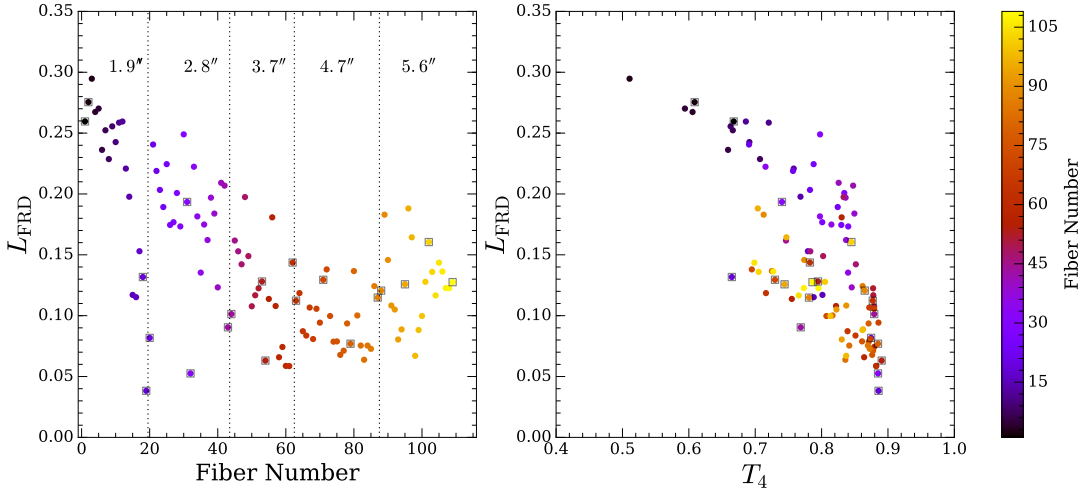

Figure A4 Performance metrics for ∇Pak. $L_{\rm FRD}$ (Equation A.2) as a function of slit location (right) and T_4 (transmission through an $f/4$ aperture). Points are color-coded by fiber number (slit position), and sky fibers are marked with black squares.

Appendix B

Grating Optimization

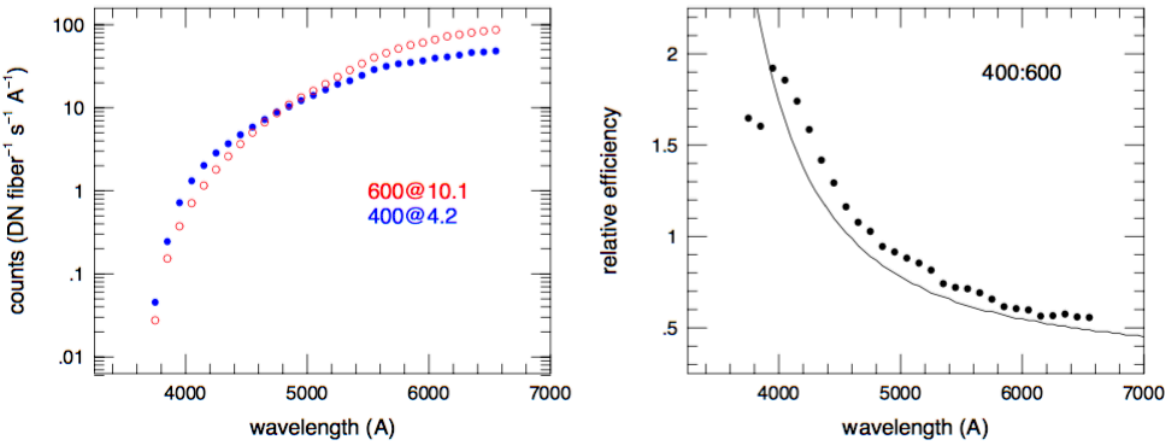

Figure B1 Efficiency comparison between 400@4.2 and 600@10.1 gratings based on dome-flat exposures using the same fibers, spectrograph camera-collimator angle, and lamp temperature and intensity. Details are provided in text. The top panel shows counts for each grating, while the bottom panel shows their ratio and the prediction (line) based on the blaze functions for idealized gratings.

We chose the 400@4.2 grating out of the library of gratings available on the WIYN Bench Spectrograph because it allows us to capture simultaneously spectra from Ca H&K to Hα while still maintaining relatively high efficiency at the blue end of the spectrum. To optimize our grating choice we compared the 400@4.2 grating to the 600@10.1 grating. The latter provides a narrower wavelength range but at higher resolution, and, most importantly,

the covered range is marginally sufficient to meet our scientific objectives. The 600@10.1 grating is often the "go to" grating for low-resolution programs centered around 5500 Å, particularly because it is the newest reflection grating and purportedly has the highest diffraction efficiency.

For testing during engineering time we compared the 400@4.2 grating set to 21.8° and the 600@10.1 grating set to 24.33°, both for a fixed camera-collimator angle of 30° (this is the nominal configuration for low-order gratings).[1] These grating incidence angles gave wavelength ranges of 3600 Å$< \lambda <$ 7867 Å and 3794 Å$< \lambda <$ 6655 Å, respectively. The blue Hydra cable (300 μm core fibers) was used to observe dome flats illuminated with identical lamp intensity (and temperature) settings. The dome lamps are known to be stable to better than 10% over a broad wavelength range. Although we were concerned that temperature instability might be a factor at the blue end of our spectral range, our results are consistent with a highly stable illumination over our full spectral range.

The fiber flux in the dome-flat spectra was measured on the raw two-dimensional images before extraction. This was done in order to exclude defocus effects from the fractional flux extracted along the trace in wavelength, and between the two grating configurations for which the detailed focus changes with wavelength are different. Identical fibers and extraction regions were measured in both configurations. The regions account for a small lateral shift along the slit due to a slight difference in the alignment angle between gratings orthogonal to the dispersion axis (this variance is just a mechanical tolerance in the grating mount). Taking advantage of the numerous broken Hydra fibers, we identified well-separated transmitting fibers that had ample separation for extracting "on" and "off" signal regions (or apertures) at all wavelengths. These apertures were 10-11 pixels wide,

[1] At these wavelengths the effective camera focal-length for this all-refractive compound optic is 277.1 mm not the nominal 285 mm quoted in reference manuals.

and were adjacent on the CCD. The resulting counts were differenced and then scaled for the corresponding exposure time and linear dispersion.

Figure B1 shows the result of this experiment. It is evident from the top panel that the 400@4.2 has greater efficiency compared to the 600@10.1 grating blueward of 4700Å. Since the spectrograph configurations were identical except for the gratings, under the assumption that the dome-flat illumination was constant, the ratio of the two curves is equivalent to the ratio of the grating blaze functions. As the bottom panel shows, this is very close to what would be expected from simply computing the theoretical blaze functions for idealized versions of these two gratings. If anything, the 400@4.2 appears to have 10% higher efficiency across all wavelengths than the idealized case.

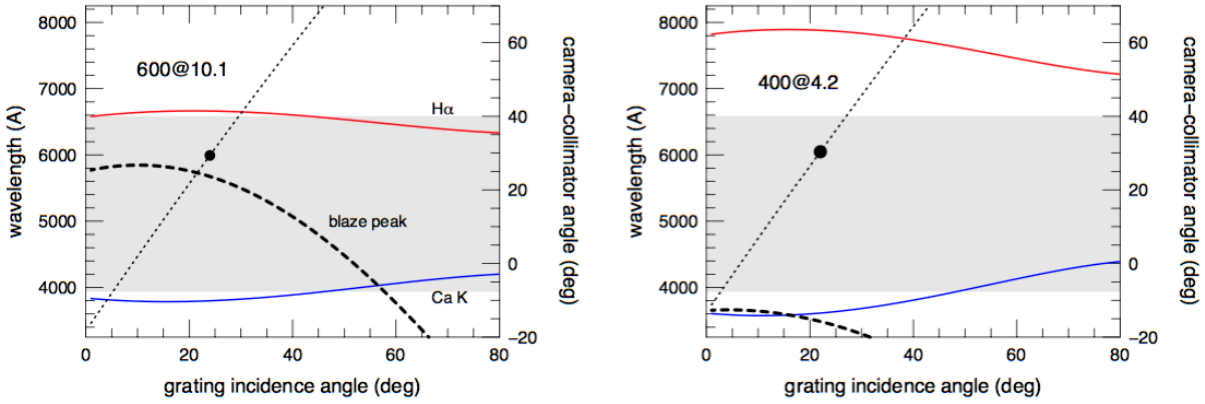

Figure B2 Wavelength blaze and coverage for the Bench Spectrograph and the 400 l/mm grating blazed at 4.2 deg (top panel) and the 600 l/mm grating blazed at 10.1 deg (bottom panel) as a function of grating incidence angle and camera-collimator angle with the central wavelength held constant. Upper and lower wavelength limits and the blaze peak are marked with the red, blue, and thick-dashed lines, respectively. The minimal desired wavelength range between the most blue-shifted Ca-K line and most redshifted Hα lines (3937-6480Å; 300-800 km s^{-1}) is shown as the grey shaded region The camera-collimator angle is marked with the thin dotted line, and corresponds to the right-hand vertical scale; the nominal value of 30 deg is marked with a dot.

Since we are working with a bench-mounted spectrograph that in principle is highly configurable, we also considered if additional spectrograph layout modification might

further optimize performance. In particular, by altering both the grating (incidence) angle and the camera-collimator angle, it is possible to change the blaze wavelength while keeping the wavelength coverage on the detector roughly constant. The concept is illustrated in B2. The effect of increasing the camera-collimator angle for low-blaze gratings shifts the blaze wavelength to the blue. This is not desirable for the 400@4.2 grating which already has a very blue blaze wavelength at the nominal camera-collimator angle of 30°, but this is potentially relevant for the 600@10.1 grating. Unfortunately, significant shifts of the blaze wavelength require very large camera-collimator angles that are both geometrically impractical on the existing optical bench and lead to an unacceptable decrease in spectral coverage. The exercise does conclude that a larger camera-collimator angle of roughly 40° would be preferable for the 600@10.1 grating, but its performance in the far blue would still fall short of the 400@4.2 grating.

Appendix C

τ Model of Star Formation

Our galaxy models are constructed from the simple stellar population (SSP) library of Bruzual & Charlot (2003) with an initial mass function from Chabrier (2003). These SSPs rely on the STELIB stellar library (Le Borgne et al. 2003). The goal of any regularized galaxy model is to assign individual SSP weights based on a modeled star formation history (SFH). Our SSP basis set is normalized to 1 $M_\odot$ and thus the SSP weights will be the total mass of stars in a give population. We let the mass of a model galaxy at lookback time, t, be

$$M(t) = \int_{t_{\rm form}}^{t} \psi(t')dt', \tag{C.1}$$

where $\psi(t)$ is the amount of mass in stars produced at loockback time t. Equation C.1 is generally true for any star formation history. For a τ model we use

$$\psi(t) = \psi_0 e^{-t/\tau_{SF}}. \tag{C.2}$$

Taking the above, our galaxy flux, $G(\lambda)$, is constructed by weighting the spectra of individual SSPs, $f_i(\lambda)$, by the mass formed during their formation age:

$$G(\lambda) = \sum_{i}^{N} f_i(\lambda) M_i, \tag{C.3}$$

where

$$M_i = \int_{t_2}^{t_1} \psi(t')dt'. \tag{C.4}$$

In practice our SSP ages are discreet and we need to choose a range of time $(t_2 - t_1)$ over which SSP contributes to star formation. We set these limits of integration such that an equal amount of mass is formed in each half of a logarithmically-spaced SSP age bin. In other words, given an SSP of age t_i, the limits of integration are

$$t_{2,i} = \frac{\log(t_{i+1}) - \log(t_i)}{2} = t_{1,i+1}. \tag{C.5}$$

We set the end points $t_{1,0} = 0$ and $t_{2,N} = t_{\rm form}$.

In the situation where $t_{\rm form}$ is less than the oldest SSP in our library the SSP mass bins will be unevenly spaced in age. To fix this problem we assign each SSP an age that is weighted by the amount of mass formed during the time assigned to its bin. In other words, the weighted age of an SSP with age t_i is the midpoint of mass bin M_i. This weighted age, $t_{i,w}$, is defined such that

$$\int_{t_1}^{t_{i,w}} \psi(t')dt' = \int_{t_{i,w}}^{t_2} \psi(t')dt'. \tag{C.6}$$

If we assume the τ model described in Eq. C.2 the weighted age is

$$t_{i,w} = \tau_{SF} \log\left(0.5\left(e^{t_1/\tau_{SF}} + e^{t_2/\tau_{SF}}\right)\right). \tag{C.7}$$

Finally, we adopt the extinction law of Charlot & Fall (2000) with a value of $A_V = 1.63$, which defines a reddening term that is constant across all SSPs,

$$R(\lambda) = e^{-\frac{A_V}{1.086}\left(\lambda/5500\ \mathring{\rm A}\right)^{-0.7}}, \tag{C.8}$$

so our final galaxy is given by

$$G(\lambda) = R(\lambda)\sum_i^N f_i(\lambda)M_i. \tag{C.9}$$

As a proxy for star formation history we define the mean light-weighted age as

$$\tau_L = \frac{\sum_k [S(\lambda_K)R(\lambda_k)\sum_i f_i(\lambda_k)M_i t_i]}{\sum_k [S(\lambda_k)R(\lambda_k)\sum_i f_i(\lambda_k)M_i]} \tag{C.10}$$

where $S(\lambda_j)$ defines the bandpass over which the age is computed. We set $S(\lambda_j)$ to be flat over 5450 Å $\leq \lambda \leq$ 5550 Å and zero everywhere else.

References

Bruzual, G., & Charlot, S. 2003, MNRAS, 344, 1000

Chabrier, G. 2003, PASP, 115, 763

Charlot, S., & Fall, S. M. 2000, ApJ, 539, 718

Le Borgne, J.-F., Bruzual, G., Pelló, R., et al. 2003, A&A, 402, 433

Appendix D

Full ∇Pak Locations and Lab Data

Table D1 : ∇Pak Fiber Locations and LabData

Fiber number	$\Delta\alpha^{a}$ (")	$\Delta\delta^{a}$ (")	diameter (")	T_{tot}	$T_4{}^{b}$	$T_{4.4}$	T_5
1	64.86	34.02	1.87	0.84	0.67	0.58	0.49
2	-31.45	34.02	1.87	0.78	0.61	0.53	0.44
3	32.52	-51.50	1.87	0.75	0.51	0.44	0.36
4	30.26	-51.50	1.87	0.75	0.61	0.53	0.44
5	28.00	-51.50	1.87	0.76	0.59	0.52	0.43
6	25.75	-51.50	1.87	0.77	0.66	0.59	0.50
7	23.49	-51.50	1.87	0.79	0.67	0.59	0.50
8	21.23	-51.50	1.87	0.79	0.71	0.64	0.55
9	18.97	-51.50	1.87	0.77	0.66	0.59	0.49
10	16.71	-51.50	1.87	0.78	0.69	0.62	0.52
11	14.45	-51.50	1.87	0.80	0.72	0.64	0.53
12	12.19	-51.50	1.87	0.77	0.69	0.61	0.51
13	9.93	-51.50	1.87	0.82	0.76	0.69	0.59
14	7.67	-51.50	1.87	0.80	0.77	0.71	0.62
15	5.41	-51.50	1.87	0.81	0.80	0.78	0.71
16	3.15	-51.50	1.87	0.80	0.79	0.76	0.70
17	0.90	-51.50	1.87	0.80	0.78	0.74	0.66
18	-25.61	34.02	1.87	0.73	0.66	0.64	0.58
19	59.03	34.02	1.87	0.86	0.89	0.88	0.85
20	65.63	39.40	2.81	0.85	0.87	0.86	0.80
21	32.44	-48.38	2.81	0.76	0.69	0.62	0.52

Table D1 – Continued

Fiber number	$\Delta\alpha$[a] (")	$\Delta\delta$[a] (")	diameter (")	$T_{\rm tot}$	T_4[b]	$T_{4.4}$	T_5
22	28.95	-48.38	2.81	0.81	0.76	0.69	0.59
23	25.45	-48.38	2.81	0.82	0.78	0.72	0.62
24	21.95	-48.38	2.81	0.84	0.82	0.77	0.67
25	18.46	-48.38	2.81	0.83	0.79	0.72	0.61
26	14.96	-48.38	2.81	0.83	0.83	0.79	0.68
27	11.46	-48.38	2.81	0.83	0.80	0.75	0.66
28	7.97	-48.38	2.81	0.85	0.83	0.78	0.67
29	4.47	-48.38	2.81	0.85	0.84	0.79	0.69
30	0.97	-48.38	2.81	0.85	0.80	0.72	0.60
31	-32.21	39.40	2.81	0.80	0.74	0.69	0.60
32	58.27	39.40	2.81	0.86	0.89	0.88	0.84
33	32.44	-44.88	2.81	0.78	0.72	0.65	0.56
34	28.95	-44.88	2.81	0.82	0.80	0.74	0.65
35	25.45	-44.88	2.81	0.84	0.84	0.80	0.73
36	21.95	-44.88	2.81	0.83	0.81	0.76	0.67
37	18.46	-44.88	2.81	0.84	0.84	0.79	0.70
38	14.96	-44.88	2.81	0.85	0.84	0.78	0.67
39	11.46	-44.88	2.81	0.85	0.85	0.80	0.69
40	7.97	-44.88	2.81	0.84	0.85	0.82	0.74
41	4.47	-44.88	2.81	0.85	0.83	0.76	0.65
42	0.97	-44.88	2.81	0.86	0.85	0.79	0.67
43	-24.85	39.40	2.81	0.79	0.77	0.75	0.70
44	66.44	46.28	3.75	0.85	0.88	0.86	0.79
45	32.62	-40.63	3.75	0.77	0.75	0.71	0.63
46	28.08	-40.63	3.75	0.81	0.78	0.74	0.66
47	23.53	-40.63	3.75	0.85	0.85	0.82	0.73
48	18.98	-40.63	3.75	0.85	0.83	0.77	0.67
49	14.44	-40.63	3.75	0.81	0.80	0.77	0.68
50	9.89	-40.63	3.75	0.85	0.88	0.86	0.78
51	5.34	-40.63	3.75	0.85	0.88	0.85	0.78
52	0.80	-40.63	3.75	0.85	0.88	0.85	0.77
53	-33.02	46.28	3.75	0.81	0.79	0.76	0.69
54	57.46	46.28	3.75	0.86	0.89	0.88	0.83
55	32.62	-36.08	3.75	0.77	0.76	0.73	0.67
56	28.08	-36.08	3.75	0.83	0.83	0.78	0.68
57	23.53	-36.08	3.75	0.83	0.82	0.79	0.73
58	18.98	-36.08	3.75	0.84	0.86	0.85	0.81

Table D1 – Continued

Fiber number	$\Delta\alpha^{a}$ (")	$\Delta\delta^{a}$ (")	diameter (")	$T_{\rm tot}$	$T_4{}^{b}$	$T_{4.4}$	T_5
59	9.89	-36.08	3.75	0.85	0.88	0.87	0.81
60	5.34	-36.08	3.75	0.85	0.88	0.87	0.83
61	0.80	-36.08	3.75	0.85	0.88	0.87	0.83
62	-24.04	46.28	3.75	0.79	0.78	0.75	0.67
63	61.95	31.25	4.69	0.87	0.88	0.85	0.78
64	33.33	-30.80	4.69	0.76	0.72	0.69	0.63
65	27.79	-30.80	4.69	0.83	0.84	0.82	0.77
66	22.25	-30.80	4.69	0.84	0.85	0.83	0.78
67	16.71	-30.80	4.69	0.86	0.87	0.85	0.78
68	11.17	-30.80	4.69	0.86	0.87	0.85	0.80
69	5.63	-30.80	4.69	0.86	0.88	0.85	0.79
70	0.09	-30.80	4.69	0.87	0.89	0.86	0.80
71	-28.53	31.25	4.69	0.78	0.73	0.70	0.64
72	33.33	-25.26	4.69	0.75	0.69	0.66	0.60
73	27.79	-25.26	4.69	0.81	0.81	0.79	0.73
74	22.25	-25.26	4.69	0.85	0.87	0.86	0.80
75	16.71	-25.26	4.69	0.85	0.86	0.84	0.79
76	11.17	-25.26	4.69	0.86	0.88	0.86	0.82
77	5.63	-25.26	4.69	0.86	0.88	0.86	0.82
78	0.09	-25.26	4.69	0.86	0.87	0.85	0.79
79	61.95	36.79	4.69	0.86	0.89	0.87	0.82
80	33.33	-19.72	4.69	0.76	0.73	0.69	0.63
81	27.79	-19.72	4.69	0.82	0.82	0.79	0.73
82	22.25	-19.72	4.69	0.84	0.84	0.82	0.78
83	16.71	-19.72	4.69	0.83	0.84	0.82	0.78
84	11.17	-19.72	4.69	0.85	0.87	0.85	0.80
85	5.63	-19.72	4.69	0.86	0.87	0.86	0.81
86	0.09	-19.72	4.69	0.85	0.86	0.83	0.75
87	-28.53	36.79	4.69	0.81	0.78	0.75	0.69
88	61.95	42.92	5.62	0.87	0.86	0.83	0.76
89	33.42	-13.37	5.62	0.77	0.71	0.67	0.58
90	26.73	-13.37	5.62	0.80	0.77	0.74	0.66
91	20.05	-13.37	5.62	0.84	0.84	0.81	0.75
92	13.37	-13.37	5.62	0.83	0.82	0.79	0.74
93	6.68	-13.37	5.62	0.83	0.83	0.81	0.76
94	0.00	-13.37	5.62	0.86	0.86	0.84	0.79
95	-28.53	42.92	5.62	0.79	0.74	0.71	0.65

Table D1 – Continued

Fiber number	$\Delta\alpha$[a] (")	$\Delta\delta$[a] (")	diameter (")	$T_{\rm tot}$	T_4[b]	$T_{4.4}$	T_5
96	33.42	-6.68	5.62	0.76	0.70	0.66	0.57
97	26.73	-6.68	5.62	0.79	0.75	0.71	0.62
98	20.05	-6.68	5.62	0.84	0.84	0.82	0.78
99	13.37	-6.68	5.62	0.85	0.86	0.84	0.79
100	6.68	-6.68	5.62	0.82	0.81	0.79	0.73
101	0.00	-6.68	5.62	0.82	0.81	0.77	0.70
102	61.95	49.64	5.62	0.86	0.84	0.80	0.71
103	33.42	0.00	5.62	0.76	0.71	0.67	0.61
104	26.73	0.00	5.62	0.79	0.77	0.74	0.68
105	0.00	0.00	5.62	0.75	0.70	0.66	0.60
106	13.37	0.00	5.62	0.78	0.73	0.69	0.63
107	6.68	0.00	5.62	0.80	0.77	0.74	0.68
108	20.05	0.00	5.62	0.81	0.80	0.76	0.70
109	-28.53	49.64	5.62	0.81	0.79	0.75	0.69

[a]Distance from fiber 105.

[b]An estimate of on-bench performance. See Equation A.1.

Appendix E

Full NGC 891 Aperture Table

Table E1 : Data Apertures

Pointing Number	Aperture Number	Constituent Fibers	S/N	r (kpc)	z (kpc)	Notes
1	1	3, 4, 5, 6, 7, 8	32.22	4.44	-0.12	g
1	2	9, 10, 11, 12, 13, 14, 15, 16, 17	26.72	5.26	-0.09	b
1	3	21	34.50	4.16	0.02	g
1	4	22, 23, 24, 25, 26, 27	31.41	4.76	0.04	g
1	5	28, 29, 30	14.92	5.52	0.08	u
1	6	33, 34, 35, 36, 37, 38, 39	30.70	4.66	0.21	g
1	7	40, 41, 42	15.89	5.51	0.24	g
1	8	45, 46, 47, 48	30.85	4.47	0.41	g
1	9	49, 50, 51	47.30	5.24	0.44	g
1	10	52	32.77	5.68	0.46	g
1	11	55, 56, 57, 58, 59	43.21	4.61	0.63	g
1	12	60	40.73	5.45	0.67	g
1	13	61	36.45	5.67	0.68	g
1	14	64, 65	48.93	4.22	0.87	g
1	15	66	43.20	4.62	0.89	g
1	16	67	37.63	4.89	0.90	g
1	17	68	39.57	5.16	0.91	g
1	18	69	35.57	5.43	0.92	g
1	19	70	32.84	5.69	0.94	g
1	20	72	36.81	4.07	1.13	g
1	21	73	48.06	4.34	1.15	g

Table E1 – Continued

Pointing Number	Aperture Number	Constituent Fibers	S/N	r (kpc)	z (kpc)	Notes
1	22	74	40.16	4.61	1.16	g
1	23	75	39.75	4.88	1.17	g
1	24	76	30.52	5.15	1.18	g
1	25	77, 78	28.73	5.55	1.20	g
1	26	80	41.76	4.06	1.40	g
1	27	81	40.79	4.33	1.41	g
1	28	82	34.46	4.60	1.43	g
1	29	83, 84	31.28	5.00	1.44	g
1	30	85, 86	20.18	5.54	1.47	g
1	31	89	38.69	4.04	1.71	g
1	32	90	36.28	4.37	1.72	g
1	33	91, 92	33.65	4.85	1.75	g
1	34	93, 94	22.94	5.50	1.77	u
1	35	96, 97	33.98	4.19	2.04	g
1	36	98, 99, 100, 101	27.62	5.16	2.08	g
1	37	103, 104, 105, 106, 107, 108	29.73	4.82	2.39	g
2	1	3, 4, 5, 6, 7, 8, 9, 10, 11, 12, 13, 14, 15, 16, 1	17.53	1.27	-0.17	u
2	2	21, 22, 23, 24, 25, 26, 27, 28, 29, 30	16.86	1.26	-0.02	u
2	3	33, 34, 35, 36, 37, 38, 39, 40, 41, 42	19.23	1.26	0.15	g
2	4	45, 46, 47, 48, 49, 50, 51, 52	32.92	1.25	0.35	g
2	5	55, 56, 57	32.22	0.69	0.55	g
2	6	58, 59	57.10	1.35	0.58	g
2	7	60, 61	35.03	1.90	0.60	g
2	8	64	107.51	0.42	0.79	g
2	9	65	88.67	0.69	0.81	b
2	10	66	98.01	0.96	0.82	g
2	11	67	77.19	1.23	0.83	g
2	12	68	83.06	1.49	0.84	g
2	13	69	71.39	1.76	0.85	g
2	14	70	72.72	2.03	0.86	g
2	15	72	60.19	0.41	1.06	g
2	16	73	70.89	0.68	1.07	g
2	17	74	65.99	0.95	1.09	g
2	18	75	73.64	1.21	1.10	g
2	19	76	67.44	1.48	1.11	g
2	20	77	62.17	1.75	1.12	g
2	21	78	52.38	2.02	1.13	g

Table E1 – Continued

Pointing Number	Aperture Number	Constituent Fibers	S/N	r (kpc)	z (kpc)	Notes
2	22	80	47.71	0.40	1.33	g
2	23	81	55.21	0.67	1.34	g
2	24	82	48.97	0.93	1.35	g
2	25	83	43.76	1.20	1.37	g
2	26	84	46.76	1.47	1.38	g
2	27	85	42.71	1.74	1.39	g
2	28	86	32.75	2.01	1.40	g
2	29	89	39.53	0.38	1.64	g
2	30	90	45.09	0.70	1.65	g
2	31	91	36.42	1.03	1.67	g
2	32	92	40.23	1.35	1.68	g
2	33	93	39.72	1.67	1.69	g
2	34	94	37.80	2.00	1.71	g
2	35	96	39.19	0.37	1.96	u
2	36	97, 98, 99, 100	31.68	1.17	2.00	g
2	37	101	24.07	1.99	2.03	u
2	38	103, 104, 105, 106, 107, 108	24.12	1.16	2.32	g
3	1	3, 4, 5, 6	36.04	-6.31	-0.17	g
3	2	7, 8	32.67	-5.98	-0.16	g
3	3	9, 10	30.33	-5.76	-0.15	g
3	4	11, 12, 13, 14	31.49	-5.43	-0.14	g
3	5	15, 16, 17	33.61	-5.05	-0.12	g
3	6	21, 22	34.32	-6.39	-0.03	g
3	7	23	34.74	-6.14	-0.01	g
3	8	24	44.63	-5.97	-0.01	g
3	9	25	36.09	-5.80	0.00	g
3	10	26	32.20	-5.63	0.01	g
3	11	27	38.62	-5.46	0.01	g
3	12	28, 29	43.28	-5.20	0.03	g
3	13	30	30.34	-4.95	0.04	g
3	14	33	30.20	-6.48	0.14	g
3	15	34	39.74	-6.31	0.15	g
3	16	35	39.95	-6.14	0.16	g
3	17	36, 37	39.93	-5.89	0.17	g
3	18	38, 39	41.54	-5.55	0.18	g
3	19	40	32.28	-5.30	0.19	g
3	20	41, 42	39.19	-5.04	0.20	g

Table E1 – Continued

Pointing Number	Aperture Number	Constituent Fibers	S/N	r (kpc)	z (kpc)	Notes
3	21	45	44.82	-6.50	0.35	g
3	22	46	34.45	-6.28	0.36	g
3	23	47	41.38	-6.06	0.37	g
3	24	48	51.50	-5.84	0.38	g
3	25	49, 50	52.58	-5.51	0.39	g
3	26	51	39.31	-5.18	0.40	g
3	27	52	37.72	-4.96	0.41	g
3	28	55	42.04	-6.51	0.57	g
3	29	56	42.89	-6.29	0.58	g
3	30	57	30.80	-6.07	0.59	g
3	31	58	37.67	-5.85	0.60	g
3	32	59	43.27	-5.41	0.62	g
3	33	60	51.86	-5.19	0.62	g
3	34	61	46.64	-4.97	0.63	g
3	35	64	56.48	-6.55	0.82	g
3	36	65	53.78	-6.28	0.83	g
3	37	66	52.05	-6.02	0.85	g
3	38	67	52.88	-5.75	0.86	g
3	39	68	48.27	-5.48	0.87	g
3	40	69	52.53	-5.21	0.88	g
3	41	70	56.41	-4.94	0.89	g
3	42	72	30.21	-6.57	1.09	g
3	43	73	30.40	-6.30	1.10	g
3	44	74	37.28	-6.03	1.11	g
3	45	75	41.55	-5.76	1.12	g
3	46	76	39.80	-5.49	1.14	g
3	47	77	38.54	-5.22	1.15	g
3	48	78	36.99	-4.95	1.16	g
3	49	80, 81	41.41	-6.44	1.36	g
3	50	82	31.02	-6.04	1.38	g
3	51	83, 84	45.44	-5.64	1.40	g
3	52	85, 86	42.57	-5.10	1.42	g
3	53	89, 90	34.96	-6.43	1.67	g
3	54	91, 94	41.67	-5.46	1.72	u
3	55	96, 97, 98	33.53	-6.28	2.00	g
3	56	99, 100	33.02	-5.47	2.04	b
3	57	101	26.35	-4.99	2.06	g

Table E1 – Continued

Pointing Number	Aperture Number	Constituent Fibers	S/N	r (kpc)	z (kpc)	Notes
3	58	103, 104, 105, 106, 107	32.75	-5.78	2.35	g
3	59	108	14.44	-5.97	2.34	u
4	1	3, 4, 5	30.85	-2.61	-0.29	g
4	2	6, 7, 8, 9	32.09	-2.22	-0.27	u
4	3	10, 11, 12	34.13	-1.84	-0.25	g
4	4	13, 14, 15	35.80	-1.51	-0.24	g
4	5	16, 17	27.74	-1.24	-0.23	g
4	6	21	36.79	-2.72	-0.14	g
4	7	22, 23	35.14	-2.47	-0.13	g
4	8	24, 25	31.81	-2.13	-0.12	u
4	9	26	30.67	-1.87	-0.10	g
4	10	27, 28	39.45	-1.62	-0.09	g
4	11	29, 30	34.55	-1.28	-0.08	g
4	12	33, 34	31.57	-2.64	0.03	g
4	13	35	32.21	-2.39	0.04	b
4	14	36, 37	35.23	-2.13	0.05	g
4	15	38	31.75	-1.88	0.07	g
4	16	39	35.41	-1.71	0.07	g
4	17	40, 41, 42	32.94	-1.37	0.09	g
4	18	45, 46, 47	36.13	-2.53	0.25	g
4	19	48, 49	36.43	-1.97	0.27	g
4	20	50, 51	30.63	-1.53	0.29	g
4	21	52	25.82	-1.20	0.30	g
4	22	55	47.43	-2.75	0.46	g
4	23	56	45.70	-2.53	0.47	g
4	24	57	48.04	-2.31	0.47	g
4	25	58	56.30	-2.09	0.48	g
4	26	59	61.84	-1.65	0.50	g
4	27	60	52.08	-1.43	0.51	g
4	28	61	46.29	-1.21	0.52	g
4	29	64	66.70	-2.80	0.71	g
4	30	65	52.32	-2.53	0.72	g
4	31	66	68.79	-2.26	0.73	g
4	32	67	64.74	-1.99	0.75	g
4	33	68	65.98	-1.73	0.76	g
4	34	69	67.64	-1.46	0.77	g
4	35	70	60.54	-1.19	0.78	g

Table E1 – Continued

Pointing Number	Aperture Number	Constituent Fibers	S/N	r (kpc)	z (kpc)	Notes
4	36	72	63.39	-2.81	0.98	g
4	37	73	61.84	-2.54	0.99	g
4	38	74	67.13	-2.28	1.00	g
4	39	75	61.83	-2.01	1.01	g
4	40	76	63.70	-1.74	1.02	g
4	41	77	74.63	-1.47	1.04	g
4	42	78	73.40	-1.20	1.05	g
4	43	80	54.02	-2.82	1.25	g
4	44	81	54.83	-2.56	1.26	g
4	45	82	55.22	-2.29	1.27	g
4	46	83	59.53	-2.02	1.28	g
4	47	84	59.67	-1.75	1.29	g
4	48	85	58.79	-1.48	1.30	g
4	49	86	63.44	-1.21	1.32	g
4	50	89	45.26	-2.84	1.55	g
4	51	90	48.15	-2.52	1.57	g
4	52	91	46.64	-2.19	1.58	g
4	53	92	54.27	-1.87	1.60	g
4	54	93	62.88	-1.54	1.61	g
4	55	94	63.54	-1.22	1.62	b
4	56	96	35.99	-2.86	1.88	g
4	57	97	38.71	-2.53	1.89	g
4	58	98	42.94	-2.21	1.91	g
4	59	99	50.66	-1.88	1.92	g
4	60	103, 104	37.05	-2.71	2.21	g
5	1	3, 4, 5, 6, 7, 8, 9	28.84	8.18	-0.05	u
5	2	21, 22, 23	34.53	8.02	0.09	u
5	3	24, 25, 26, 27	32.17	8.61	0.12	u
5	4	28, 29, 30	29.14	9.21	0.14	g
5	5	33, 34, 35, 36, 37	31.51	8.18	0.27	u
5	6	38, 39, 40, 41, 42	31.36	9.03	0.30	g
5	7	45, 46	33.97	7.94	0.46	g
5	8	47, 48, 49	35.40	8.49	0.49	g
5	9	50, 51	35.38	9.04	0.51	g
5	10	52	26.61	9.37	0.52	g
5	11	55, 56	31.87	7.93	0.68	u
5	12	57, 58	38.87	8.37	0.70	g

Table E1 – Continued

Pointing Number	Aperture Number	Constituent Fibers	S/N	r (kpc)	z (kpc)	Notes
5	13	59, 60	38.64	9.03	0.73	b
5	14	61	29.54	9.36	0.75	g
5	15	64	32.18	7.77	0.93	g
5	16	65	33.43	8.04	0.94	g
5	17	66	32.61	8.31	0.96	g
5	18	67	34.51	8.58	0.97	g
5	19	68	32.32	8.85	0.98	b
5	20	69, 70	39.66	9.25	1.00	g
5	21	72, 73	37.69	7.89	1.21	g
5	22	74, 75	34.54	8.43	1.23	g
5	23	76, 77	31.02	8.97	1.25	g
5	24	78	20.86	9.37	1.27	g
5	25	80, 81, 82	32.69	8.02	1.48	g
5	26	83, 84, 85, 86	31.04	8.96	1.52	g
5	27	89, 90, 91, 93, 94	29.55	8.51	1.81	u
5	28	96, 97, 98, 99, 100, 101	21.37	8.53	2.13	u
5	29	103, 104, 105, 106, 107, 108	14.11	8.51	2.46	u
6	1	3, 4, 5, 6, 7	31.32	-10.36	-0.07	g
6	2	8, 9, 10, 11, 12	32.56	-9.82	-0.04	g
6	3	13, 14, 15, 16, 17	31.27	-9.27	-0.02	g
6	4	21, 22	33.65	-10.50	0.08	g
6	5	23, 24	30.22	-10.16	0.09	g
6	6	25, 26	32.27	-9.82	0.11	g
6	7	27, 28	32.60	-9.49	0.12	g
6	8	29, 30	33.97	-9.15	0.14	g
6	9	33, 34	30.92	-10.51	0.25	g
6	10	35, 36	30.27	-10.17	0.26	g
6	11	37, 38, 39	34.88	-9.75	0.28	g
6	12	40, 41	30.60	-9.32	0.30	g
6	13	42	24.60	-9.07	0.31	g
6	14	45, 46	38.81	-10.50	0.45	g
6	15	47	30.95	-10.17	0.47	g
6	16	48	30.21	-9.95	0.48	g
6	17	49	33.36	-9.73	0.49	g
6	18	50	31.23	-9.51	0.50	g
6	19	51	34.04	-9.29	0.51	g
6	20	52	32.74	-9.07	0.52	g

Table E1 – Continued

Pointing Number	Aperture Number	Constituent Fibers	S/N	r (kpc)	z (kpc)	Notes
6	21	55, 56	40.23	-10.51	0.67	g
6	22	57, 58	42.90	-10.07	0.69	g
6	23	59	32.33	-9.52	0.72	g
6	24	60, 61	41.65	-9.19	0.73	g
6	25	64, 66	38.74	-10.40	0.94	g
6	26	67, 68	38.71	-9.73	0.96	g
6	27	69, 70	39.44	-9.19	0.99	g
6	28	72, 73	33.74	-10.54	1.20	g
6	29	74, 75	31.00	-10.01	1.22	g
6	30	76, 77	31.28	-9.47	1.25	g
6	31	78	24.56	-9.07	1.26	g
6	32	80, 81, 82	32.51	-10.42	1.47	g
6	33	83, 84, 85	35.24	-9.62	1.51	g
6	34	86	22.69	-9.08	1.53	g
6	35	89, 90, 91, 92, 93	33.08	-10.06	1.80	u
6	36	94	17.97	-9.09	1.84	u
6	37	96, 97, 98, 99, 100, 101	25.52	-9.91	2.13	g
6	38	103, 104, 105, 107, 108	13.73	-9.96	2.45	u

[g]Good

[b]Bad - Wavelength solution appears to be wrong by more than $\sim$100 km s^{-1}

[u]Ugly - Spectrum appears to be overly noisy despite acceptable signal/noise

Appendix F

Full Index Measurement Table

Table F1 : NGC 891 Index Measurements

Pointing Number	Aperture Number	$r_{\rm proj}$ (kpc)	z (kpc)	D_n4000	$H\delta_A$ (Å)	Mgb (Å)	$\langle$Fe$\rangle$ (Å)	[MgFe] (Å)
1	1	4.44	-0.12	1.64 ± 0.04	5.91 ± 0.85	1.99 ± 0.47	0.76 ± 0.37	1.36 ± 0.32
1	2	5.26	-0.09	1.20 ± 0.02	4.20 ± 0.78	1.43 ± 0.56	0.95 ± 0.46	1.35 ± 0.35
1	3	4.16	0.02	1.37 ± 0.03	2.63 ± 1.01	2.27 ± 0.56	1.54 ± 0.40	1.91 ± 0.34
1	4	4.76	0.04	1.29 ± 0.02	4.64 ± 0.62	2.09 ± 0.49	1.07 ± 0.40	1.51 ± 0.33
1	5	5.52	0.07	1.11 ± 0.05	7.10 ± 1.77	2.49 ± 0.95	-0.16 ± 0.92	nan ± nan
1	6	4.67	0.21	1.29 ± 0.02	5.19 ± 0.71	1.73 ± 0.52	0.81 ± 0.41	1.03 ± 0.39
1	7	5.51	0.24	1.32 ± 0.05	5.38 ± 1.59	1.66 ± 0.94	0.67 ± 0.91	0.86 ± 0.85
1	8	4.47	0.41	1.17 ± 0.02	6.28 ± 0.64	1.52 ± 0.49	1.46 ± 0.39	1.65 ± 0.32
1	9	5.24	0.44	1.51 ± 0.03	1.90 ± 0.85	1.89 ± 0.39	1.40 ± 0.28	1.77 ± 0.23
1	10	5.68	0.46	1.63 ± 0.05	2.02 ± 1.25	1.89 ± 0.54	1.60 ± 0.45	1.95 ± 0.36
1	11	4.61	0.63	1.61 ± 0.03	2.30 ± 0.71	1.86 ± 0.35	1.52 ± 0.30	1.79 ± 0.22
1	12	5.45	0.67	1.84 ± 0.04	2.08 ± 0.84	1.85 ± 0.48	1.46 ± 0.33	1.76 ± 0.29
1	13	5.67	0.68	1.84 ± 0.05	2.40 ± 0.83	2.11 ± 0.40	1.62 ± 0.36	1.90 ± 0.26
1	14	4.22	0.87	1.71 ± 0.04	1.50 ± 0.78	1.85 ± 0.36	1.37 ± 0.37	1.65 ± 0.25
1	15	4.62	0.89	1.72 ± 0.04	0.81 ± 0.90	2.20 ± 0.46	1.50 ± 0.45	1.95 ± 0.30
1	16	4.89	0.90	1.75 ± 0.04	1.56 ± 0.96	2.46 ± 0.55	1.33 ± 0.54	1.95 ± 0.38
1	17	5.16	0.91	1.74 ± 0.04	1.61 ± 0.83	2.48 ± 0.52	1.52 ± 0.50	2.06 ± 0.34
1	18	5.43	0.92	1.58 ± 0.04	1.19 ± 0.75	1.90 ± 0.47	1.31 ± 0.42	1.66 ± 0.29
1	19	5.69	0.94	1.75 ± 0.04	0.08 ± 0.90	1.92 ± 0.51	1.79 ± 0.50	1.96 ± 0.33
1	20	4.07	1.14	1.62 ± 0.04	1.59 ± 0.94	2.48 ± 0.55	1.13 ± 0.54	1.79 ± 0.39
1	21	4.34	1.15	1.63 ± 0.03	0.92 ± 0.82	2.23 ± 0.36	1.63 ± 0.34	2.06 ± 0.24
1	22	4.61	1.16	1.65 ± 0.04	2.07 ± 0.98	2.33 ± 0.45	1.37 ± 0.47	1.89 ± 0.30
1	23	4.88	1.17	1.57 ± 0.03	0.86 ± 0.71	2.25 ± 0.33	1.45 ± 0.38	1.87 ± 0.26
1	24	5.15	1.18	1.60 ± 0.03	1.33 ± 0.72	2.41 ± 0.52	2.00 ± 0.48	2.31 ± 0.34

Table F1 – Continued

Pointing Number	Aperture Number	$r_{\rm proj}$ (kpc)	z (kpc)	D_n4000	$H\delta_A$ (Å)	Mgb (Å)	$\langle$Fe$\rangle$ (Å)	[MgFe] (Å)
1	25	5.55	1.20	1.56 ± 0.03	0.10 ± 0.85	2.15 ± 0.47	1.29 ± 0.48	1.84 ± 0.32
1	26	4.06	1.40	1.63 ± 0.03	0.53 ± 0.67	1.93 ± 0.41	1.53 ± 0.36	1.77 ± 0.26
1	27	4.33	1.42	1.54 ± 0.03	0.54 ± 0.72	2.20 ± 0.39	1.43 ± 0.38	1.86 ± 0.26
1	28	4.60	1.43	1.55 ± 0.03	0.67 ± 0.71	2.22 ± 0.49	1.64 ± 0.48	2.00 ± 0.32
1	29	5.00	1.44	1.50 ± 0.03	0.69 ± 0.75	2.09 ± 0.48	1.58 ± 0.48	1.91 ± 0.32
1	30	5.54	1.47	1.42 ± 0.04	-1.41 ± 1.21	1.72 ± 0.73	0.53 ± 0.79	1.10 ± 0.58
1	31	4.04	1.71	1.54 ± 0.03	0.18 ± 0.79	2.93 ± 0.39	1.20 ± 0.33	1.96 ± 0.27
1	32	4.37	1.72	1.52 ± 0.03	0.49 ± 0.82	2.24 ± 0.44	1.36 ± 0.37	1.88 ± 0.28
1	33	4.85	1.75	1.65 ± 0.03	1.01 ± 0.76	2.42 ± 0.48	1.27 ± 0.33	1.79 ± 0.28
1	34	5.50	1.77	1.87 ± 0.05	-0.46 ± 0.99	1.71 ± 0.62	1.85 ± 0.48	1.82 ± 0.40
1	35	4.19	2.04	1.54 ± 0.03	-0.83 ± 0.90	2.95 ± 0.40	1.20 ± 0.32	2.09 ± 0.27
1	36	5.16	2.08	1.55 ± 0.03	0.82 ± 0.90	2.47 ± 0.50	1.26 ± 0.39	1.92 ± 0.32
1	37	4.82	2.39	1.28 ± 0.02	-0.50 ± 0.93	1.76 ± 0.48	1.24 ± 0.42	1.56 ± 0.31
2	1	1.27	-0.17	1.41 ± 0.08	-0.71 ± 2.54	2.95 ± 1.02	1.68 ± 0.78	2.22 ± 0.64
2	2	1.26	-0.02	1.10 ± 0.04	7.57 ± 1.44	1.47 ± 1.06	0.65 ± 0.68	1.06 ± 0.63
2	3	1.26	0.15	1.25 ± 0.04	6.53 ± 1.07	0.83 ± 0.75	-0.01 ± 0.69	nan ± nan
2	4	1.25	0.35	1.45 ± 0.02	2.99 ± 0.64	1.91 ± 0.36	1.65 ± 0.38	1.86 ± 0.25
2	5	0.69	0.55	1.68 ± 0.03	0.39 ± 0.72	1.95 ± 0.44	1.53 ± 0.39	1.84 ± 0.29
2	6	1.35	0.58	1.81 ± 0.04	1.59 ± 0.64	2.22 ± 0.33	1.71 ± 0.29	2.09 ± 0.21
2	7	1.90	0.60	1.83 ± 0.05	1.05 ± 1.10	2.19 ± 0.49	1.39 ± 0.39	1.86 ± 0.31
2	8	0.42	0.79	1.88 ± 0.03	0.21 ± 0.61	2.26 ± 0.19	1.56 ± 0.15	1.94 ± 0.12
2	9	0.69	0.81	1.76 ± 0.03	1.16 ± 0.51	1.21 ± 0.24	0.67 ± 0.19	1.08 ± 0.14
2	10	0.96	0.82	1.81 ± 0.02	0.66 ± 0.45	2.09 ± 0.24	1.24 ± 0.21	1.73 ± 0.16
2	11	1.23	0.83	1.84 ± 0.03	1.09 ± 0.69	2.12 ± 0.35	1.24 ± 0.25	1.72 ± 0.21
2	12	1.49	0.84	1.75 ± 0.03	0.42 ± 0.65	1.88 ± 0.24	1.50 ± 0.24	1.81 ± 0.16

Table F1 – Continued

Pointing Number	Aperture Number	$r_{\rm proj}$ (kpc)	z (kpc)	D_n4000	$H\delta_A$ (Å)	Mgb (Å)	$\langle$Fe$\rangle$ (Å)	[MgFe] (Å)
2	13	1.76	0.85	1.67 ± 0.04	0.14 ± 0.82	2.45 ± 0.24	1.54 ± 0.22	1.97 ± 0.17
2	14	2.03	0.86	1.67 ± 0.04	1.51 ± 1.01	1.74 ± 0.38	1.09 ± 0.27	1.56 ± 0.22
2	15	0.41	1.06	1.76 ± 0.03	0.35 ± 0.60	2.04 ± 0.27	1.59 ± 0.24	1.88 ± 0.18
2	16	0.68	1.07	1.72 ± 0.03	0.72 ± 0.57	1.59 ± 0.37	1.06 ± 0.24	1.38 ± 0.20
2	17	0.95	1.08	1.68 ± 0.02	-0.21 ± 0.56	2.18 ± 0.29	1.21 ± 0.29	1.76 ± 0.20
2	18	1.21	1.10	1.71 ± 0.03	0.89 ± 0.53	2.06 ± 0.29	1.15 ± 0.23	1.64 ± 0.17
2	19	1.48	1.11	1.69 ± 0.03	1.31 ± 0.68	2.04 ± 0.33	1.29 ± 0.24	1.76 ± 0.19
2	20	1.75	1.12	1.68 ± 0.03	-0.04 ± 0.80	2.61 ± 0.35	1.58 ± 0.32	2.14 ± 0.23
2	21	2.02	1.13	1.53 ± 0.04	1.09 ± 0.78	1.76 ± 0.42	0.37 ± 0.38	1.00 ± 0.35
2	22	0.40	1.33	1.69 ± 0.03	-0.22 ± 0.81	1.87 ± 0.36	1.35 ± 0.39	1.67 ± 0.28
2	23	0.67	1.34	1.68 ± 0.03	0.58 ± 0.65	2.07 ± 0.37	1.07 ± 0.27	1.51 ± 0.25
2	24	0.93	1.35	1.65 ± 0.02	0.05 ± 0.73	1.85 ± 0.34	1.49 ± 0.35	1.73 ± 0.23
2	25	1.20	1.36	1.60 ± 0.03	-0.26 ± 0.65	2.24 ± 0.48	1.57 ± 0.44	1.95 ± 0.34
2	26	1.47	1.38	1.65 ± 0.03	0.14 ± 0.69	2.28 ± 0.46	1.50 ± 0.38	1.86 ± 0.30
2	27	1.74	1.39	1.60 ± 0.04	0.61 ± 0.91	2.19 ± 0.44	1.30 ± 0.45	1.81 ± 0.31
2	28	2.01	1.40	1.56 ± 0.05	0.70 ± 0.96	1.85 ± 0.78	1.51 ± 0.56	1.65 ± 0.50
2	29	0.38	1.64	1.58 ± 0.04	-0.92 ± 0.97	1.96 ± 0.41	1.28 ± 0.43	1.75 ± 0.28
2	30	0.70	1.65	1.55 ± 0.03	-0.55 ± 0.79	1.88 ± 0.54	0.91 ± 0.38	1.38 ± 0.31
2	31	1.03	1.67	1.69 ± 0.04	0.42 ± 0.84	1.64 ± 0.63	0.49 ± 0.53	1.09 ± 0.41
2	32	1.35	1.68	1.60 ± 0.04	0.81 ± 0.90	1.81 ± 0.48	0.87 ± 0.34	1.39 ± 0.32
2	33	1.68	1.69	1.66 ± 0.04	2.20 ± 1.04	1.88 ± 0.58	1.16 ± 0.43	1.64 ± 0.36
2	34	2.00	1.71	1.63 ± 0.04	0.73 ± 0.89	1.45 ± 0.54	0.56 ± 0.47	0.98 ± 0.40
2	35	0.36	1.96	1.51 ± 0.04	-0.46 ± 1.03	-0.20 ± 0.51	-0.34 ± 0.41	0.26 ± 0.36
2	36	1.18	2.00	1.53 ± 0.03	0.45 ± 0.78	1.80 ± 0.43	0.88 ± 0.35	1.32 ± 0.28
2	37	1.99	2.03	1.44 ± 0.06	0.37 ± 1.58	0.55 ± 1.16	1.30 ± 0.72	0.94 ± 1.02

Table F1 – Continued

Pointing Number	Aperture Number	$r_{\rm proj}$ (kpc)	z (kpc)	D_n4000	$H\delta_A$ (Å)	Mgb (Å)	$\langle$Fe$\rangle$ (Å)	[MgFe] (Å)
2	38	1.16	2.32	1.35 ± 0.03	0.25 ± 0.95	1.60 ± 0.57	0.80 ± 0.48	1.22 ± 0.37
3	1	-6.31	-0.17	1.52 ± 0.02	4.36 ± 0.50	1.42 ± 0.38	1.30 ± 0.30	1.43 ± 0.24
3	2	-5.98	-0.16	1.29 ± 0.02	4.49 ± 0.70	1.34 ± 0.49	1.14 ± 0.36	1.36 ± 0.30
3	3	-5.76	-0.15	1.30 ± 0.02	3.37 ± 0.72	1.89 ± 0.52	0.78 ± 0.45	1.31 ± 0.34
3	4	-5.43	-0.14	1.18 ± 0.01	3.06 ± 0.57	2.07 ± 0.51	1.22 ± 0.42	1.70 ± 0.32
3	5	-5.05	-0.12	1.18 ± 0.01	5.42 ± 0.56	1.76 ± 0.49	1.33 ± 0.37	1.53 ± 0.29
3	6	-6.39	-0.03	1.16 ± 0.01	5.14 ± 0.40	1.30 ± 0.39	0.93 ± 0.35	1.13 ± 0.26
3	7	-6.13	-0.01	1.16 ± 0.01	4.03 ± 0.47	0.88 ± 0.46	0.57 ± 0.36	0.80 ± 0.28
3	8	-5.97	-0.01	1.13 ± 0.01	3.85 ± 0.49	0.58 ± 0.35	0.33 ± 0.31	0.55 ± 0.23
3	9	-5.80	0.00	1.09 ± 0.01	4.46 ± 0.50	1.36 ± 0.46	0.81 ± 0.40	1.14 ± 0.30
3	10	-5.63	0.01	1.19 ± 0.02	3.11 ± 0.81	1.30 ± 0.46	0.84 ± 0.43	1.09 ± 0.32
3	11	-5.46	0.01	1.21 ± 0.01	4.54 ± 0.46	1.75 ± 0.35	0.92 ± 0.32	1.35 ± 0.24
3	12	-5.20	0.03	1.19 ± 0.01	4.70 ± 0.46	1.79 ± 0.34	0.54 ± 0.27	1.09 ± 0.24
3	13	-4.95	0.04	1.20 ± 0.01	3.63 ± 0.63	1.28 ± 0.57	0.56 ± 0.43	0.91 ± 0.37
3	14	-6.48	0.14	1.26 ± 0.01	5.66 ± 0.41	0.94 ± 0.43	0.95 ± 0.38	1.07 ± 0.29
3	15	-6.31	0.15	1.17 ± 0.01	5.07 ± 0.42	1.18 ± 0.33	0.86 ± 0.27	1.14 ± 0.21
3	16	-6.14	0.15	1.21 ± 0.01	4.88 ± 0.50	0.99 ± 0.36	0.74 ± 0.31	0.82 ± 0.24
3	17	-5.89	0.17	1.15 ± 0.01	4.11 ± 0.51	1.04 ± 0.40	0.68 ± 0.33	0.92 ± 0.25
3	18	-5.55	0.18	1.21 ± 0.01	4.16 ± 0.55	1.17 ± 0.36	0.66 ± 0.28	0.99 ± 0.22
3	19	-5.29	0.19	1.26 ± 0.02	1.92 ± 0.84	0.90 ± 0.54	0.96 ± 0.36	1.02 ± 0.35
3	20	-5.04	0.20	1.30 ± 0.02	3.18 ± 0.58	1.28 ± 0.33	1.10 ± 0.28	1.27 ± 0.21
3	21	-6.50	0.35	1.28 ± 0.02	4.71 ± 0.71	1.61 ± 0.35	1.09 ± 0.31	1.35 ± 0.23
3	22	-6.28	0.36	1.25 ± 0.02	1.06 ± 0.93	1.33 ± 0.57	1.04 ± 0.44	1.24 ± 0.35
3	23	-6.06	0.37	1.22 ± 0.01	2.99 ± 0.57	1.96 ± 0.36	1.10 ± 0.29	1.55 ± 0.23
3	24	-5.84	0.38	1.20 ± 0.01	2.99 ± 0.55	1.71 ± 0.29	1.05 ± 0.26	1.43 ± 0.19

Table F1 – Continued

Pointing Number	Aperture Number	$r_{\rm proj}$ (kpc)	z (kpc)	D_n4000	$H\delta_A$ (Å)	Mgb (Å)	$\langle$Fe$\rangle$ (Å)	[MgFe] (Å)
3	25	-5.51	0.39	1.24 ± 0.01	2.28 ± 0.44	1.61 ± 0.33	1.09 ± 0.24	1.27 ± 0.20
3	26	-5.18	0.40	1.37 ± 0.02	2.30 ± 0.55	2.04 ± 0.38	1.06 ± 0.32	1.55 ± 0.26
3	27	-4.96	0.41	1.42 ± 0.02	0.05 ± 0.79	1.76 ± 0.41	1.15 ± 0.36	1.43 ± 0.28
3	28	-6.51	0.57	1.55 ± 0.02	2.40 ± 0.57	2.13 ± 0.38	1.26 ± 0.36	1.74 ± 0.26
3	29	-6.29	0.58	1.47 ± 0.02	4.63 ± 0.64	1.94 ± 0.35	1.63 ± 0.33	1.86 ± 0.23
3	30	-6.07	0.59	1.48 ± 0.02	1.23 ± 0.70	2.33 ± 0.49	1.26 ± 0.43	1.77 ± 0.32
3	31	-5.85	0.60	1.53 ± 0.02	0.90 ± 0.66	1.70 ± 0.40	1.48 ± 0.32	1.70 ± 0.25
3	32	-5.41	0.61	1.60 ± 0.03	0.46 ± 0.68	2.05 ± 0.38	1.10 ± 0.30	1.56 ± 0.24
3	33	-5.19	0.62	1.69 ± 0.03	1.54 ± 0.62	1.85 ± 0.27	1.39 ± 0.23	1.73 ± 0.17
3	34	-4.97	0.63	1.55 ± 0.02	1.14 ± 0.68	1.81 ± 0.40	1.29 ± 0.30	1.58 ± 0.24
3	35	-6.55	0.82	1.68 ± 0.02	0.06 ± 0.40	1.75 ± 0.25	1.31 ± 0.19	1.52 ± 0.15
3	36	-6.29	0.83	1.47 ± 0.01	0.69 ± 0.43	1.90 ± 0.26	1.03 ± 0.26	1.44 ± 0.20
3	37	-6.02	0.84	1.47 ± 0.02	0.34 ± 0.51	2.15 ± 0.31	1.20 ± 0.25	1.66 ± 0.20
3	38	-5.75	0.86	1.60 ± 0.02	-0.12 ± 0.46	2.44 ± 0.22	1.33 ± 0.23	1.88 ± 0.17
3	39	-5.48	0.87	1.54 ± 0.01	1.73 ± 0.47	1.83 ± 0.31	0.91 ± 0.30	1.36 ± 0.23
3	40	-5.21	0.88	1.48 ± 0.02	-0.18 ± 0.58	1.78 ± 0.26	1.27 ± 0.23	1.55 ± 0.17
3	41	-4.94	0.89	1.56 ± 0.01	0.82 ± 0.42	2.20 ± 0.25	1.19 ± 0.21	1.69 ± 0.16
3	42	-6.57	1.09	1.56 ± 0.02	0.34 ± 0.72	2.16 ± 0.53	1.21 ± 0.50	1.78 ± 0.35
3	43	-6.30	1.10	1.56 ± 0.02	-0.60 ± 0.78	1.91 ± 0.51	0.98 ± 0.42	1.53 ± 0.32
3	44	-6.03	1.11	1.60 ± 0.02	0.33 ± 0.55	1.79 ± 0.44	1.17 ± 0.34	1.55 ± 0.26
3	45	-5.76	1.12	1.53 ± 0.02	0.13 ± 0.50	2.33 ± 0.32	1.07 ± 0.31	1.67 ± 0.25
3	46	-5.49	1.14	1.47 ± 0.02	0.04 ± 0.53	2.30 ± 0.36	1.17 ± 0.31	1.63 ± 0.26
3	47	-5.22	1.15	1.50 ± 0.02	0.81 ± 0.55	1.91 ± 0.34	0.86 ± 0.33	1.34 ± 0.26
3	48	-4.96	1.16	1.50 ± 0.02	0.08 ± 0.59	1.52 ± 0.36	1.07 ± 0.35	1.41 ± 0.24
3	49	-6.44	1.36	1.46 ± 0.02	0.60 ± 0.57	2.30 ± 0.35	1.28 ± 0.29	1.67 ± 0.23

Table F1 – Continued

Pointing Number	Aperture Number	$r_{\rm proj}$ (kpc)	z (kpc)	D_n4000	$H\delta_A$ (Å)	Mgb (Å)	$\langle$Fe$\rangle$ (Å)	[MgFe] (Å)
3	50	-6.04	1.38	1.40 ± 0.02	0.45 ± 0.72	1.56 ± 0.58	1.14 ± 0.39	1.24 ± 0.33
3	51	-5.64	1.40	1.44 ± 0.01	1.12 ± 0.52	2.44 ± 0.33	0.94 ± 0.26	1.52 ± 0.23
3	52	-5.10	1.42	1.38 ± 0.01	0.96 ± 0.52	1.54 ± 0.35	0.74 ± 0.29	1.14 ± 0.23
3	53	-6.43	1.67	1.39 ± 0.02	-0.06 ± 0.80	2.14 ± 0.41	0.65 ± 0.35	1.41 ± 0.28
3	54	-5.46	1.72	1.46 ± 0.02	1.17 ± 0.56	2.12 ± 0.31	0.46 ± 0.30	1.24 ± 0.25
3	55	-6.29	2.00	1.42 ± 0.02	0.79 ± 0.74	3.66 ± 0.39	0.65 ± 0.34	1.59 ± 0.38
3	56	-5.47	2.04	1.35 ± 0.02	1.97 ± 0.66	2.40 ± 0.40	0.68 ± 0.36	1.53 ± 0.29
3	57	-4.99	2.06	1.36 ± 0.03	1.38 ± 0.88	1.94 ± 0.55	0.04 ± 0.48	0.54 ± 0.79
3	58	-5.78	2.35	1.33 ± 0.02	2.09 ± 0.64	2.81 ± 0.39	0.18 ± 0.35	1.02 ± 0.48
3	59	-5.97	2.34	1.27 ± 0.04	1.84 ± 1.44	3.40 ± 1.10	-0.14 ± 0.69	1.12 ± 1.14
4	1	-2.61	-0.29	1.68 ± 0.05	7.41 ± 0.86	1.36 ± 0.51	0.70 ± 0.41	0.90 ± 0.34
4	2	-2.23	-0.27	0.97 ± 0.10	5.07 ± 0.77	1.98 ± 0.49	2.08 ± 0.52	2.21 ± 0.39
4	3	-1.84	-0.25	1.16 ± 0.02	4.57 ± 0.79	1.51 ± 0.51	1.08 ± 0.40	1.32 ± 0.32
4	4	-1.51	-0.24	1.22 ± 0.02	3.07 ± 0.73	1.01 ± 0.42	1.36 ± 0.35	1.13 ± 0.28
4	5	-1.24	-0.23	1.14 ± 0.02	3.90 ± 0.83	0.72 ± 0.63	0.97 ± 0.46	0.90 ± 0.44
4	6	-2.72	-0.14	1.12 ± 0.02	4.68 ± 0.69	1.21 ± 0.47	0.76 ± 0.37	0.91 ± 0.29
4	7	-2.47	-0.13	1.10 ± 0.01	3.28 ± 0.73	1.41 ± 0.46	0.92 ± 0.42	1.24 ± 0.30
4	8	-2.13	-0.12	1.13 ± 0.02	4.03 ± 0.71	1.49 ± 0.54	0.86 ± 0.40	1.02 ± 0.34
4	9	-1.87	-0.10	1.36 ± 0.02	4.32 ± 0.81	1.61 ± 0.44	0.57 ± 0.47	1.06 ± 0.35
4	10	-1.62	-0.09	1.27 ± 0.01	5.54 ± 0.44	1.86 ± 0.34	1.04 ± 0.32	1.36 ± 0.25
4	11	-1.28	-0.08	1.32 ± 0.02	3.67 ± 0.55	1.86 ± 0.40	0.86 ± 0.32	1.29 ± 0.28
4	12	-2.64	0.03	1.13 ± 0.01	5.53 ± 0.69	1.14 ± 0.52	0.69 ± 0.42	0.90 ± 0.33
4	13	-2.39	0.04	1.15 ± 0.01	3.44 ± 0.57	1.05 ± 0.54	0.91 ± 0.39	1.02 ± 0.33
4	14	-2.13	0.06	1.29 ± 0.02	4.70 ± 0.56	1.41 ± 0.41	0.82 ± 0.36	1.19 ± 0.27
4	15	-1.88	0.07	1.35 ± 0.03	5.97 ± 0.74	2.37 ± 0.45	1.41 ± 0.40	1.86 ± 0.31

Table F1 – Continued

Pointing Number	Aperture Number	$r_{\rm proj}$ (kpc)	z (kpc)	D_n4000	$H\delta_A$ (Å)	Mgb (Å)	$\langle$Fe$\rangle$ (Å)	[MgFe] (Å)
4	16	-1.71	0.07	1.27 ± 0.02	5.63 ± 0.64	1.11 ± 0.46	1.38 ± 0.33	1.31 ± 0.30
4	17	-1.37	0.09	1.29 ± 0.02	3.87 ± 0.60	1.83 ± 0.42	1.11 ± 0.36	1.51 ± 0.27
4	18	-2.52	0.24	1.23 ± 0.01	5.18 ± 0.42	1.50 ± 0.43	1.20 ± 0.38	1.34 ± 0.28
4	19	-1.97	0.27	1.33 ± 0.01	4.44 ± 0.56	1.85 ± 0.47	1.95 ± 1.03	1.76 ± 0.41
4	20	-1.53	0.29	1.38 ± 0.01	4.19 ± 0.55	1.75 ± 0.49	1.07 ± 0.46	1.44 ± 0.34
4	21	-1.20	0.30	1.39 ± 0.02	2.37 ± 0.68	2.02 ± 0.64	0.82 ± 0.57	1.35 ± 0.46
4	22	-2.75	0.46	1.50 ± 0.02	1.44 ± 0.54	2.09 ± 0.33	1.34 ± 0.29	1.71 ± 0.22
4	23	-2.53	0.47	1.59 ± 0.02	1.27 ± 0.68	2.06 ± 0.37	1.36 ± 0.33	1.75 ± 0.24
4	24	-2.31	0.47	1.62 ± 0.02	1.73 ± 0.65	2.24 ± 0.38	1.43 ± 0.28	1.90 ± 0.23
4	25	-2.09	0.48	1.65 ± 0.01	0.94 ± 0.45	2.10 ± 0.27	1.27 ± 0.25	1.71 ± 0.18
4	26	-1.65	0.50	1.67 ± 0.01	2.00 ± 0.42	2.14 ± 0.28	1.43 ± 0.21	1.82 ± 0.17
4	27	-1.43	0.51	1.69 ± 0.02	1.70 ± 0.51	2.12 ± 0.30	1.49 ± 0.27	1.89 ± 0.19
4	28	-1.21	0.52	1.67 ± 0.02	1.44 ± 0.46	1.92 ± 0.38	1.33 ± 0.32	1.66 ± 0.24
4	29	-2.80	0.71	1.84 ± 0.02	0.78 ± 0.37	2.03 ± 0.22	1.40 ± 0.20	1.77 ± 0.14
4	30	-2.53	0.72	1.62 ± 0.01	1.14 ± 0.47	1.85 ± 0.29	1.44 ± 0.23	1.67 ± 0.19
4	31	-2.26	0.73	1.70 ± 0.01	0.69 ± 0.39	2.11 ± 0.21	1.51 ± 0.19	1.85 ± 0.14
4	32	-1.99	0.74	1.71 ± 0.01	0.38 ± 0.31	2.25 ± 0.20	1.58 ± 0.20	1.96 ± 0.14
4	33	-1.73	0.76	1.66 ± 0.01	0.41 ± 0.37	2.23 ± 0.21	1.33 ± 0.20	1.80 ± 0.15
4	34	-1.46	0.77	1.65 ± 0.01	0.40 ± 0.36	2.29 ± 0.20	1.53 ± 0.19	1.96 ± 0.14
4	35	-1.19	0.78	1.72 ± 0.01	0.48 ± 0.40	2.35 ± 0.22	1.55 ± 0.22	1.99 ± 0.16
4	36	-2.81	0.98	1.63 ± 0.01	0.45 ± 0.44	2.11 ± 0.21	1.37 ± 0.18	1.79 ± 0.14
4	37	-2.54	0.99	1.68 ± 0.01	0.82 ± 0.37	2.22 ± 0.21	1.48 ± 0.22	1.88 ± 0.15
4	38	-2.27	1.00	1.64 ± 0.01	1.11 ± 0.30	2.18 ± 0.22	1.35 ± 0.18	1.78 ± 0.14
4	39	-2.01	1.01	1.64 ± 0.01	0.36 ± 0.33	2.29 ± 0.23	1.49 ± 0.20	1.91 ± 0.15
4	40	-1.74	1.02	1.62 ± 0.01	0.44 ± 0.27	2.35 ± 0.21	1.63 ± 0.19	2.03 ± 0.14

Table F1 – Continued

Pointing Number	Aperture Number	$r_{\rm proj}$ (kpc)	z (kpc)	D_n4000	$H\delta_A$ (Å)	Mgb (Å)	$\langle$Fe$\rangle$ (Å)	[MgFe] (Å)
4	41	-1.47	1.04	1.64 ± 0.01	0.44 ± 0.26	2.46 ± 0.19	1.54 ± 0.17	2.05 ± 0.13
4	42	-1.20	1.05	1.66 ± 0.01	0.32 ± 0.27	2.26 ± 0.20	1.39 ± 0.17	1.83 ± 0.13
4	43	-2.82	1.25	1.62 ± 0.02	1.35 ± 0.46	2.32 ± 0.27	1.18 ± 0.21	1.79 ± 0.18
4	44	-2.56	1.26	1.58 ± 0.01	0.22 ± 0.44	2.30 ± 0.25	1.40 ± 0.21	1.88 ± 0.17
4	45	-2.29	1.27	1.58 ± 0.01	0.23 ± 0.42	2.23 ± 0.25	1.40 ± 0.23	1.84 ± 0.17
4	46	-2.02	1.28	1.57 ± 0.01	0.38 ± 0.34	2.06 ± 0.24	1.49 ± 0.22	1.81 ± 0.15
4	47	-1.75	1.29	1.59 ± 0.01	0.18 ± 0.32	2.20 ± 0.24	1.35 ± 0.20	1.79 ± 0.16
4	48	-1.48	1.30	1.57 ± 0.01	0.32 ± 0.35	2.13 ± 0.24	1.49 ± 0.21	1.87 ± 0.15
4	49	-1.21	1.32	1.58 ± 0.01	0.14 ± 0.30	2.22 ± 0.23	1.39 ± 0.19	1.80 ± 0.15
4	50	-2.84	1.55	1.56 ± 0.02	-0.05 ± 0.54	1.96 ± 0.31	1.31 ± 0.27	1.70 ± 0.20
4	51	-2.52	1.57	1.57 ± 0.02	0.15 ± 0.47	1.91 ± 0.28	1.30 ± 0.25	1.61 ± 0.19
4	52	-2.19	1.58	1.58 ± 0.02	0.83 ± 0.51	2.03 ± 0.29	1.39 ± 0.25	1.80 ± 0.19
4	53	-1.87	1.60	1.61 ± 0.01	0.22 ± 0.42	1.93 ± 0.26	1.40 ± 0.23	1.69 ± 0.17
4	54	-1.54	1.61	1.62 ± 0.01	-0.23 ± 0.35	1.79 ± 0.21	1.30 ± 0.20	1.58 ± 0.14
4	55	-1.22	1.62	1.54 ± 0.01	0.36 ± 0.30	1.56 ± 0.25	1.29 ± 0.21	1.47 ± 0.15
4	56	-2.85	1.88	1.55 ± 0.03	-1.50 ± 0.77	2.58 ± 0.38	0.79 ± 0.34	1.45 ± 0.32
4	57	-2.53	1.89	1.47 ± 0.02	-0.55 ± 0.66	2.02 ± 0.37	1.14 ± 0.33	1.46 ± 0.25
4	58	-2.21	1.91	1.48 ± 0.02	0.62 ± 0.56	1.90 ± 0.32	1.37 ± 0.27	1.63 ± 0.21
4	59	-1.88	1.92	1.42 ± 0.01	-0.27 ± 0.43	1.62 ± 0.30	1.23 ± 0.26	1.57 ± 0.20
4	60	-2.71	2.21	1.28 ± 0.02	1.65 ± 0.64	1.53 ± 0.43	0.91 ± 0.31	1.25 ± 0.25
5	1	8.18	-0.05	2.36 ± 0.09	0.80 ± 0.89	1.55 ± 0.52	0.25 ± 0.40	0.81 ± 0.40
5	2	8.02	0.09	1.14 ± 0.02	7.10 ± 0.58	0.57 ± 0.42	0.58 ± 0.33	0.53 ± 0.26
5	3	8.61	0.12	1.26 ± 0.02	3.33 ± 0.62	1.23 ± 0.49	1.04 ± 0.36	1.05 ± 0.29
5	4	9.21	0.14	1.23 ± 0.02	3.36 ± 0.65	0.92 ± 0.52	0.14 ± 0.42	0.53 ± 0.40
5	5	8.18	0.27	1.31 ± 0.03	2.96 ± 0.74	1.09 ± 0.48	1.15 ± 0.34	0.93 ± 0.29

Table F1 – Continued

Pointing Number	Aperture Number	$r_{\rm proj}$ (kpc)	z (kpc)	D_n4000	$H\delta_A$ (Å)	Mgb (Å)	$\langle$Fe$\rangle$ (Å)	[MgFe] (Å)
5	6	9.03	0.30	1.31 ± 0.02	4.30 ± 0.58	0.63 ± 0.42	0.37 ± 0.36	0.27 ± 0.44
5	7	7.94	0.46	1.17 ± 0.02	2.05 ± 0.76	1.77 ± 0.42	1.51 ± 0.34	1.68 ± 0.27
5	8	8.49	0.49	1.20 ± 0.01	3.58 ± 0.56	1.36 ± 0.39	1.72 ± 0.35	1.65 ± 0.27
5	9	9.04	0.51	1.37 ± 0.02	3.18 ± 0.68	1.86 ± 0.39	1.59 ± 0.33	1.85 ± 0.25
5	10	9.37	0.53	1.41 ± 0.03	1.03 ± 0.75	2.02 ± 0.56	1.35 ± 0.46	1.78 ± 0.35
5	11	7.93	0.68	1.48 ± 0.03	0.73 ± 0.84	2.13 ± 0.47	1.26 ± 0.37	1.85 ± 0.29
5	12	8.37	0.70	1.56 ± 0.02	2.45 ± 0.57	2.12 ± 0.34	1.51 ± 0.29	2.01 ± 0.22
5	13	9.03	0.73	1.76 ± 0.03	0.39 ± 0.64	1.63 ± 0.34	1.84 ± 0.28	1.72 ± 0.23
5	14	9.36	0.74	1.96 ± 0.05	1.34 ± 0.76	2.04 ± 0.41	0.54 ± 0.39	1.14 ± 0.36
5	15	7.77	0.93	1.40 ± 0.03	2.00 ± 0.80	2.24 ± 0.49	1.50 ± 0.41	1.86 ± 0.31
5	16	8.04	0.94	1.61 ± 0.03	3.35 ± 0.67	2.86 ± 0.40	1.13 ± 0.38	1.71 ± 0.31
5	17	8.31	0.96	1.57 ± 0.03	1.50 ± 0.71	2.14 ± 0.46	1.46 ± 0.36	1.79 ± 0.28
5	18	8.58	0.97	1.67 ± 0.03	1.29 ± 0.67	1.75 ± 0.37	1.62 ± 0.34	1.68 ± 0.24
5	19	8.85	0.98	1.61 ± 0.03	2.34 ± 0.74	1.73 ± 0.43	1.06 ± 0.38	1.29 ± 0.29
5	20	9.25	1.00	1.51 ± 0.02	1.69 ± 0.54	2.38 ± 0.34	1.16 ± 0.28	1.83 ± 0.22
5	21	7.89	1.21	1.70 ± 0.03	0.31 ± 0.65	2.65 ± 0.35	1.09 ± 0.29	1.71 ± 0.24
5	22	8.43	1.23	1.58 ± 0.03	2.87 ± 0.64	2.25 ± 0.39	0.92 ± 0.31	1.30 ± 0.29
5	23	8.97	1.25	1.58 ± 0.03	0.60 ± 0.70	3.25 ± 0.40	1.12 ± 0.34	2.02 ± 0.30
5	24	9.37	1.27	1.41 ± 0.04	3.11 ± 1.18	2.58 ± 0.61	0.04 ± 0.51	nan ± nan
5	25	8.02	1.48	1.49 ± 0.03	0.77 ± 0.67	2.31 ± 0.40	0.72 ± 0.31	1.31 ± 0.29
5	26	8.96	1.52	1.43 ± 0.02	-1.04 ± 0.71	3.55 ± 0.38	1.44 ± 0.33	2.32 ± 0.28
5	27	8.51	1.81	2.03 ± 0.06	-1.98 ± 0.82	0.13 ± 0.42	1.02 ± 0.33	0.37 ± 0.60
5	28	8.53	2.13	1.63 ± 0.04	-0.27 ± 1.09	2.29 ± 0.53	2.67 ± 0.47	2.51 ± 0.36
5	29	8.51	2.46	0.97 ± 0.03	2.69 ± 1.37	0.39 ± 1.06	3.36 ± 0.82	1.28 ± 1.76
6	1	-10.37	-0.07	1.62 ± 0.03	2.78 ± 0.68	1.58 ± 0.42	1.56 ± 0.31	1.60 ± 0.26

Table F1 – Continued

Pointing Number	Aperture Number	$r_{\rm proj}$ (kpc)	z (kpc)	D_n4000	$H\delta_A$ (Å)	Mgb (Å)	$\langle$Fe$\rangle$ (Å)	[MgFe] (Å)
6	2	-9.82	-0.04	1.21 ± 0.02	2.80 ± 0.62	1.32 ± 0.45	0.90 ± 0.33	1.08 ± 0.27
6	3	-9.27	-0.02	1.12 ± 0.01	3.74 ± 0.54	1.64 ± 0.41	1.23 ± 0.34	1.34 ± 0.27
6	4	-10.50	0.08	1.33 ± 0.01	4.19 ± 0.45	1.81 ± 0.40	1.21 ± 0.36	1.52 ± 0.27
6	5	-10.16	0.09	1.27 ± 0.02	4.07 ± 0.56	1.59 ± 0.47	0.75 ± 0.41	1.14 ± 0.32
6	6	-9.82	0.11	1.21 ± 0.01	4.37 ± 0.47	1.36 ± 0.44	0.55 ± 0.39	0.86 ± 0.33
6	7	-9.49	0.12	1.21 ± 0.01	4.08 ± 0.47	1.45 ± 0.42	1.17 ± 0.36	1.33 ± 0.27
6	8	-9.15	0.14	1.28 ± 0.01	5.32 ± 0.42	1.38 ± 0.40	0.62 ± 0.36	0.95 ± 0.28
6	9	-10.51	0.25	1.33 ± 0.02	5.50 ± 0.47	1.77 ± 0.41	0.85 ± 0.39	1.32 ± 0.30
6	10	-10.17	0.26	1.28 ± 0.01	2.65 ± 0.52	1.53 ± 0.42	0.60 ± 0.40	1.09 ± 0.30
6	11	-9.75	0.28	1.28 ± 0.01	5.07 ± 0.47	1.32 ± 0.36	0.50 ± 0.35	0.89 ± 0.27
6	12	-9.32	0.30	1.28 ± 0.01	4.51 ± 0.47	1.23 ± 0.45	0.55 ± 0.39	0.87 ± 0.31
6	13	-9.07	0.31	1.34 ± 0.02	5.84 ± 0.63	1.42 ± 0.55	0.93 ± 0.48	1.13 ± 0.36
6	14	-10.50	0.45	1.17 ± 0.01	4.19 ± 0.44	1.72 ± 0.36	1.03 ± 0.31	1.37 ± 0.23
6	15	-10.17	0.47	1.23 ± 0.01	5.08 ± 0.51	0.82 ± 0.44	1.24 ± 0.40	1.05 ± 0.32
6	16	-9.95	0.48	1.22 ± 0.01	5.07 ± 0.52	1.73 ± 0.46	1.16 ± 0.43	1.46 ± 0.31
6	17	-9.73	0.49	1.25 ± 0.01	5.37 ± 0.49	1.85 ± 0.42	0.87 ± 0.39	1.32 ± 0.30
6	18	-9.51	0.50	1.26 ± 0.01	6.13 ± 0.50	1.62 ± 0.47	1.16 ± 0.38	1.39 ± 0.30
6	19	-9.29	0.51	1.32 ± 0.01	5.06 ± 0.50	1.52 ± 0.44	1.07 ± 0.38	1.32 ± 0.28
6	20	-9.07	0.52	1.37 ± 0.01	5.48 ± 0.45	1.79 ± 0.42	0.93 ± 0.39	1.41 ± 0.29
6	21	-10.51	0.67	1.43 ± 0.01	4.42 ± 0.39	1.74 ± 0.34	1.19 ± 0.31	1.49 ± 0.23
6	22	-10.07	0.69	1.48 ± 0.01	3.59 ± 0.38	1.86 ± 0.31	1.30 ± 0.28	1.62 ± 0.20
6	23	-9.52	0.72	1.52 ± 0.02	3.77 ± 0.48	1.72 ± 0.42	1.10 ± 0.39	1.41 ± 0.28
6	24	-9.19	0.73	1.57 ± 0.01	4.42 ± 0.36	1.86 ± 0.32	1.20 ± 0.29	1.53 ± 0.21
6	25	-10.40	0.94	1.58 ± 0.02	1.93 ± 0.47	1.60 ± 0.38	1.19 ± 0.32	1.43 ± 0.24
6	26	-9.73	0.96	1.60 ± 0.02	2.80 ± 0.45	1.97 ± 0.35	1.40 ± 0.32	1.76 ± 0.23

Table F1 – Continued

Pointing Number	Aperture Number	$r_{\rm proj}$ (kpc)	z (kpc)	D_n4000	$H\delta_A$ (Å)	Mgb (Å)	$\langle$Fe$\rangle$ (Å)	[MgFe] (Å)
6	27	-9.19	0.99	1.53 ± 0.02	2.27 ± 0.48	2.03 ± 0.37	1.37 ± 0.33	1.76 ± 0.24
6	28	-10.54	1.20	1.62 ± 0.03	0.78 ± 0.60	2.38 ± 0.41	1.44 ± 0.36	1.87 ± 0.27
6	29	-10.01	1.22	1.69 ± 0.03	1.37 ± 0.73	2.32 ± 0.38	1.78 ± 0.35	2.13 ± 0.25
6	30	-9.47	1.25	1.66 ± 0.04	1.23 ± 0.77	2.47 ± 0.42	1.58 ± 0.37	2.02 ± 0.27
6	31	-9.07	1.26	1.66 ± 0.05	3.36 ± 0.93	1.44 ± 0.61	1.18 ± 0.47	1.35 ± 0.37
6	32	-10.42	1.47	1.59 ± 0.03	0.35 ± 0.68	2.17 ± 0.40	1.48 ± 0.34	1.86 ± 0.25
6	33	-9.62	1.51	1.49 ± 0.02	0.75 ± 0.63	1.78 ± 0.38	1.57 ± 0.29	1.71 ± 0.23
6	34	-9.08	1.53	1.51 ± 0.04	2.78 ± 1.08	2.17 ± 0.59	1.14 ± 0.46	1.72 ± 0.37
6	35	-10.06	1.80	1.91 ± 0.04	1.20 ± 0.68	1.93 ± 0.39	1.06 ± 0.30	1.58 ± 0.24
6	36	-9.09	1.84	1.83 ± 0.07	1.98 ± 1.21	-0.17 ± 0.80	1.10 ± 0.55	nan ± nan
6	37	-9.91	2.13	1.29 ± 0.02	1.60 ± 0.82	2.01 ± 0.55	1.24 ± 0.42	1.72 ± 0.34
6	38	-9.96	2.45	0.99 ± 0.03	7.07 ± 1.24	1.26 ± 0.96	1.72 ± 0.77	1.59 ± 0.67